

Fuel and Core Design Options to Overcome the Heavy Metal Loading Limit and Improve Performance and Safety of Liquid Salt Cooled Reactors

Reactor Concepts Research Development and Demonstration

Bojan Petrovic
Georgia Institute of Technology

In collaboration with:
University of Tennessee

Tom O'Connor, Federal POC
David Holcomb, Technical POC

FINAL REPORT

Fuel and Core Design Options to Overcome the Heavy Metal Loading Limit and Improve Performance and Safety of Liquid Salt Cooled Reactors

Prepared by:

Dr. Bojan Petrovic¹ (PI) (Bojan.Petrovic@gatech.edu)¹
Dr. G. Ivan Maldonado² (Co-PI) (Ivan.Maldonado@utk.edu)²

¹ Nuclear and Radiological Engineering
Georgia Institute of Technology
770 State St., Atlanta, GA 30332-0745

² Department of Nuclear Engineering
University of Tennessee
315 Pasqua Engineering Bldg, Knoxville, TN 37996-2300

Performed Under:
NEUP 12-3870, SRC#00128483
Under Prime Contract No. DE-AC07-05ID14517
(GT Project 2506H22, Research Agreement RD059)

TPOC: David Holcomb
Project Manager: Thomas O'Connor

Rev. 1
April 14, 2016

List of graduate students and postdocs that participated over the course of the project
(fully or partially funded)

Georgia Institute of Technology

Pietro Avigni
L. Michael Huang
Christopher Kingsbury
Spenser Lewis

University of Tennessee

Ondrej Chvala
Cole Gentry
Nathan George
Keith Ottinger

Table of Contents

List of Figure.....	vii
List of Tables.....	xii
1. Executive Summary	13
2. Project.....	17
2.1 Project.....	17
2.2 Objectives.....	17
2.3 Tasks and organization of the report.....	18
2.3.a Tasks.....	18
2.3.b Organization of the report.....	19
2.4 Milestones and Deliverables.....	19
2.4.a Milestones.....	19
2.4.b Deliverables	19
2.5 Personnel.....	20
2.6 Publications	21
3. Baseline AHTR Design.....	23
3.1 Fuel assembly	23
3.2 Control blade.....	25
3.3 Fuel plate	26
3.4 Fuel - TRISO particle	28
3.5 Coolant.....	28
3.6 References for this Chapter.....	29
4. Neutronics Methods and Models Development	30
4.1 Codes used	30
4.1.a SCALE.....	30
4.1.b SERPENT.....	30
4.2 Challenges in AHTR reactor physics calculations and options available in SERPENT	31
4.3 Evaluation of existing methods and SCALE Models.....	35
4.3.a SCALE 1D, 2D and 3D models.....	35
4.3.b Axial model height for improved efficiency.....	35
4.3.c Homogenization of TRISO particle layers	36
4.3.d MC run parameters	37
4.3.e Moderator material and structure.....	39
4.3.f Continuous energy (CE) vs multigroup (MG) simulations and procedure to generate MCDancoff.....	39
4.3.g Doppler Broadening in SCALE.....	42
4.3.h Depletion – use of Linear and Non-Linear Reactivity Models (LRM vs NLRM)	43

4.4	Evaluation of existing methods and SERPENT Models.....	46
4.4.a	Employing Random TRISO Particle Dispersion vs Regular Lattice Arrangements.....	46
4.4.b	Effect of Partial Layer Homogenization	49
4.4.c	Effect of Number of Depletion Regions	50
4.4.d	Effect of Photo-Neutron Reactions.....	52
4.4.e	Effect of Plate Spacers.....	53
4.5	Two-step procedure and models.....	55
4.5.a	Future Work Recommended for Two-step procedure and models.....	64
4.6	References for this Section.....	79
5.	Parametric Neutronics Studies	81
5.1	SCALE Studies.....	81
5.2	SERPENT Studies.....	85
5.2.a	Enrichment Effect.....	85
5.2.b	Packing Fraction Effect.....	87
5.2.c	Effect of Carbon to Heavy Metal Ratio	90
5.2.d	Assembly Size Effect.....	101
5.2.e	Design Considerations for Employing FCM Fuel Form	103
6.	Reactivity Control (Tasks 6).....	105
6.1	Burnable Poisons.....	105
6.2	Control Blades	110
7.	Thermal-Hydraulics Studies and Pseudo-Continuous Refueling (Tasks 5).....	113
7.1	Single channel.....	113
7.1.a	Matlab model and evaluations.....	113
7.1.b	RELAP5 single channel evaluations.....	116
7.2	Assembly models.....	119
7.2.a	1/3 assembly RELAP5 model	119
7.2.b	3D thermal-hydraulic analysis of the assembly.....	122
7.3	Reactor model.....	128
7.3.a	AHTR reactor RELAP5 model.....	128
7.4	Mechanical and thermal evaluations on the fuel assembly	130
7.4.a	Evaluation of lift force on the assembly	130
7.4.b	Heat loss to bypass flow.....	134
7.5	Computational Fluid Dynamics evaluations	135
7.5.a	2D CFD modeling	135
7.5.b	3D CFD modeling	138
7.5.c	General CFD flow evaluations	139

7.6	Neutronics in support of thermal-hydraulic modeling	143
7.6.a	Scale core model, reactivity feedback, power profiles	143
7.6.b	Neutronics modeling for online refueling	144
7.6.c	Input File Creation	145
7.7	Online refueling	148
7.7.a	Description of online refueling procedure	148
7.7.b	Pseudo-continuous refueling	149
7.7.c	2D modeling of the assembly removal	151
8.	Full Core Depletion Analyses	158
8.1	3-D Coupled Neutronic and Thermal Hydraulic Depletion Demonstration	158
8.2	FHR Multi-batch Loading Study	162
8.2.a	FHR Model used for the Optimization	162
8.2.b	Optimization Setup	164
8.3	References for this Section	166
9.	Fuel Cycle Cost Evaluation and Optimization (Tasks 1-3)	167
9.1	Re-stating the problem	167
9.2	Methodology for calculating fuel cost and fuel cycle cost	168
9.2.a	Previous and preliminary analyses	168
9.2.b	Improved fuel fabrication cost model and FCC model	168
9.3	Analyses and brute-force scoping coverage of the fuel design phase space	169
9.3.a	Depletion Analysis, Cycle Length and Discharge Burnup	170
9.3.b	Enriched Uranium Cost	171
9.3.c	Fuel Fabrication and Fuel Cycle Cost	171
9.3.d	Refueling outage	172
9.3.e	Integrated FCC	172
9.4	Importance of fuel-design-dependent FCC analysis	176
9.5	Findings of the parametric scoping FCC study	177
9.6	References for sections 9.1 to 9.5	178
9.7	FCC optimization model	180
9.7.a	Artificial Neural Network Models	180
9.7.b	Cost Model Integration	182
9.7.c	Optimization	183
10.	Thorium Fuel and In-Situ Breeding (Tasks 4)	187
10.1	QUADRISO Arrangement	187
10.2	Thorium Bearing Plate Arrangement	198
10.3	References for this Section	201
11.	Summary of Finding and Recommended Future Work	202
	Appendix A– Baseline AHTR Design Specifications	206

List of Figure

Figure 3-1. Assembly reference dimensions	24
Figure 3-2. Assembly derived dimensions	24
Figure 3-3. Fuel assembly structure [2]	25
Figure 3-4. Horizontal positioning of the assemblies in the core [2]	25
Figure 3-5. control blade geometry [2]	26
Figure 3-6. Geometrical configuration of the fuel plate [2]	27
Figure 3-7. Dimensions of the fuel plate	27
Figure 3-8. Dimensions of the fuel plate - detail	27
Figure 3-9. Triso particle geometry configuration [2]	28
Figure 4-1. SERPENT parallel performance vs MPI tasks	33
Figure 4-2. Reactivity Physical Transform Strategies Considered in ORNL Study [1]	34
Figure 4-3. Fuel assembly model geometry with 18 planks rotated 60 degrees. Dark grey is graphite, lighter grey is sintered carbon, blue is fuel stripe, and light blue is FLiBe	35
Figure 4-4. Effect of changing level of homogenization on accuracy and runtime	36
Figure 4-5. Predicted K-infinity and standard deviation with different number of particles run	37
Figure 4-6. Runtime as number of particles are increased.	37
Figure 4-7. Predicted K-infinity and standard deviation as number of generations are increased ...	38
Figure 4-8. Predicted K-infinity with increasing number of generations skipped	38
Figure 4-9. Flow chart describing MCDancoff Factor generation methodology.	40
Figure 4-10. Difference in predicted K-infinity between CE and MG depletion with BOC MCDancoff Factor. The red lines are the error propagated standard deviation of the difference in K-infinity ...	41
Figure 4-11. Probability distribution function for neutrons borne in fuel over range of energies of interest	42
Figure 4-12. Microscopic cross-sections for total ^{235}U cross-sections and ^{238}U absorption cross-section.	43
Figure 4-13. K-infinity as a function of FPD with a linear trend line showing how reactivity is non-linear. The red dashed line shows where K-infinity is equal to 1.	44
Figure 4-14. Cycle length as number of batches is increased for the NLRM and LRM.	45
Figure 4-15. Difference between NLRM and LRM in days as number of batches are increased.	45
Figure 4-16. X-ray radiograph of an AGR-3/4 compact [8]	46
Figure 4-17. SERPENT 2 Model of AHTR Fuel Assembly with randomly dispersed TRISOs	47
Figure 4-18. SERPENT 2 Model of AHTR Fuel Assembly with regular lattice TRISOs	48
Figure 4-19. K-infinity Difference between Regular Lattice and Random Dispersion	48
Figure 4-20. Error of Partial and Full Coating Homogenization Compared to Full Coating Treatment	49
Figure 4-21. Illustration of Lumped Depletion(top) vs. Stripe Subdivided Depletion (bottom)	50
Figure 4-22. K-infinity Difference versus 9 Depletion Sub-divisions per Fuel Stripe	51
Figure 4-23. Power Densities at 0 GWd/MTHM of each Sub-Division Model Normalized to Assembly Average	51

Figure 4-24. Gamma Cross Sections of Interest for AHTR [16].....	52
Figure 4-25. 2D Assembly model without Spacers (Left) and with Spacers (Right)	53
Figure 4-26. Impact of Spacers Upon k-infinity	54
Figure 4-27. Comparison of AHTR and LWR Flux Spectrum.....	56
Figure 4-28. Comparison of AHTR and LWR Coolant Density Reduction Coefficient.....	57
Figure 4-29. Depiction of Semi 1-D Mini-Core Simplification.....	59
Figure 4-30. Radial 1-D model power distribution comparisons	61
Figure 4-31. Axial 1-D model power distribution comparisons	61
Figure 4-32. Supercell models with control blade inserted (left) and withdrawn (right).....	62
Figure 4-33. Illustration of SERPENT 2 Peripheral Power Peaking	65
Figure 4-34. Plate Subdivision Power Peaking of Single Tri-Section Facing Reflector (Left) and Two Tri-Sections Facing Reflector (Right).....	65
Figure 4-35. SERPENT 2 minus Core Simulator Relative Node Averaged Power Distribution Differences for 3-D Full Core with Control Blades Withdrawn for NESTLE (Left) and PARCs (Right)	66
Figure 4-36. 3-D Full Core with Control Blades Inserted NESTLE Relative Power Distributions (Left), SERPENT 2 minus NESTLE Node Averaged Power Distribution Differences (Right)	66
Figure 4-37. Relative Power 1-D Averaged Axial Profile	69
Figure 4-38. Fuel Temperature 1-D Averaged Axial Profile	69
Figure 4-39. Coolant Temperature 1-D Averaged Axial Profile	70
Figure 4-40. Coolant Density 1-D Averaged Axial Profile.....	70
Figure 4-41. Relative Power 2-D Averaged Radial Profile PARCS TH	71
Figure 4-42. Fuel Temperature 2-D Averaged Radial Profile PARCS TH	72
Figure 4-43. Coolant Temperature 2-D Averaged Radial Profile PARCS TH.....	73
Figure 4-44. Coolant Density 2-D Averaged Radial Profile PARCS TH.....	74
Figure 4-45. Relative Power 2-D Averaged Radial Profile PIETRO MODEL BASED TH (Section 7.1.a)	75
Figure 4-46. Fuel Temperature 2-D Averaged Radial Profile PIETRO MODEL BASED TH (Section 7.1.a)	76
Figure 4-47. Coolant Temperature 2-D Averaged Radial Profile PIETRO MODEL BASED TH (Section 7.1.a)	77
Figure 4-48. Coolant Density 2-D Averaged Radial Profile PIETRO MODEL BASED TH (Section 7.1.a)	78
Figure 5-1. Cycle Length (FPD) as a function of packing fraction and number of fuel layers.....	82
Figure 5-2. Burnup (MWd/tHM) as a function of packing fraction and number of fuel layers.....	82
Figure 5-3. Cycle length (FPD) as a function of packing fraction and enrichment.....	83
Figure 5-4. Burnup (MWd/tHM) as a function of packing fraction and enrichment.....	83
Figure 5-5. Cycle Length as a function of packing fraction and number of batches.	84
Figure 5-6. K-infinity Effects of Altering Enrichment.....	85
Figure 5-7. Cycle Length Effects of Altering Enrichment	86
Figure 5-8. Maximum Discharge Burnup Effects of Altering Enrichment	86
Figure 5-9. Effects of Altering Packing Fraction on k-infinity.....	88
Figure 5-10. Cycle Length Effects of Altering Packing Fraction	88

Figure 5-11. Maximum Discharge Burnup Effects of Altering Packing Fraction.....	89
Figure 5-12. Fuel Stripe Thickness Perturbations: 50% Smaller Fuel Region (Left), Base Case (Middle), Whole Plate (Right)	90
Figure 5-13. Effects of Altering Fuel Region Thickness on k-infinity.....	91
Figure 5-14. Cycle Length Effects of Altering Fuel Region Thickness.....	91
Figure 5-15. Maximum Discharge Burnup Effects of Altering Fuel Region Thickness.....	92
Figure 5-16. Meat and Coolant Thickness Perturbations: 50% Reduced Meat (Left), Base Case (Middle), 50% Reduced Coolant (Right).....	93
Figure 5-17. Effects of Altering Meat / Coolant Region Thickness upon k-infinity	93
Figure 5-18. Cycle Length Effects of Altering Meat / Coolant Region Thickness.....	94
Figure 5-19. Maximum Discharge Burnup Effects of Altering Meat / Coolant Region Thickness	94
Figure 5-20. Y-Shape Thickness Perturbations: 37.5% Smaller (Left), Base Case (Middle), 100% Larger (Right).....	95
Figure 5-21. Effects of Altering Y Shape Thickness upon k-infinity	96
Figure 5-22. Cycle Length Effects of Altering Y Shape Thickness.....	96
Figure 5-23. Maximum Discharge Burnup Effects of Altering Y Shape Thickness.....	97
Figure 5-24. Channel Box Wall Thickness Perturbations: 50% Smaller (Left), Base Case (Middle), 100% Larger (Right)	98
Figure 5-25. Control Blade Worth Effects of Altering Assembly Edge Thickness.....	98
Figure 5-26. Number of Fuel Plates per Tri-Section: 3-Plate (Left), 6-Plate Base Case (Middle), 12-Plate (Right).....	99
Figure 5-27. Effects of Altering Number of Plates upon k-infinity.....	99
Figure 5-28. Cycle Length Effects of Altering Number of Plates	100
Figure 5-29. Maximum Discharge Burnup Effects of Altering Number of Plates.....	100
Figure 5-30. Effects of Altering Assembly Size upon k-infinity.....	101
Figure 5-31. Cycle Length Effects of Altering Assembly Size	102
Figure 5-32. Maximum Discharge Burnup Effects of Altering Assembly Size.....	102
Figure 5-33. Effects of using FCM / UN Fuels upon k-infinity.....	103
Figure 5-34. Cycle Length Effects of using FCM / UN Fuels	104
Figure 5-35. Maximum Discharge Burnup Effects of using FCM / UN Fuels	104
Figure 6-1. Effects of using Burnable Poisons upon k-infinity	106
Figure 6-2. Cycle Length Effects of using Burnable Poisons.....	106
Figure 6-3. Maximum Discharge Burnup Effects of using Burnable Poisons	107
Figure 6-4. Fuel Temperature Coefficient High Temperature Effects of using Burnable Poisons....	107
Figure 6-5. Fuel Temperature Coefficient Low Temperature Effects of using Burnable Poisons....	108
Figure 6-6. Plate Temperature Coefficient Effects of using Burnable Poisons	108
Figure 6-7. Control Blade Worth Effects of using Burnable Poisons.....	109
Figure 6-8. Increased Control Blade Length: Base Case (Left), 47% Longer (Middle), 141% Longer (Right)	110
Figure 6-9. Effects of Altering Control Blade Channel Size upon k-infinity.....	111
Figure 6-10. Control Blade Worth Effects of Altering Control Blade Size	111
Figure 6-11. Control Blade Worth Effects of Altering Control Blade Material.....	112
Figure 7-1. Typical temperature distribution of the average AHTR fuel plate	113

Figure 7-2. Maximum temperature distribution as a function of the coolant gap and fuel stripe thickness	115
Figure 7-3. Single channel RELAP5-3D model.....	116
Figure 7-4. Centerline temperature profile for the 20 axial nodes model.....	117
Figure 7-5. Nodalization diagram of the RELAP5-3D model of the AHTR fuel assembly.....	119
Figure 7-6. Conduction enclosure of the fuel plate (top view)	120
Figure 7-7. Heat transfer coefficient as a function of Reynolds	125
Figure 7-8. Temperature distribution of the single plate (1630x400 nodes).....	126
Figure 7-9. 3D Temperature distribution results.....	127
Figure 7-10. Possible control rod design changes.	132
Figure 7-11. Downward force as a function of the plate thickness.	133
Figure 7-12. Temperature distribution at the top of the plate for 3% external flow.....	134
Figure 7-13. Turbulent solution, Re=9100 (pathlines colored by velocity magnitude)	136
Figure 7-14. Assembly inlet, turbulent solution.....	137
Figure 7-15. Streamlines	138
Figure 7-16. Solidworks models of the assembly inlet	140
Figure 7-17. Mesh at the outlet of the channels (2D model).....	140
Figure 7-18. Geometry of the model and preliminary results (Scale Adaptive Simulation) for the normal vorticity at random instants of time	141
Figure 7-19. Geometric configuration for simulation of assembly outlet.....	142
Figure 7-20. Horizontal cross section of the core	145
Figure 7-21. Location of the assembly in which the rod is inserted.....	146
Figure 7-22. Fuel assembly removal transient.....	148
Figure 7-23. Velocity magnitude contours as a function of time	155
Figure 7-24. Velocity magnitude contours at the assembly inlet	156
Figure 8-1. K- effective Profile for Illustrative Coupled Neutronic and Thermal Hydraulics AHTR Depletion Calculation in 3-D with NESTLE.....	159
Figure 8-2. 3-D Relative Power and Burnup Distributions for Coupled Neutronics and Thermal Hydraulic AHTR Depletion Calculations with the Two-Step Procedure.....	160
Figure 8-3. 3-D Coolant Density and Fuel Temperature Distributions for Coupled Neutronics and Thermal Hydraulic AHTR Depletion Calculations with the Two-Step Procedure	161
Figure 8-4. Best LP found in LWROpt optimization	165
Figure 8-5. BOC RPF for the best LP found by LWROpt.....	166
Figure 9-1. Fuel plate FCC vs. packing fractions for different fabrication cost scenarios (all cases assume 10% enriched fuel, 2-batch refueling).	177
Figure 9-2. Flowchart of the overall fuel design optimization methodology.	180
Figure 9-3. Architecture of the MLP with 3 inputs and one output. The hidden layers are shown to have arbitrary size.	181
Figure 9-4. ANN MCDancoff Factor regression model compared with Multiple Polynomial regression MCDancoff Factor model.....	182
Figure 9-5. Flowchart of DE global heuristic optimization algorithm.....	183
Figure 9-6. Visualization of mutation. The red, green, and blue arrow show 3 random members contributing their parameter vectors to the mutation linear transformation.....	184

Figure 9-7. Visualization of recombination. Each value of u_j comes from either x_j or v_j depending on a random number and if it is larger than CR.	184
Figure 9-8. Evolution of the best solution over the design space with enrichment held constant at 19.75% and number of batches held at 3.33.....	185
Figure 9-9. Evolution of the best solution in the multi-dimensional design space.	186
Figure 9-10. Fuel cycle cost (\$/MWh) quickly converging as algorithm progresses through generations.....	186
Figure 10-1. K-infinity vs. EFPD and vs Burnup	188
Figure 10-2. ^{232}Th Mass vs. Burnup (top) and vs EFPD (bottom)	189
Figure 10-3. ^{233}U Mass vs. Burnup (top) vs EFPD (bottom).....	190
Figure 10-4. ^{235}U Mass vs. Burnup (top) vs EFPD (bottom).....	191
Figure 10-5. ^{239}Pu Mass vs. Burnup (top) vs EFPD (bottom)	192
Figure 10-6. Combined ^{233}U , ^{235}U , ^{239}Pu , and ^{241}Pu Mass vs. Burnup.....	193
Figure 10-7. Reactivity Plot (Th,U) O_2 Mixed Kernel.....	194
Figure 10-8. Pa^{233} Mass Plot (Th,U) O_2 Mixed Kernel	195
Figure 10-9. Total Fissile Mass Plot (Th,U) O_2 Mixed Kernel	195
Figure 10-10. K-infinityPlot (Th,U) C_2 Mixed Kernel.....	196
Figure 10-11. Pa^{233} Mass Plot (Th,U) C_2 Mixed Kernel.....	196
Figure 10-12. Total Fissile Mass Plot (Th,U) C_2 Mixed Kernel	197
Figure 10-13. Illustration of Plate Positioning.....	198
Figure 10-14. Illustration of Plate Power Distribution.....	198
Figure 10-15. K-infinity Plot vs Plate Positioning.....	199
Figure 10-16. Pa^{233} Mass Plot Plate Positioning.....	199
Figure 10-17. K-infinity Plot Number of Plates.....	200
Figure 10-18. Pa^{233} Mass Plot Number of Plates.....	200
Figure 10-19. Total Fissile Mass Plot Number of Plates.....	201

List of Tables

Table 2-1. Proposed and actual deliverables.....	20
Table 3-1. Triso particle parameters.....	28
Table 4-1. Effect of changing level of homogenization on accuracy, runtime, and uncertainty.	36
Table 4-2. Difference in predicted K-infinity and MCDancoff Factor generated at 900 K and 1200 K.	43
Table 4-3. Assessment Photo-Nuclear Effects	53
Table 4-4. 13-group few group structure.....	59
Table 4-5. 4-Group few group structures	60
Table 5-1. CHM ratio at different number of fuel layers and packing fractions.	81
Table 8-1. Constraint weights and limits used for the optimization.....	164
Table 8-2. Comparison of the constraint values for the initial guess and optimized LPs.....	165
Table 9-1. Discharge BU (GWd/MTU) and cycle length (EFPD) for 1 through 3 batches.	170
Table 9-2. Cost of enriched uranium (\$/kg).....	171
Table 9-3. Total fabrication cost (\$/kgU) summary for various fuel designs and cost scenarios. ...	172
Table 9-4. Fuel cycle cost (FCC) (\$/MWhe), including the outage cost, for the 'Lo' fuel fabrication cost scenario.	173
Table 9-5. Fuel cycle cost (FCC) (\$/MWhe), including the outage cost, for the 'Mid' fuel fabrication cost scenario.....	174
Table 9-6. Fuel cycle cost (FCC) (\$/MWhe), including the outage cost, for the 'Hi' fuel fabrication cost scenario.	175
Table 9-7. Results comparing the fit of the regression models.	182
Table 9-8. Fuel manufacturing cost model in \$/kgU.....	182
Table 9-9. Results from optimization showing the algorithmic solution is better than tabulated results.....	185

1. Executive Summary

The research performed in this project addressed the issue of low heavy metal loading and the resulting reduced cycle length with increased refueling frequency, inherent to all FHR designs with solid, non-movable fuel based on TRISO particles. Studies performed here focused on AHTR type of reactor design with plate (“plank”) fuel.

Proposal to FY12 NEUP entitled “Fuel and Core Design Options to Overcome the Heavy Metal Loading Limit and Improve Performance and Safety of Liquid Salt Cooled Reactors” was selected for award, and the 3-year project started in August 2012. A 4-month NCE was granted and the project completed on December 31, 2015. The project was performed by Georgia Tech (Prof. Bojan Petrovic, PI) and University of Tennessee (Prof. Ivan Maldonado, Co-PI), with a total funding of \$758,000 over 3 years.

In addition to two Co-PIs, the project directly engaged 6 graduate students (at doctoral or MS level) and 2 postdoctoral researchers. Additionally, through senior design projects and graduate advanced design projects, another 23 undergraduate and 12 graduate students were exposed to and trained in the salt reactor technology. We see this as one of the important indicators of the project’s success and effectiveness. In the process, 1 journal article was published (with 3 journal articles in preparation), together with 8 peer-reviewed full conference papers, 8 peer-reviewed extended abstracts, as well as 1 doctoral dissertation and 2 master theses.

The work included both development of models and methodologies needed to adequately analyze this type of reactor, fuel, and its fuel cycle, as well as extensive analyses and optimization of the fuel and core design.

Modeling challenges reflected the fact that no commercial code system has full capability to efficiently model this type of fuel assembly design with double heterogeneity, nor a system existed for coupled neutronics/thermal-hydraulics full core analyses. Therefore substantial efforts were needed to successfully resolve these challenges.

The development of models and methodology included:

- In-depth analyses were performed to understanding subtleties of AHTR reactor physics, and reasons for inaccuracies in current models.
- Two codes (SCALE and SERPENT) were selected for analyses to provide additional confidence in results through cross-verification.
- Specific modeling and analysis methodology approaches were developed and implemented to extend applicability of these codes to AHTR fuel. Examples include addressing random packing of TRISO particles, improving accuracy of multigroup method via the so called systematic MCDancoff factor approach, and implementing non-linear reactivity model.
- Sensitivity studies were performed to establish practical simulation methodology, providing results of adequate accuracy at acceptable computational resources.

Moreover a two-step hybrid methodology (stochastic generation of functionalized nuclear data combined with deterministic multigroup calculations) was developed to enable practical (rapid) evaluation of AHTR performance, full core 3-D model, with thermal-hydraulic feedback and depletion capability. . Simulations. Similar capabilities exist for LWRs, but not for AHTRs, and this new methodology and computational tools (expanded version of NESTLE) significantly improve our FHR/AHTR analysis and evaluation capability.

A novel comprehensive fuel cost model was developed. In the past, a standard model for pelletized oxide fuel cost was typically extrapolated and applied to TRISO based FHR fuel. However, due to the substantially different fuel design in AHTR, this could lead to (and or analysis demonstrated that, indeed, it does lead to) biased results. The new model accounts for specific and inherent features of plank fuel, e.g. potentially high fabrication cost of TRISO particles, and substantially different amount of structural materials and fuel elements needed to accommodate the same amount of HM for different fuel assembly designs. This model presents another significant new capability for analysis of AHTR.

Finally, a method for optimizing fuel assembly design was developed to allow effective search for optimum solution(s).

These improvements in modeling and analysis methodology enabled successfully completing project tasks, and obtaining the following findings that will guide future AHTR development and optimization.

Parametric studies were performed to scope the design space, primarily with respect to fuel enrichment (5% to 19.75%) and TRISO packing fraction (10% to 50%), but also examining impact of other design parameters (such as fuel plate thickness, number of plates, etc. As expected, the main driver for neutronic performance is the carbon-to-heavy metal (CHM) ratio, but fine tuning the design (i.e., achieving the same CHM with less or more lumped fuel) may provide further incremental improvements. Increasing the HM loading (e.g. via PF increase) increases somewhat the cycle length, but less than the amount of added fuel would suggest, due to reduced amount of moderator and worse fuel utilization, On the other hand, increasing the amount of moderator improves fuel utilization and discharge burnup, but reduces the amount of fuel and cycle length. This trade-off must be carefully optimized, by considering fuel cycle cost (FCC), as subsequently discussed.

One possibility to address this issue could be using thorium-bearing fuel with in-situ breeding. However, analyses that were performed have shown that over the range of scenarios thorium-based fuel failed to achieve a break-even performance, even less gains. Therefore, focus and efforts were shifted back to other options.

Two primary means for reactivity control were evaluated, use of burnable absorbers and use of control rods. Their purpose is somewhat different and both are envisioned to be used. Burnable absorbers were examined using several absorber materials, in BISO and QUADTRISO configuration.

Given their similar performance, BISO may be preferred due to simpler fabrication. With respect to absorber depletion rate, no ideal candidate was identified. Some materials depleted faster than desired, some slower than desired. Additionally, feedback coefficient was positive in some cases. A follow-up study looking at more complex designs should aim to develop improved solutions. Control rod (CR) worth was evaluated as well. The baseline design did not provide satisfactory shut down margin. Therefore, CR design modification was evaluated consisting of extending the CR wing length. This provides adequate hold-down, assuming that this solution is acceptable from the fuel element structural viewpoint.

Systematic thermal-hydraulic studies were performed, from simple in-house 1-D models and analyses, to 2-D and simplified 2-D analyses, to using the REALP code, and eventually using CFD in fairly complex simulations to assess flow distribution in on-line refueling transients. The results of these thermal-hydraulic studies were used:

- To inform neutronics analyses
- To provide single-channel parameters to be used in two-step full core coupled neutronics/thermal-hydraulics simulations
- To inform FCC optimization on thermal performance limits (regressed to simplified models)
- To evaluate thermal performance in pseudo-continuous refueling transients

The pseudo-continuous refueling aims to resolve the low HM loading issue by replacing/refueling fuel elements, one at a time, in regular and frequent intervals, while the reactor is operating at full power, or a fraction of power (on-line on-power refueling). Conceptually, this is similar to continuous refueling, or to the pebble bed refueling approach, and thus has potential to reduce FCC, provide flexibility, and reduce excess reactivity, but would also potentially introduce new significant other challenges. Analyses were performed considering primarily the flow redistribution and thermal performance. Additional issues of buoyancy, lift force, timing sequence and similar were considered as well. Performed analyses suggest that this approach is feasible from the neutronics and thermal-hydraulics standpoint, but the mechanical aspect, refueling topology, and alternative reactivity control need to be further studied.

The two-step procedure was used to evaluate full core parameters and perform preliminary fuel shuffle optimization studies. It was effective in reducing the radial assembly peaking factor by 27% from the baseline uniform loading.

The new comprehensive fuel cost model was combined with uncertainties in fuel cost and outage cost assumptions, and with extensive parametric studies (considering fuel enrichment, packing fraction, and number of batches), to identify preferable region(s) of fuel design space. This region generally tends to favor higher enrichment, in particular for higher fuel fabrication cost since more fissile material is processed per kgU. Low outage cost deemphasizes importance of longer cycle allowing use of more batches with improved fuel utilization, while the high outage cost necessitates using fewer batches to achieve longer cycles. While higher packing fraction increases HM loading, negative effect of reduced moderation and worsened fuel utilization typically overrides increased cycle length. Overall, preferable fuel designs tend to have enrichment in the 15% to 19.75% (with

higher values preferred), and the packing fraction not higher than 30% (and sometimes in the 10% to 20% range). These analyses were performed with a fixed number of TRISO particle layers.

On the other hand, optimization performed with the developed optimization algorithm and tool, does not require performing calculations for all possible combinations, while at the same time considers variable number of layers and optimum points between the initial discrete values. Using this tool to optimize FCC led to consistent results as the previous brute force search approach, but provided additional insights. This tool offers an effective way to perform future optimization studies if additional changes in fuel design are to be considered. It is important that in both cases fuel design options were identified that have potential to be competitive in the broader context of AHTR attractive features.

Enabled by the new tools and capabilities developed in this project, the extensive analyses performed have identified promising fuel design parameters, under the assumptions considered, and elucidated intricate inter-relations between different parameters. Future more detailed analyses will benefit from the new tools available, from the good starting point, and from the improved understanding of the critical trade-offs. In particular, recommended future work includes:

- Further optimize reactivity control – both burnable absorbers, and control rods, as well as a separate approach for pseudo-continuous refueling
- Utilize two-step procedure/tools to perform:
 - Realistic full core design and multicycle evaluation
 - Realistic reactivity control over the cycle
 - Evaluate full core thermal performance
 - Optimize feed enrichment
 - Evaluate feedback for safety/transients considerations
- Refine FCC optimization:
 - For the fuel design phase space of practical interest
 - Using updated assumptions, in particular reduced uncertainty in TRISO cost
 - Consider fuel lumping arrangements to reduce FCC

On a broader level:

- Consider alternatives to TRISO fuel, and
- Use developed tools to plan future experiments related to AHTR

Overall, the project has completed the planned tasks and achieved its target objectives. Its results advance the status of AHTR research and provide guidance to addressing the issue of low HM loading.

2. Project

2.1 Project

Proposal to FY12 NEUP entitled “Fuel and Core Design Options to Overcome the Heavy Metal Loading Limit and Improve Performance and Safety of Liquid Salt Cooled Reactors” was selected for award, and the 3-year project started in August 2012. A short 4-month NCE was granted and the project completed on December 31, 2015. The project was performed by Georgia Tech (Prof. Bojan Petrovic, PI) and University of Tennessee (Prof. Ivan Maldonado, Co-PI), with a total funding of \$758,000 over 3 years.

2.2 Objectives

A common feature of all Fluoride-salt High-temperature Reactors (FHRs) with solid non-movable fuel, including the ORNL design with plank fuel, Advanced High Temperature Reactor (AHTR), is the volumetrically low heavy metal (HM) loading. Combined with the design objective to maintain—for economic reasons—certain level of volumetric core power density, it leads to high specific power (expressed in power per mass of HM, e.g., W/gHM), resulting in fast fuel depletion, and therefore challenging cycle length, i.e. requiring frequent (and costly) reloading outage. To aggravate the situation, increasing the amount of fuel (e.g., by increasing its volumetric fraction), while keeping the core volume fixed, necessitates removing moderator and leads to reduced fuel utilization, thus lessening the benefits of adding fuel. The fact that TRISO fuel is expected to be more expensive than the PWR pelletized oxide fuel, further challenges fuel cycle cost (FCC) and adds to the complexity of the problem.

The overarching objective of this project was to examine traditional as well as novel approaches to address this low HM loading and fuel cycle length challenge. This is one of the enabling technologies necessary to make the AHTR with its attractive performance features also a viable candidate for commercial deployment.

To achieve this objective, in-depth studies were performed to understand the subtleties of the AHTR core physics, to identify the feasible region of the fuel/core design phase space, and to identify and select the most promising options.

2.3 Tasks and organization of the report

2.3.a Tasks

The tasks from the proposal may be summarized as follows, focusing on the essential aspect and intent, and skipping the details.

Task 1 – Fuel cost model.

The challenge here was that the standard LWR fuel cost model is not applicable to TRISO/plank fuel, and would lead to inaccurate and/or biased results. A new fuel cost model needed to be developed, accounting for large uncertainties in cost assumptions (since no commercial TRISO/plank fuel has been ever made), and relevant indirect effects (e.g., outage cost). This model needed to be coupled with a LRM or NLRM model to emulate multi-batch refueling.

Task 2 – Systematic FCC assessment for “standard” plank fuel

This task required performing many depletion analyses with multi-dimensional parameter variation (such as enrichment and packing fraction), coupling the results to the model identified in Task 1, and identifying general trends and areas in the design space with promising fuel designs.

Task 3 – Improved fuel design(s) with reduced FCC

This task aimed at examining design changes (e.g., changing fuel assembly dimensions, number of fuel plates, etc.), based on the results of Task 2, that would further reduce FCC.

We note that Tasks 1, 2 and 3 are tightly coupled, i.e., all three may be regarded as a comprehensive single large task, and presentation of the results in this report will therefore not follow sharp boundaries between them.

Task 4 – Thorium fuel and in-situ breeding

This task attempted to resolve the low HM loading issue by in-situ breeding in thorium-bearing fuel.

Task 5 – Pseudo-continuous refueling

This task aimed to resolve the low HM loading issue by replacing/refueling fuel elements, one at a time, in regular and frequent intervals, while the reactor is operating at full power, or a fraction of power (on-line on-power refueling). At the high level, this is similar to continuous refueling, or to the pebble bed refueling approach, and would reduce FCC, provide flexibility, and reduce excess reactivity, but would also potentially introduce new significant other challenges.

Task 6 – Reactivity control

This task aimed to evaluate reactivity control options through the use of control rods and/or burnable absorbers.

The need for adjustment of existing and development and verification of new methods and methodologies necessary to perform analyses was mentioned in the proposal, but not identified as a separate task. This

effort turned out to be significant due to inadequacy of existing methods and codes to accurately and efficiently analyze AHTR type of reactor. Therefore, sections have been included in the report documenting these efforts.

2.3.b Organization of the report

The report is organized to document the work performed to satisfy all tasks (Task 1 through 6), as well as the development and verification of models, methods and methodologies. However, topics and tasks have been rearranged to present results in a more logical order.

- Chapter 1 is Executive Summary. Chapter 2 (this chapter) provides programmatic project details.
- Chapter 3 introduces the baseline fuel and core design, defined based on the ORNL design work. All studies that don't explicitly describe fuel or core, assume that this design is used, i.e., typically, only the difference to this baseline design is listed.
- Chapter 4 summarizes efforts related to establishing adequate methods, methodologies and models for AHTR analyses.
- Chapter 5 presents parametric neutronic studies involving variation of fuel design parameters (such as enrichment or packing fraction variation). Some of these results feed into Task 2.
- Chapter 6 covers Task 6, Reactivity Control.
- Chapter 7 describes efforts related to attempts to devise pseudo-continuous refueling, including significant thermal-hydraulic analyses that were performed to understand ramifications of on-line on-power refueling.
- Chapter 8 presents results of full core analysis, made possible by development of the "two-step procedure", a new tool providing significant new capabilities for analysis of AHTR reactor type.
- Chapter 9 presents and interprets results of Tasks 1, 2 and 3, from the FCC model development, to exhaustive search over the fuel design phase space to identify preferable regions, to new optimization methodology.
- Chapter 10 describes analyses performed to assess potential for thorium in-situ breeding to extend cycle length. These efforts, somewhat expected, did not provide
- Chapter 11 summarizes findings and recommendations.

2.4 Milestones and Deliverables

2.4.a Milestones

The project identified 8 milestones in PICS:NE. They were completed practically on time. Specifically, 5 milestones were completed on time, 2 with a formal delay of only 1 day (due to open/close status of PICS, but clearly on time), and 1 with a one month delay.

2.4.b Deliverables

As shown in Table 2-1, all proposed deliverables were met or exceeded. Out of two doctoral students listed at UT, one completed his dissertation with a topic related to this project, while the other worked on the project, but the topic of his dissertation is different. Other listed PhD and MS students worked on the topics related to this NEUP project.

Table 2-1. Proposed and actual deliverables.

Proposed Deliverables / Outcomes	Actual (fully or partially funded on the project)
2 PhD students, 1 postdoc	UT: 2 PhD (completed), 2 post-docs GT: 2 PhD (nearing completion) 2 MS (completed)
Issue Quarterly and Annual Reports	Completed (All reports issued)
Report results via conference and journal papers	1 Journal article 3 Journal articles in preparation 8 Peer reviewed conference papers 8 Peer reviewed extended abstracts

2.5 Personnel

In addition to PI (at GT) and Co-PI (at UT), project engaged 2 MS students, 4 PhD students, and 2 post-docs (listed on cover page ii), i.e., a total of 10 people performed research directly related to the project.

Additionally, a number of undergraduate and graduate students were engaged through senior and graduate design classes to be trained in and to work on design projects related to salt technology. Specifically:

- Spring 2015: 2 graduate design teams, with 9 graduate students
- Spring 2016: 4 senior design teams, and 1 mixed team, with 23 undergraduate and 3 graduate students
- Total (design classes): 23 undergraduate and 12 graduate students.

Thus, over 40 student (23 undergraduate, 18 graduate) were exposed to and trained in the salt technology.

2.6 Publications

In addition to the quarterly reports, results of the research have been documented, published and disseminated through:

- Journal articles (1 published, 3 in preparation)
- Peer reviewed papers in conference proceedings (8)
- Peer reviewed extended summaries (8)
- Doctoral dissertations (1 completed, 2 in progress)
- Master theses (2)

Journal papers (1 published, 3 in preparation)

1. P. Avigni, B. Petrovic, "Fuel Element and Full Core Thermal-Hydraulic Analysis of the AHTR for the Evaluation of the LOFC Transient, *Annals of Nuclear Energy*, **64**, 499-510 (2014).

Peer reviewed papers in Conference Proceedings (8)

1. P. Avigni, B. Petrovic, M. E. Ricotti, "Preliminary Thermal-Hydraulic Analysis of the AHTR Fuel Element," *Proc. 15th International Topical Meeting on Nuclear Reactor Thermal Hydraulics (NURETH-15)*, Pisa, Italy, May 12-15, 2013.
2. P. Avigni, B. Petrovic, "Preliminary Evaluation of the Fuel Assembly At-Power Removal Transient of the Advanced High Temperature Reactor," *Proc. 2014 Intl. Congress on Advances in Nuclear Power Plants (ICAPP 2014)*, Charlotte, NC, April 6-9, 2014, Paper 14311, pp. 78-85 (2014).
3. M. Huang, B. Petrovic, "Use of MCDancoff Correction Factor for Multi-Group Fuel Depletion Analyses of Liquid Salt Cooled Reactors", *Proc. PHYSOR 2014*, Kyoto, Japan, September 28 – October 3, 2014.
4. C. Kingsbury, B. Petrovic, "Updated Fuel Cycle Cost Model of the Fluoride-salt-cooled High-temperature Reactor (FHR) Based on Neutronic Calculations Using MC Dancoff Factors", *Proc. Advances in Nuclear Fuel Management V (ANFM 2015)*, Hilton Head Island, SC, March 29 – April 1, 2015.
5. N.P. Luciano, K.E. Ottinger, P.E. Collins, C. Gentry, N. George, A.J. Pawel, K. Kenner, S. Hart, O. Chvala, G.I. Maldonado, F. Fejt, "The NESTLE 3D Nodal Core Simulator: Modern Reactor Models," *Proc. M&C+SNA+MC 2015*, Nashville, TN, April 19-23, 2015.
6. P. Avigni, B. Petrovic, "Pseudo-3D Steady State Thermal-Hydraulic Modeling of the Advanced High Temperature Reactor Fuel Assembly, *Proc. NURETH-16*, Chicago, Aug. 30 – Sep. 4, 2016, on CD-ROM, American Nuclear Society, LaGrange Park, IL (2015).
7. C.A. Gentry, G.I. Maldonado, K.S. Kim, "Development of Two-Step Analysis Procedure for the Advanced High Temperature Reactor," Accepted, *PHYSOR 2016*, Sun Valley, Idaho, May 1-5. 2016.
8. C. Kingsbury, B. Petrovic, "A Model for Assessing FHR Fuel Fabrication and Fuel Cycle Cost", Accepted, *ICAPP 2016*.

Peer reviewed extended summaries (8)

1. C. Gentry, N. George, O. Chvala, G.I. Maldonado, S. Lewis, P. Avigni, B. Petrovic, "Core Physics Parametric Studies for Liquid Salt Cooled Reactors," *Trans. Am. Nucl. Soc.*, **108**, 831-833 (2013).
2. P. Avigni, B. Petrovic, "Modeling and Parametric Studies of the AHTR Fuel Element," *Trans. Am. Nucl. Soc.*, **108**, (2013).
3. N. George, C. Gentry, O. Chvala, G.I. Maldonado, "Two Dimensional Calculations for Liquid Salt Cooled Reactors," *Trans. Am. Nucl. Soc.*, **109**, 1339-1342 (2013)
4. S. Lewis, B. Petrovic, "Determining the Equivalent Reactivity of a LSCR 2D Fuel Assembly and 3D Full Core Models," *Trans. Am. Nucl. Soc.*, **109**, 1402-1404 (2013).
5. S. Lewis, B. Petrovic, "Simplified Fuel Cycle Cost Model Applied to LCSR Parametric Studies," *Trans. Am. Nucl. Soc.*, **109**, 1476-1479 (2013).
6. P. Avigni, B. Petrovic, "Preliminary 2D Analysis of the AHTR Fuel Assembly Removal Transient," *Trans. Am. Nucl. Soc.*, **113**, 1404-1407 (2015).
7. L. M. Huang, B. Petrovic, "Automated MCDancoff Factor Generation for Liquid Salt Cooled Reactor Parametric Studies," *Trans. Am. Nucl. Soc.*, **113**, 1254-1257 (2015).
8. C. Gentry, G. I. Maldonado, O. Chvala, B. Petrovic, "Burnable Poison Reactivity Control for the Advanced High Temperature Reactor," *Trans. Am. Nucl. Soc.*, **113**, 1265-1267 (2015).

M.Sc. Theses

1. Spenser Lewis, "Simplified Core Physics and Fuel Cycle Cost Model for Preliminary Evaluation of LSCR Fueling Options," MS Thesis, Georgia Institute of Technology, Atlanta, GA (2014).
2. Christopher Kingsbury, "Fuel Cycle Cost and Fabrication Model for Fluoride-Salt High-Temperature Reactor (FHR) "Plank" Fuel Design Optimization," MS Thesis, Georgia Institute of Technology, Atlanta, GA (2015).

Ph.D. Dissertations

1. Cole Gentry, "Development of a Reactor Physics Analysis Procedure for the Plank-Based and Liquid Salt-Cooled Advanced High Temperature Reactor," PhD Dissertation, University of Tennessee, Knoxville, TN (2015).

3. Baseline AHTR Design

The ORNL AHTR fuel and core design was used as the baseline for this project. All studies described in this report that don't explicitly describe fuel or core, implicitly assume that this ORNL AHTR design was used. If some changes to the baseline design were made, typically, only the differences to this baseline design are specified.

The general design of the AHTR is described in two ORNL reports ([1], [2]); these two reports use slightly different numbers for specific design parameters, because the more recent design has been partly optimized. We decided to consider the most recent design as a reference design for the general parameters, but some features that are not fully defined in the most recent report are taken from the initial, non-optimized design.

A document has been prepared, included in Appendix A, which summarizes relevant geometric properties and materials, based on the work developed at ORNL and related projects over the past decade years. It provides a description of the features of the plant from a large-scale point of view to the small scale. It should be consulted as necessary. When not specifically stated otherwise, fuel and core design used in subsequent chapters correspond to that in the document.

Sections of the report covering fuel element are also replicated in this Chapter.

3.1 Fuel assembly

The fuel assembly is made of 18 fuel plates, grouped in 3 clusters of 6 plates each. Each plate is 2.55 cm thick. The entire fuel assembly is fabricated from high temperature materials.

The plates in the assembly are 6 m long, the active (fueled) part is 5.5 m (of the total 6 m), and the remaining part (25 cm on top and bottom) are made of reflector material. The plates are enclosed in a hexagonal carbon-carbon fuel channel box (density 1.95 g/cm³), which is 1 cm thick. The outer apothem of the box is 22.5 cm, corresponding to 45 cm distance between two parallel outer faces of the box wall. The three symmetric regions (groups of plates) are separated by a Y shaped support structure that is 4 cm thick and made of C-C composite (density 1.95 g/cm³). The coolant channels are 0.7 cm thick, except for the first and last channel of every region, that are half of the full thickness (0.35 cm). Figure 3-1 shows the reference dimensions of the horizontal cross section of the assembly, while Figure 3-2 shows some dimensions that can be derived from the reference dimensions.

A three dimensional view of the fuel assembly structure is given in Figure 3-3.

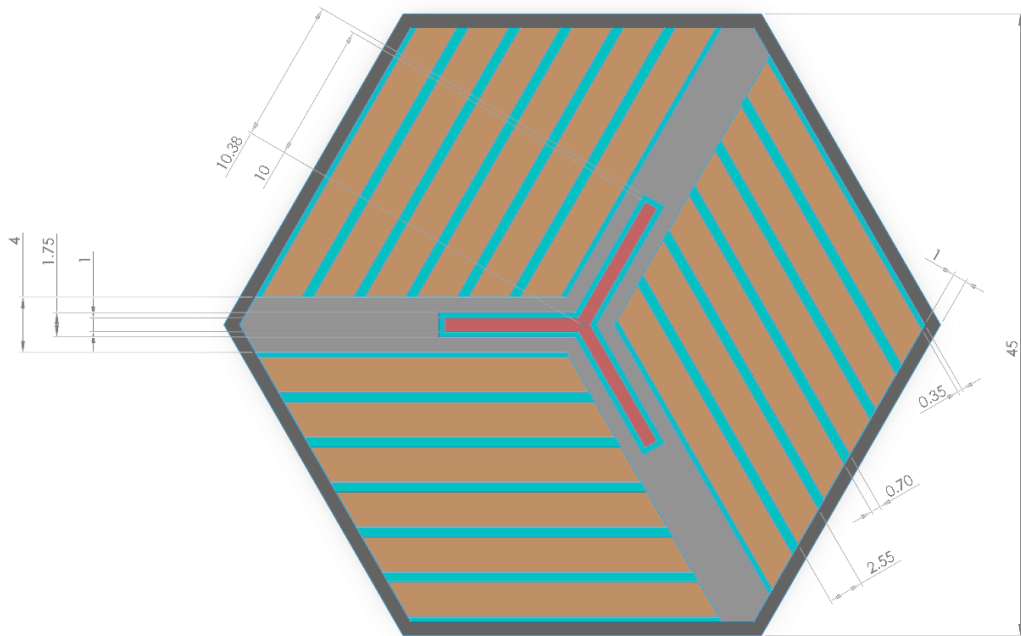


Figure 3-1. Assembly reference dimensions

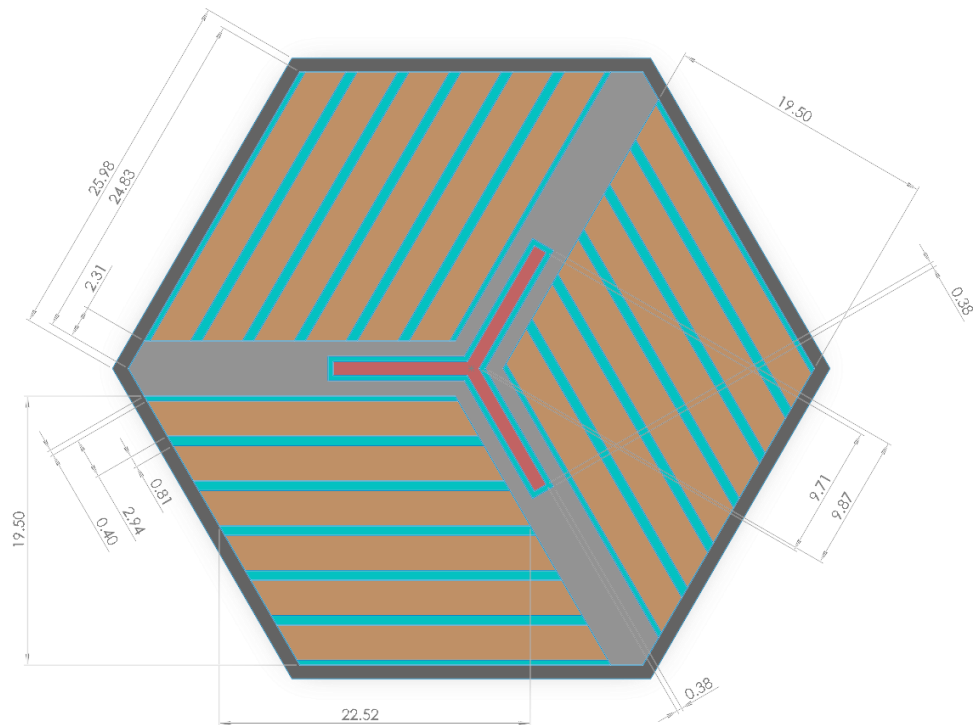


Figure 3-2. Assembly derived dimensions

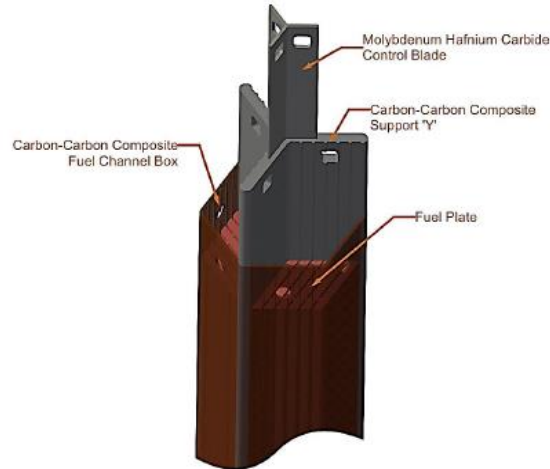


Figure 3-3. Fuel assembly structure [2]

The gap between nearby assemblies is 1.8 cm, in order to accommodate mechanical distortion. The triangular fuel assembly pitch is then 46.8 cm. Figure 3-4 shows the horizontal cross section of 7 neighboring assemblies.

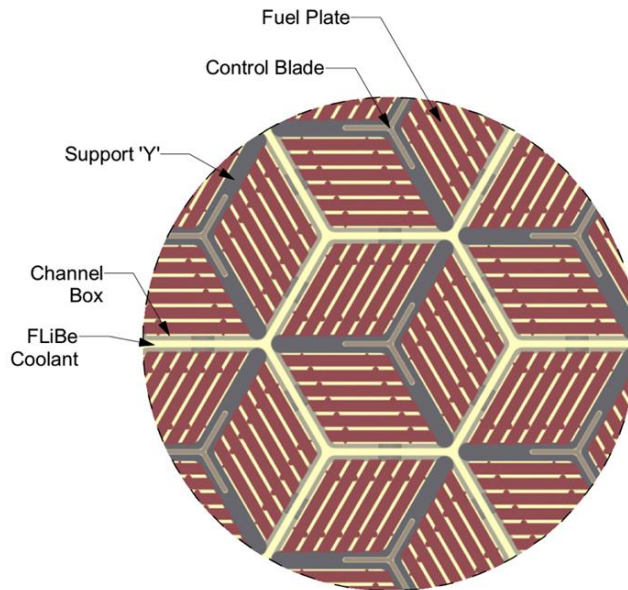


Figure 3-4. Horizontal positioning of the assemblies in the core [2]

3.2 Control blade

Each assembly has its own control rod; each control rod has low reactivity worth. The control rod is Y-shaped and it is inserted into the central Y-shaped support. The control rod is made of molybdenum hafnium carbide (MHC) alloy, that functions as absorber and structural. MHC is a commercial, particle-strengthened molybdenum-based alloy with 1.2%w hafnium and 0.1%wt carbon. The density is 10.28 g/cm³.

The leader rod attaches at the top of the control rod, using grapping holes. The leader rod serves to move the control rod up and down. The dimensions of the rod and the slot are:

- CR slot: each wing is 10.38 cm long (with respect to center of assembly) and 1.75 cm thick.
- CR: each wing is 10 cm long (with respect to center of assembly) and 1 cm thick.

Figure 3-5 shows the control rod geometric configuration.

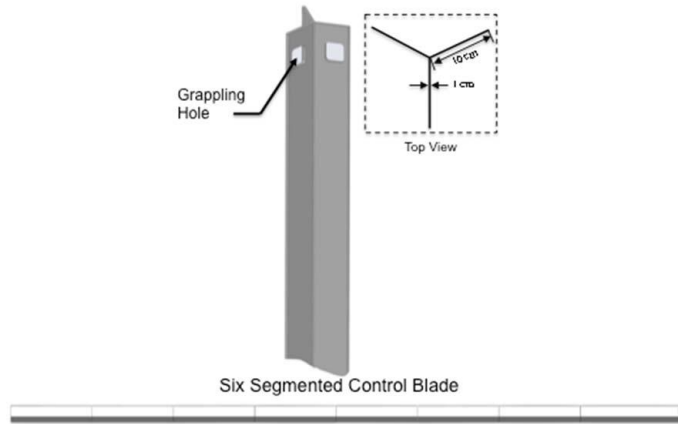


Figure 3-5. control blade geometry [2]

3.3 Fuel plate

The LSCR fuel plank is shaped as a parallelepiped with two fuel stripes sandwiching a central carbon slab. There is a thin 1mm pyrocarbon sleeve (“cladding”) around the fuel stripes to prevent erosion of TRISO particles. The TRISO fuel particles are randomly dispersed within the fuel strip with a 40% packing fraction in the 2011 model. This can be modeled with a TRISO spherical square lattice with a pitch of 0.09265 cm. The newer 2012 reference design has a carbon to heavy metal ratio that is twice as high at 400 compared to the 2011 design. It also has 9% enrichment down from 19.75% enrichment. The enrichment was lowered to reduce the fuel cycle cost and the initial capital investment. The fuel stripe could be made smaller or the packing fraction can be reduced to produce a higher CHM ratio. It is recommended that the fuel stripe thickness be set to contain six fuel layers and a 20% packing fraction. This gives a square pitch of 0.116736 cm. High density graphite matrix is inside the fuel stripe in between the TRISO particles. The density of the carbon matrix is 1.75 g/cm³. Burnable poison particles included near the center of the plate. There are two semi-cylindrical spacers on each of the fuel planks. Figure 3-7 gives a general idea of the configuration of the plate; Figure 3-7 and Figure 3-8 present the dimensions of the plate.

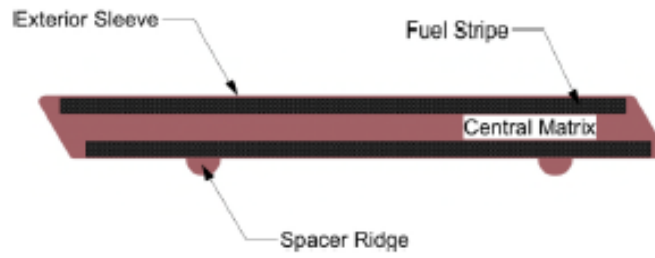


Figure 3-6. Geometrical configuration of the fuel plate [2]

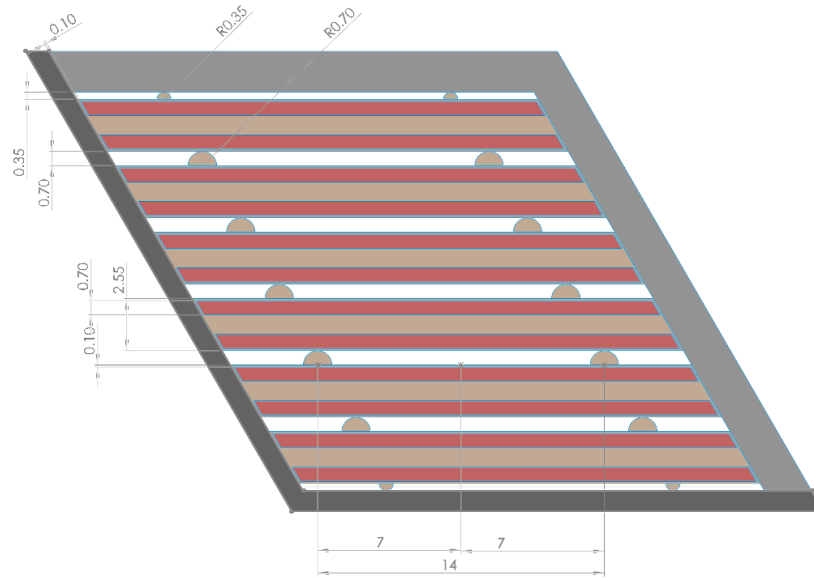


Figure 3-7. Dimensions of the fuel plate

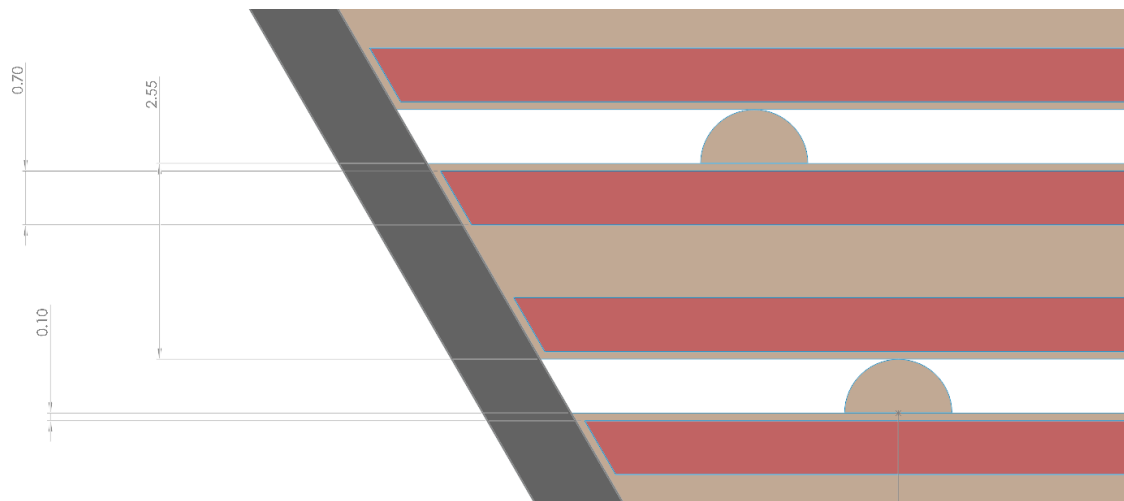


Figure 3-8. Dimensions of the fuel plate - detail

3.4 Fuel - TRISO particle

The TRISO fuel particle consists of four layers: an outer pyrocarbon layer, silicon carbide layer, an inner pyrocarbon layer, and a less dense carbon buffer layer. Inside of these layers is a uranium oxycarbide fuel kernel. Figure 3-9 shows the geometry with the outer layers cut out of the TRISO fuel particle. This fuel is the same as the AGR fuel developed under DOE-NE sponsorship. The reference irradiation experiment for the fuel type used for the AHTR is AGR-5/6. Table 3-1 shows the respective dimensions of the TRISO fuel particle.

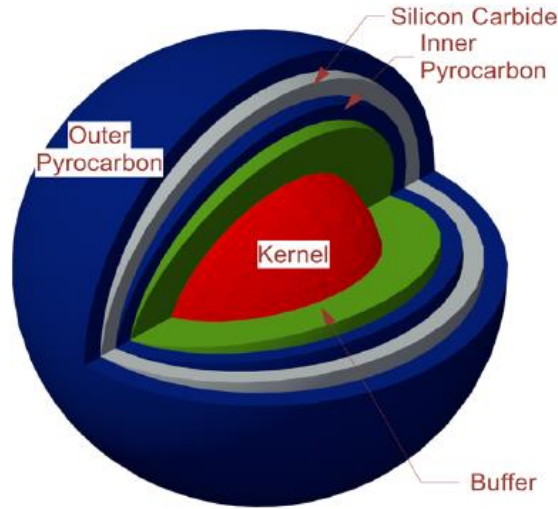


Figure 3-9. Triso particle geometry configuration [2]

Table 3-1. Triso particle parameters

Region	Parameter	value μm	Material	ρ (g/cm ³)
Kernel	diameter	427	UCO	10.9
Buffer	thickness	100	Porous graphite	1
IPyC	thickness	35	Pyrolytic graphite	1.9
SiC	thickness	35	SiC	3.2
OPyC	thickness	40	Pyrolytic graphite	1.87
Fuel Particle	diameter	847	----	----

3.5 Coolant

FLiBe (2LiF-BeF₂) is used as coolant for the primary system. The Beryllium also provides some moderation. Lithium is ideally isotopically pure Li7 to minimize tritium production. 99.995%wt Li7 enrichment is generally considered the reference enrichment that can be practically achieved. The FLiBe salt is transparent. The density is 1950 kg/m³ at 700°C (it is temperature dependent). The melting point is 459°C.

3.6 References for this Chapter

1. Holcomb, D. E., Ilas, D., Varma, V. K., Cisneros, A. T., Kelly, R. P., & Gehin, J. C., "Core and Refueling Design Studies for the Advanced High Temperature Reactor," ORNL/TM-2011/365, Oak Ridge National Laboratory, Oak Ridge, Tenn. (September 2011).
2. V. K. Varma, D. E. Holcomb, F. J. Peretz, E. C. Bradley, D. Ilas, A. L. Qualls, N. M. Zaharia, "AHTR Mechanical, Structural, and Neutronic Preconceptual Design," ORNL/TM-2012/230, Oak Ridge National Laboratory, Oak Ridge, Tennessee (September 2012).

4. Neutronics Methods and Models Development

4.1 Codes used

Reactor physics analysis of the AHTR presents significant challenges to standard codes, due to the double heterogeneity of TRISO-based fuel, which as a rule has not been implemented and therefore may need to be addressed via approximate or ad hoc methods. Additionally, the experience with FHR modelling is limited, which makes analyses more susceptible to undetected errors.

Therefore, we have adopted approach in which two different code systems are used, SCALE and SERPENT. Obtaining comparable results independently from two different codes increases confidence in validity of results.

4.1.a SCALE

Georgia Tech has focused on using SCALE. This code package has been developed by ORNL. It is widely used in the US, therefore, its general features will not be described here. However, it should be noted that its application for FHR analyses has been limited, mainly documented in ORNL studies.

4.1.b SERPENT

University of Tennessee has focused on using SERPENT, this code is gaining popularity internationally for reactor-physics analyses. Additionally, UT access to the TITAN supercomputer at ORNL facilitated making large SERPENT runs viable.

4.2 Challenges in AHTR reactor physics calculations and options available in SERPENT

Most production level lattice physics codes generally employ some deterministic means of solving the neutron transport problem such as Method of Characteristics (MOC) or Collision Probabilities (CP), which are generally very fast methods but, as mentioned previously, require some condensation of the high fidelity energy dependent cross-section data on account of memory constraints. This reduction from high energy fidelity to some coarser multi-group structure is typically achieved by assuming pin-cell regularity and solving an equivalent 1-D pin model, possibly with a 2-D coupling correction, to provide flux distributions for flux weighted averaging of the cross-section data.

However, the longer neutron diffusion length combined with the rotational arrangement of fuel plates within the assemblies makes it difficult to derive an accurate plate-cell model from which to obtain a flux solution for flux weighted cross-section condensation. Two forms of reactivity equivalent adjustments, one involving a physical transformation and the other a Dancoff correction factor, were investigated and employed in the original ORNL studies [1]. Both of these methods require a reference solution, generally furnished by high fidelity Monte Carlo models, from which to adjust parameters to obtain reactivity equivalency. Both these approaches, though feasible as means of employing the faster deterministic lattice physics methods, introduce some additional error in that they typically assume the reactivity equivalent parameter will hold for the entirety of the fuel depletion. Also, both methods are questionable with regards to power distribution accuracy given that they only ensure reactivity equivalence, and additionally are greatly challenged by models in which burnable poison material is present in the homogenization region.

Recent advances in Monte Carlo simulation techniques, problem parallelization, computer resource utilization strategies, and computer memory capacities have made the use of continuous energy Monte Carlo codes for lattice physics calculations and subsequent generation of homogenized cross-section and diffusion parameters an increasingly viable option. Use of continuous energy Monte Carlo models with sufficient neutron histories essentially eliminate errors associated with geometry and energy fidelity reductions rendering them more accurate relative to the reactivity equivalence approaches. One such candidate code which was specifically designed for lattice physics application is the Monte Carlo code SERPENT 2 [2].

SERPENT 2, and its predecessors SERPENT 1 and PSG, were originally designed with a slightly more narrow scope than typical Monte Carlo codes in that they focused less on shielding applications and more so on homogenization and other assembly-level reactor physics calculations, thus making it possible to optimize the calculation routines and obtain significant performance improvement as compared to general-purpose Monte Carlo codes [3]. SERPENT 2 exhibits a number of advantageous features that makes it well suited for this research as listed below:

2. Ability to generate few-group B1 critical spectrum corrected homogenized cross-sections and diffusion parameters including discontinuity factors for fuel and reflectors.
3. Option for explicit treatment of randomly dispersed fuel particles

4. Ability to model graphite as a bounded atom system using thermal scattering libraries
5. Flexible application of Cross-section Unionized Energy speed-up technique based on user memory demands and availability
6. Use of Woodcock delta-tracking for reduced computational overhead
7. Use of Chebyshev Rational Approximation Method (CRAM) for burnup depletion modeling
8. Equilibrium Xenon distribution feature to help with treatment of Monte Carlo Xenon Oscillation

SERPENT 2 provided a means of performing 2D parametric analysis to supplement the SCALE results as well for generating cross-sections libraries and reference benchmarks for the Two-Step procedure development described in section 0

Neutronic simulations were conducted on the TITAN supercomputer for the Advanced High Temperature Reactor (AHTR) to help support a coupled neutronics and thermal-hydraulics simulation method referred to as the above-noted two-step procedure, as well as to investigate alternative fuel designs. These simulations were conducted using the Monte Carlo based neutron transport code SERPENT 2.

For the development of the two-step procedure, TITAN was used both for generating cross-section libraries, a necessary component of the two-step procedure, and for producing a high fidelity reference model with which to benchmark the accuracy of the finally developed two-step procedure. Provided in this report are only select figures which highlight the more significant accomplishments, however, an entire detailed discussion may be found in the UTK dissertation "Development of a Reactor Physics Analysis Procedure for the Plank-Based and Liquid Salt-Cooled Advanced High Temperature Reactor" by Cole Gentry.

SERPENT 2 was found to scale fairly well. The dominant controlling factor on the SERPENT scaling appears to be based on the ratio of the number of Neutrons simulated Per Generation (NPG) over the number of MPI tasks. When this value becomes low, then the scaling becomes poor. When this ratio is high, then scaling can be very good and was calculated in some cases to be 86% of ideal scaling. When using 1200 nodes on the full core test case about 67% scaling was observed. Whereas when using 4800 nodes on the full core test case, scaling had diminished to only 24%. The number of nodes at which ideal scaling significantly diminishes will ultimately be model dependent based largely on the NPG/ MPI ratio, but also on model geometry and composition.

The more significant shortcoming of SERPENT 2 scaling is the problem of memory decomposition. Currently, SERPENT 2 copies the entire problem, and therefore memory footprint, to all MPI tasks. Though this can be decomposed further, in theory, a practical implementation will likely not be applied to SERPENT 2 for some time yet. For all models considered for AHTR studies, thus far, this did not prove to be a problem.

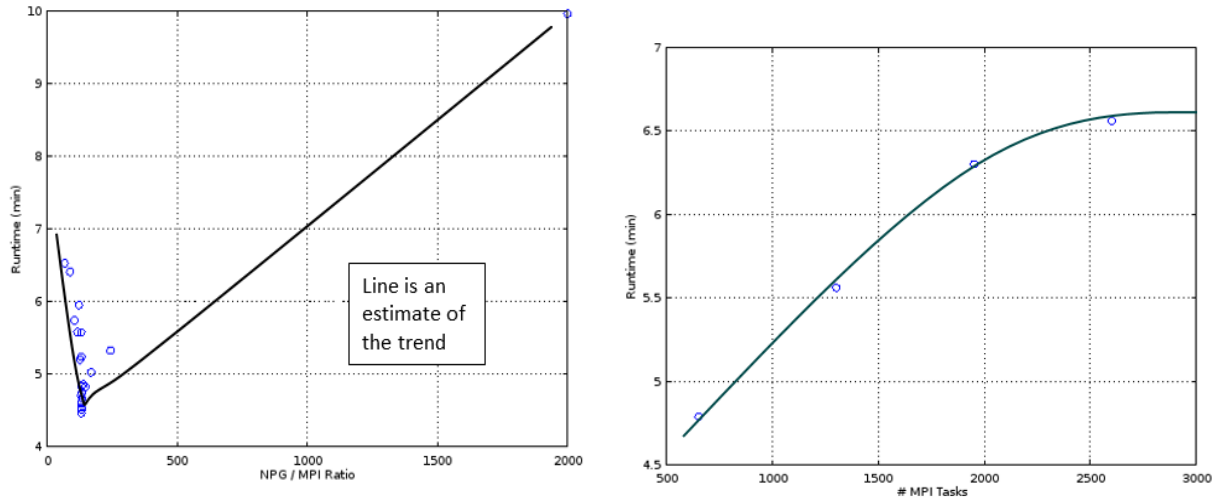


Figure 4-1. SERPENT parallel performance vs MPI tasks

The most current research in the plate based AHTR design comes from the previously mentioned ORNL studies summarized in documents ORNL/TM-2011/365 and ORNL/TM-2012/320 [1,4]. In these studies, neutronic models were simulated for a plate type assembly design based upon thermal-hydraulic and mechanical considerations. This base design was analyzed using two different fuel enrichments (19.75% and 9%), a variety of fuel region thicknesses to adjust the Carbon to Heavy Metal (CHM) ratio, using Europium burnable poison spheres for reactivity hold down, and a variety of core refueling batching schemes. Neutronic performance metrics consisted of reactivity feedback coefficients, power distributions, isotopic burnups, and cycle length assessments. Cycle length approximations were obtained by means of simple Linear and Non-Linear Reactivity models and Equilibrium Core evaluations.

Two major multigroup model types served as the drivers for depletion analysis in this study. One model utilized a Reactivity Physical Transform (RPT) approach in which a combination of both particle homogenization and geometry transformation are applied such that reactivity equivalence with the true model is maintained but the detailed treatment of the TRISO particle is avoided [5]. The RPT approaches considered by the ORNL study are illustrated in Figure 4-2. . The second model type maintained explicit treatment of TRISO particles in a regular arrangement, but applied a Dancoff reactivity equivalency factor for the multigroup treatment. For both model types, entire assemblies were represented with a single depletion region, and for full core analysis a single depletion region was often times used to represent multiple assemblies.

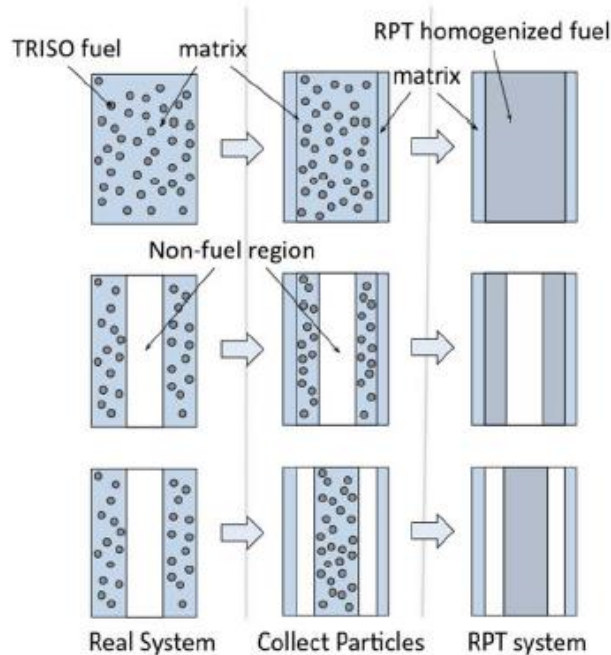


Figure 4-2. Reactivity Physical Transform Strategies Considered in ORNL Study [1]

Though these initial studies are believed to provide meaningful results, and have since been further supplemented by additional analysis by Lewis et. al. [6], it can easily be seen that much analysis still remains both with regards to design optimization and model fidelity improvement. The most problematic issues with the modeling approaches used in the ORNL studies are the simulation runtimes as well as model fidelity. With regards to model fidelity, an RPT treatment loses the ability to reliably predict plate power distributions and is easily defeated by the expected eventual use of burnable poisons within the plates. Additionally, no strong coupling to thermal-hydraulics is present to assess at power steady state and transient safety. With regards to runtimes, simulations of 3-D full core models using the SERPENT 2 Monte Carlo code with explicit TRISO particle treatment, conducted as part of this research, indicate that when even using 19,200 AMD Opteron cores on the ORNL TITAN supercomputer, runtimes can take as long as 1.24 wall clock hours in order to obtain a fairly converged stripe-wise power distribution. The ORNL studies reported a factor of 20 speedup when applying the RPT approximation, however on the aforementioned full core model this would still require minutes of runtime on a comparably large number of processors [1], thus also implying a need for access to world-class supercomputers to perform analyses. It can easily be seen then that simulating multiple state-points (i.e. burnups and / or perturbation cases) along with any sort of strong thermal-hydraulic coupling will take hours if not days to complete. Combined with the desire of seeking equilibrium cycle conditions and iterating over many assembly designs, the problem of design optimization quickly becomes untenable. Therefore, it becomes desirable to seek an alternative means of simulation that allows both an improved degree of model accuracy as well as reduced simulation runtime. The classical two-step procedure utilized in LWR modeling is believed to provide such a means of simulation.

4.3 Evaluation of existing methods and SCALE Models

4.3.a SCALE 1D, 2D and 3D models

Neutron transport calculations are modeled using SCALE6.1 with KENO Monte Carlo Transport. The SCALE model was developed from the 2011 Oak Ridge AHTR base design which has a carbon-to-heavy metal ratio of ~ 200 . The model development progressed from an infinite TRISO lattice to a pseudo 1D plank, to an infinite height fuel assembly model, and then to an infinite height full core model. The infinite height fuel assembly model was found to be the most practical model to use for parametric and optimization studies. The pseudo 1D plank model was found to be inaccurate and did not capture many physical effects properly. The infinite height full core model is a very good approximation to the 3D full core model since the core is relatively tall.

4.3.b Axial model height for improved efficiency

The runtimes of the full core models are impractically long for parametric design studies. Instead, 2D fuel assembly models are used in parametric studies. Infinite z-dimension is represented by certain finite height, representing to a certain number of TRISO unit cells, with reflective boundary conditions on the top and bottom. Studies were performed to find how many layers of TRISO particles high the assembly model with reflective boundary conditions should have. With too few layers, reflection on the boundary would occur too often. With too many layers, the model becomes more complex. It was found that runtime was minimized with a lattice of 100 TRISO particles tall. SCALE6.1 does not have the option to model randomly distributed TRISO particles, therefore a regular cubic lattice is used. Studies performed by SERPENT suggest that this results in an error of a few hundred pcm. Figure 4-3 is an image of the fuel assembly model in SCALE.

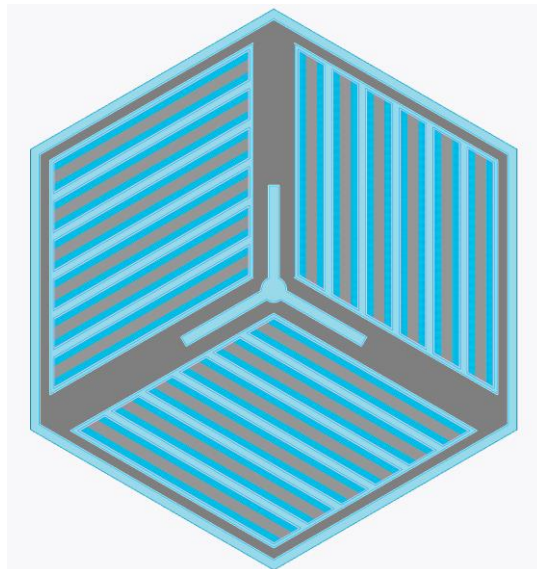


Figure 4-3. Fuel assembly model geometry with 18 planks rotated 60 degrees. Dark grey is graphite, lighter grey is sintered carbon, blue is fuel stripe, and light blue is FLiBe.

4.3.c Homogenization of TRISO particle layers

A study was performed to see if homogenization of the fuel planks to reduce runtime without sacrificing significant accuracy. The fuel assembly with fully double heterogeneous geometry was compared to two homogenization scenarios. The first simulation was to homogenize the protective carbon and SiC layers of the TRISO particle with the carbon matrix within the fuel stripe. The second was to also homogenize the UCO fuel kernel with the rest of the TRISO particle and the carbon fuel stripe matrix. The results are shown in Figure 4-4 and Table 4-1. Homogenizing the protective layers of the TRISO particle with the carbon matrix has a very small effect on K-infinity of only 22 pcm. The effect on runtime is very significant reducing the runtime from 1550 minutes down to only 1200 minutes. Homogenizing the fuel kernel results in a massive change in K-infinity, more than 5000 pcm while only a modest reduction in runtime.

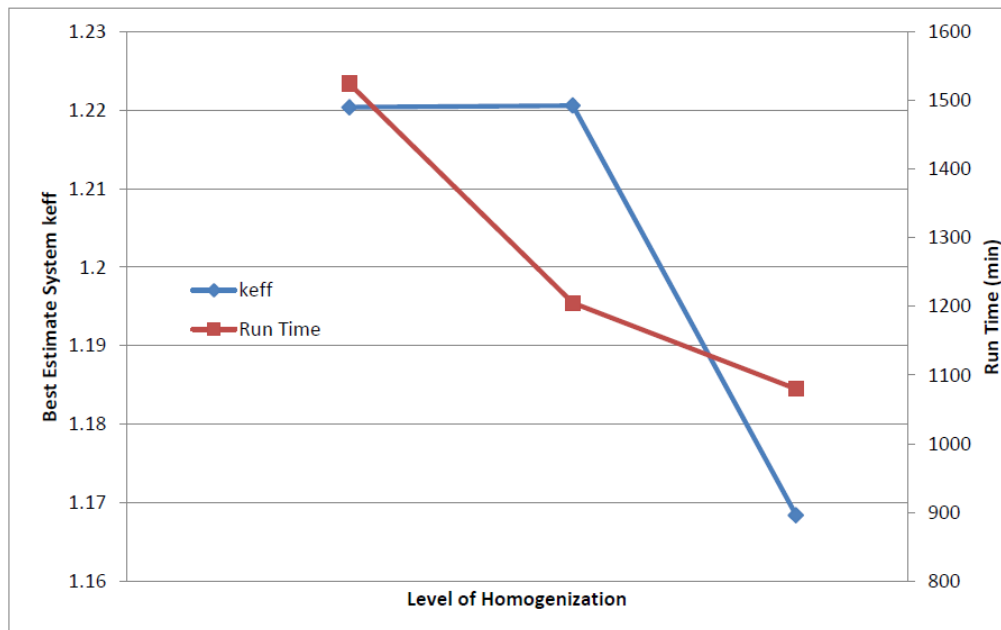


Figure 4-4. Effect of changing level of homogenization on accuracy and runtime.

Table 4-1. Effect of changing level of homogenization on accuracy, runtime, and uncertainty.

	Level of Homogenization	Run Time (min)	keff	Uncertainty
Control	1	1524.18115	1.22036	0.00020
Homogenized Layers	2	1204.94922	1.22058	0.00029
Homogenized Layers and Fuel	3	1079.81848	1.1684	0.00022

Once the geometry of the model was developed parametric runtime studies were performed to optimize source convergence, runtime, and precision. Number of particles, number of generations, and number of inactive generations were adjusted to explore how the model would perform. These parametric studies were performed with the CSAS6 sequence using KENOVI Monte Carlo Transport solver and the continuous energy ENDF/B-VII cross-section library.

4.3.d MC run parameters

As the number of particles are increased the precision improves and the runtime increases. The precision improves slower as number of particles increase while runtime increases almost linearly. The tests were performed with 100 generations and 10 inactive generations. Figure 4-5 shows predicted K-infinity for simulations run with a different number of particles and the standard deviation of K-infinity as number of particles increase. Figure 4-6 shows runtime as a function of number of particles.

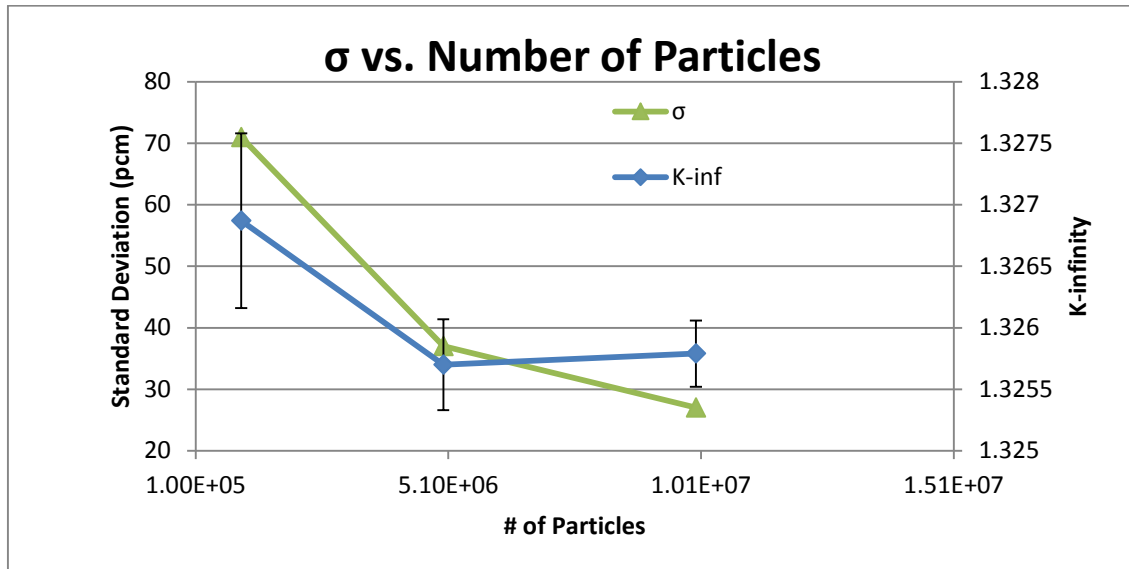


Figure 4-5. Predicted K-infinity and standard deviation with different number of particles run.

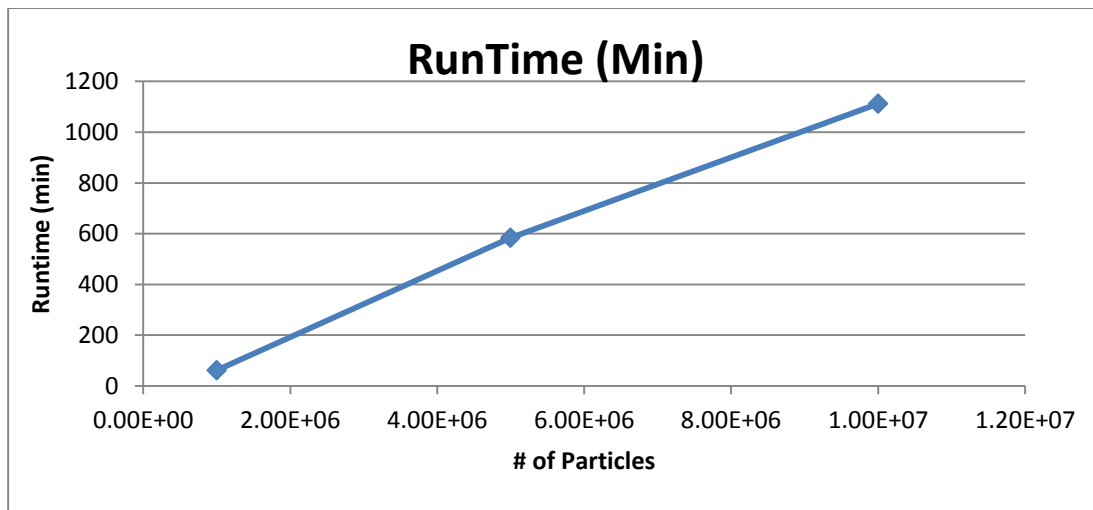


Figure 4-6. Runtime as number of particles are increased.

Tests were done to observe performance as number of generations are increased and number of particles held constant. Each run has 10% of the generations skipped. Figure 4-7 shows predicted K-

infinity calculated with different number of generations and the standard deviation of K-infinity as number of generations are increased. Precision appears to stop improving when more than 100 generations are used. Number of generations only has a small effect on precision. Also, the runtimes for the simulations are very close. The simulations too approximately 390 minutes each. Each simulation ran with 10 million particles.

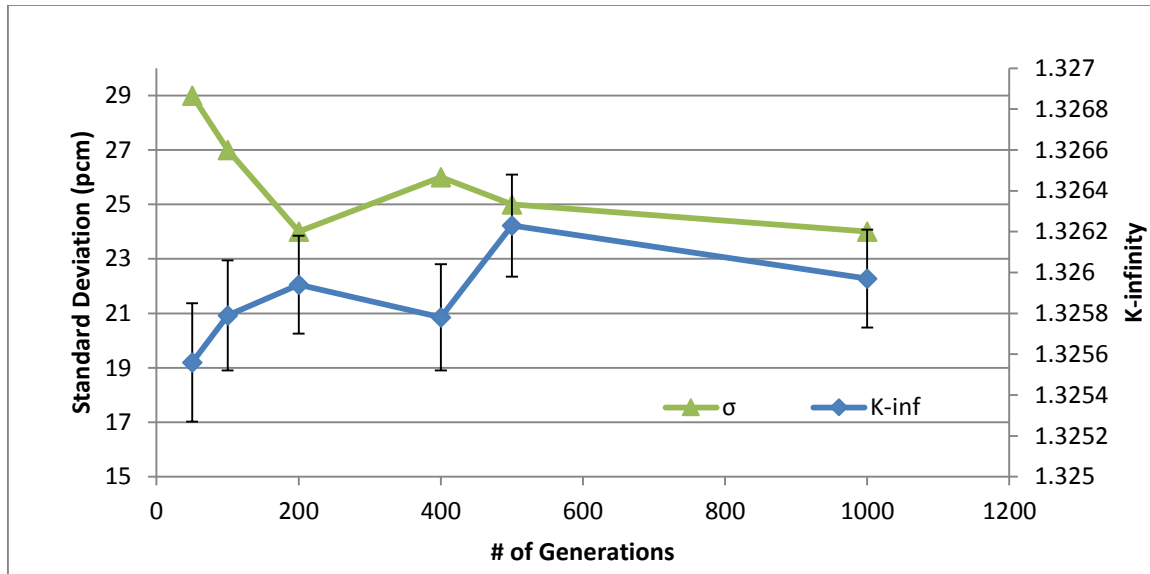


Figure 4-7. Predicted K-infinity and standard deviation as number of generations are increased.

The third parameter affecting simulation performance studied is number of generations skipped. Each simulation was run with only 10,000 particles to get a quick feel for how fast the source converges for the model. Figure 4-8 shows predicted K-infinity produced with different number of generations skipped. It appears that the source is nearly converged after 10 skipped generations.

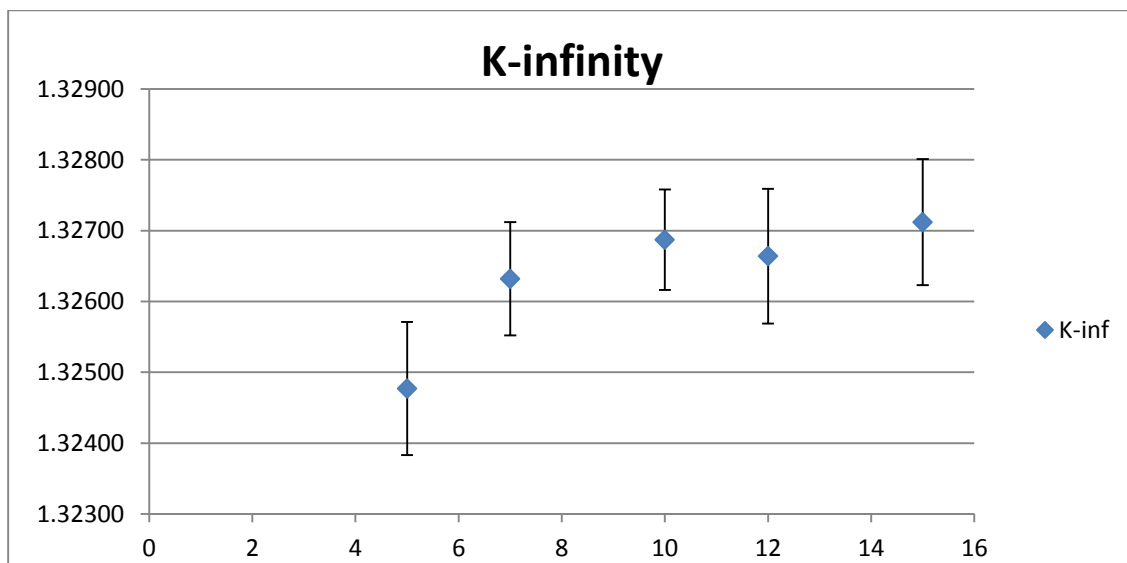


Figure 4-8. Predicted K-infinity with increasing number of generations skipped.

4.3.e Moderator material and structure

Some initial studies were performed to compare graphite with other potential moderator and structural materials. Also the effect of modeling graphite vs. amorphous carbon in the fuel plank carbon matrix was tested to better understand the impact of having correct $s(\alpha, \beta)$ scattering matrix libraries. Other moderator materials that are compared are SiC, zirconium hydride, and yttrium hydride.

Silicon carbide has favorable thermal and mechanical properties. It is of interest to understand how much replacing graphite structural materials in the fuel assembly would affect performance. When the structural materials are changed from graphite to SiC predicted K-infinity at BOC decreases from 1.32644 down to 1.20173. This is much too large of a performance hit to further consider SiC as a moderator.

Stable metal hydrides are of interest as moderator and structural materials since the high atomic hydrogen density makes them effective at slowing neutrons down. Simulations were run with CE CSAS6 KENOVI with the central graphite structure replaced with $ZrH_{1.6}$ and YH_2 . The fuel assembly with the graphite central structure gives a predicted K-infinity of 1.35617. The zirconium hydride and yttrium hydride central structure models give a predicted K-infinity of 1.41662 and 1.19601 respectively. While $ZrH_{1.6}$ gives better neutronic performance and could lead to a design with a higher power density, it is unstable at higher temperatures and would require running the core at lower temperatures to ensure a safe margin. This would lead to a significantly lower thermal efficiency. It would be of interest to see a future study done on the economics of a slightly less efficient design that achieves a higher power density. Further study of zirconium hydride moderator performance in the LSCR is beyond the scope of this research. Yttrium hydride had very poor performance. This is likely due to the slightly lower atomic density of hydrogen and because yttrium has a relatively high thermal absorption cross-section of around 1.28 b.

The structure of the sintered material in the carbon matrix is uncertain, but it is understood that the structure is different from graphite. In order to test the effect of the $s(\alpha, \beta)$ scattering matrix being used in the fuel plank carbon matrix two simulations are run, one using the graphite material library in the fuel plank carbon matrix and one using atomic carbon. The difference in K-infinity between using the scattering matrix in the fuel plank matrix is 130 pcm \pm 60 pcm.

4.3.f Continuous energy (CE) vs multigroup (MG) simulations and procedure to generate MCDancoff

Due to the very long runtime of depletion calculations required to accurately model non-linear burnup the Multi-group Approximation is used. The multi-group approximation requires correction for resonance self-shielding effects to accurately model the flux. SCALE6.1 only has built in functionality to correct for LWR geometries. The LSCR requires a brute force approach to estimate a MCDancoff Factor that can correct for shadowing effects of the double heterogeneous geometry. The MCDancoff Factor is used to correct resonance self-shielding calculations for the double

heterogeneous fuel. Calculating K-infinity without the MCDancoff Factor can result in an error of over 5000 pcm. The MCDancoff Factor is calculated by first performing a continuous energy neutron transport calculation (CE). Then two MCDancoff Factors are guessed and used in two multi-group transport calculations (MG). The results are used to linearly extrapolate an estimated MCDancoff Factor. If this MCDancoff Factor does not provide a K-infinity within $\pm 2\sigma_{K\text{-infinity}}$ of the CE calculation then a 2nd order polynomial extrapolation is used to estimate the MCDancoff Factor. This is repeated at 2nd order until the MCDancoff Factor provides a K-infinity that converges to the CE predicted K-infinity. Once a MCDancoff Factor provides a satisfactory result it is then later used for depletion calculations. Figure 4-9 is a flow chart showing the methodology for calculating the MCDancoff Factor. MCDancoff Factors are calculated over sampled designs over the design space. Regression is performed to create a MCDancoff Factor surrogate model to allow for quick and flexible sampling when performing depletion parametric studies and for developing the physics model used in optimization.

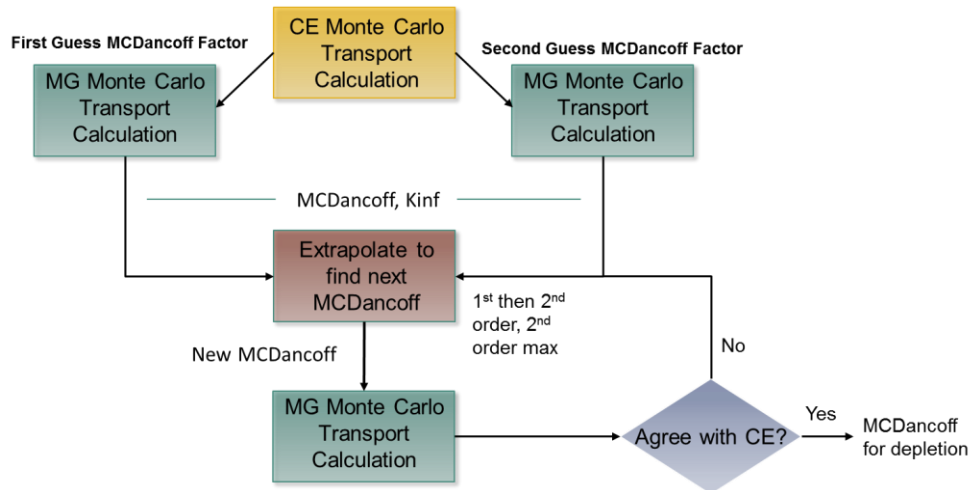


Figure 4-9. Flow chart describing MCDancoff Factor generation methodology.

The MCDancoff Factor is generated at BOC and used each burnstep over the cycle length. To ensure that the BOC MCDancoff Factor is valid over the whole cycle length MG depletion with a MCDancoff correction is compared to CE depletion. Figure 4-10 shows $\Delta K\text{-infinity}$ between CE and MG depletion and $\pm 2\sigma$ of CE depletion. This demonstrates that the BOC generated MCDancoff Factor provides a correction for MG depletion calculations resulting a predicted K-infinity that is in agreement with CE depletion predicted K-infinity over the cycle length.

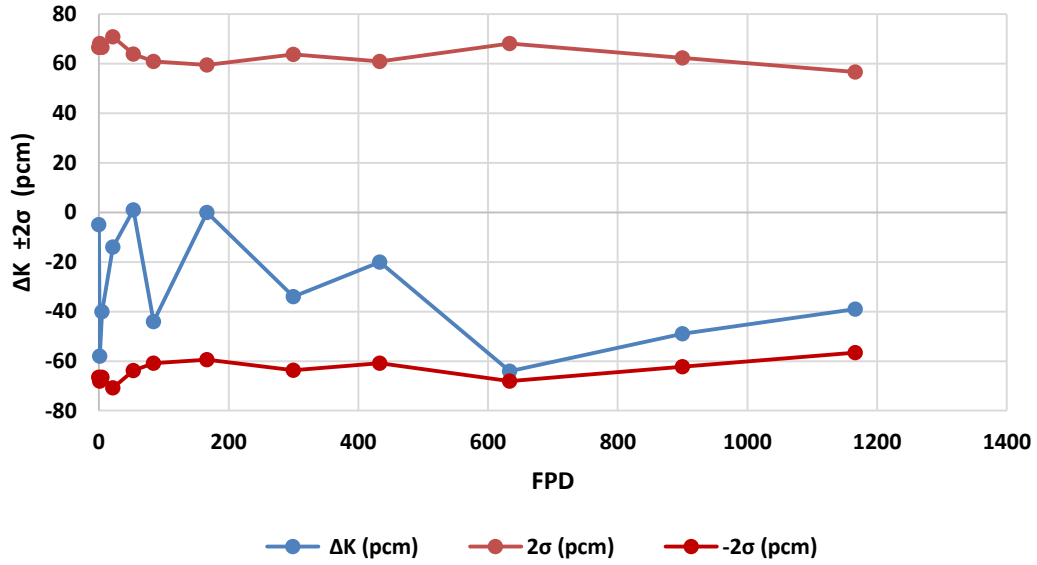


Figure 4-10. Difference in predicted K-infinity between CE and MG depletion with BOC MCDancoff Factor. The red lines are the error propagated standard deviation of the difference in K-infinity.

4.3.g Doppler Broadening in SCALE

The CE transport calculations in SCALE6.1 lack the ability to perform Doppler Broadening, approximating cross-sections for temperatures in between data points. This forces the cross-sections measured at 900 K and at 1200 K to be used when the temperatures are in between. This results in a large error of around 1000 pcm when trying to model correct temperatures in CE transport. MG transport calculations have the Doppler Broadening feature available. The process for generating MCDancoff Factors was performed at 900 K and 1200 K and the MCDancoff Factors were compared. Figure 4-11 shows the probability distribution vs. energy of a neutron born in fuel. Figure 4-12 shows the absorption cross-section of ^{238}U and the fission cross-section of ^{235}U . It can be seen from these two figures only about 10% or less of the probability distribution of neutrons born in fuel lie in the resonance region of the fuel. Table 4-2 shows that the difference in the MCDancoff Factor generated at these two temperatures is less than 10% of the difference in K-infinity. Since the temperatures modeled in the fuel is between 900 K and 1200 K the error in the MCDancoff Factor should be significantly less than 177 pcm.

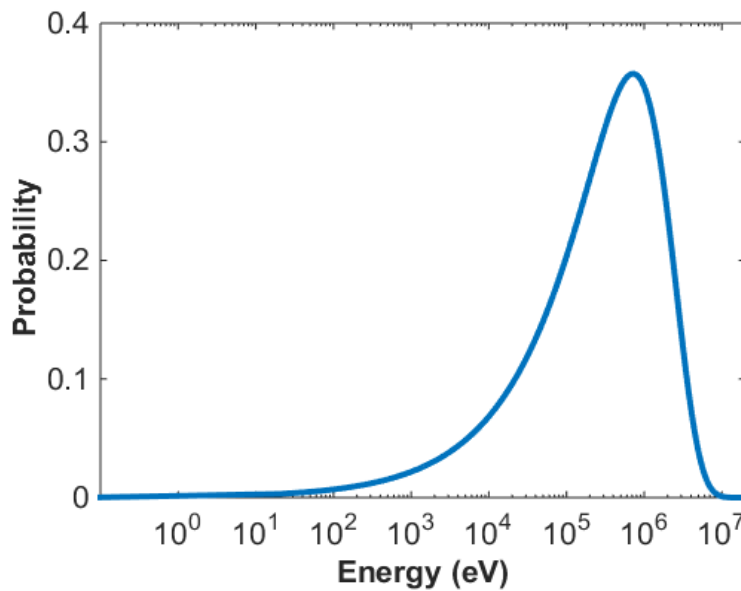


Figure 4-11. Probability distribution function for neutrons borne in fuel over range of energies of interest.

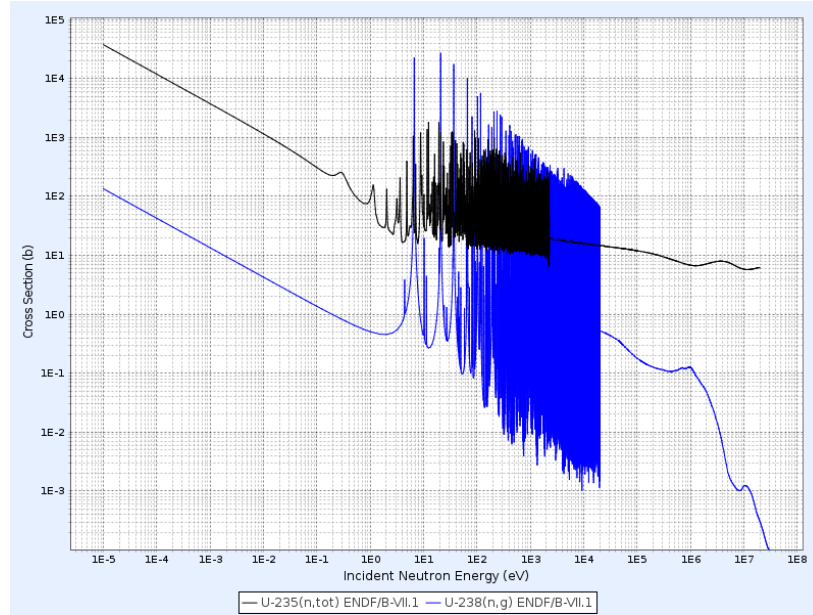


Figure 4-12. Microscopic cross-sections for total ^{235}U cross-sections and ^{238}U absorption cross-section.

Table 4-2. Difference in predicted K -infinity and MCDancoff Factor generated at 900 K and 1200 K.

Temp	900 K	1200 K	Δ (pcm)
CE K -infinity	1.55551	1.53600	1951
MG K -infinity	1.5558	1.53572	2008
MCDancoff	0.87165	0.86988	177

Once the MCDancoff Factor is generated using set temperature data a model is fit using MCDancoff data over the whole design space. A single channel thermal hydraulics model is used to provide average temperatures for the fuel, moderator, and coolant in the fuel assembly. The thermal hydraulics model was developed by Pietro Avigni (Section 7.1.a) and the results were fit with a multiple polynomial regression model for quick flexible sampling and to avoid porting the scripts from MATLAB into Python.

4.3.h Depletion – use of Linear and Non-Linear Reactivity Models (LRM vs NLRM)

Depletion calculations are performed with the TRITON6-depl sequence in SCALE6.1 with the KENO Monte Carlo neutron transport solver in multi-group. Each calculation uses 23 burnsteps with 3 burnsteps in the first 6 days to account for the rapid reactivity drop due to xenon buildup before equilibrium. Figure 4-13 shows predicted K -infinity over the cycle length for the 2011 base case. Depleting the fuel results in a non-linear change in K -infinity. The trend-line shows a very poor fit for the change in reactivity over the cycle length. The non-linear reactivity behavior is most likely due to the higher enrichment of the fuel and the epithermal neutron spectrum.

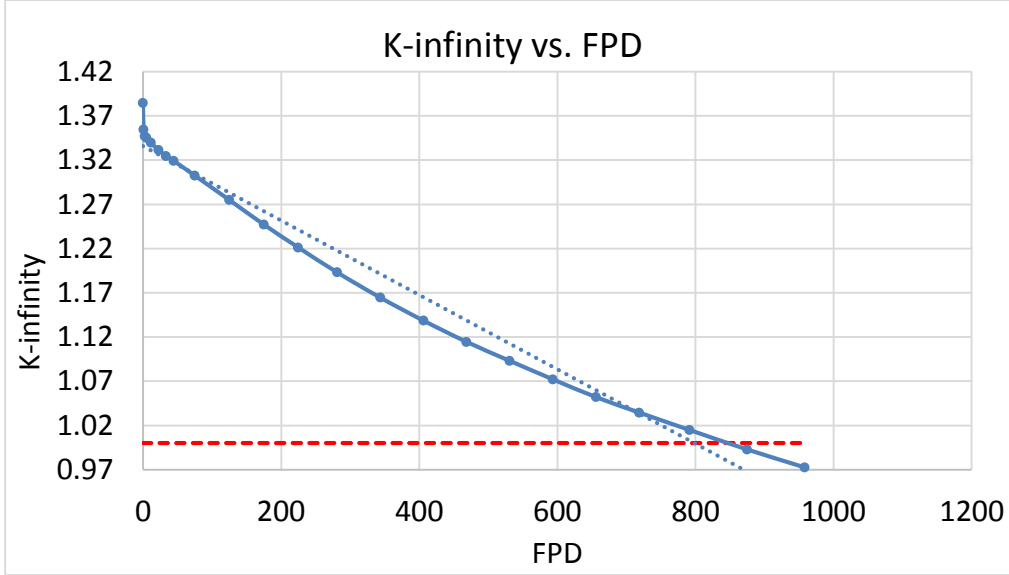


Figure 4-13. K -infinity as a function of FPD with a linear trend line showing how reactivity is non-linear. The red dashed line shows where K -infinity is equal to 1.

Due to the epithermal spectrum and higher enrichment of the LSCR the drop in reactivity over a fuel cycle is non-linear. This Linear Reactivity Approximation is inaccurate in predicting cycle length of multi-batch fuel cycles for this design. A simple Non-linear Reactivity Model has been found to be more accurate in predicting multi-batch cycle lengths. The full core leakage correction factor model developed by Spencer Lewis was adapted to include higher dimensionality by relating to the CHM ratio and was fit with multiple polynomial regression. Figure 4-14 shows residence time for the NLRM and the LRM as a function of batches. The difference in cycle length as a function of batches between LRM and NLRM are compared in Figure 4-15. The following equations are used to calculate the NLRM:

$$\begin{aligned}\rho(b) &= y^0 + y^1 b + \dots + y^{(m)} b^m \\ \rho_{EOEC} &= \frac{1}{n} \sum_{i=1}^n \rho(b_i^{EOEC}) \\ \rho_{EOEC} &= \frac{1}{n} \sum_{i=1}^n \rho\left(\frac{ib_i^{EOEC}}{n}\right) \\ \rho_{EOEC} &= \frac{1}{n} \sum_{i=1}^n y^0 + \frac{y^1 ib_{discharge}}{n^2} + \dots + y^{(m)} \left(\frac{ib_{discharge}}{n}\right)^m \\ \rho_{EOEC} &= y^0 + \frac{y^1 b_{discharge}}{n^2} \sum_{i=1}^n i + \dots + \frac{y^{(m)} b_{discharge}^m}{n^{m+1}} \sum_{i=1}^n i^m \\ 0 &= y^0 + \frac{y^1 b_{max}}{n^2} \sum_{i=1}^n i + \dots + \frac{y^{(m)} b_{max}^m}{n^{m+1}} \sum_{i=1}^n i^m\end{aligned}$$

As number of batches increase the residence time of the fuel increases. The increase in the difference in residence time diminishes as the number of batches increases further. Figure 4-14 shows cycle length as number of batches increase for the NLRM and LRM. Figure 4-15 show the difference in cycle length between the two models as number of batches increase. The results show that the LRM gives an error in predicted cycle length greater than 2σ , where the standard error is approximately 4 days. The difference between the models increases as the number of batches increase. It is apparent that the LRM consistently underestimates cycle length compared to the NLRM.

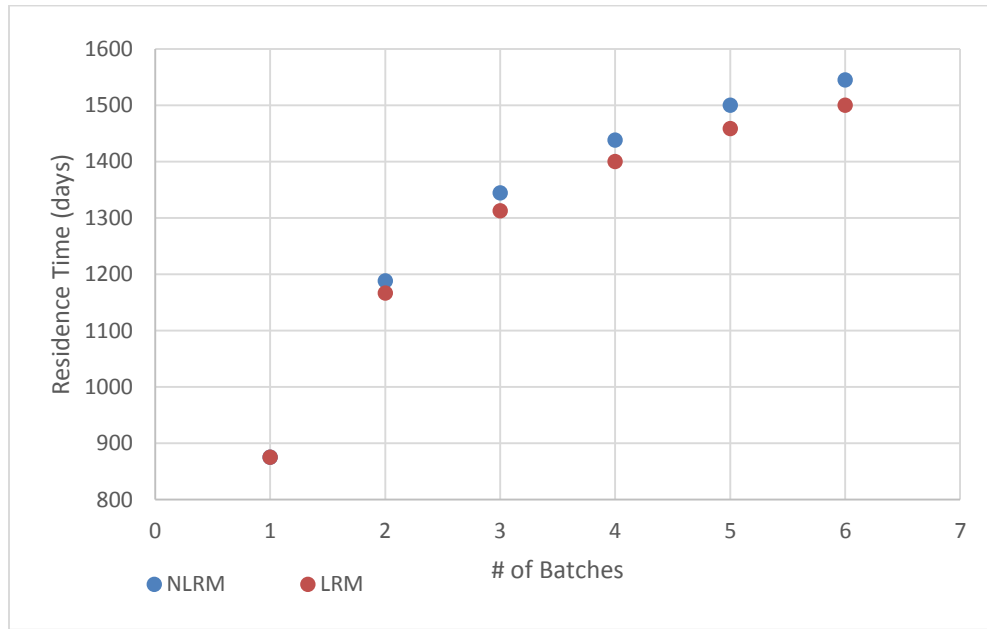


Figure 4-14. Cycle length as number of batches is increased for the NLRM and LRM.

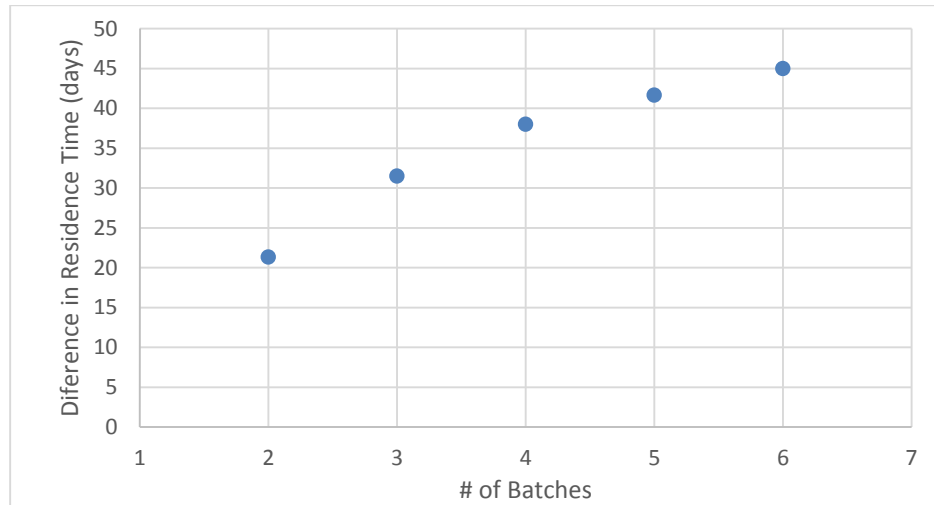


Figure 4-15. Difference between NLRM and LRM in days as number of batches are increased.

4.4 Evaluation of existing methods and SERPENT Models

4.4.a Employing Random TRISO Particle Dispersion vs Regular Lattice Arrangements

First, and somewhat most apparent of the modeling challenges, is the accurate and expedient treatment of the TRISO particles within the fuel stripes. Due to the novelty of the AHTR fuel design, a specific fuel fabrication process has yet to be developed. Multiple methods for fabricating graphite TRISO particle compacts for cylinders and spheres have been considered including powder and particle mixture pressing, particle overcoat pressing, and molten matrix injection into random closed packed particles, each having their own strengths and challenges [7]. It was assumed for this research that the most likely manufacturing process would be the graphite over coated particle pressing technique due to its recent use in manufacturing irradiation specimens for Advanced Gas-cooled Reactors (AGRs) [8]. What is important in this assumption is that the resulting compact should be a nearly random particle dispersion with some non-random packing clustering near the dye wall as shown in Figure 4-16. . In theory it may be possible to pre-structure the particles into a hexagonal closed-pack prior to compression which would help to achieve packing fractions near 50% post compression, but it is likely that the uniform arrangement will not be perfectly maintained during compression, and so the random dispersion assumption still likely accurate [9].

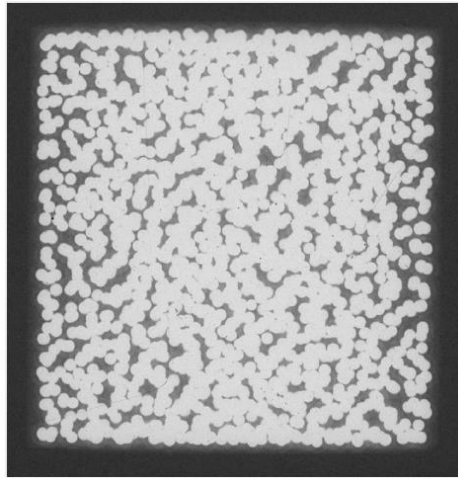


Figure 4-16. X-ray radiograph of an AGR-3/4 compact [8]

Given that the actual dispersion will be mostly random, it was then believed that the most accurate approach for modeling the particles would be by explicitly treating each particle individually in a random dispersion. SERPENT 2 provides a random dispersion module for the generation of random dispersion realizations, and has sufficient geometry definitions to meet the needs of this research as shown in Figure 4-17. . Though this method was believed to be the most faithful to what would be the actual fuel geometry it suffered from longer runtimes due to the detailed tracking of individual particle locations and the requirement of several realizations to obtain a representative average [11].

Because of the demands on runtime accompanying the multiple realizations of a random dispersion treatment, an alternative regular lattice particle arrangement was considered as shown in Figure

4-18. . It should be noted that this lattice treatment allowed clipping of particles at the stripe edges for the sake of model simplicity, and that subsequently the particle lattice pitch was adjusted to ensure the correct fuel volume representation. Such a treatment removes the statistical aspect of the random dispersion realization and alleviates the need for multiple realization for an average representation, but also introduced possible sources of error from alteration of the local fuel-to-moderator ratio, provision of streaming paths along the lattice planes, and of course the unphysical clipping of particles [12].

To assess the significance of this error, five random dispersion realizations were simulated and compared against the regular lattice particle arrangement. As can be seen in Figure 4-19, the difference in reactivity between random dispersion and regular lattice treatments are not insignificant, in some cases exceeding 300 ± 43 pcm, but are not so large as to invalidate the regular lattice treatment. More importantly though is the comparison of the assembly averaged flux spectrum presented [16], wherein the spectra appear to be nearly identical between the random dispersion realizations and the regular lattice arrangement at beginning of cycle (BOC) conditions. This is believed to be indicative that few group homogenized cross-sections generated using a regular lattice particle arrangement will be very similar to cross-sections generated from a random dispersion treatment, and so justifies the use of a regular particle arrangement. It should be noted for completeness that the one-standard deviation Monte Carlo statistical uncertainties for the flux spectrum were predominantly $<0.1\%$ Relative Standard Error (RSE) with the exception of the very low flux regions where uncertainties were as high as 11% RSE.

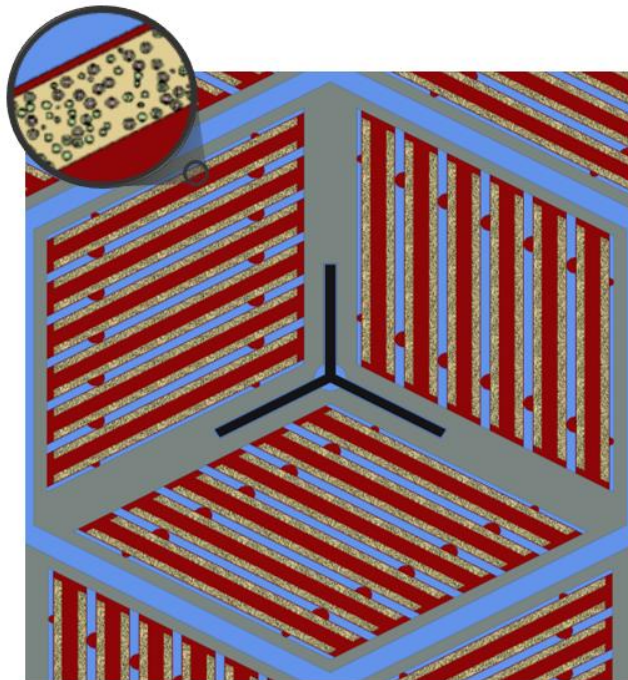


Figure 4-17. SERPENT 2 Model of AHTR Fuel Assembly with randomly dispersed TRISOs

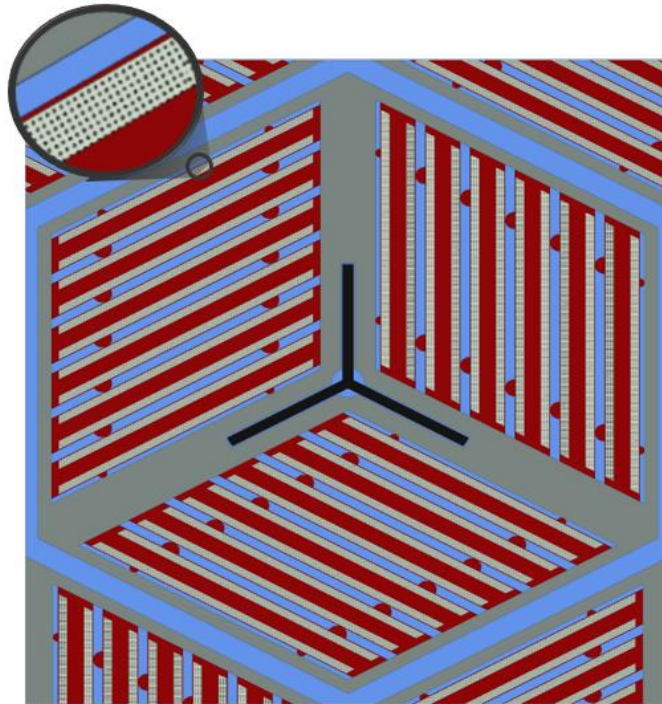


Figure 4-18. SERPENT 2 Model of AHTR Fuel Assembly with regular lattice TRISOs

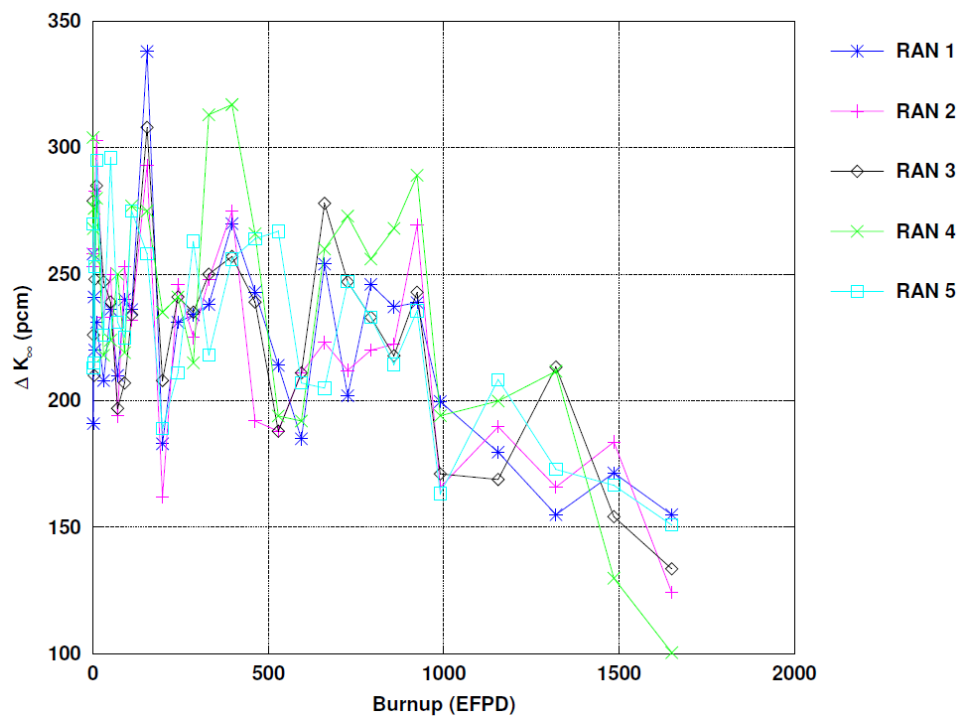


Figure 4-19. K-infinity Difference between Regular Lattice and Random Dispersion

4.4.b Effect of Partial Layer Homogenization

With these results it was decided that an explicit treatment of individual TRISO particles could most expediently and accurately be simulated using a regular lattice arrangement. In addition to this treatment, a common runtime reduction technique of partial homogenization of particle coatings (i.e. homogenizing buffer / IPyC layers together and OPyC / matrix together), was utilized to reduce transport runtimes while maintaining reactivity and flux characteristics effectively unaltered [13]. Figure 4-20 shows that the error introduced by partial coating homogenization, and in fact also full coating homogenization, is essentially negligible (Note: error uncertainties for both cases were less than 43 pcm). Partial homogenization was chosen rather than full homogenization to maintain some level of consistency with the ORNL study which employed only partial homogenization when considering explicit TRISO particle treatment.

Other techniques that were reviewed in this research for the treatment of TRISO particles included the Chord Length Sampling technique, a Collision Probability treatment, the SCALE-NEWT Double Het treatment, and the SERPENT 2 implicit TRISO model treatment [10, 13, 14]. However, each of these were ultimately rejected on the grounds of either insufficient theoretical or implementational maturity.

Additionally, the RPT method was considered as a possible runtime reduction technique and was partially utilized in the energy group optimization portion of this research as will be discussed later, but was ultimately decided against in the cross-section generation model on account of its lack of physicality and added necessity of equivalency parameter search.

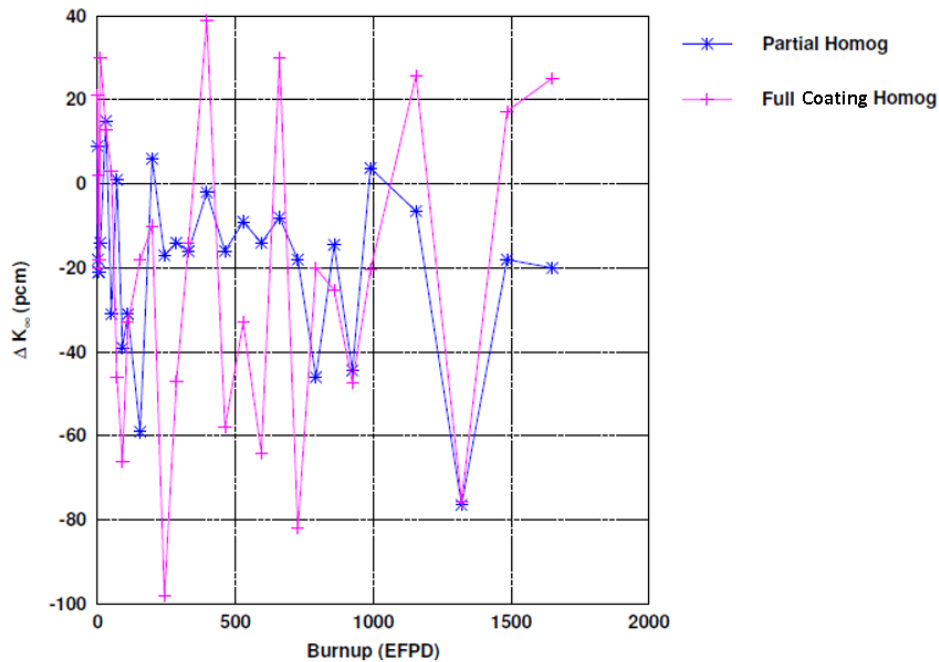


Figure 4-20. Error of Partial and Full Coating Homogenization Compared to Full Coating Treatment

Much as in the case of LWRs, one must consider the level of subdivision of depletion regions necessary in order to ensure accuracy. Individual depletion of every fuel TRISO particle is not only an impractical endeavor but rather an impossible one due to the memory restrictions of current computers. As such, some degree of fuel depletion lumping will be necessary to make the simulation problem tenable. Practicality dictates that not only should fuel lumping be employed to make the simulation obtainable, but also expedient where at all possible, meaning increasing the degree of lumping to optimize runtime and memory usage with respect to model accuracy. As such, this important concern for developing an accurate two-step procedure was considered in this research.

4.4.c Effect of Number of Depletion Regions

To assess the impact of fuel depletion, lumping models were created with varying degrees of lumping ranging from 2 depletion zones for a given assembly, one representing plate top stripes and the other plate bottom stripes, all the way to 329 depletion zones with 9 depletion zones for each stripe. Depletion zone subdividing was generally performed only along the length of stripes rather than the thickness of stripes given that the stripes width is relatively thin compared to the stripe length. An illustration of the stripe depletion subdivision is presented in Figure 4-21.

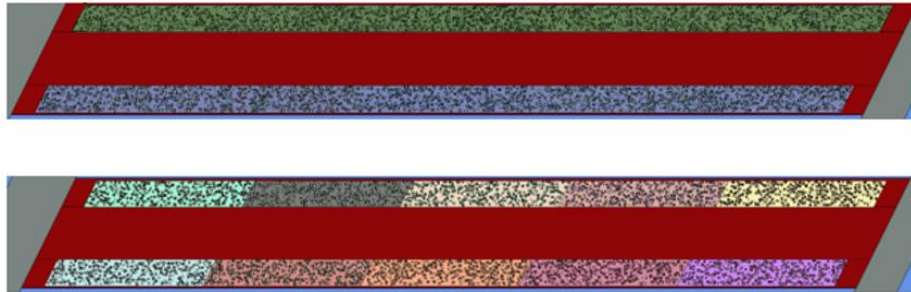


Figure 4-21. Illustration of Lumped Depletion(top) vs. Stripe Subdivided Depletion (bottom)

A comparison of model reactivity was made using the different levels of depletion subdivision, the results of which can be observed in Figure 4-22. To clarify the labeling of the results, “Lumped” refers to two depletion regions for the entire model, one for all instances of the “upper” fuel stripe within all plate and one for all instances of the “lower” fuel stripe within all plates. Furthermore, cases labeled as “Subd” denote the number of subdivisions applied along the length of every stripe, implying that all stripe instances are depleted independently and are then further subdivided. Since each of 3 tri-sections in an assembly has 6 plates with 2 stripes each, this corresponds to $3 \times 6 \times 2 = 36$ stripes per fuel assembly. So, for “Subd 1” 36 depletion regions were simulated, one for each stripe, whereas for “Subd 9” 329 depletion regions were simulated, 9 for each stripe.

It can be observed in the results that model differences with respect to the Subd 9 model generally increased with accumulating burnup and are largest for cases with the fewest lumped depletion zones. However, the error even for two depletion zone model was not extraordinarily large and this quickly decreased in magnitude as the number of depletion zones was increased (Note: again error uncertainties were less than 43 pcm). Ultimately, five subdivisions per stripes, totaling 180 total depletion zones, was deemed to be sufficiently accurate for lattice physics simulations without

demanding an overwhelming amount of computer memory and runtime. It should be noted that another parameter of interest that should be considered in future studies of depletion region refinement is the stripe-wise power distribution, which was not investigated in this study.

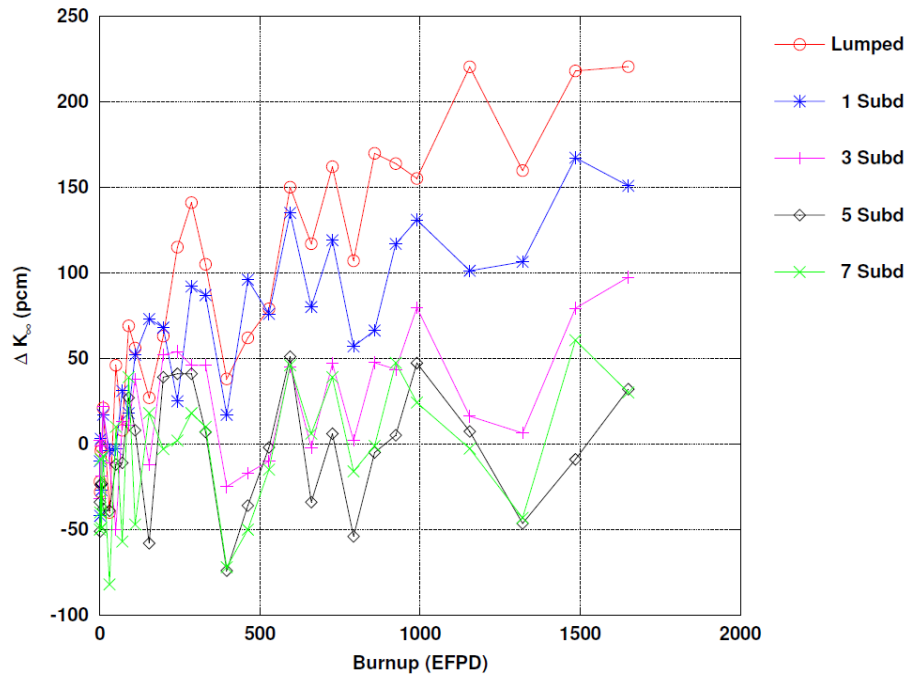


Figure 4-22. *K*-infinity Difference versus 9 Depletion Sub-divisions per Fuel Stripe

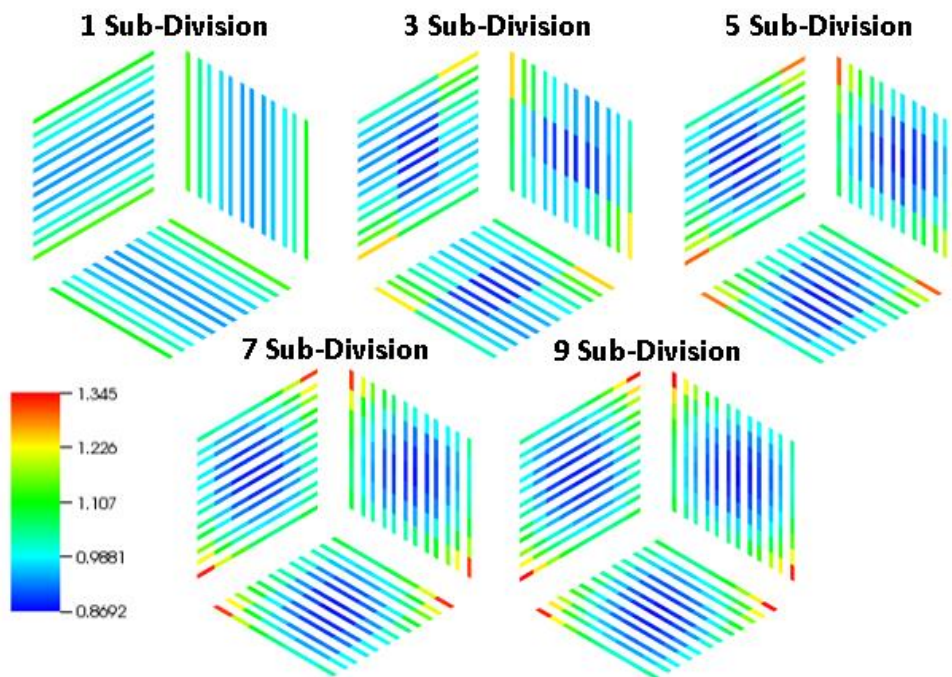


Figure 4-23. Power Densities at 0 GWd/MTM of each Sub-Division Model Normalized to Assembly Average

One important current shortcoming of the SERPENT 2 code that warranted investigation is the lack of capability for simulating coupled photo-nuclear reactions. The ^9Be isotope which is a constituent of the FLiBe coolant exhibits a few notable photo-neutron reactions, as illustrated by the cross-section profiles in Figure 4-24, that the SERPENT 2 code currently does not treat. Therefore, a 2-D single assembly model was created and simulated using the Monte Carlo code MCNP6 to assess the potential photo-nuclear effects [15].

4.4.d Effect of Photo-Neutron Reactions

As can be seen in Table 4-3, the MCNP6 simulation with photo-nuclear physics tracking NP mode has an essentially identical reactivity as the N mode simulation with tracking of only neutron interactions. Thus, indicating that the photo-neutron reactions of ^9Be are not large enough to call into question the accuracy of the SERPENT 2 model with regards to the absence of photo-nuclear effects. It should be noted that the SERPENT 2 difference with MCNP6 is slightly higher than expected, but still believed sufficiently small such that it might be attributed to minor differences in model setup and not a need for concern. Possible explanations for this difference could either be small inconsistencies in cross-section treatment or a small shifting of the regular lattice TRISO grid in the MCNP6 model such that the particle clipping and subsequently fuel volume was altered. Again, the error was thought to be sufficiently small such that the exact cause for the difference was not pursued.

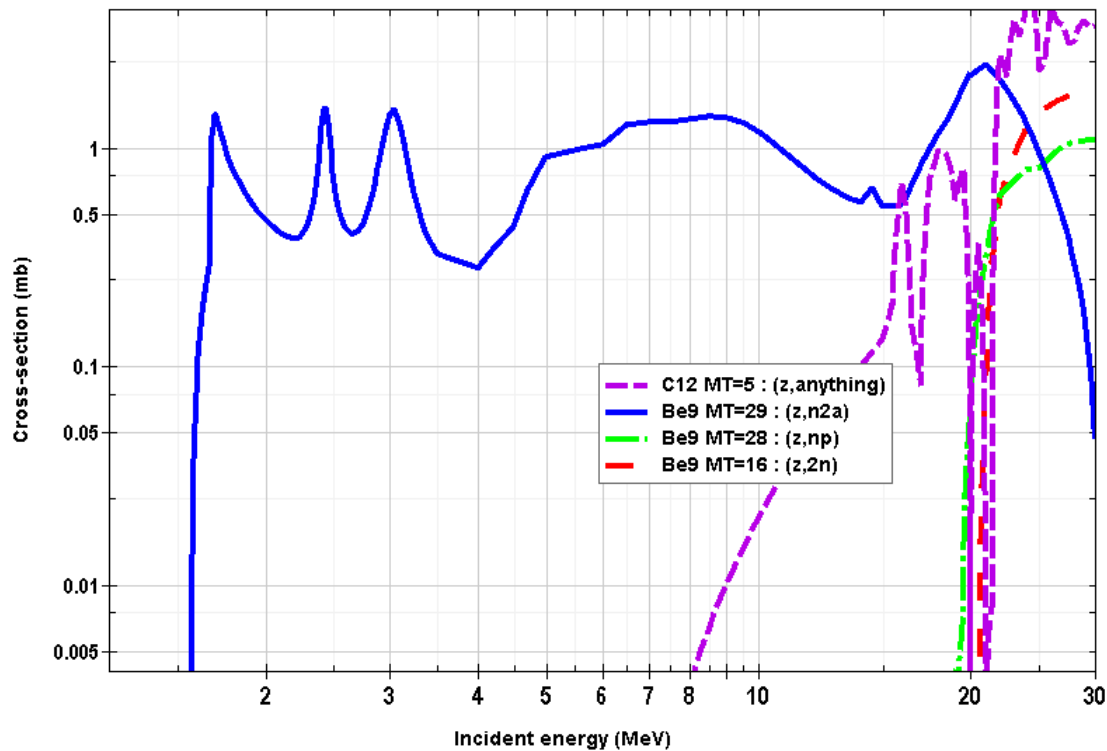


Figure 4-24. Gamma Cross Sections of Interest for AHTR [16]

Table 4-3. Assessment Photo-Nuclear Effects

MCNP 6.1 NP mode k-infinity	MCNP 6.1 N mode diff (pcm)	SERPENT 2 diff (pcm)
1.35587 +/- 10	16 +/- 14	232 +/- 20

Over the course of the project, model improvements have gradually been made in order to help improve the accuracy of results. One such improvement was the application of a fuel volume correction algorithm for clipped regular lattice particle arrangements. In this algorithm, a Secant Iteration is employed to search for the particle pitch that produces the correct fuel volume in the model (i.e. where the fuel volume error is nearly zero). The SERPENT 2 volume approximator is used for estimating the fuel volume error between iterations. The primary motivation for implementing this method is so as to more accurately employ the regular lattice particle arrangement and avoid the statistical fluctuations of utilizing a random particle dispersion scheme.

4.4.e Effect of Plate Spacers

The next major improvement was the addition of the plate spacers into the model as illustrated in Figure 4-25. These spacers are assumed to be made of the same carboneous material as the rest of the plate and also assumed to effectively span the entire length of the fuel plates.

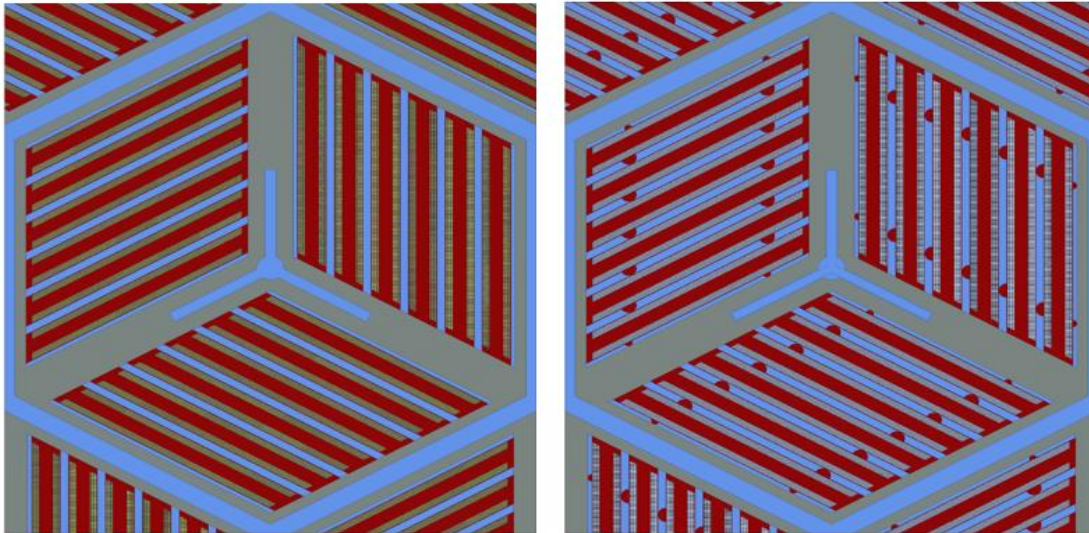


Figure 4-25. 2D Assembly model without Spacers (Left) and with Spacers (Right)

It can be seen in Figure 4-26 that the addition of the plate spacers to the model does have some effect, whereby the extra carbon increases k-infinity by over 1000 pcm for most of the assembly life time which is easily explained by the increased moderation and softening of the neutron spectrum. This ultimately translates into an increased maximum discharge burnup and cycle length, with largest differences of about ~10 GWd/MTHM for discharge burnup and ~20 days for cycle length. It is believed that though these differences are significant and worth noting, they are not so large as to invalidate the results of models absent of plate spacers.

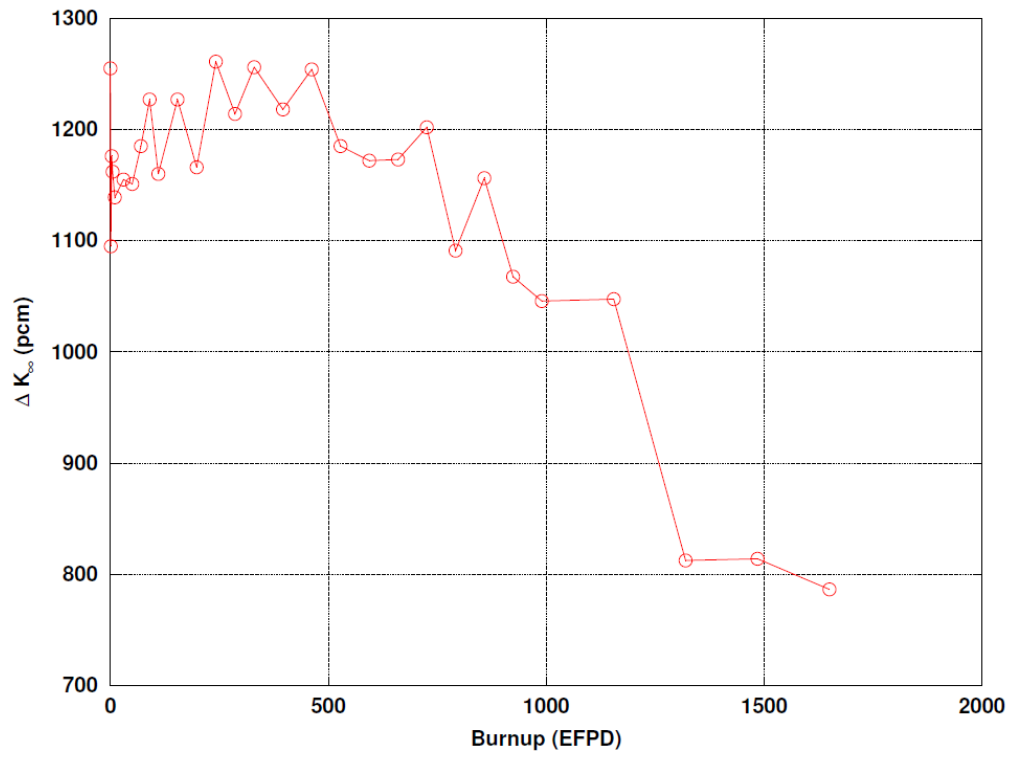


Figure 4-26. Impact of Spacers Upon k -infinity

4.5 Two-step procedure and models

Preliminary neutronic and core characteristic analyses of this reactor design have been demonstrated with Monte Carlo based core models. However, these models are computationally expensive and not conducive for design optimization studies or direct coupling to thermal hydraulics models for capturing thermal feedback effects [1,4]. As such, it is then necessary to develop a computationally expedient modeling method to provide a means for improved safety and economics analysis. The conventional two-step procedure utilized for modeling Light Water Reactors (LWRs), which employs deterministic transport theory based “lattice physics” to generate assembly-homogenized and few energy group collapsed cross sections for use in advanced 3-D nodal diffusion simulators [17-19], furnishes a reference approach from which to base a new more efficient modeling method for the AHTR. However, differences between LWR and AHTR core designs and overall neutronics behaviors demands adaption of the original procedure to accurately capture the physics characteristics of the AHTR. This adaption will result in new two-step procedure specifically tailored for AHTR modeling.

The first and most obvious of these differences is the use of TRISO particles, which are normally not applied in LWR applications. Growing interest in alternative LWR fuel designs and accident tolerant fuels has led to the development of fairly accurate treatments of TRISO particles in the lattice physics pin-cell calculations, an example of which can be found in the SCALE-NEWT software [10]. However, most production level codes consider TRISOs dispersed strictly in either spheres or cylinders for pebble or pellet applications and not in plates. Though the addition of a plate treatment may seem a small triviality, and in fact should not be difficult to implement, it must be kept in mind that the plates are not all arranged in a nearly 1-D fashion, but rather are rotationally oriented around the assembly center. Combining this fact with the longer neutron diffusion length it can be seen that deriving an accurate pin-cell model, or in this case plate-cell model, for the initial lattice physics multi-group energy group reduction is considerably more challenging.

The increased diffusion length is essentially a result of using graphite as the primary moderator rather than light water. The carbon in graphite being a larger atom than the hydrogen in water exhibits poorer moderation of neutrons in any individual collision, however graphite as a whole displays a lower parasitic absorption than light water and subsequently an overall superior moderating ratio and subsequently longer diffusion length. Graphite’s solid crystalline structure allows for thermal neutrons to interact with graphite crystals in a coherent scattering manner rather than only individual atom collisions resulting in more complex scattering behaviors and in general greater up-scattering than water. The longer diffusion length not only confounds the accurate simulation of a plate-cell model, but also increases the sensitivity of a given fuel assembly to the influences of its surrounding neighbor assemblies. This leads to a challenging of the infinite assembly assumption employed by the lattice physics calculations, and in order to preserve the accuracy of this assumption one needs to either increase the number of energy groups used in the coarse group structure or consider multi-assembly super cells rather than single assembly cells.

AHTR not only exhibits a longer neutron diffusion length, but the combined effects of graphite's scattering properties and the AHTR's higher operating temperature also lead to an altering of the core flux spectrum, as shown in Figure 4-27. We can see in the figure that the thermal spectrum peak is shifted to higher energies as compared to a typical LWR spectrum, which puts it in closer proximity to the low lying plutonium resonances typical of high temperature reactor designs. This ultimately means that the energy regions of interest, and subsequently few-group energy boundaries, will be different from those utilized in the LWR two-step procedure.

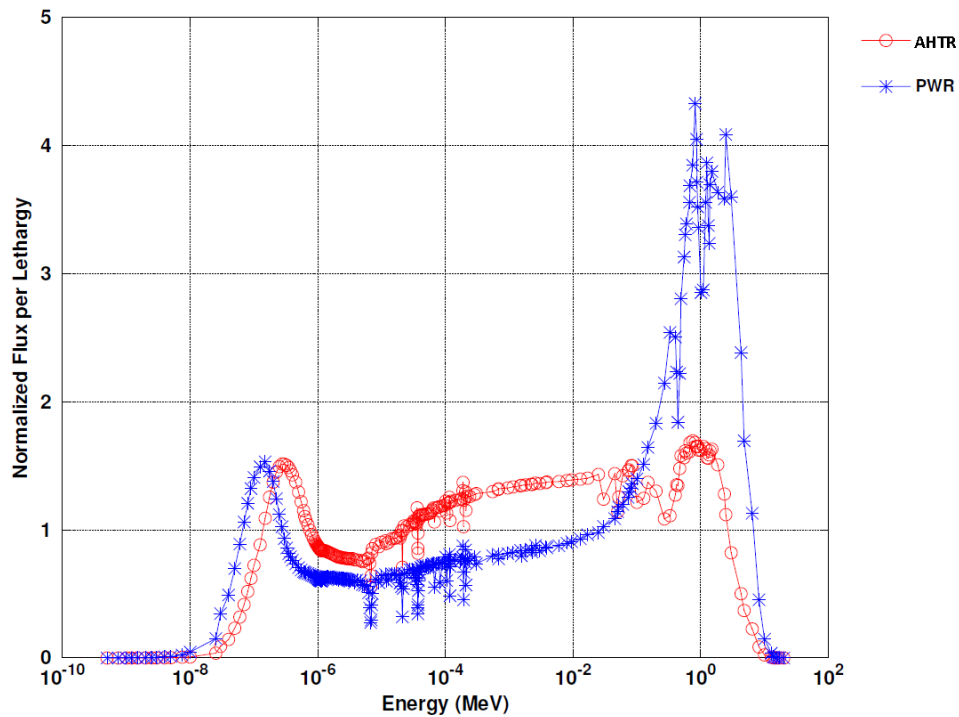


Figure 4-27. Comparison of AHTR and LWR Flux Spectrum

The need for few-group energy group structure reassessment is further accentuated by the use of an exterior graphite reflector. It has been observed that a large flux gradient exists between the fuel and reflector regions with significant alteration in fuel spectrum which is evident in the outer most assemblies. Therefore, accurately capturing the neutronics of the reflector will require the development of an appropriate reflector model, and a sufficient number of energy groups will be necessary to correctly represent the strong flux gradient between fuel and reflector.

The final challenge, though not entirely unique to the AHTR, is the accurate treatment of control blades throughout the two-step procedure. Given that the FLiBe coolant has a much smaller negative reactivity coefficient than the water in LWRs, as depicted in Figure 4-28, use of a chemical poison shim in the coolant would likely introduce an undesirable positive coolant density reactivity coefficient. Therefore, primary reactivity control must be performed using the control blades. Such a control strategy often does not require the partial insertion of all control elements across the whole core, but rather of only a select few based on fuel burnout and cycle fluctuations. This implies that the infinite assembly assumption for the control blade inserted scenario will be incorrect and in need of adjustment to appropriately account for leakage with the neighboring uncontrolled assemblies.

All of these items must be addressed in order to develop an AHTR adapted two-step procedure. The primary points that can be derived from above is that AHTR requires the development of an appropriate lattice physics model, a re-optimization of the few-group energy group structure, the development of an accurate reflector model, and a leakage adjustment of the control blade insertion lattice results to account for control blade insertion heterogeneity.

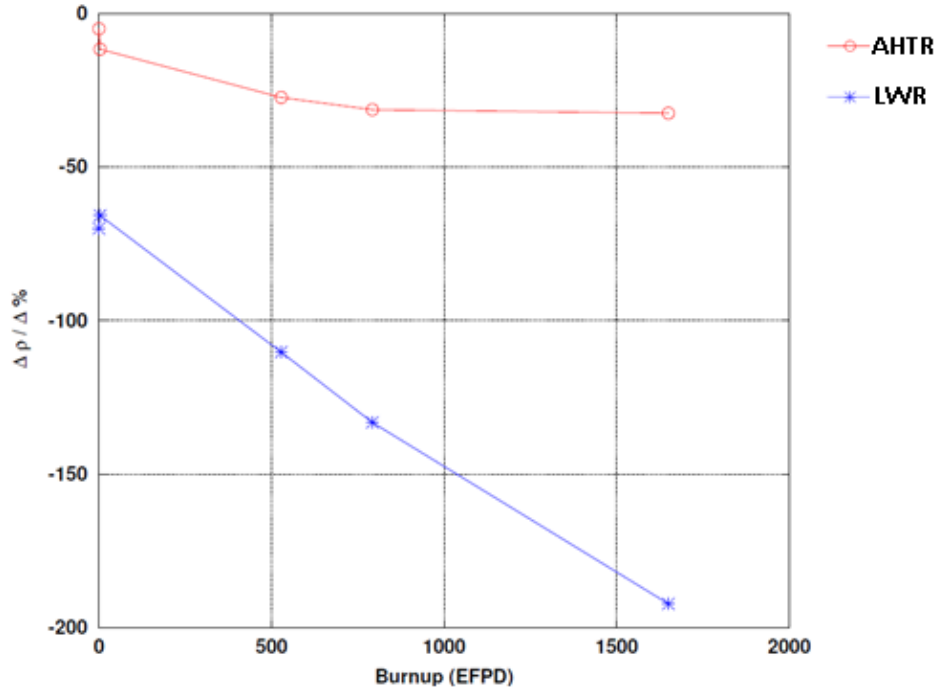


Figure 4-28. Comparison of AHTR and LWR Coolant Density Reduction Coefficient

After establishing the initial framework of the two-step procedure—meaning establishment of the lattice physics model and connection to the core simulator—focus then shifted to re-optimizing the few-group energy group structure to ensure accuracy of the infinite assembly assumption. Longer diffusion lengths, altered flux spectrum, and the presence of steep flux gradients near the reflector all challenge the original few-group energy group structure used in traditional LWR two-step procedures. To address this, an algorithm for determining coarse energy group structure for homogenized cross sections proposed by Kim et al. for the very high temperature reactor (VHTR) was employed [9].

In this algorithm, core models are simulated for a variety of expected representative operating conditions such as various fuel burnup profiles, operating temperatures, control blade insertion patterns, and a multitude of other possible core configurations. Similarly, single infinite assembly models are also simulated to span the possible assembly configurations, considering assembly burnup, operating temperature, control rod position, etc. In all full core and single assembly simulations, multigroup collapsed values (typically 100+ energy groups, but for this research, 190

energy groups) for assembly zone wise fluxes, absorption cross sections, and $\nu \cdot \Sigma_{fiss}$ cross sections are edited for use in further optimization.

These 190 energy group values are then progressively condensed via flux weighted averaging such that the infinite assembly model cross sections can be substituted into the corresponding equivalent full core assembly counterparts without exceeding a set error limit. Starting with the highest energy group, this algorithm attempts to combine the first two energy groups, and if the infinite assembly approximation error remains below the set point, it attempts to combine into the compound group the next lowest energy group, and so on. This process repeats until all energy groups are consolidated or the infinite assembly approximation error set point exceeded. If the error set point is exceeded, the condensation stops, a group boundary is drawn, and a new group consolidation begins at the boundary as a new collection of condensed groups. This process continues until all energy groups have been considered, with the resulting group boundaries representing the new few-group structure.

To help reduce the size of the full core model and subsequently the number of assembly zones considered in the algorithm, a 1-D mini-core, illustrated in Figure 4-29, was derived which provided flux spectrum conditions for the interior and peripheral assemblies that were nearly equivalent to the 2-D full core model. This mini-core model was simulated under a select number of representative operating conditions and core configurations using the Method of Characteristics (MOC) code KARMA due to its speed of simulation [10].

Initial use of the algorithm, along with the mini-core models, resulted in a 13-group structure as shown in Table 4-4. Though this structure does obtain good reaction rate errors, the number of groups was considered excessive since the HTGR, which has a longer diffusion length than the AHTR, only requires 10 energy groups for accurate results [11]. Additionally, NESTLE only supports few groups structures of up to four energy groups, necessitating further reduction of the few group structure. Through manual manipulation of the few group boundaries, two 4-group structures, which are defined in Table 4-5, were ascertained. Option 1 provided reaction rate errors nearly equivalent to the 13-group structure. Option 2 resulted in worse reaction rate errors but ultimately provides a better group structure for ensuring an accurate reflector model.

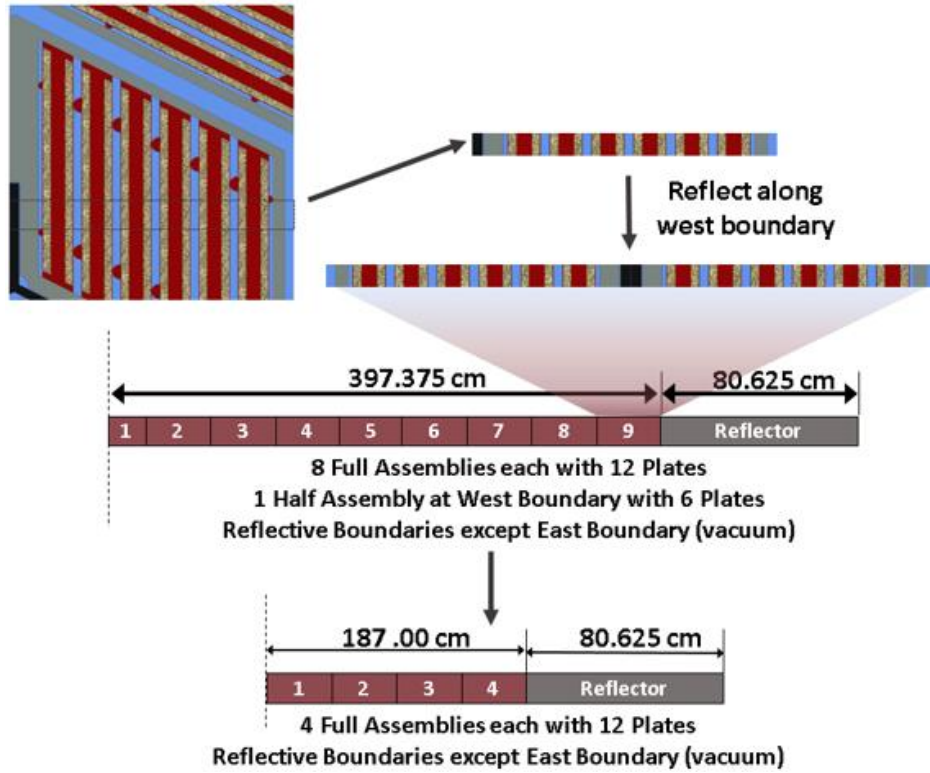


Figure 4-29. Depiction of Semi 1-D Mini-Core Simplification

Table 4-4. 13-group few group structure

Group #	Group Boundaries (MeV)	
	Upper Bound	Lower Bound
1	2.0000E+01	1.4739E-04
2	1.4739E-04	4.5000E-07
3	4.5000E-07	2.9074E-07
4	2.9074E-07	2.5103E-07
5	2.5103E-07	2.2769E-07
6	2.2769E-07	1.8443E-07
7	1.8443E-07	1.4572E-07
8	1.4572E-07	1.1157E-07
9	1.1157E-07	8.1968E-08
10	8.1968E-08	5.6922E-08
11	5.6922E-08	3.5500E-08
12	3.5500E-08	1.2396E-08
13	1.2396E-08	1.0000E-12

Table 4-5. 4-Group few group structures

Group boundaries (MeV)				
Option 1			Option 2	
Group #	Upper Bound	Lower Bound	Upper Bound	Lower Bound
1	2.0000E+01	9.1188E-03	2.0000E+01	9.1188E-03
2	9.1188E-03	2.9023E-05	9.1188E-03	2.9023E-05
3	2.9023E-05	7.3000E-07	2.9023E-05	1.8554E-06
4	7.3000E-07	1.0000E-12	1.8554E-06	1.0000E-12

To establish a precise reflector, a full core simulation would need to be performed because the reflector cannot be represented as a single reflector block with infinite boundary conditions like the fuel. However, a detailed full core simulation is computationally expensive, so a semi 1-D model similar to a 1-D 8.5 assembly full core model (Figure 4-29) was modeled in SERPENT for the radial reflector, and a single 3-D assembly was modeled with axial reflector/coolant regions and infinite radial boundary conditions for the axial reflector and coolant cross sections. The 1-D model is considered a semi 1-D model because the TRISO particles are modeled in SERPENT as true spheres with full 3-D representation but with the enclosing macrogeometry having reflective boundary conditions in all directions except the radial direction.

Though this simplified 1-D model can be used to generate homogenized cross sections, diffusion parameters, and discontinuity factors, the discontinuity factors and diffusion coefficients generated by this approach would not be sufficient in the diffusion 2-D and 3-D full core models. This is due to the fact that the full core diffusion model requires six discontinuity factors, one for each face of the hexagonal node. The semi 1-D model only generates two meaningful discontinuity factors: one for the single core facing surface, and one for the exterior facing reflector surface. To surmount this, the cross sections and diffusion coefficient were adjusted by the appropriate ratio of discontinuity factors to effectively fold the assembly discontinuity factors (ADFs) into these terms and allow the ADFs in the core simulator to be set to 1.0 on all sides. This is illustrated for the radial and axial reflector regions in Equation (2) and the axial coolant region in Equation (3).

$$\widehat{D}^r = \frac{F_{fR}}{F_{rL}} D^r \quad \widehat{\Sigma}_i^r = \frac{F_{fR}}{F_{rL}} \Sigma_i^r, \quad (2)$$

where

F_{fR} = Fuel Region Discontinuity Factor at Fuel / Reflector Interface,

F_{rL} = Reflector Region Discontinuity Factor at Fuel / Reflector Interface.

$$\widehat{D}^c = \frac{F_{rR} F_{fR}}{F_{cL} F_{rL}} D^c \quad \widehat{\Sigma}_i^c = \frac{F_{rR} F_{fR}}{F_{cL} F_{rL}} \Sigma_i^c, \quad (3)$$

where

F_{fR} = Fuel Region Discontinuity Factor at Fuel / Reflector Interface,

F_{rL} = Reflector Region Discontinuity Factor at Fuel / Reflector Interface,

F_{rR} = Reflector Region Discontinuity Factor at Reflector / Coolant Interface,

F_{CL} = Coolant Region Discontinuity Factor at Reflector / Coolant Interface.

Accuracy of this approach was assessed by using a 1-D finite difference code to replicate the SERPENT models used for generating the cross sections. It was discovered during these evaluations that the Option 1 4-group structure provided significantly worse power distribution agreement than Option 2 when assessing the radial reflector model, as can be seen in Figure 8. Both energy group options had eigenvalue agreements within the 2.8 pcm uncertainty of the semi 1-D SERPENT model. A similar result was observed for the axial model as well (Figure 9), though not to the same degree of significance. A likely explanation for this behavior is that the energy group optimization only considered the accuracy of using infinite single assembly models and not the accuracy of reflector energy group condensation. Because Option 2 provided better power distribution agreement, it was selected as the group to use for full core benchmarking of the two-step procedure.

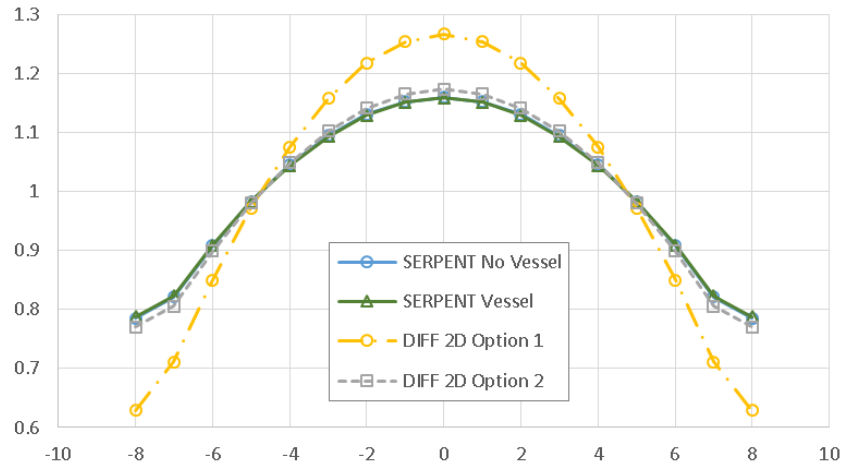


Figure 4-30. Radial 1-D model power distribution comparisons

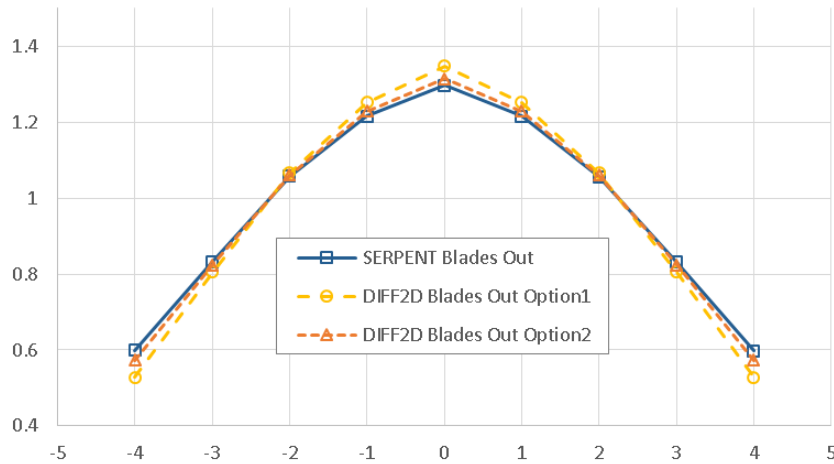


Figure 4-31. Axial 1-D model power distribution comparisons

The single infinite assembly model is not a correct treatment for cases in which the control blades are inserted. This is due to the fact that the control blades will be serving as primary reactivity control, implying that controlled assemblies will likely be surrounded by uncontrolled assemblies. This directly counters the infinite assembly assumption of the single cell model. As such, the infinite assembly approximation alone will not accurately represent the flux conditions experienced by a controlled assembly, and so some correction must be applied.

To perform this correction, an approach similar to the ADF adjustment used in the reflector modeling can be applied. This was accomplished by (1) assuming a checkerboard insertion scheme as the more realistic model for control blades in the core, (2) performing supercell simulations (Figure 10) to obtain ADFs for controlled and uncontrolled assemblies, and (3) multiplying the infinite assembly cross sections and diffusion coefficients by the ratio of control-blade-withdrawn ADF over the control-blade-inserted ADF to obtain leakage corrected values. Using this approach, leakage adjustments were generated to correct the infinite assembly control blade cross sections to account for the control blade heterogeneity of true operation as shown in Equation 4.

$$\hat{D}^I = \frac{F_O}{F_I} D^I \quad \hat{\Sigma}_i^I = \frac{F_O}{F_I} \Sigma_i^I, \quad (4)$$

where,

F_O = Discontinuity Factor of Central Assembly with Control Blade Withdrawn,

F_I = Discontinuity Factor of Central Assembly with Control Blade Inserted.

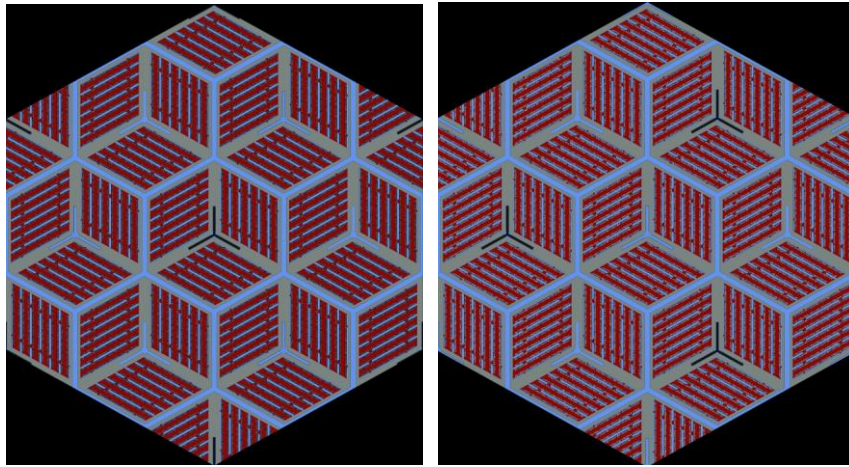


Figure 4-32. Supercell models with control blade inserted (left) and withdrawn (right)

In this work a Two-Step procedure was developed for the AHTR so as to afford a means for strongly coupled neutronics and thermal hydraulic simulations currently absent in the reactor physics area. This leads the way to performing fuel cycle, core/assembly design, and safety margin assessments for steady state and slow transient conditions. Additionally, this procedure greatly reduces the computational expense of performing such simulations so as to allow for a means of expedient design optimization.

The finalized AHTR Two-Step procedure was then benchmarked using comparisons between core simulator and reference high fidelity Monte Carlo models of 2-D and 3-D uniform fresh cores with control blades fully withdrawn and fully inserted in a checkerboard arrangement. In these benchmarks, good agreement was obtained with regards to model eigenvalue and assembly power distribution. For the NESTLE core simulator 2-D and 3-D full core models, eigenvalue agreement was within 130 pcm and power distribution errors within 3.5% RMS error. However an underlying weakness was discovered in the validity of the radial uniformity assumption of the 1-D ADF adjustment of the radial reflector cross-sections which should be addressed in future development of this Two-Step procedure. Finally, a neutronic and thermal hydraulic coupled 3-D full core depletion model was simulated using the completed Two-Step procedure which demonstrated the functionality of the current procedure and its overall utility in reducing resource requirements.

4.5.a Future Work Recommended for Two-step procedure and models

With regards to expanding on the work herein presented, the following items are suggested as the focus of future work:

1. Further optimization of the few-group energy group structure

Due to the limitations of NESTLE, the few-group energy group structure was limited to only 4 energy groups. Though the energy group structure presented herein is believed to be fairly well optimized for 4 energy groups, it is believed that much improved accuracy could be obtained with additional energy groups in the few group structure as well as further manual manipulation of the group boundaries with consideration for both the infinite assembly approximation accuracy and homogenized reflector accuracy. Ongoing development of an N-Group version of NESTLE will ultimately facilitate exploring the utility of using a greater number of energy groups.

2. Improvement of the reflector model so as to capture the underlying 1/3 azimuthal periodic power shift

The reflector model considered in this study, though fairly computationally inexpensive due to its simplified core representation, is unable to precisely represent core azimuthal asymmetries, such as the underlying 1/3 azimuthal periodic power shift, due to its azimuthal uniformity assumption. This may be addressed in future works by considering 2-D whole core models for reflector cross-section generation. In these 2-D models, one could edit multiple azimuthal reflector regions for cross-sections and in this way capture the non-uniform azimuthal effects. Additionally, since a 2-D representation can provide a means for editing ADFs for all 6 faces of a hexagonal reflector node, one could treat the ADFs explicitly in the core simulator rather than by means of a cross-section adjustment. This explicit treatment of the ADFs may also help in accurately representing any non-uniformities that may be present in the full core model.

3. Implementation of plate power reconstruction

Though plate power reconstruction is not thought to be essential for limiting safety performance evaluations, it would still prove useful in performing more accurate assessments of fuel utilization, isotopic tracking, and design optimization. SERPENT 2 provides the means of defining tallies with which to calculate form factors, but these tallies must be converted into a format usable by the core simulator which has yet to be done. Additionally, depletion region subdivision resolution may need to be further investigated to determine what level of subdividing may be needed to ensure stripe-wise power distribution convergence.

4. Establishment and Optimization of realistic batch-based AHTR fuel cycles

The final item suggested for future development is the establishment and optimization of batch-based multicycles for realistic AHTR operation. Defining the specific fuel, core, and control blade management characteristics that would provide a path to licensing and operational management of a future AHTR. For this purpose, adaptation of multicycle optimization tools such as BWROpt [20] will prove to be extremely helpful to accomplish this task

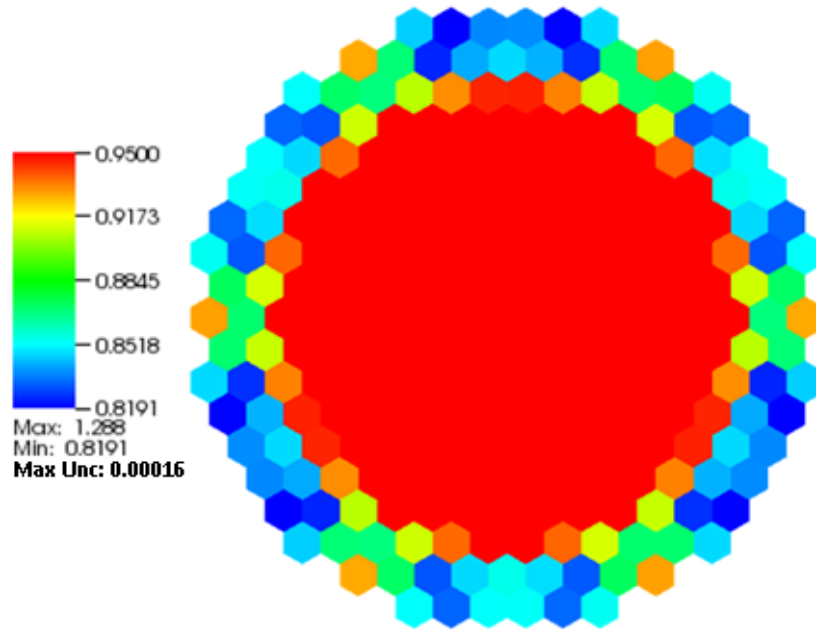


Figure 4-33. Illustration of SERPENT 2 Peripheral Power Peaking

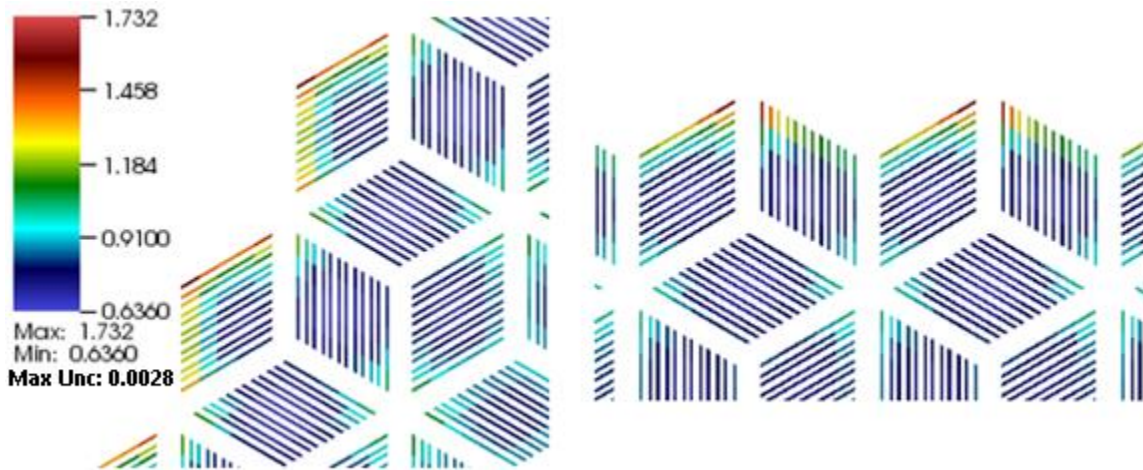


Figure 4-34. Plate Subdivision Power Peaking of Single Tri-Section Facing Reflector (Left) and Two Tri-Sections Facing Reflector (Right)

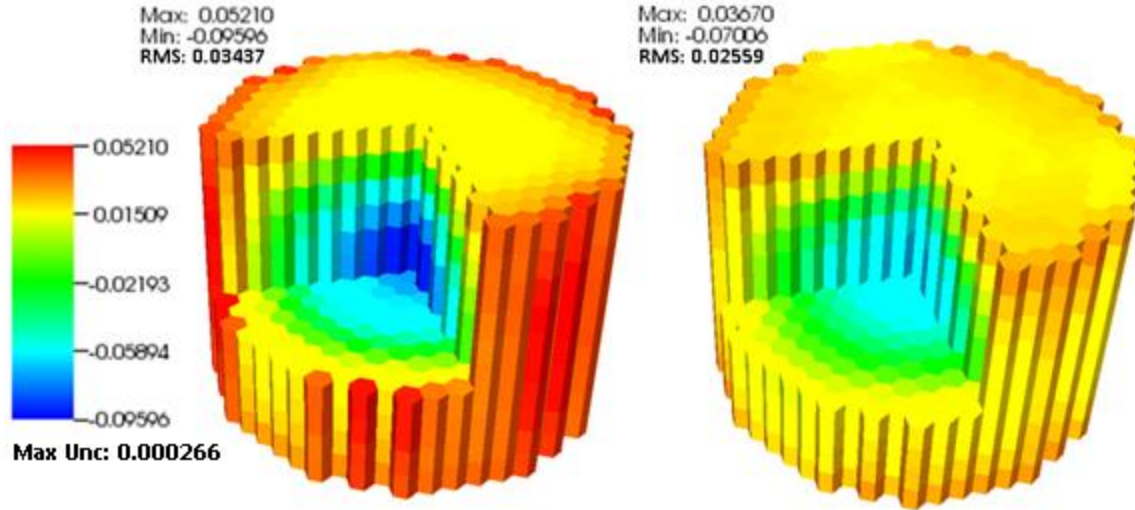


Figure 4-35. SERPENT 2 minus Core Simulator Relative Node Averaged Power Distribution Differences for 3-D Full Core with Control Blades Withdrawn for NESTLE (Left) and PARCs (Right)

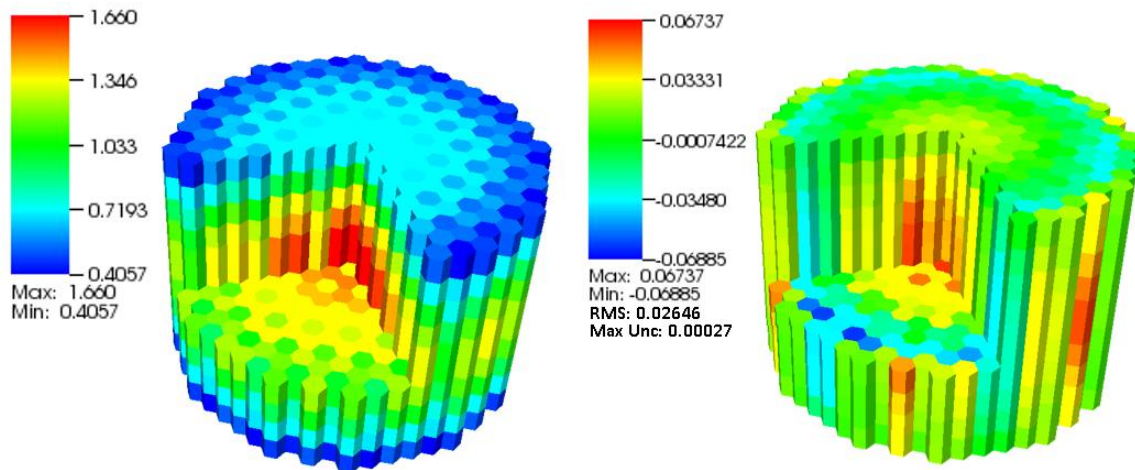


Figure 4-36. 3-D Full Core with Control Blades Inserted NESTLE Relative Power Distributions (Left), SERPENT 2 minus NESTLE Node Averaged Power Distribution Differences (Right)

Since the writing of the last report, an ORNL team led by Aaron Wysocki, Ben Betzler, and Nick Brown, has independently extended a version of the NRC reactor core simulator PARCS for FHR applications, denoted as PARCS-FHR. This version of PARCS includes thermal and hydraulic models and properties for FLiBe salt, graphite, fuel compacts, and silicon carbide. The development of this version of PARCS constitutes a significant effort conducted as part of the Advanced Demonstration and Test Reactor study for the DOE Office of Nuclear Energy in support of a point design for a fluoride high temperature salt-cooled engineering demonstration reactor [21].

The details of the above-noted ORNL-led implementation of PARCS-FHR are currently still ongoing and in process of being formally documented. The thermal-hydraulic model based on an approximate cylindricized form of the fuel plate so as to leverage PARCS' cylindrical thermal

conduction model. The PARCS-FHR model, utilizing the same few group neutron cross-section data as was used for NESTLE, provided a means of performing a code-to-code comparison for validation of the NESTLE Thermal-Hydraulic models.

It should be noted that these results from PARCS-FHR are still considered preliminary in nature. Initial comparisons revealed significant differences between the NESTLE and PARCS-FHR thermal-hydraulic models such that further investigation was warranted. NESTLE polynomials were derived from the PARCS-FHR model so as to test and ensure that NESTLE could in fact replicate the results of PARCS when models were made essentially identical, leading to eigenvalue agreement of 108 pcm, 133 pcm with excellent TH agreement. This indicated initial model was error and it was found that mistakes were made in the derivation of polynomials from Pietro's single channel analysis (Section 7.1.a) as well as the coolant polynomials. These were re-derived and found to give similar levels of agreement as the exactly matching PARCS model with the only exception being the 2D averaged relative power distribution. Being that the PARCS TH model and the single channel based TH model were arrived at nearly independently, this helps boost confidence that TH is correct.

COOLANT POLYNOMIALS

$$\rho = 127.8 - 0.029332642U \quad (4-1)$$

where,

ρ = Density (lbm/ft³),

U = Internal Energy (BTU/lbm).

$$T = 890.33 + 1.733U \quad (4-2)$$

where,

T = Temperature (°F),

U = Internal Energy (BTU/lbm).

PARCS TH MODEL BASED FUEL POLYNOMIALS

$$T = 1286.4 + 2.6448L \quad (4-3)$$

where,

T = Average Fuel Temperature (°F),

L = Linear Power Density (kW/ft).

$$h = 0.28 \quad (4-4)$$

where,

h = Effective Heat Transfer Coefficient (kw/ft²-°F),

T = Average Fuel Temperature (°F).

$$T = 1286.4 + 2.0154L \quad (4-5)$$

where,

T = Fuel Surface Temperature (°F),

L = Linear Power Density (kW/ft).

$$C_p = 0.4178 + 0.0002T - 2 \times 10^{-7}T^2 \quad (4-6)$$

where,

C_p = Fuel Specific Heat,

T = Average Fuel Temperature (°F).

FUEL POLYNOMIALS DERIVED FROM PIETRO's MASTERS WORK (see Section 7.1.a)

$$T = 1344.5 - 9.9985L + 0.237L^2 \quad (4-7)$$

where,

T = Average Fuel Temperature (°F),

L = Linear Power Density (kW/ft).

$$h = 1.0407 - 0.0011T + 4 \times 10^{-7}T^2 \quad (4-8)$$

where,

h = Effective Heat Transfer Coefficient (kW/ft²-°F),

T = Average Fuel Temperature (°F).

$$T = 1283.5 - 6.5167L + 0.1506L^2 \quad (4-9)$$

where,

T = Fuel Surface Temperature (°F),

L = Linear Power Density (kW/ft).

$$C_p = 0.3269 + 7 \times 10^{-5}T \quad (4-10)$$

where,

C_p = Fuel Specific Heat,

T = Average Fuel Temperature (°F).

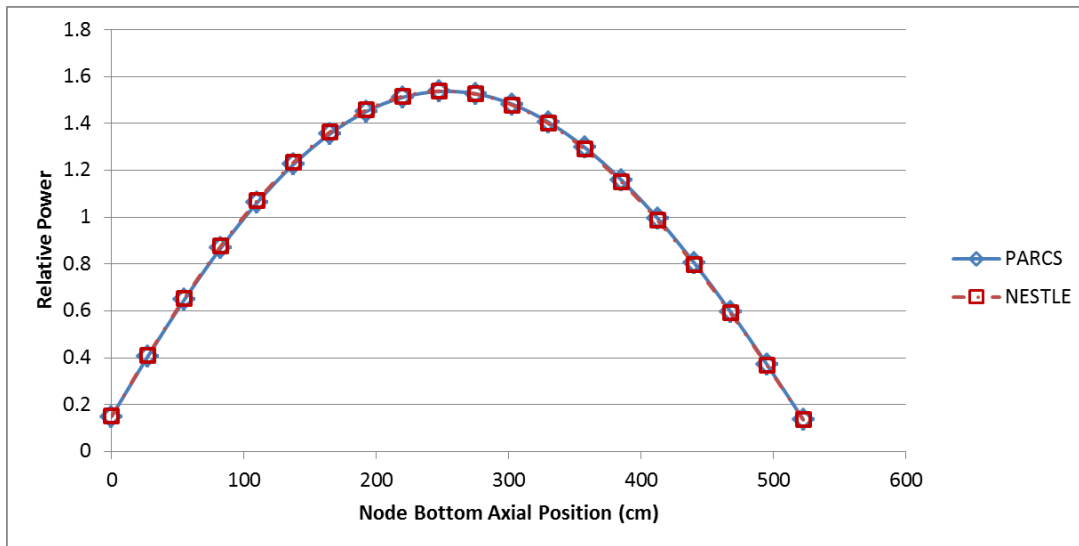


Figure 4-37. Relative Power 1-D Averaged Axial Profile

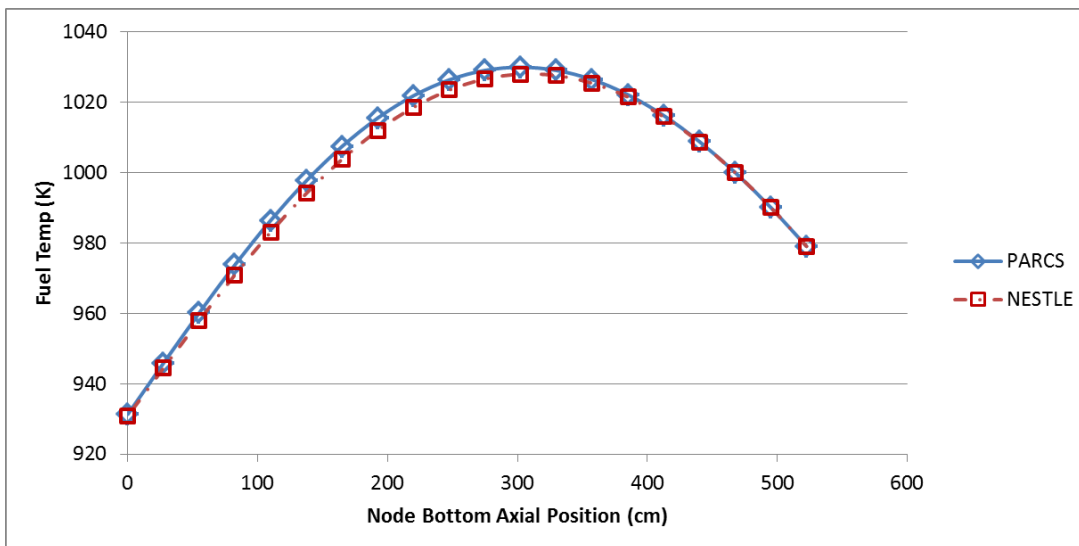


Figure 4-38. Fuel Temperature 1-D Averaged Axial Profile

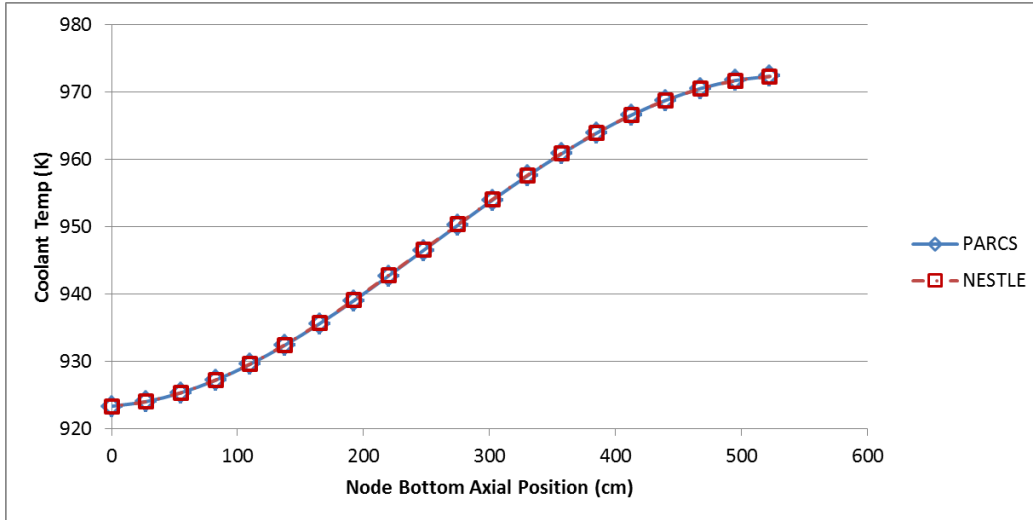


Figure 4-39. Coolant Temperature 1-D Averaged Axial Profile

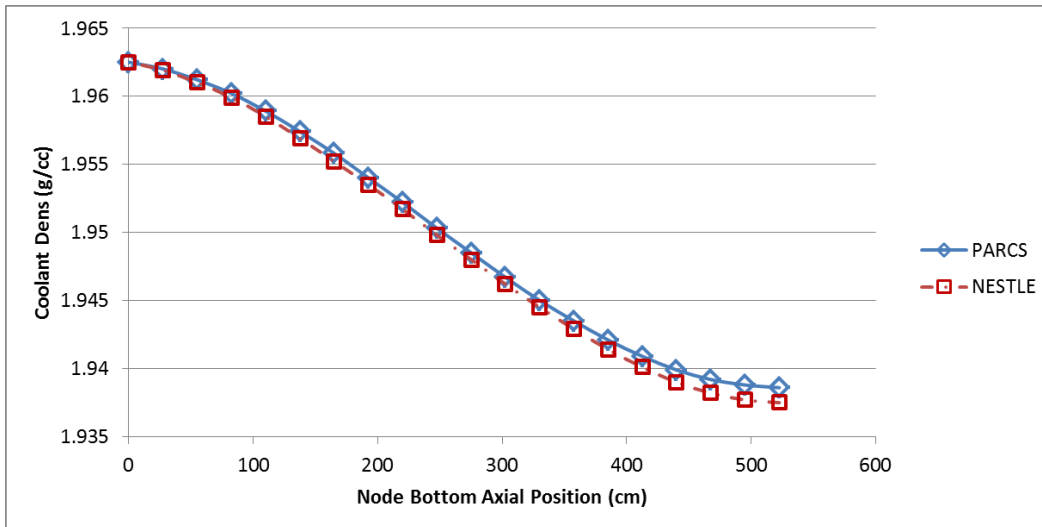


Figure 4-40. Coolant Density 1-D Averaged Axial Profile

Fuel and Core Design Options of LSCR

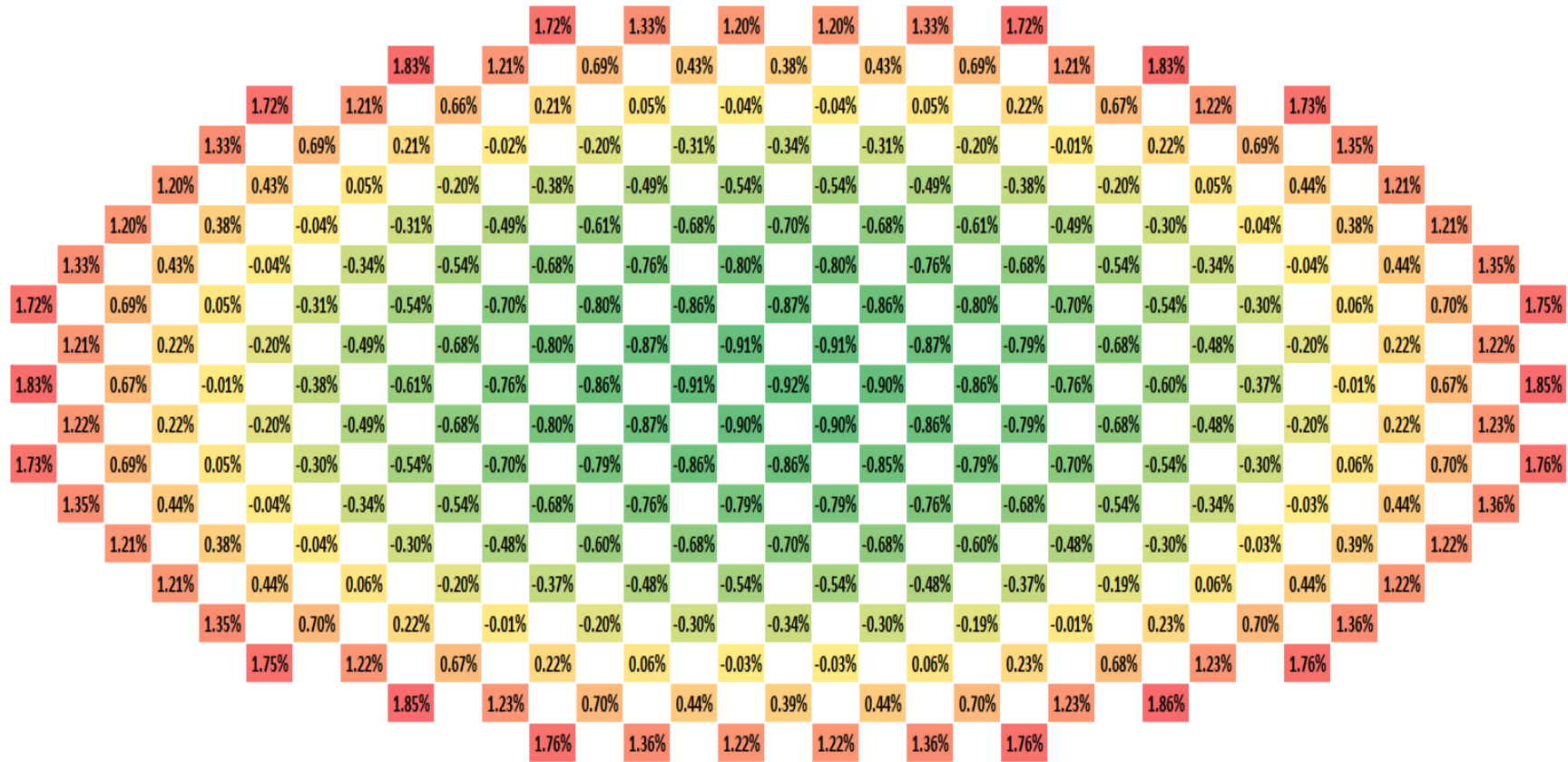


Figure 4-41. Relative Power 2-D Averaged Radial Profile PARCS TH

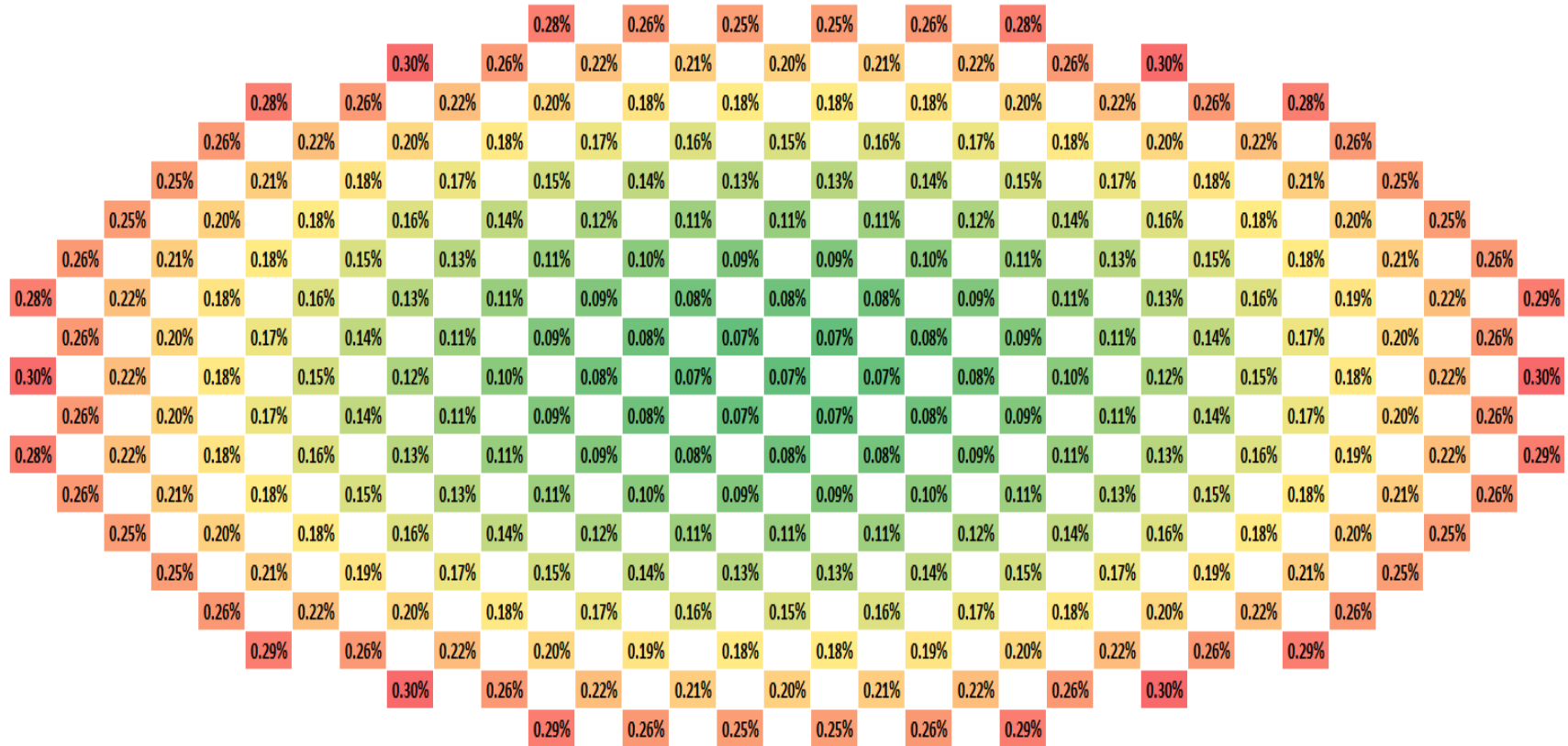


Figure 4-42. Fuel Temperature 2-D Averaged Radial Profile PARCS TH

Fuel and Core Design Options of LSCR

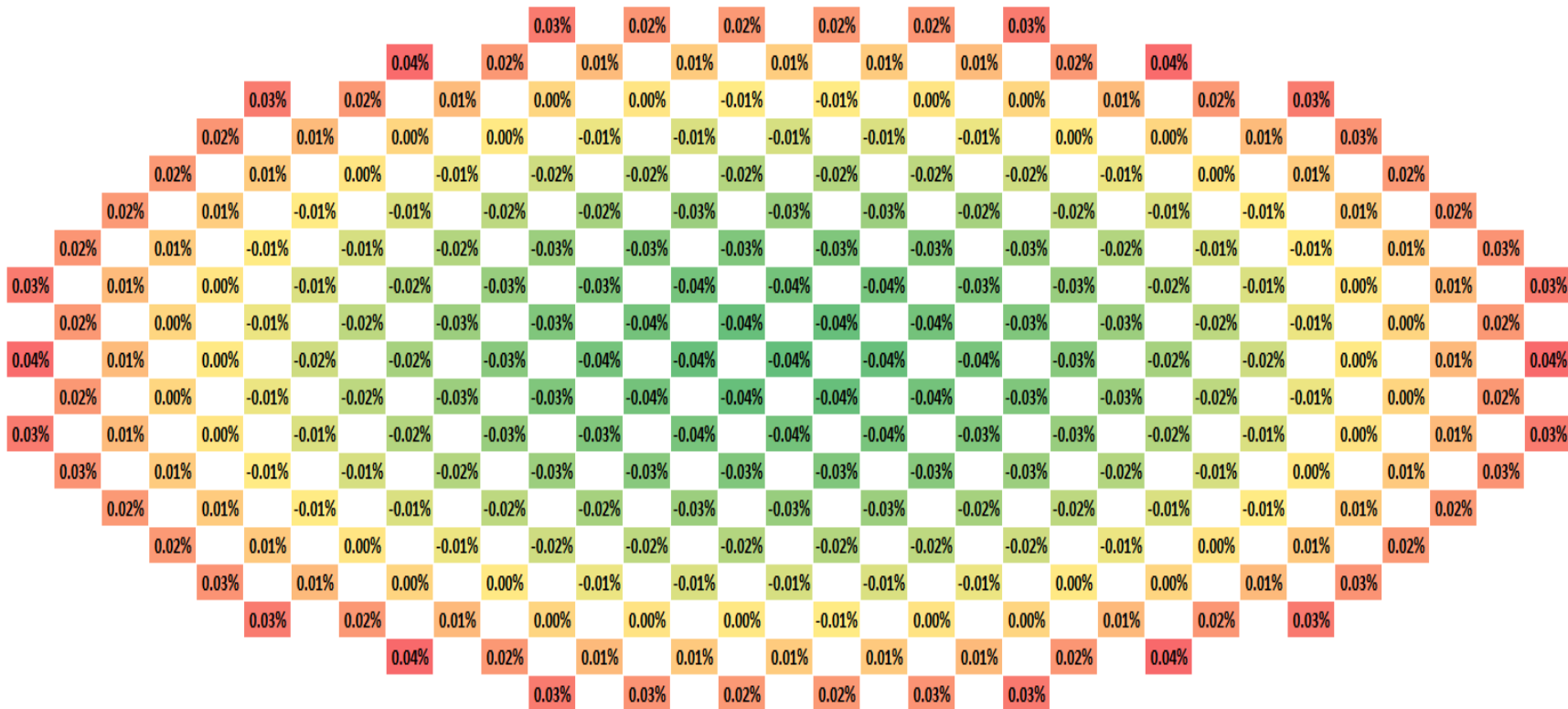


Figure 4-43. Coolant Temperature 2-D Averaged Radial Profile PARCS TH

Fuel and Core Design Options of LSCR

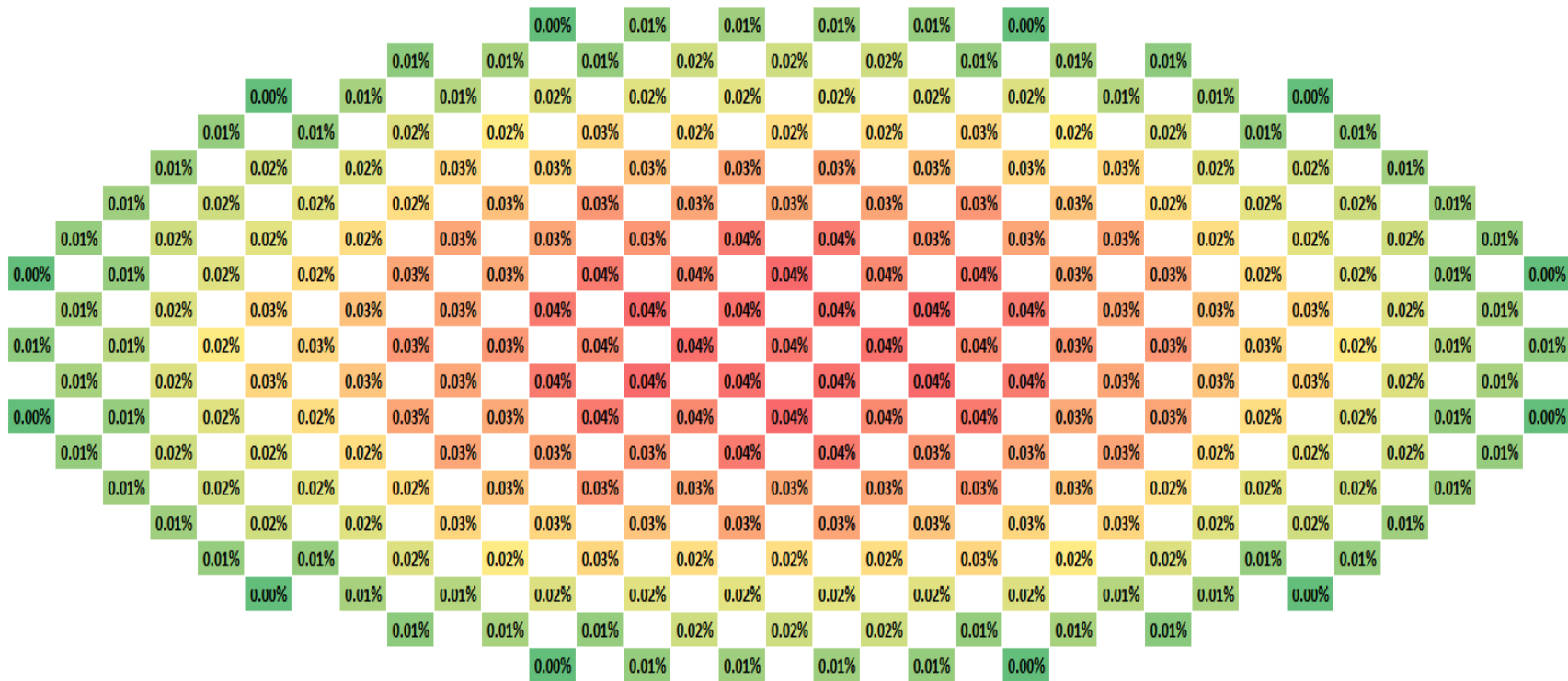


Figure 4-44. Coolant Density 2-D Averaged Radial Profile PARCS TH

Fuel and Core Design Options of LSCR

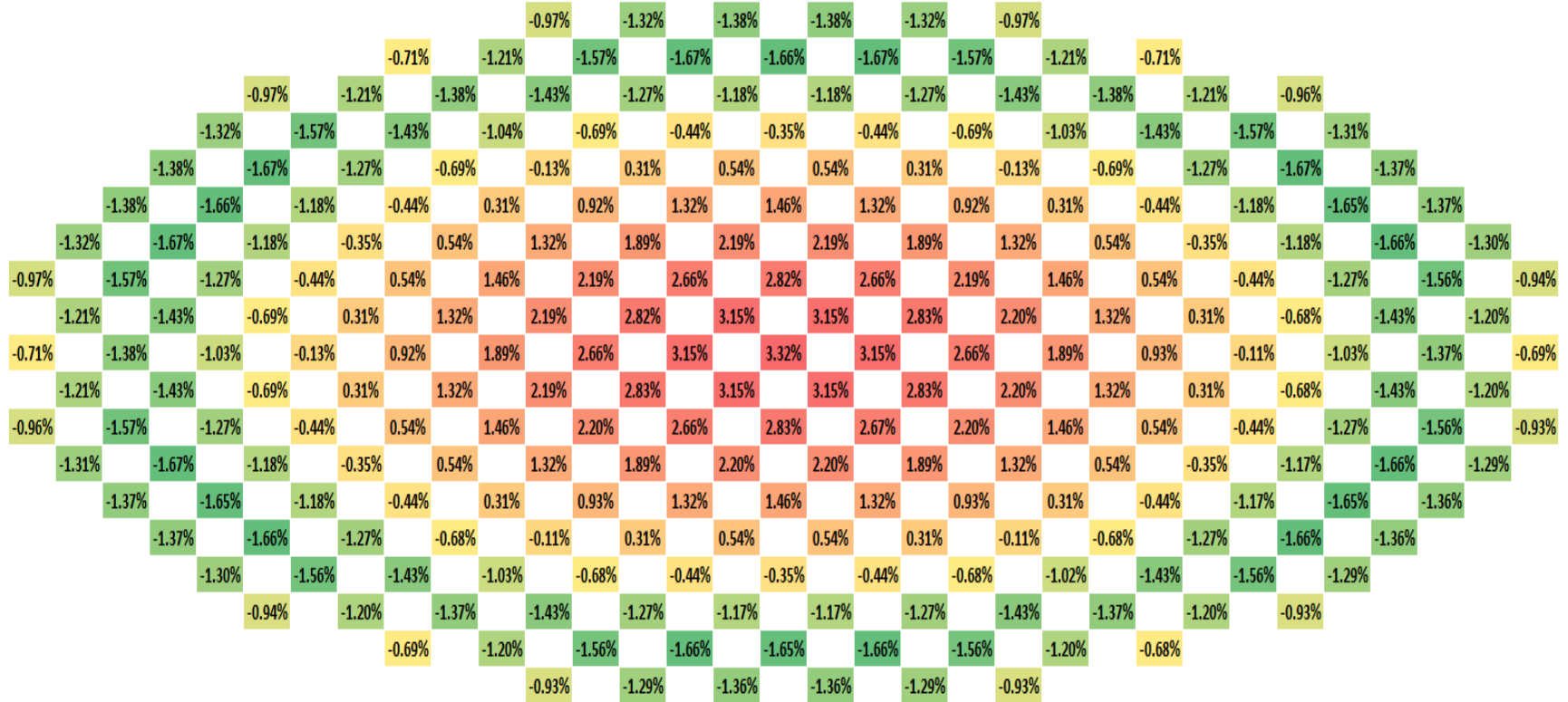


Figure 4-45. Relative Power 2-D Averaged Radial Profile PIETRO MODEL BASED TH (Section 7.1.a)

Fuel and Core Design Options of LSCR

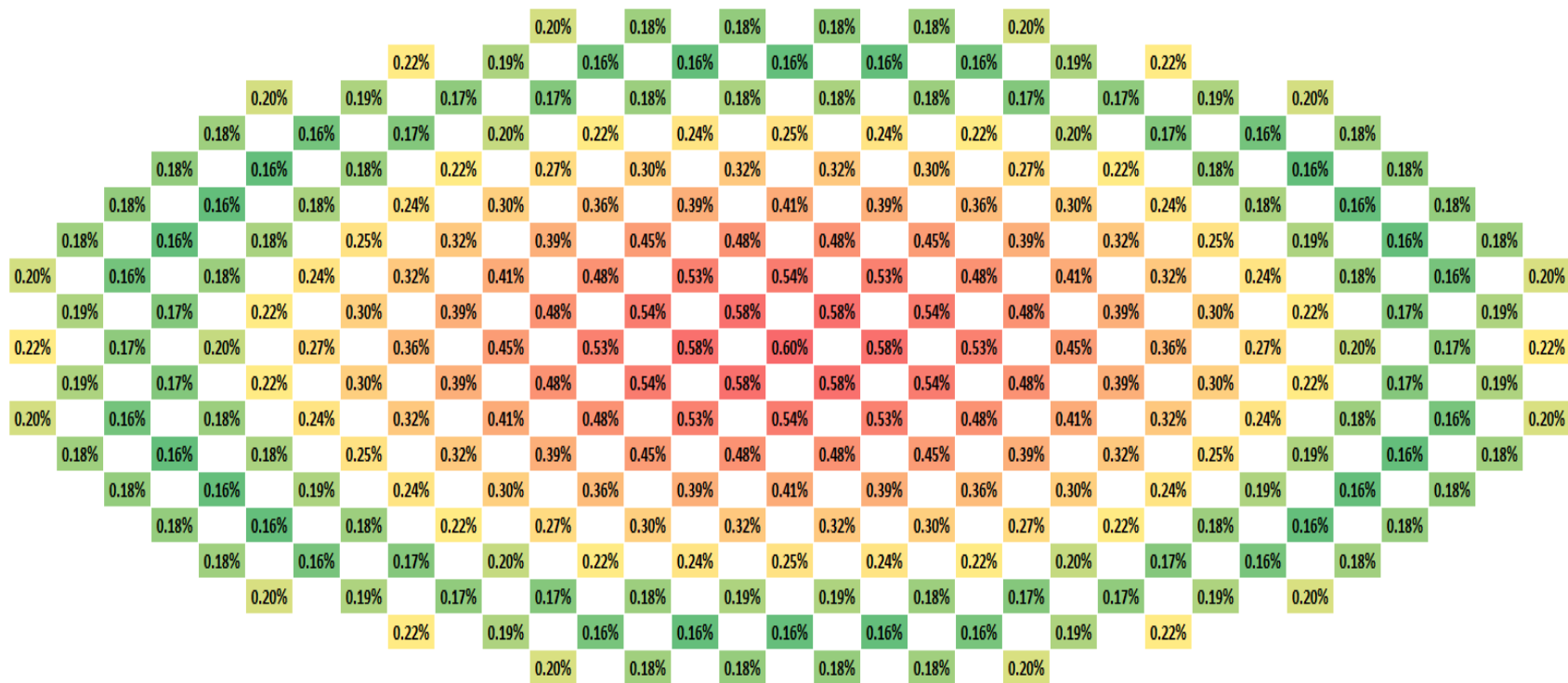


Figure 4-46. Fuel Temperature 2-D Averaged Radial Profile PIETRO MODEL BASED TH (Section 7.1.a)

Fuel and Core Design Options of LSCR

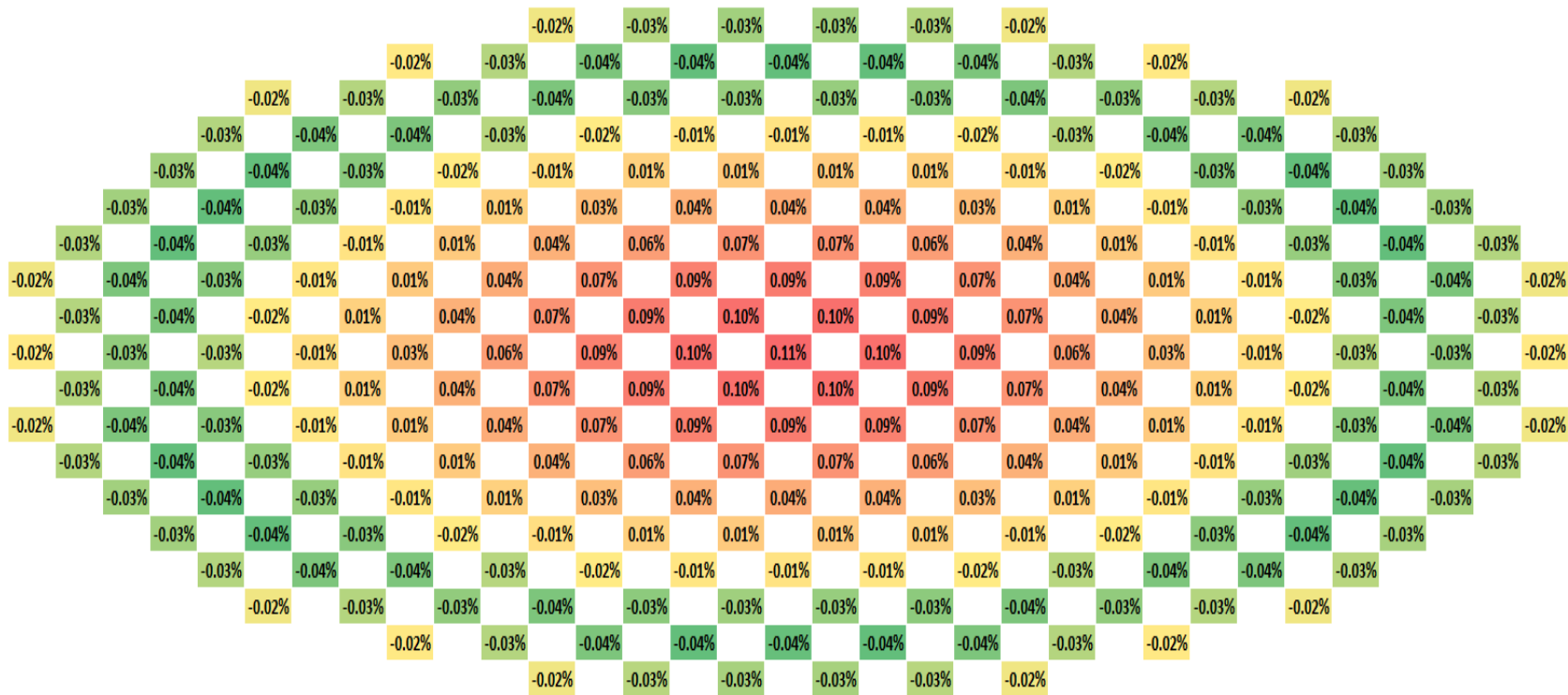


Figure 4-47. Coolant Temperature 2-D Averaged Radial Profile PIETRO MODEL BASED TH (Section 7.1.a)

Fuel and Core Design Options of LSCR

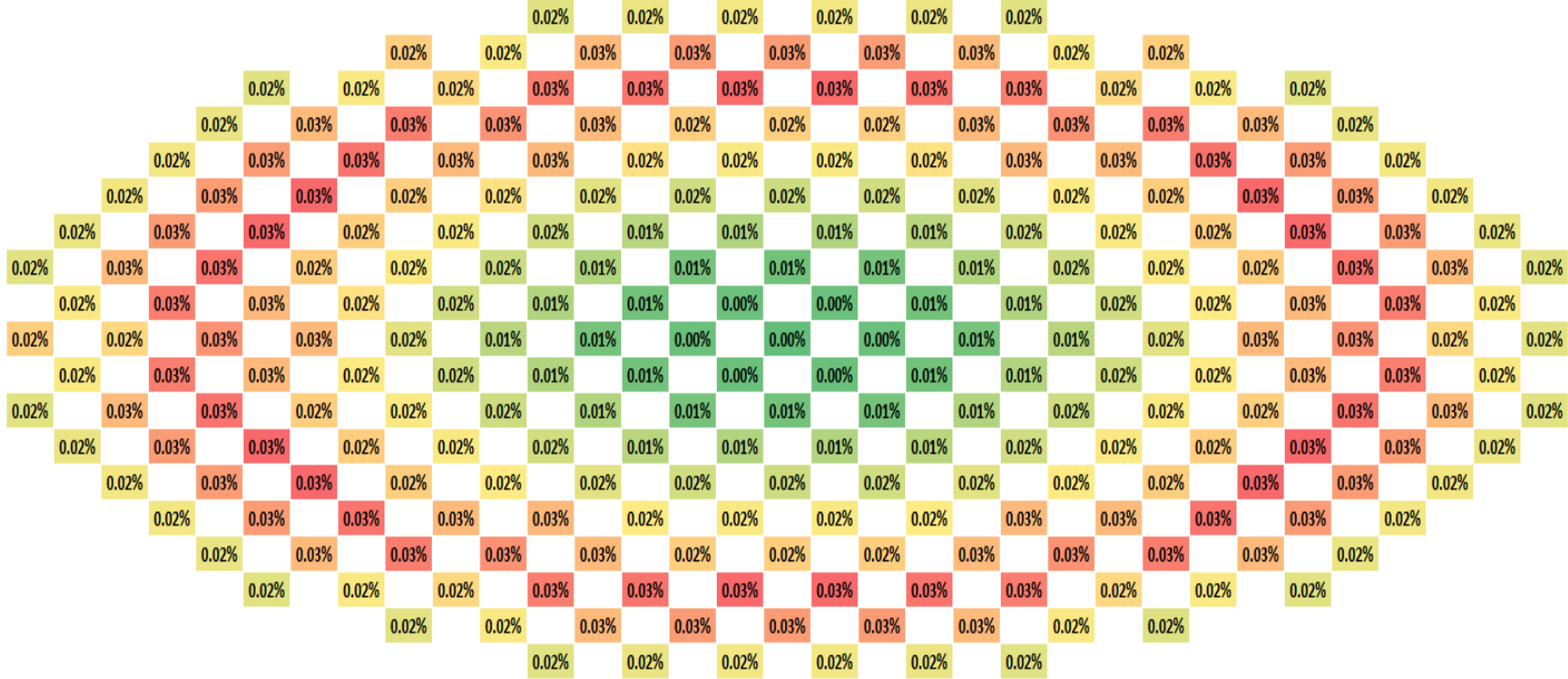


Figure 4-48. Coolant Density 2-D Averaged Radial Profile PIETRO MODEL BASED TH (Section 7.1.a)

4.6 References for this Section

1. D.E. Holcomb, D. Ilas, V.K. Varma, A.T. Cisneros, R.P. Kelly, J.C. Gehin, "Core and Refueling Design Studies for the Advanced High Temperature Reactor", Oak Ridge National Laboratory, ORNL/TM-2011/365, September 2011.
2. J. Leppänen. "Serpent– a Continuous-energy Monte Carlo Reactor Physics Burnup Calculation Code", VTT Technical Research Centre of Finland. August 16, 2012.
3. J. Leppänen, M. Pusa, T. Viitanen, V. Valtavirta, T. Kaltiaisenaho, "The Serpent Monte Carlo Code: Status, Development, and Applications in 2013", *Annals of Nuclear Energy*, IN PRESS, September 2014.
4. V.K. Varma, D.E. Holcomb, F.J. Peretz, E.C. Bradley, D. Illas, A.L. Qualls, N.M. Zaharia, "AHTR Mechanical, Structural, and Neutronic Preconceptual Design", Oak Ridge National Laboratory, ORNL/TM-2012/320, September 2012.
5. Yonghee Kim and Min Baek, "Elimination of Double Heterogeneity through a Reactivity-Equivalent Physical Transformation", *Proceeding of GLOBAL 2005*, Paper No. 548, Tsukuba, Japan, Oct 9-13, 2005.
6. S.M. Lewis, "Simplified Core Physics and Fuel Cycle Cost Model for Preliminary Evaluation of LSCR Fueling Options", Georgia Institute of Technology, Master's Thesis, May 2014.
7. P.J. Pappano, T.D. Burchell, J.D. Hunn, M.P. Trammell, "A Novel Approach to Fabricating Fuel Compacts for the Next Generation Nuclear Plant (NGNP)", *Journal of Nuclear Materials*, **381**, pg. 25-38, 2008.
8. J.D. Hunn, R.A. Lowden, J.H. Miller, B.C. Jolly, M.P. Trammell, A.K. Kercher, F.C. Montgomery, C.M. Silva, "Fabrication and Characterization of Driver-Fuel Particles, Designed-To-Fail Fuel Particles, and Fuel Compacts for the US AGR-3/4 Irradiation Test", *Nuclear Engineering and Design*, **271**, pg. 123-130, 2014.
9. R.N. Morris, P.J. Pappano, "Estimation of Maximum Coated Particle Fuel Compact Packing Fraction", *Journal of Nuclear Materials*, **361**, pg. 18-29, 2007.
10. *Scale: A Comprehensive Modeling and Simulation Suite for Nuclear Safety Analysis and Design*, ORNL/TM-2005/39, Version 6.1, June 2011. Available from Radiation Safety Information Computational Center at Oak Ridge National Laboratory as CCC-785.
11. C. Liang, W. Ji, "A Novel Extension of Chord Length Sampling Method for TRISO-Type Applications", *Trans. Am. Nucl. Soc.*, **107**, pp. 551-553, 2012.

12. J. Leppänen, M. DeHart, "HTGR Reactor Physics and Burnup Calculations Using the Serpent Monte Carlo Code" *Trans. Am. Nucl. Soc.* **101**, 2009.
13. W. Ji, "Neutronics Analysis of Stochastic Distribution of Fuel Particles in Very High Temperature Gas-Cooled Reactors", Dissertation, *University of Michigan*, 2008.
14. R. Sanchez, "Renormalized Treatment of the Double Heterogeneity with the Method of Characteristics", *PHYSOR* 2004.
15. T. Goorley, et al., "Initial MCNP6 Release Overview", *Nuclear Technology*, **180**, pp 298-315, Dec 2012.
16. M.B. Chadwick, M. Herman, P. Obložinský, M.E. Dunn, Y. Danon, A.C. Kahler, D.L. Smith, B. Pritychenko, G. Arbanas, R. Arcilla, R. Brewer, D.A. Brown, R. Capote, A.D. Carlson, Y.S. Cho, H. Derrien, K. Guber, G.M. Hale, S. Hoblit, S. Holloway, T.D. Johnson, T. Kawano, B.C. Kiedrowski, H. Kim, S. Kunieda, N.M. Larson, L. Leal, J.P. Lestone, R.C. Little, E.A. McCutchan, R.E. MacFarlane, M. MacInnes, C.M. Mattoon, R.D. McKnight, S.F. Mughabghab, G.P.A. Nobre, G. Palmiotti, A. Palumbo, M.T. Pigni, V.G. Pronyaev, R.O. Sayer, A.A. Sonzogni, N.C. Summers, P. Talou, I.J. Thompson, A. Trkov, R.L. Vogt, S.C. van der Marck, A. Wallner, M.C. White, D. Wiarda, P.G. Young, "ENDF/B-VII.1: Nuclear Data for Science and Technology: Cross Sections, Covariances, Fission Product Yields and Decay Data", *Nuclear Data Sheets*, **112**, pg 2887-3152, 2011.
17. H. Finnemann, F. Bennewitz, M.R. Wagner, "Interface Current Techniques for Multidimensional Reactor Calculations", *Atomkernenergie*, **30**, pg. 123-128, 1977.
18. K. Koebke, "A New Approach to Homogenization and Group Condensation", IAEA Technical Committee Meeting on Homogenization Methods in Reactor Physics, Lugano, Switzerland, November 1978.
19. K.S. Smith, "Spatial Homogenization Methods For Light Water Reactor Analysis", Doctoral Dissertation, Massachusetts Institute of Technology, June 1980.
20. K. Ottinger and G. I. Maldonado, "BWROPT: A Multi-Cycle BWR Fuel Cycle Optimization Code," *Nuclear Engineering and Design*, **291**, pg. 236-243, Sep. 2015.
21. A. Qualls, N. Brown, B. Betzler, J. Carbajo, M. Greenwood, R. Hale, T. Harrison, J. Powers, K. Robb, J. Terrell, A. Wysocki. Fluoride Salt-Cooled High-Temperature Demonstration Reactor Point Design, ORNL/TM-2016/85 (Oak Ridge, TN: UT-Battelle, LLC, Oak Ridge National Laboratory, February 2016).

5. Parametric Neutronics Studies

This chapter describes analyses and parametric studies performed to evaluate and understand neutronic behavior (reactivity and cycle length). These studies did not account or aim to minimize fuel cycle cost, which is discussed in a later Chapter.

5.1 SCALE Studies

A depletion parametric study was performed over the design space, varying number of fuel layers, packing fraction, and enrichment. The results were obtained by sampling over the design space with a Periodic Latin Hypercube design and using an ANN regression model to enable displaying tabular results. The resulting predicted cycle length and burnup for each design are very dependent on CHM. Table 5-1 shows carbon-to-heavy metal ratio as number of fuel layers and packing fraction are changed. Figure 5-1 shows cycle length as a function of number of fuel layers and packing fraction. Figure 5-2 shows burnup as a function of number of fuel layers and packing fraction. Cycle length reaches a maximum at 40% packing fraction and 5.5 fuel layers. At this point the design is optimally moderated. Burnup increases with increasing CHM ratio to a point where the fuel loading becomes too low to maintain a long enough cycle length. The best fuel utilization occurs somewhere around 3.5 fuel layers and 20% packing fraction. Cycle length and burnup increase with increasing enrichment. The design with an optimal fuel cycle cost must balance better fuel utilization with longer cycle lengths.

Table 5-1. CHM ratio at different number of fuel layers and packing fractions.

FL/PF	10.00	12.14	14.29	16.43	18.57	20.71	22.86	25.00	27.14	29.29	31.43	33.57	35.71	37.86	40.00
9	377.74	331.88	297.80	271.31	250.01	232.46	217.69	205.07	194.13	184.54	176.05	168.48	161.67	155.51	149.91
8	424.96	373.36	335.02	305.22	281.26	261.52	244.90	230.70	218.39	207.61	198.06	189.54	181.88	174.95	168.64
7	485.67	426.70	382.89	348.82	321.44	298.88	279.89	263.66	249.59	237.26	226.35	216.62	207.86	199.94	192.74
6	566.61	497.82	446.70	406.96	375.02	348.69	326.54	307.60	291.19	276.81	264.08	252.72	242.51	233.27	224.86
5	679.93	597.38	536.04	488.35	450.02	418.43	391.85	369.12	349.43	332.17	316.89	303.26	291.01	279.92	269.83
4	849.91	746.73	670.05	610.44	562.53	523.03	489.81	461.40	436.79	415.21	396.12	379.08	363.76	349.90	337.29
3	1133.22	995.63	893.40	813.92	750.04	697.38	653.08	615.21	582.38	553.62	528.16	505.44	485.01	466.53	449.72
2	1699.83	1493.45	1340.10	1220.88	1125.06	1046.06	979.62	922.81	873.58	830.43	792.24	758.16	727.52	699.80	674.58

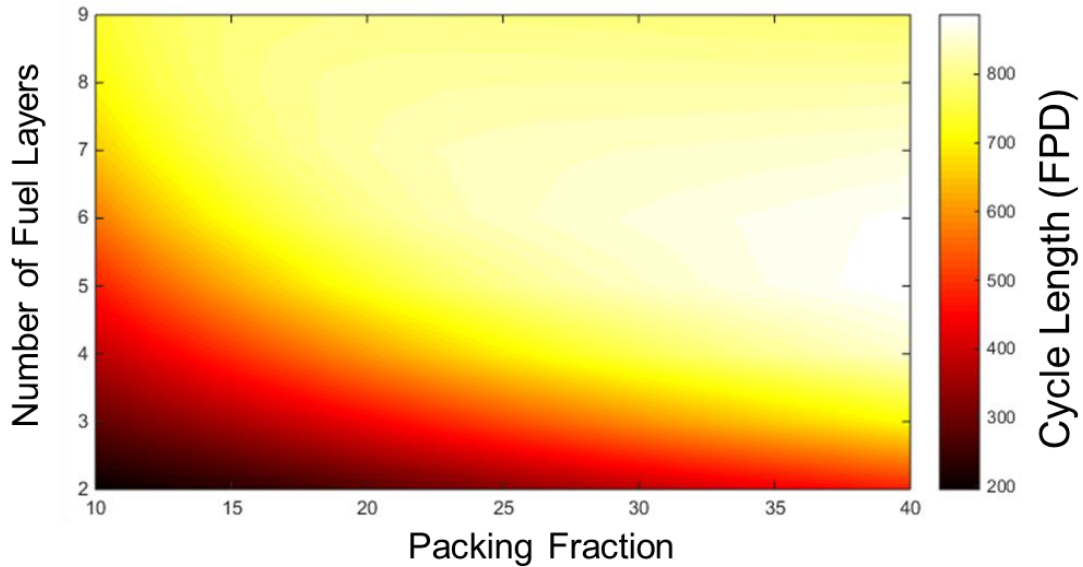


Figure 5-1. Cycle Length (FPD) as a function of packing fraction and number of fuel layers.

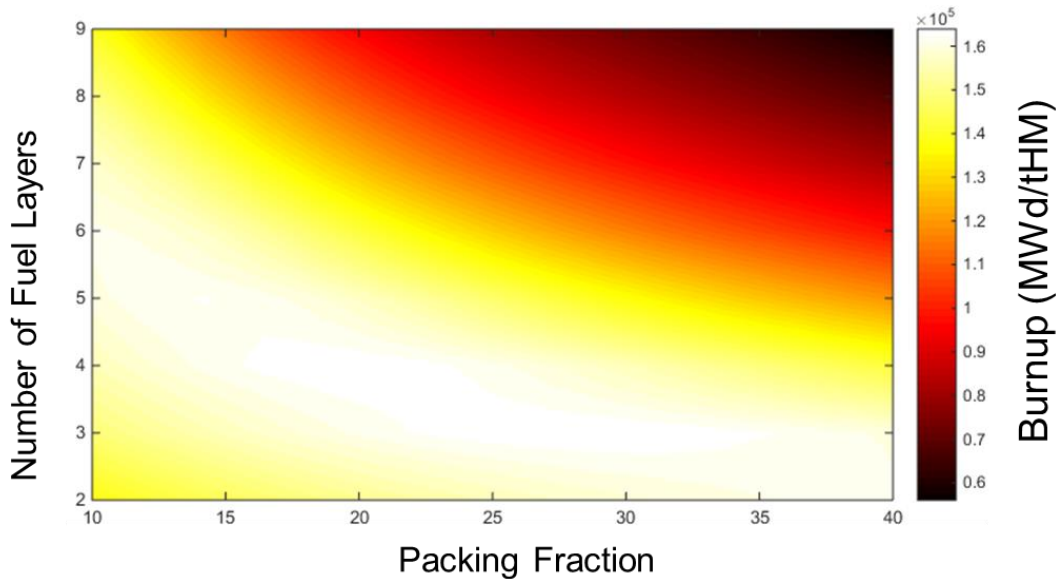


Figure 5-2. Burnup (MWd/tHM) as a function of packing fraction and number of fuel layers.

Fuel performance is very dependent on enrichment. As enrichment increases the cycle length and burnup increases rapidly. This provides the expectation that the optimal and most economic fuel design will have the maximum allowable enrichment of 19.75%. Figure 5-3 shows cycle length as a function of enrichment and packing fraction. It can be seen that at 20% enrichment cycle length increases with increasing packing fraction, however at around 10% enrichment

cycle length peaks at 25% packing fraction. Figure 5-4 shows burnup as a function of enrichment and packing fraction.

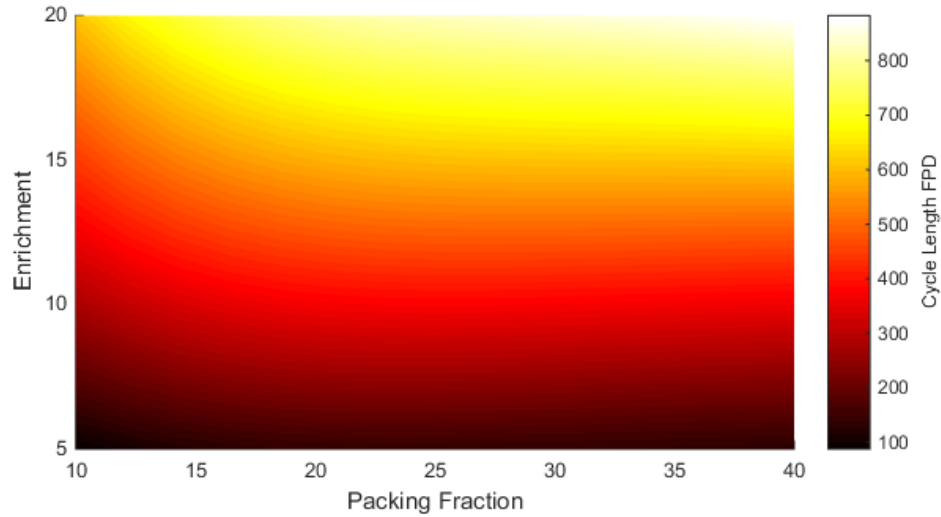


Figure 5-3. Cycle length (FPD) as a function of packing fraction and enrichment.

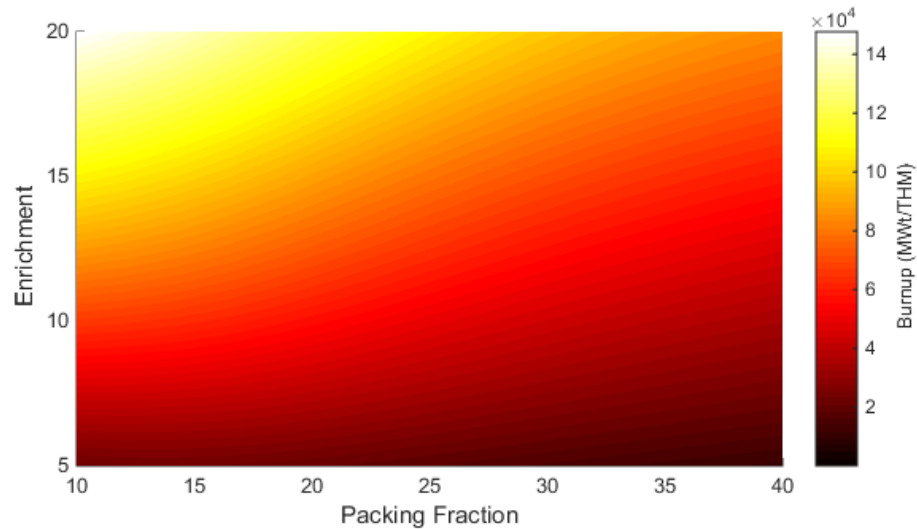


Figure 5-4. Burnup (MWd/tHM) as a function of packing fraction and enrichment.

Parametric studies were also performed to see the effect of changing parameters has on multi-batch refueling performance. Figure 5-5 shows cycle length as a function of number refueling batches and packing fraction. The figure shows that as CHM decreases the cycle length increases. At lower packing fractions multi-batch reloading seems to be less beneficial.

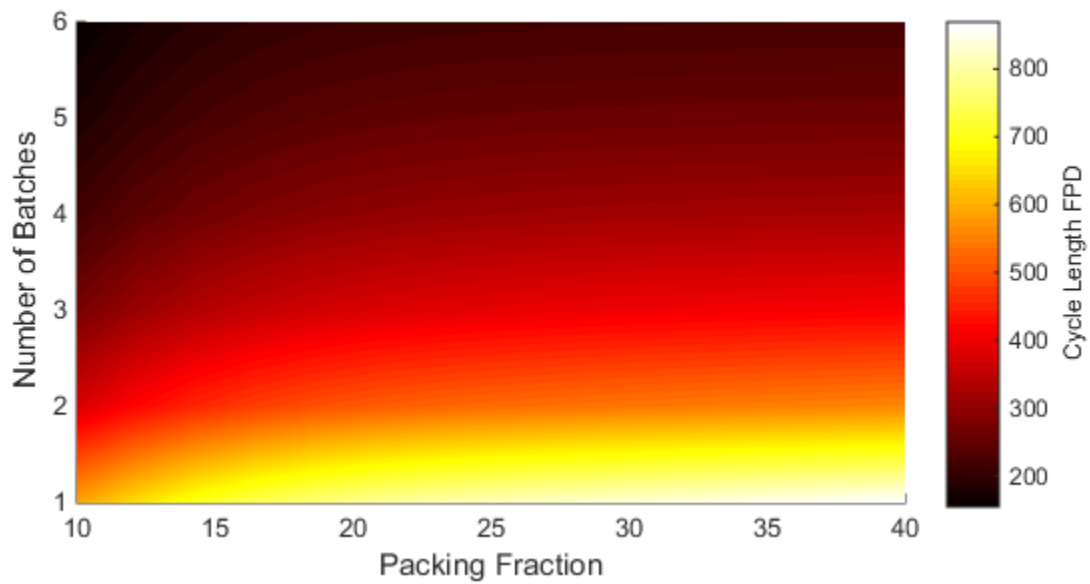


Figure 5-5. Cycle Length as a function of packing fraction and number of batches.

5.2 SERPENT Studies

5.2.a Enrichment Effect

As in the previous study, it can be observed that lowering enrichment of course leads to a lower k -infinity value which translates into shorter cycle lengths. Higher enrichment also leads to a higher maximum discharge burnup which is expected due to the extended length of operation with effectively the same heavy metal mass loading. It can be seen that lowering enrichment has a spectrum softening effect, likely due to decreased absorption of thermal neutron caused by the lower U-235 concentration. Relative maximum power density is observed to be greater in the higher enriched cases during early life due to the increased spatial self-shielding effect of the fuel. This however is swapped in later life as the highly enriched fuel is burned out and the lower enriched fuel produces more Plutonium. Fuel temperature coefficients are more negative for lower enriched fuel due to the increased presence of U-238 providing a greater Doppler broadening induced poisoning effect. Plate temperature coefficients begin similar for all enrichments at early life, but lower enriched fuel quickly becomes more negative due to the increased production of Plutonium with its low lying capture resonance. Effects on coolant temperature and density reduction coefficient were found to be negligible. As expected control rod worth was observed to increase with decreasing enrichment due to decreased fuel shielding of the control blade and subsequent increased control blade exposure to thermal flux.

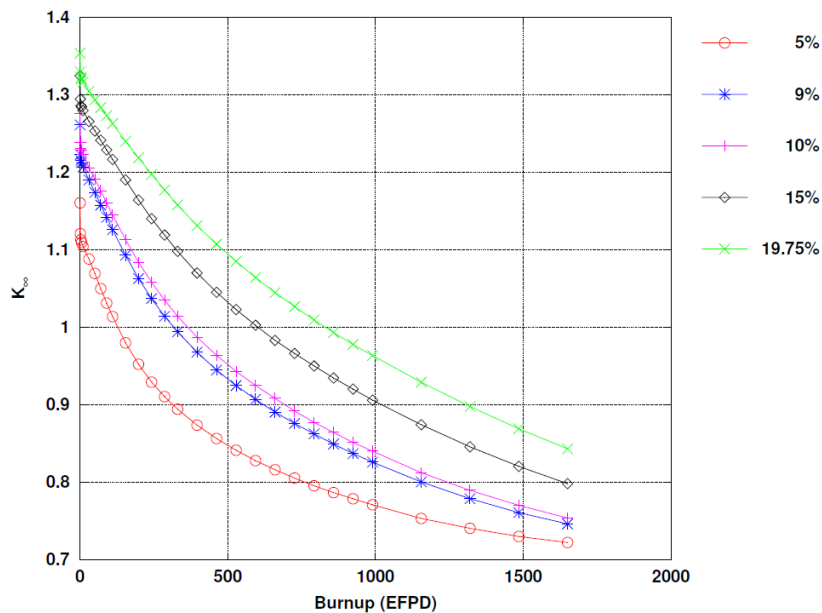


Figure 5-6. K -infinity Effects of Altering Enrichment

Fuel and Core Design Options of LSCR

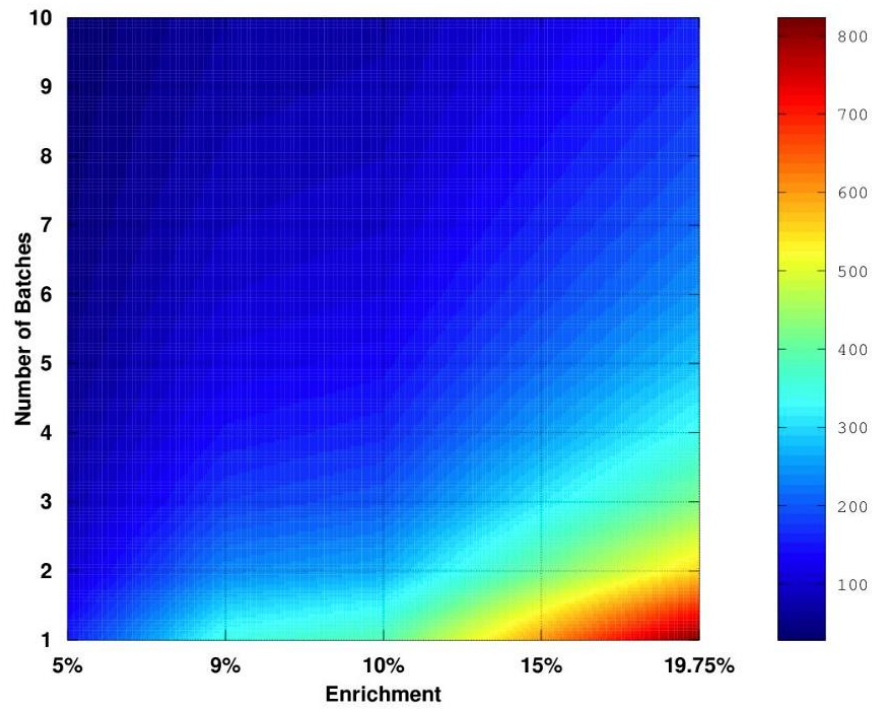


Figure 5-7. Cycle Length Effects of Altering Enrichment

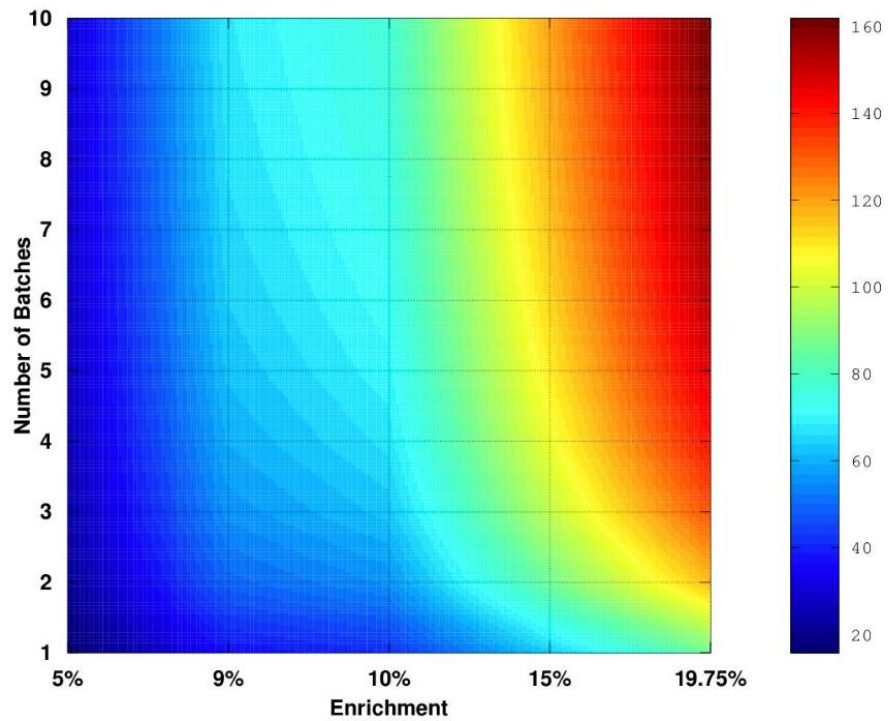


Figure 5-8. Maximum Discharge Burnup Effects of Altering Enrichment

5.2.b Packing Fraction Effect

As was seen in the previous study, decreasing packing fraction leads to an increased reactivity at beginning of fuel life due to the increased moderation and softening of the neutron spectrum. However, lack of fuel dramatically shortens the effective cycle length, requiring much more frequent refueling. One thing about the effects of altering the packing fraction that is notable is that maximum discharge burnup is actually optimized around 20% packing fraction rather than 10%. This is due to the large increase in cycle length one obtains when going from 10% to 20% which is not repeated to nearly the magnitude when going from 20% to 30% or even to higher packing fractions.

As expected, decreased packing fraction leads to an increased maximum relative power density in the fuel, which of course is due to the same power needing to be produced in a less fuel volume. However, subdivision maximum power density is decreased in the lower packing fraction cases due to the lower fuel concentration allowing greater diffusion of thermal neutrons towards the interior of each tri-section. Please note that power density plots were truncated to only 500 EFPD due to data limitations for the 10% packing fraction results, but that trends generally continued in the same manner for the higher burnups of the higher packing fraction cases.

The fuel temperature is observed to become less negative as the packing fraction decreases due to both the lowered U-238 concentration and greater resonance escape probability caused by the increased Carbon to Heavy Metal (CHM) ratio. Plate temperature coefficient is observed to be nearly the same for all packing fractions at beginning of fuel life, but is observed to be more negative for lower packing fraction cases due to the elevated thermal spectrum peak again caused by the increased CHM ratio which leads to more effective thermal resonance capture of the Plutonium. It should be noted that the coolant density reduction coefficient does appear to become more positive with decreasing packing fraction. As expected control blade worth increases with decreasing packing fraction again due to the decreased fuel volume.

Fuel and Core Design Options of LSCR

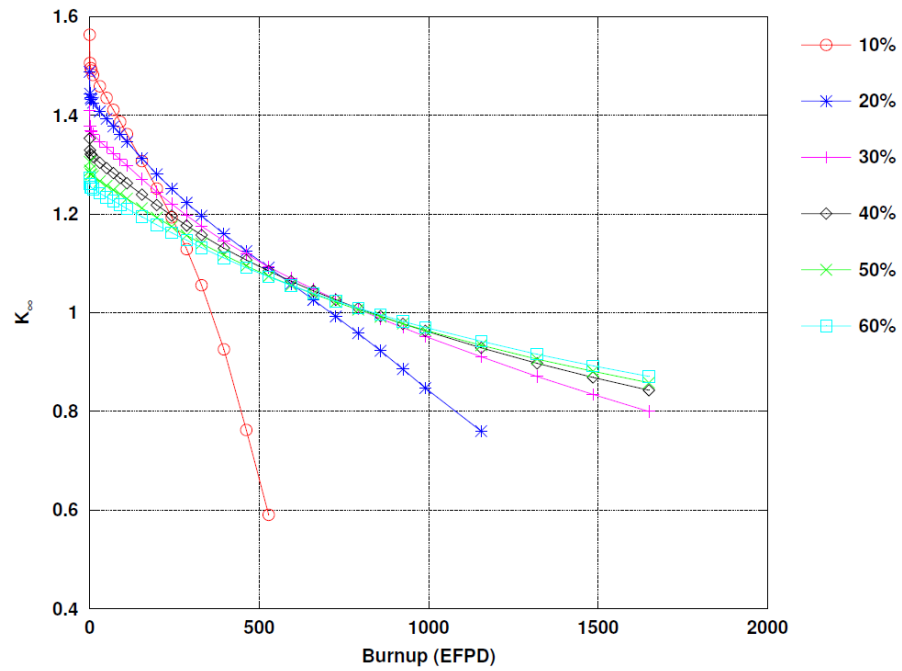


Figure 5-9. Effects of Altering Packing Fraction on k -infinity

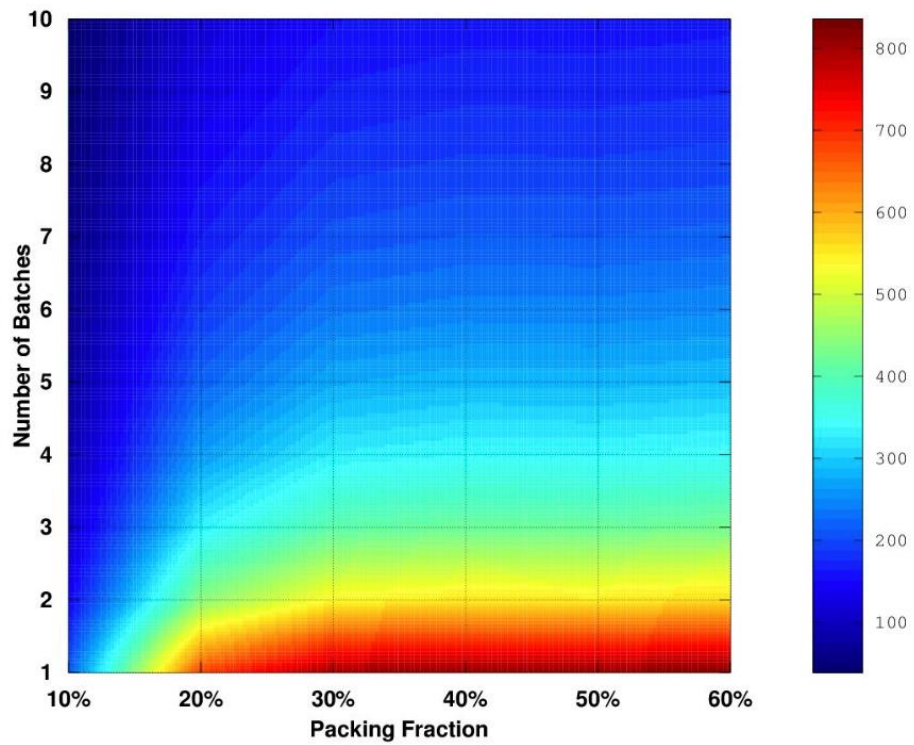


Figure 5-10. Cycle Length Effects of Altering Packing Fraction

Fuel and Core Design Options of LSCR

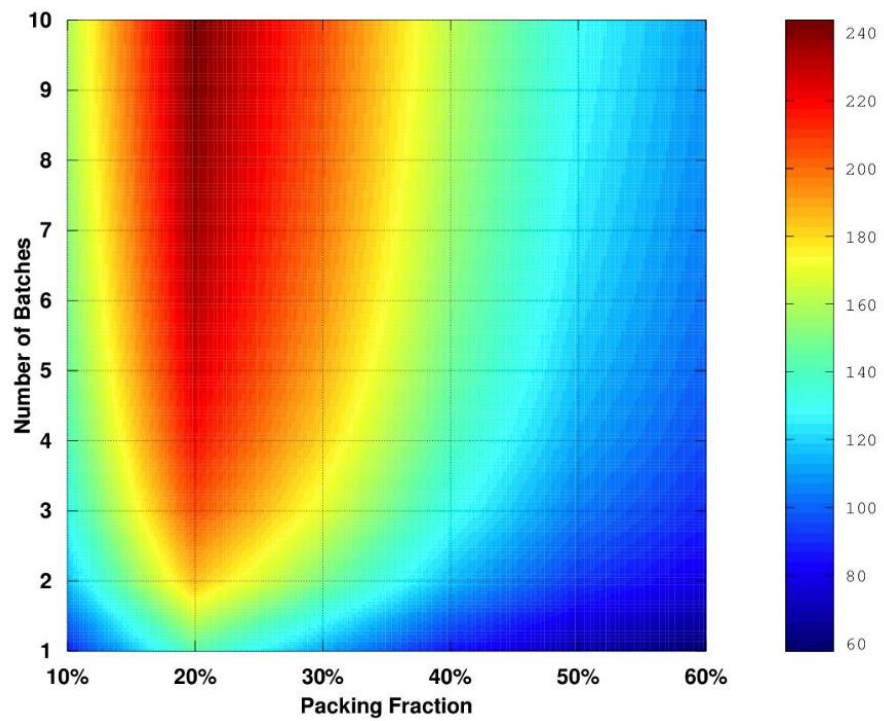


Figure 5-11. Maximum Discharge Burnup Effects of Altering Packing Fraction

5.2.c Effect of Carbon to Heavy Metal Ratio

Fuel Region and Coolant Channel Thickness Effect

In this consideration of fuel region thickness effects, the analysis was performed slightly differently than before in that fuel volume was maintained constant while adjusting the fuel region thickness (i.e. fuel packing fraction was adjusted to maintain volume). It can be seen that as the fuel region becomes smaller, reactivity, cycle length, and maximum discharge burnup all increase substantially. This of course is due to the increased resonance escape brought on by the fuel lumping effect of reducing the fuel stripe thickness. Reducing the fuel stripe thickness also improves maximum relative fuel power density due to the improved thermal diffusion, but this also causes subdivision maximum relative power density to worsen. It appears that increasing the fuel stripe thickness has little effect on the fuel temperature coefficient and control blade worth, but that shrinking the stripe thickness makes the coefficient more positive and increases the control blade worth. Changing the fuel stripe thickness appears to have had a negligible impact on the other reactivity coefficients.

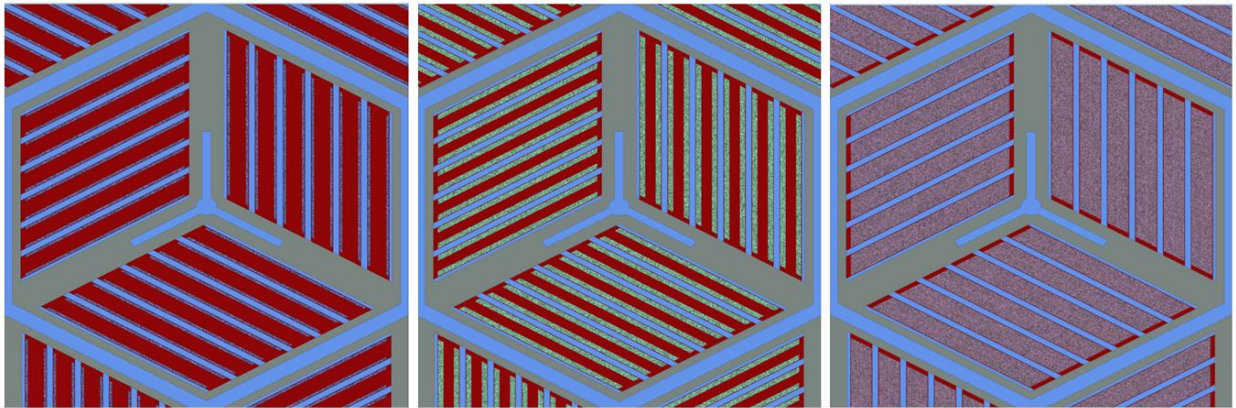


Figure 5-12. Fuel Stripe Thickness Perturbations: 50% Smaller Fuel Region (Left), Base Case (Middle), Whole Plate (Right)

Fuel and Core Design Options of LSCR

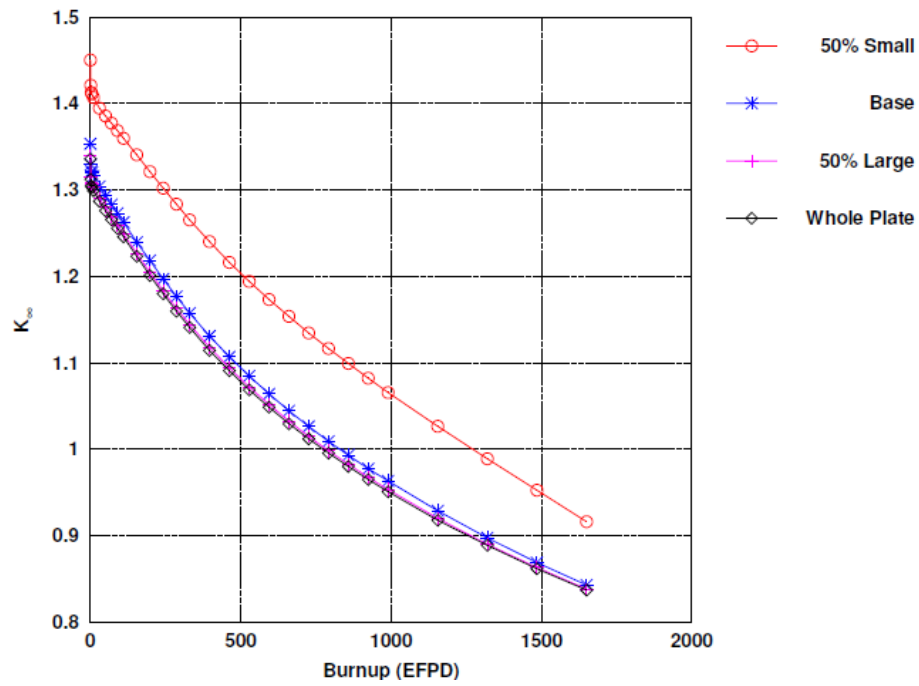


Figure 5-13. Effects of Altering Fuel Region Thickness on k -infinity

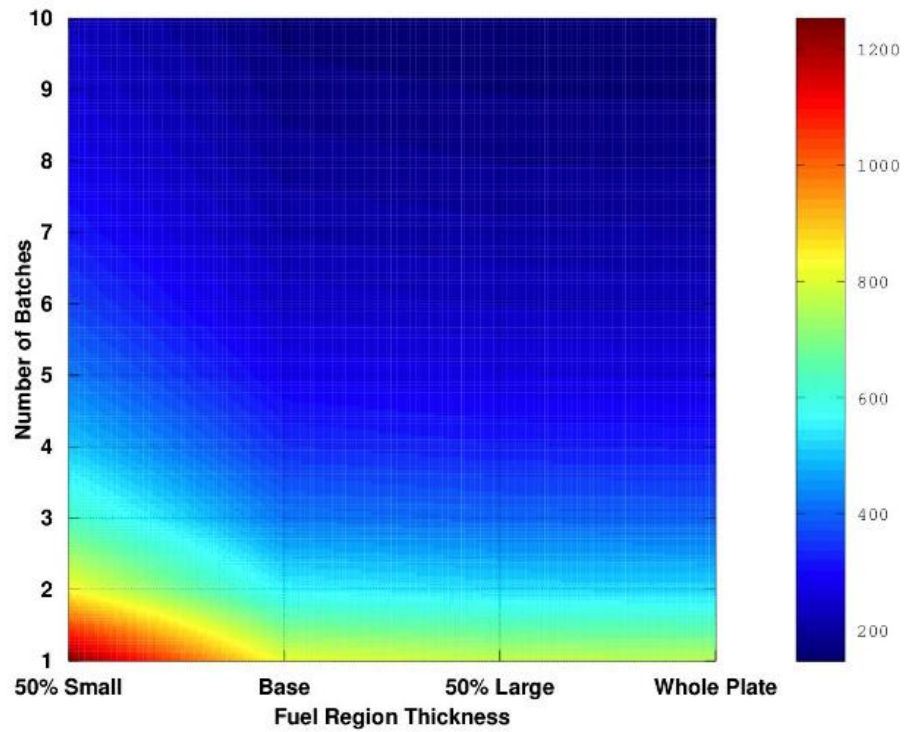


Figure 5-14. Cycle Length Effects of Altering Fuel Region Thickness

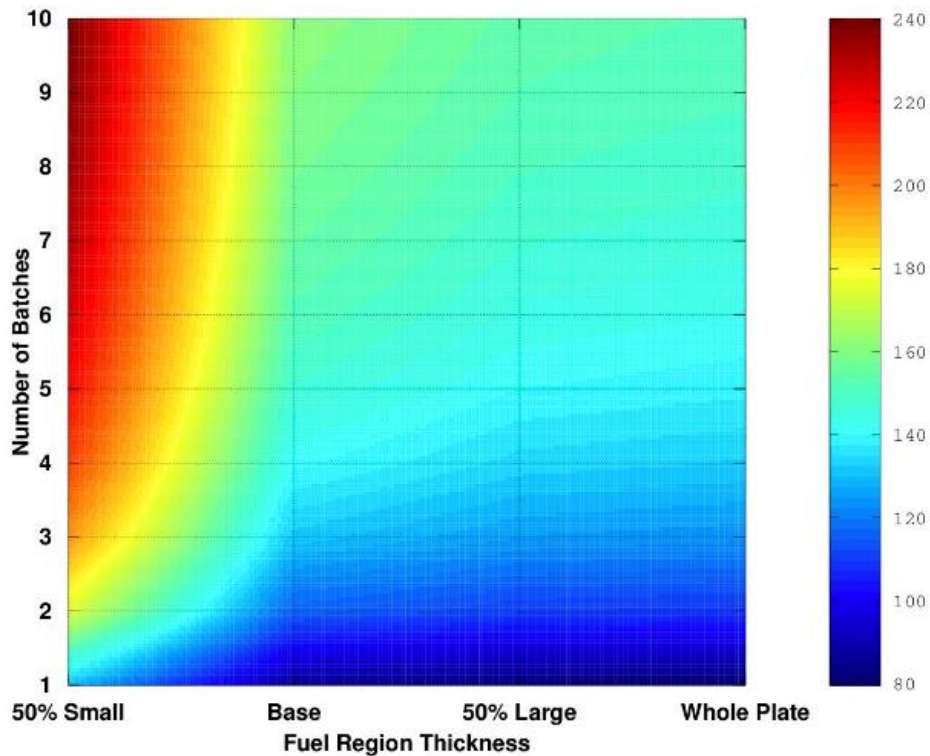


Figure 5-15. Maximum Discharge Burnup Effects of Altering Fuel Region Thickness

Reducing the meat thickness seemingly decreases reactivity, cycle length, and maximum discharge burnup up to a point where the decreased moderation is offset by the fuel lumping effect, at which point reactivity begins to increase again. Increasing meat thickness appears to worsen the maximum relative power density whereas decreasing the thickness has the reverse effect. The fuel temperature coefficient was largely unaffected by changes in meat / coolant thickness, but it was found that plate temperature coefficient generally became more positive as meat thickness decreased. Increasing coolant thickness appears to make the coolant density reduction coefficient more negative which indicates that the initially small effect of the coolant density reduction in the base design is likely due to the relatively small concentration of coolant rather than the neutronic inertness of the coolant. Control blade worth appears to increase with decreasing meat thickness possibly due to the harder flux spectrum caused by the reduced moderating volume.

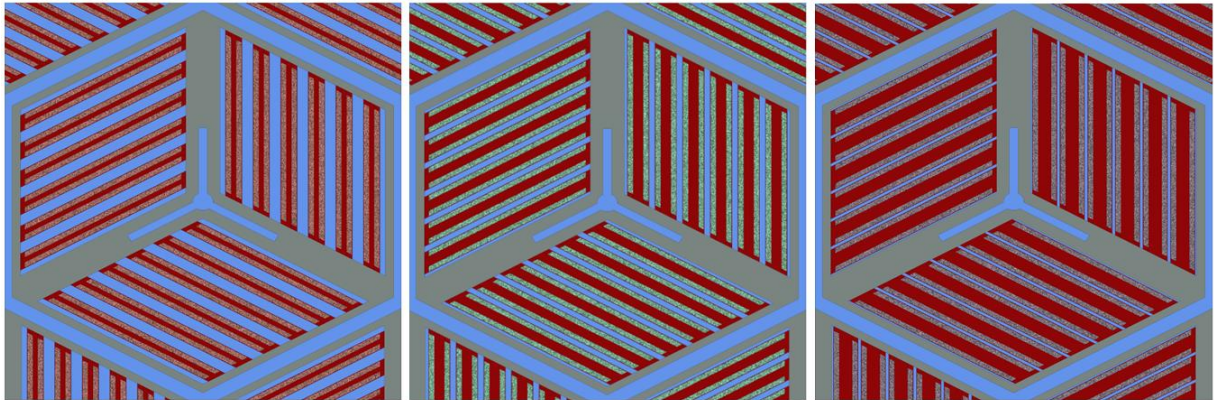


Figure 5-16. Meat and Coolant Thickness Perturbations: 50% Reduced Meat (Left), Base Case (Middle), 50% Reduced Coolant (Right)

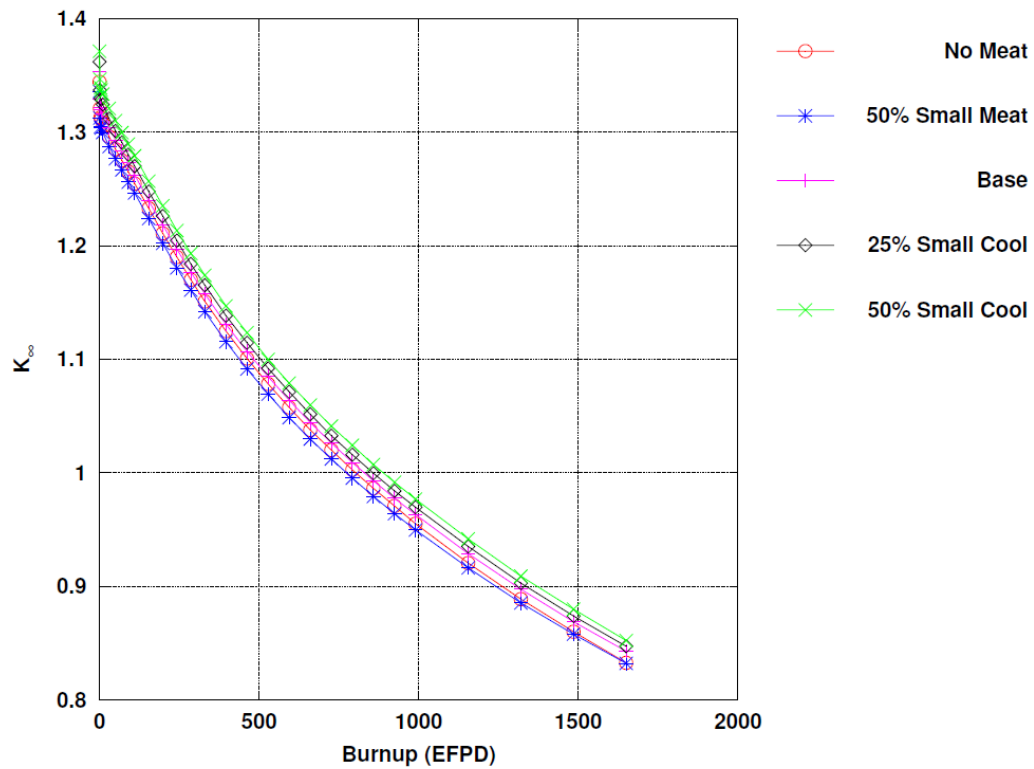


Figure 5-17. Effects of Altering Meat / Coolant Region Thickness upon k -infinity

Fuel and Core Design Options of LSCR

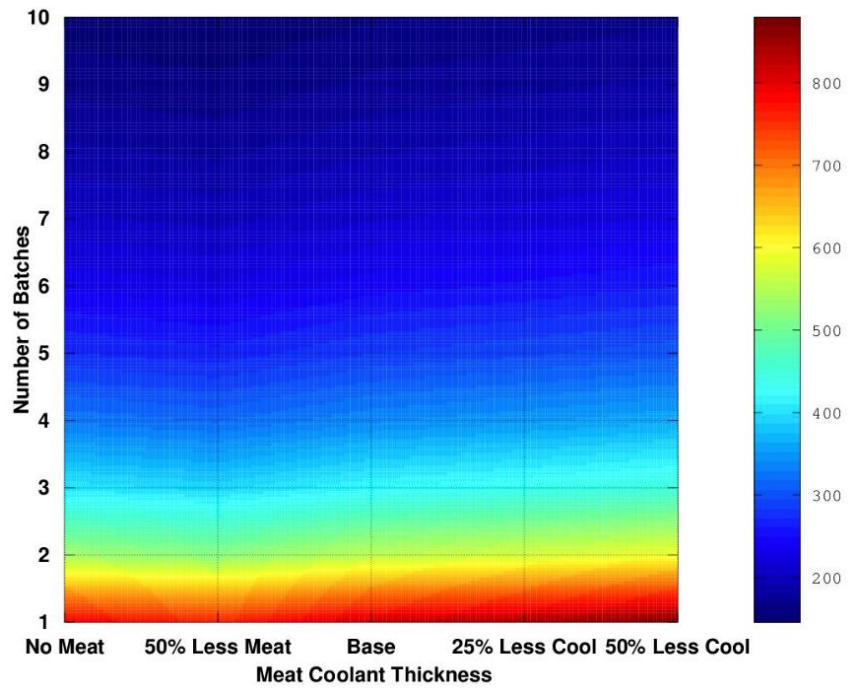


Figure 5-18. Cycle Length Effects of Altering Meat / Coolant Region Thickness

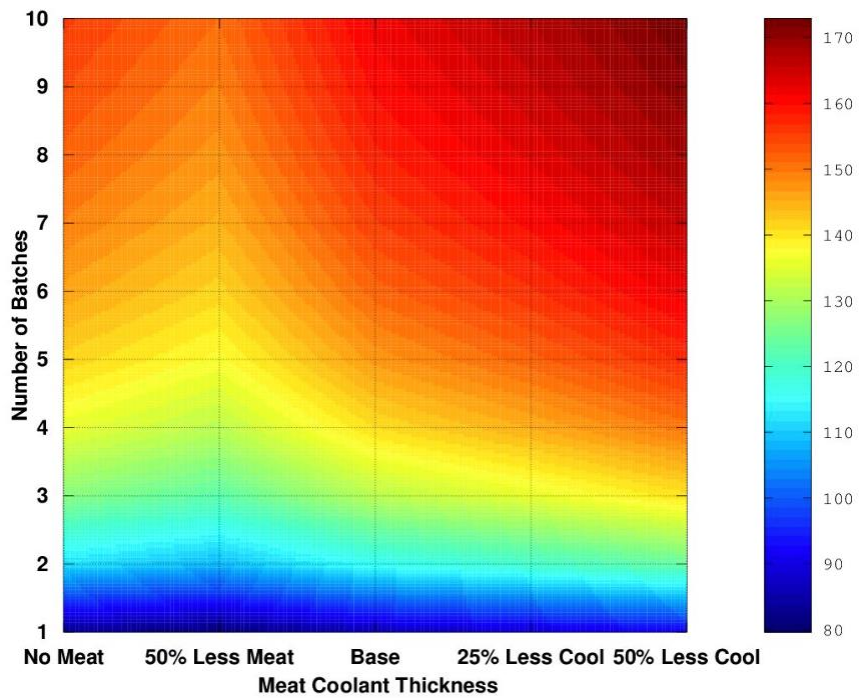


Figure 5-19. Maximum Discharge Burnup Effects of Altering Meat / Coolant Region Thickness

Y-Shape Thickness Effect

Increasing Y-Shape thickness as expected increases reactivity, cycle length, and maximum discharge burnup due to the increased moderator volume. It also tends to worsen relative maximum power density as it draws power out to the regions already problematic in this regard. Fuel temperature reactivity coefficient appears to become more positive with increasing Y-thickness due to the softening of the spectrum leading to less flux in the resonance energy bands, however all other reactivity coefficient remained mostly unaffected. Initially, control blade worth actually decreases with increased Y-thickness, but this behavior then swaps as the fuel becomes depleted. A possible explanation for this behavior is that the thermal flux is initially drawn towards the peripheral peak power regions at beginning of life resulting in lower central thermal fluxes, but as this burns out the thermal flux begins to shift more towards the assembly center where moderator concentrations are still high but the fuel is not so depleted.

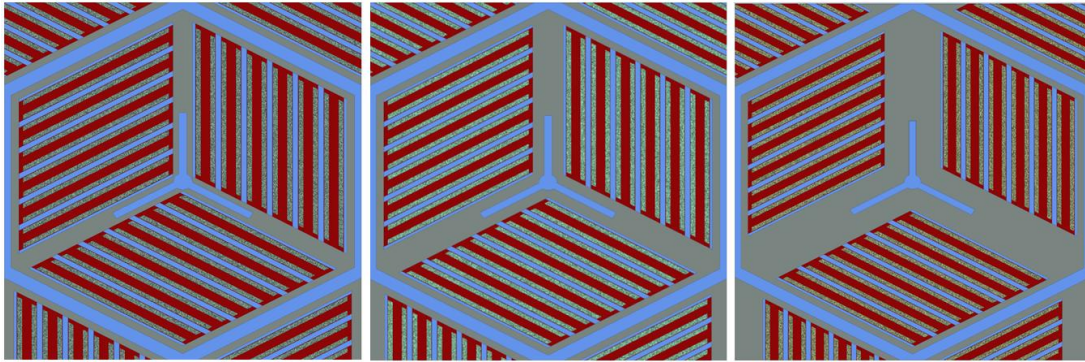


Figure 5-20. Y-Shape Thickness Perturbations: 37.5% Smaller (Left), Base Case (Middle), 100% Larger (Right)

Fuel and Core Design Options of LSCR

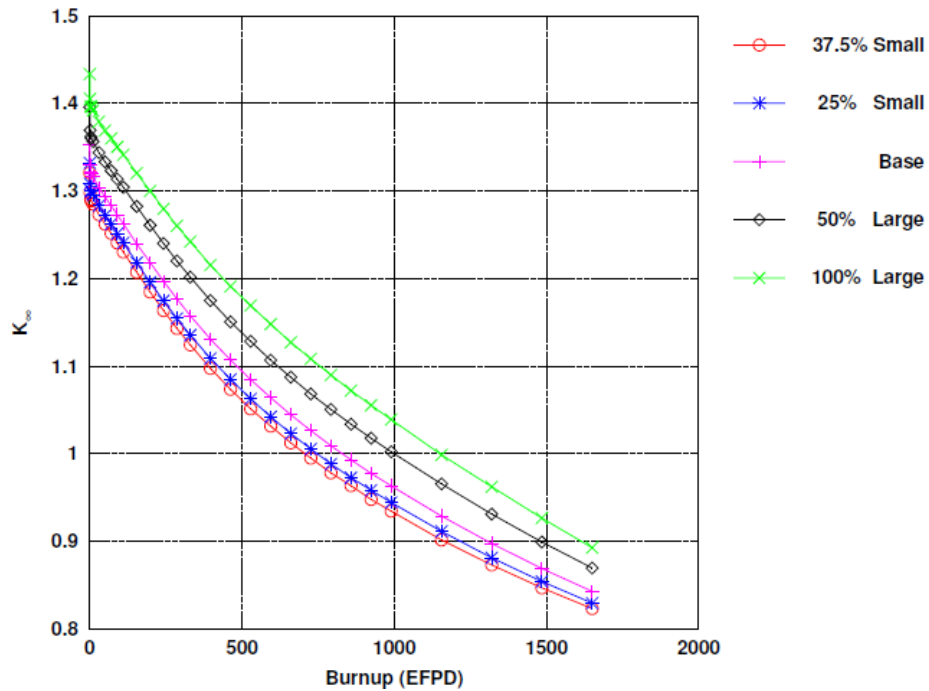


Figure 5-21. Effects of Altering Y Shape Thickness upon k -infinity

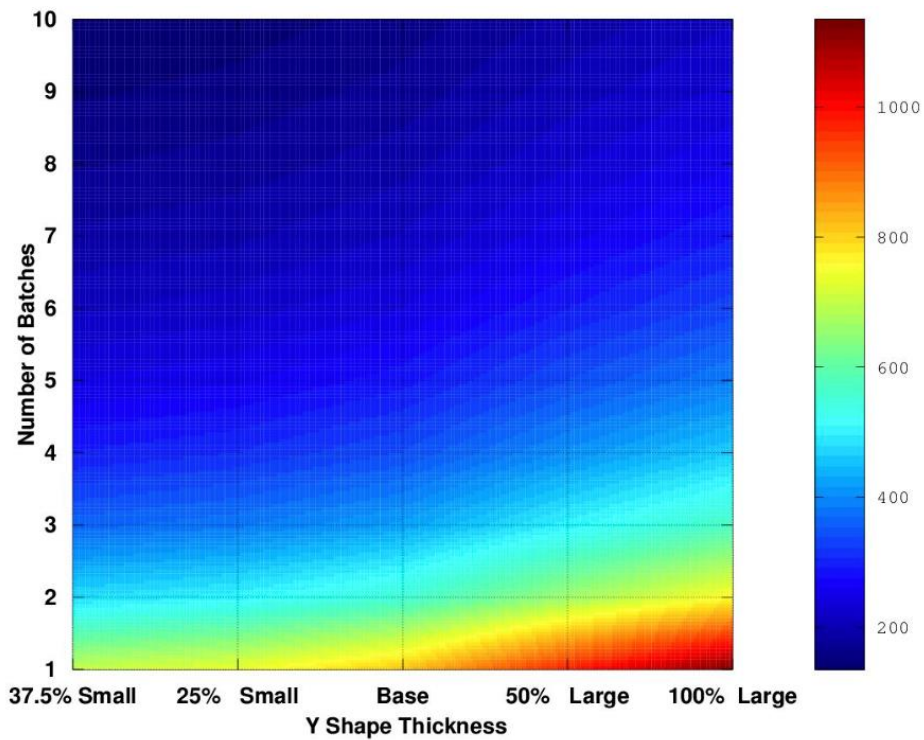


Figure 5-22. Cycle Length Effects of Altering Y Shape Thickness

Fuel and Core Design Options of LSCR

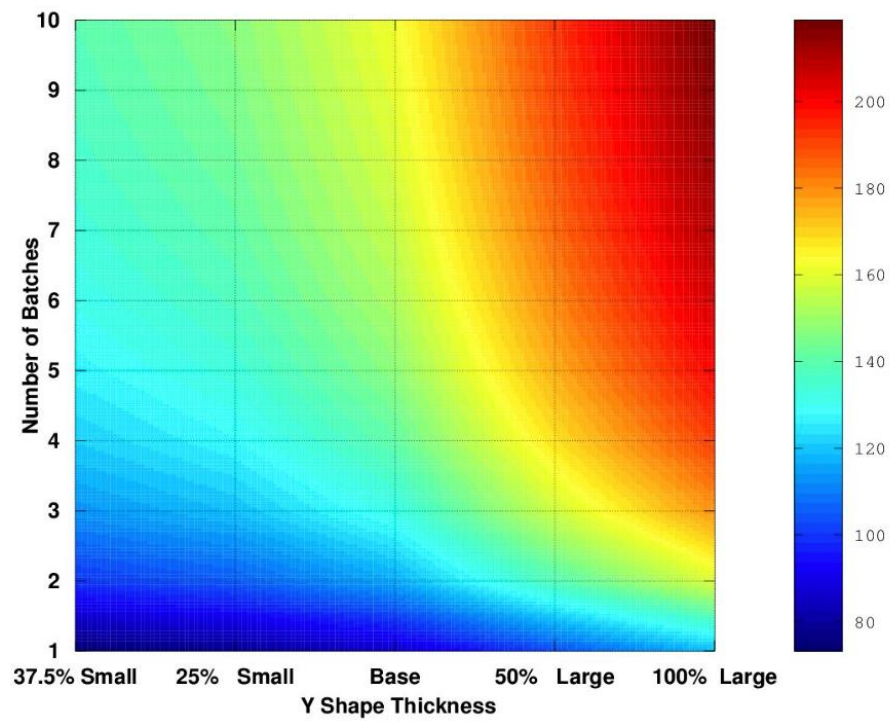


Figure 5-23. Maximum Discharge Burnup Effects of Altering Y Shape Thickness

Channel Box Wall Thickness Effect

Increasing the assembly edge thickness results in generally the same behaviors as increasing the Y-thickness in that reactivity, cycle length, and maximum discharge burnup are all increased, and that maximum relative power distribution starts high towards the assembly periphery but then becomes less due to burnout. It is likely that if one were to compare these results against the Y-thickness cases in term of CHM ratio that the magnitudes of the behavior changes would be similar. One notable difference that was observed though was that increasing the assembly edge thickness resulted in a decrease in control blade worth, likely due to the increased thermalization at the periphery of the assembly.

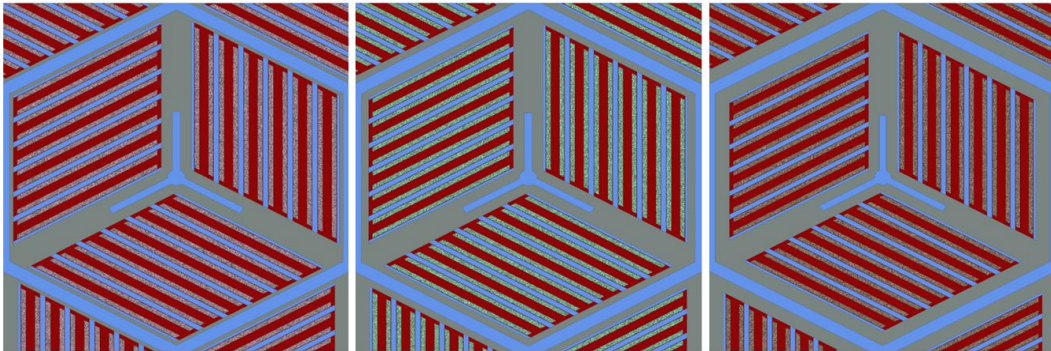


Figure 5-24. Channel Box Wall Thickness Perturbations: 50% Smaller (Left), Base Case (Middle), 100% Larger (Right)

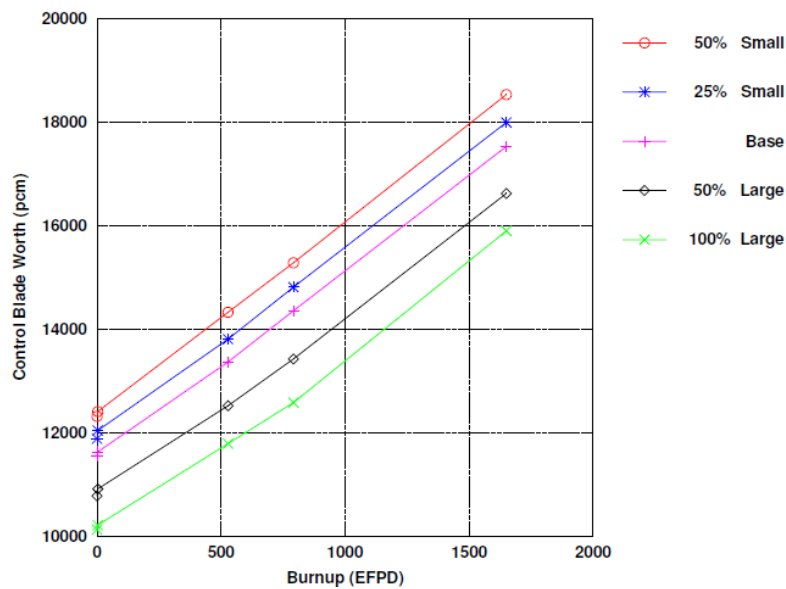


Figure 5-25. Control Blade Worth Effects of Altering Assembly Edge Thickness

Number of Plates Effect

As seen previously, decreasing the number of fuel plates while making the plates fatter so as to preserve moderator and fuel volume results in a fuel lumping effect, an increase in resonance escape probability, and an elevation in reactivity, cycle length, and maximum discharge burnup. Using fatter plates also appears to improve maximum relative power density some. This improved moderation though comes the cost of making the fuel temperature coefficient less negative. The other reactivity coefficients were not dramatically effected, and control blade worth not terribly altered except at higher burnups where fatter plates tended to exhibit a greater control blade worth.

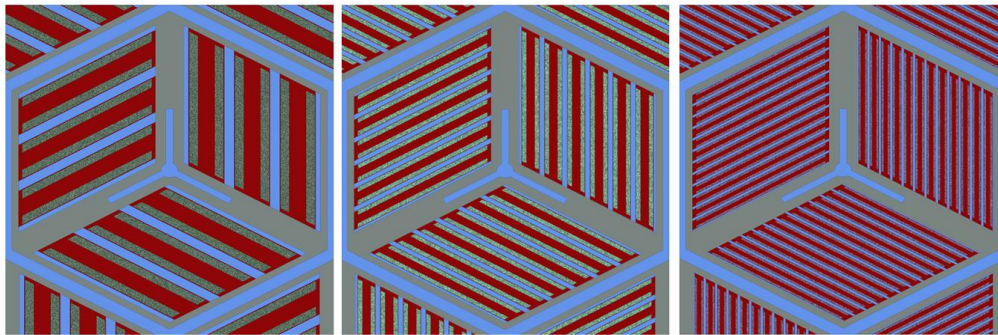


Figure 5-26. Number of Fuel Plates per Tri-Section: 3-Plate (Left), 6-Plate Base Case (Middle), 12-Plate (Right)

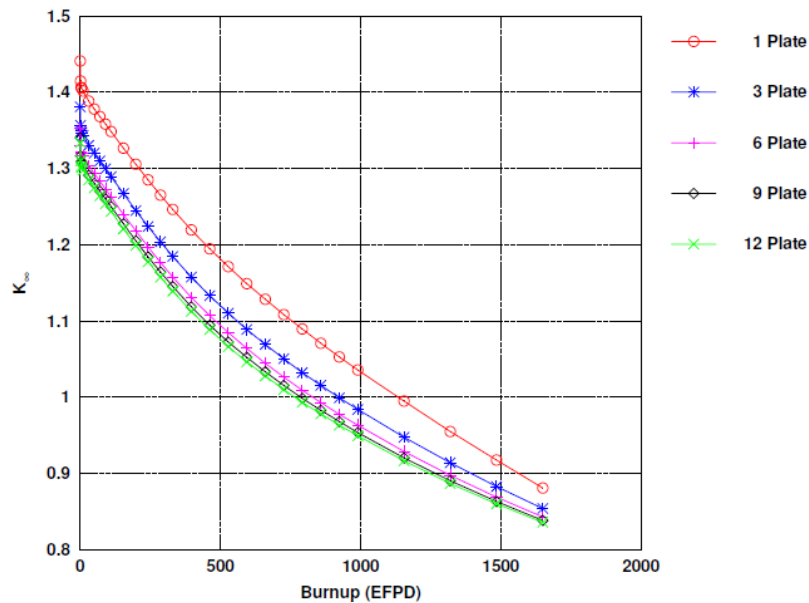


Figure 5-27. Effects of Altering Number of Plates upon k -infinity

Fuel and Core Design Options of LSCR

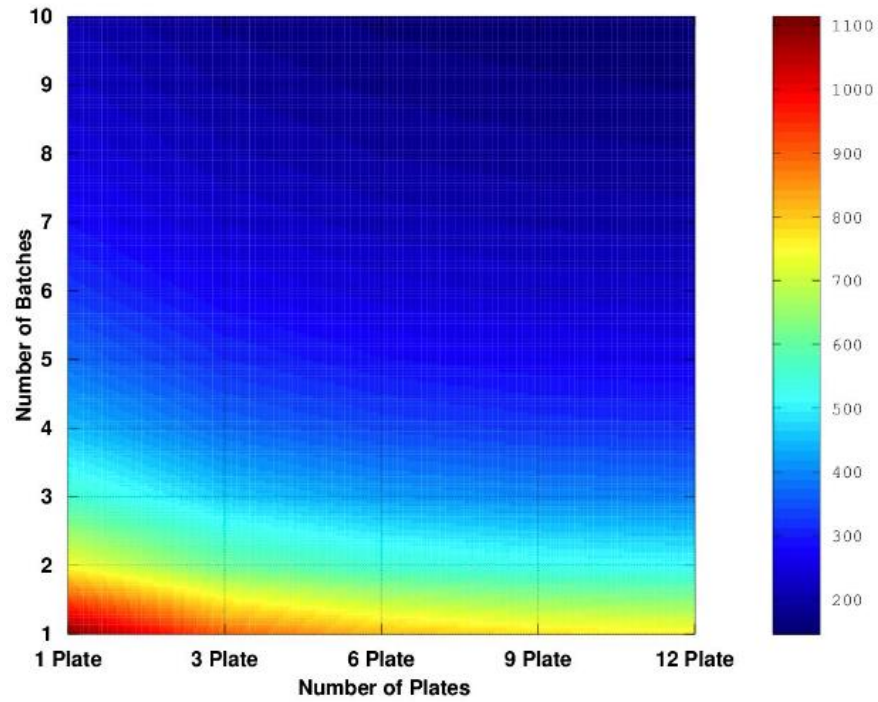


Figure 5-28. Cycle Length Effects of Altering Number of Plates

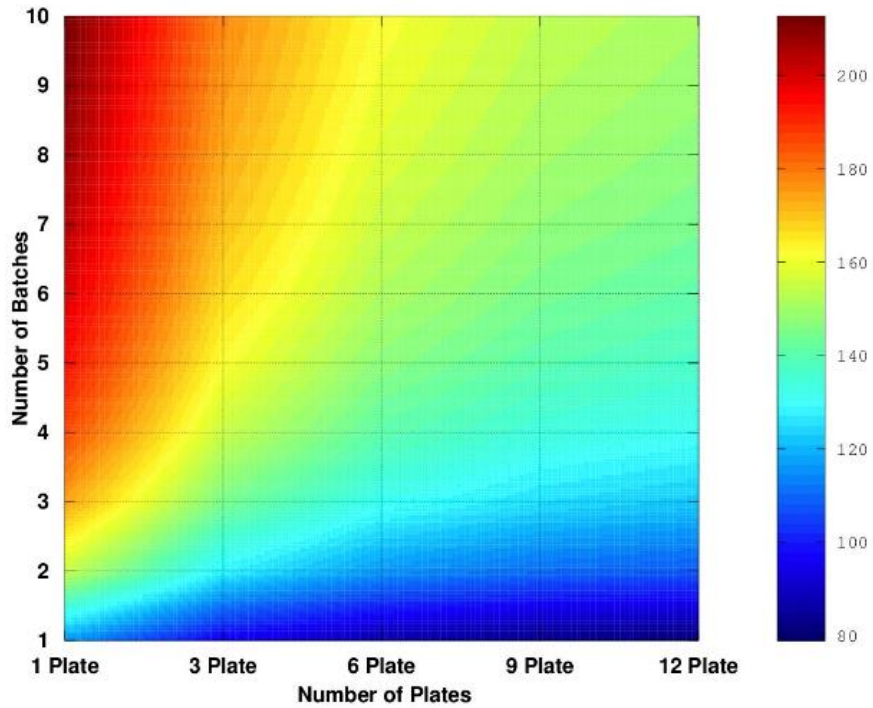


Figure 5-29. Maximum Discharge Burnup Effects of Altering Number of Plates

5.2.d Assembly Size Effect

Increasing of assembly size while preserving all proportionalities results in increased reactivity, cycle length, and maximum discharge burnup. However it generally results in larger relative power density peaks, a less negative fuel temperature reactivity coefficient, and a reduction control blade worth.

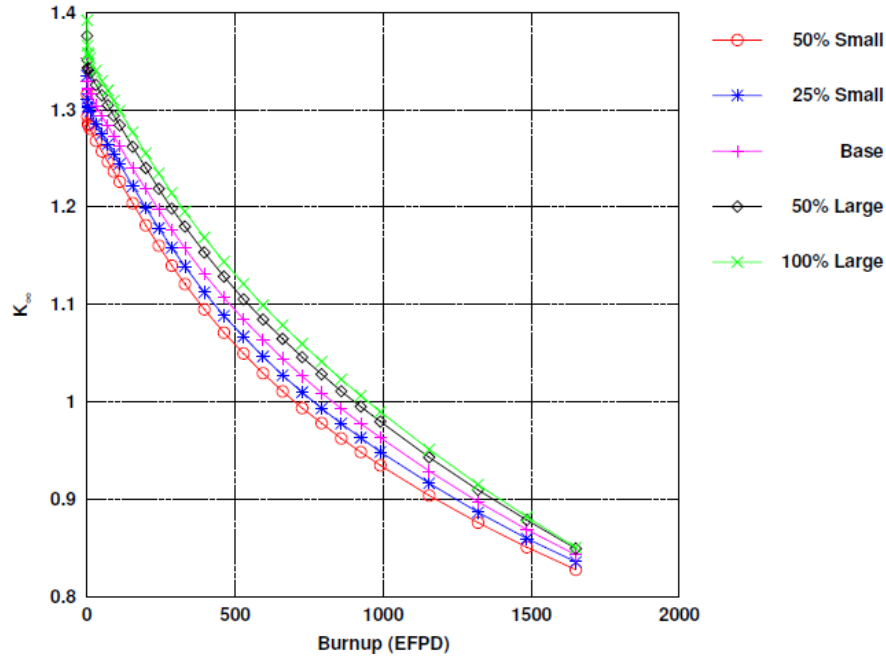


Figure 5-30. Effects of Altering Assembly Size upon k -infinity

Fuel and Core Design Options of LSCR

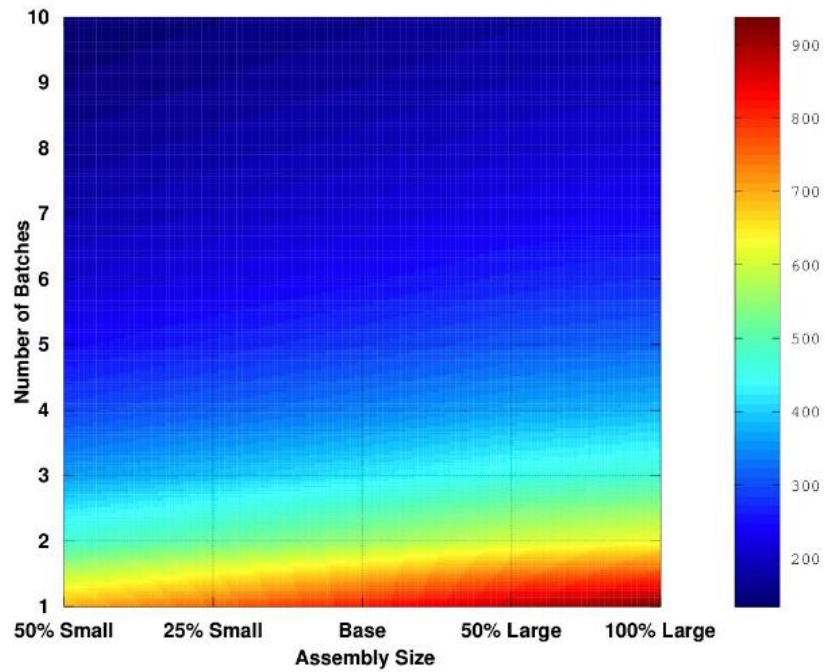


Figure 5-31. Cycle Length Effects of Altering Assembly Size

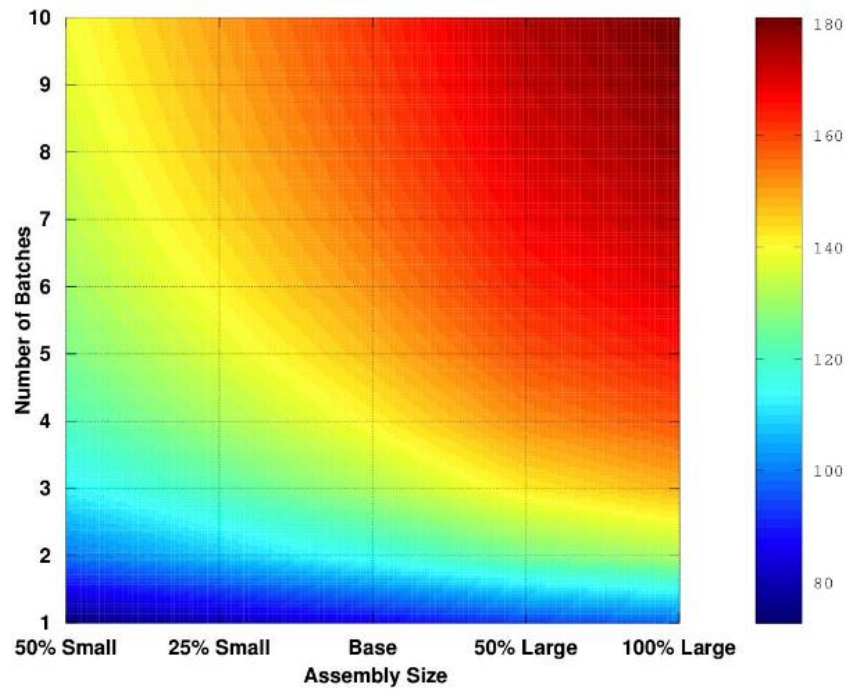


Figure 5-32. Maximum Discharge Burnup Effects of Altering Assembly Size

5.2.e Design Considerations for Employing FCM Fuel Form

One design consideration that has been proposed for improved safety has been the use of the Fully Ceramic Microencapsulated (FCM) fuel form which utilizes a SiC matrix material for the fuel. This was investigated for use in the fuel plates (i.e. swapping the original plate carbon material for FCM) along with the employment of UN fuel kernels, however FCM generally results in poorer cycle performance and UN kernels obtain a significantly lower burnup than typical UCO kernels. UN and FCM also experience higher relative power density peaks, but this is likely less important due to the high thermal tolerance of the FCM material. The fuel temperature reactivity coefficient is mostly unaffected by the use of UN kernels but is made more negative by using FCM. All other reactivity coefficients were largely unaffected. Utilizing UN kernels tends to lower control blade worth whereas utilizing FCM increases it.

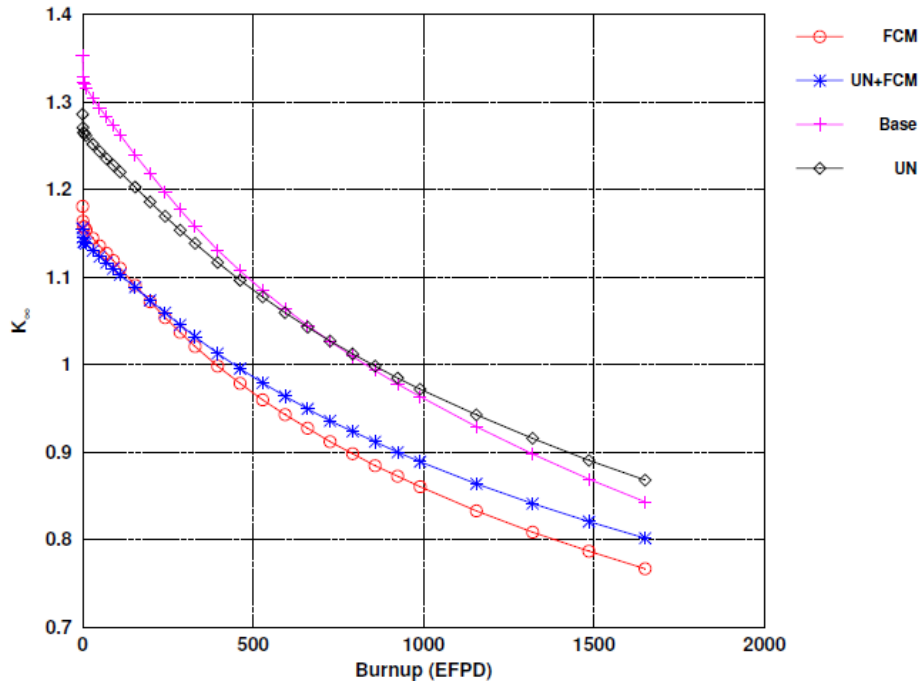


Figure 5-33. Effects of using FCM / UN Fuels upon k -infinity

Fuel and Core Design Options of LSCR

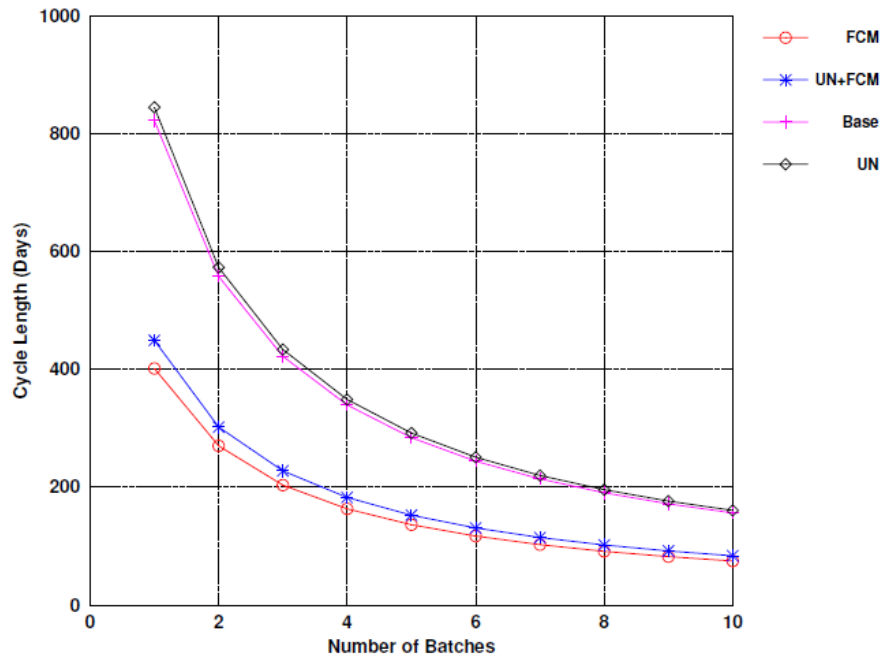


Figure 5-34. Cycle Length Effects of using FCM / UN Fuels

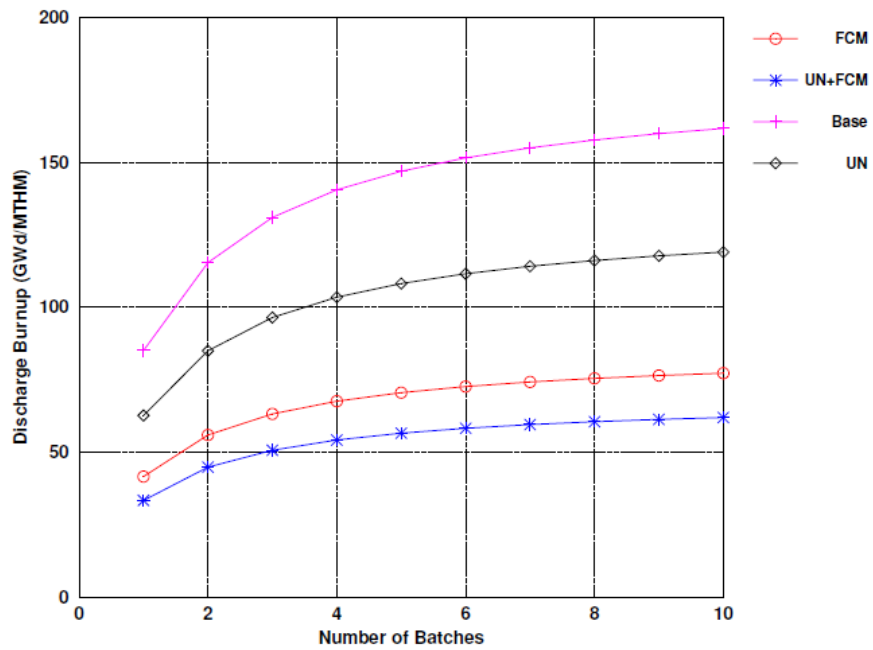


Figure 5-35. Maximum Discharge Burnup Effects of using FCM / UN Fuels

6. Reactivity Control (Tasks 6)

6.1 Burnable Poisons

As in previous analysis, poisons were investigated for a number of different materials in both QUADRISO and BISO form. It should be noted that BISO models were simulated with BISO particles dispersed within the fuel stripe region rather than the meat region of the fuel plates. As was seen in the previous analysis, Cd in both BISO and QUADRISO forms as well as Gd in QUADRISO form tend to burnout too quickly, whereas B in the BISO form and both forms of Ir, Er, and Eu tend to not burn out quickly enough with Eu being the most egregious offender. Poisons in these forms had only a negligible effect on the maximum relative power densities. Fuel temperature reactivity coefficients were observed to be slightly different between the high temperature branch case and low temperature branch case and so both sets of results are presented, but it is generally observed that the temperature coefficient is lowered by the introduction of poison. The reason for the differences between high and low temperature branches is not currently understood, but is presented simply to show the difference. Of greatest note though is the beginning of life plate temperature coefficients which are negative for Ir, Er, Eu, and only slightly B, but is positive for Gd and Cd. The plate temperature coefficient (changing the graphite temperature only) does eventually become negative for all poison, but this initial positiveness could be problematic for Gd and Cd. Control blade worth, though slightly effected by the addition of poison is not dramatically altered.

Fuel and Core Design Options of LSCR

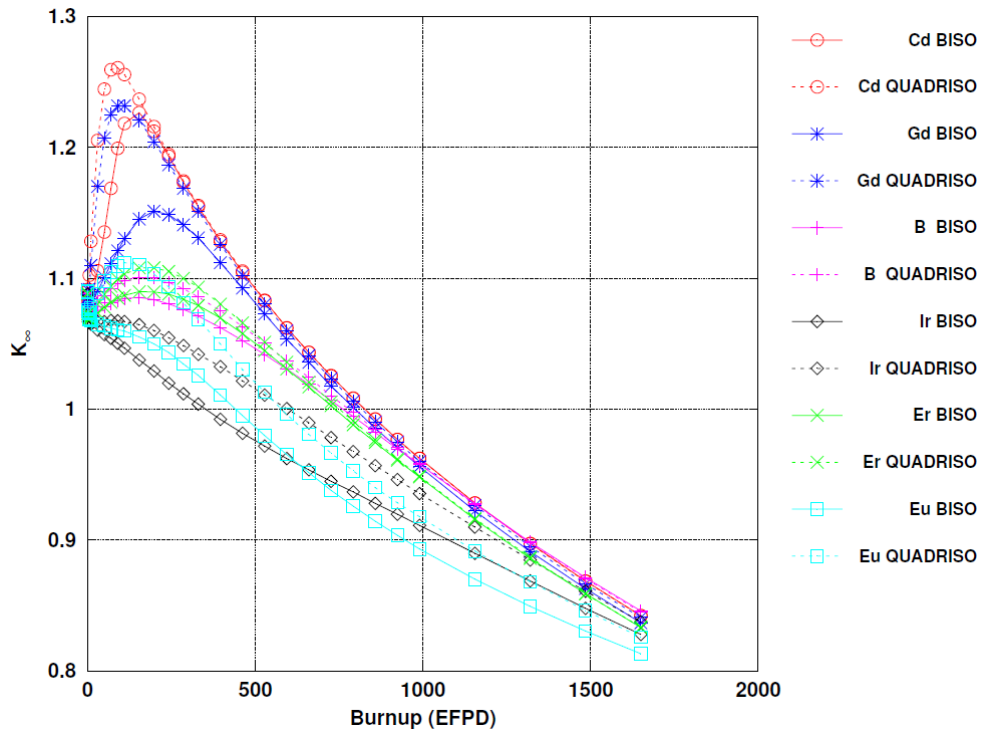


Figure 6-1. Effects of using Burnable Poisons upon k -infinity

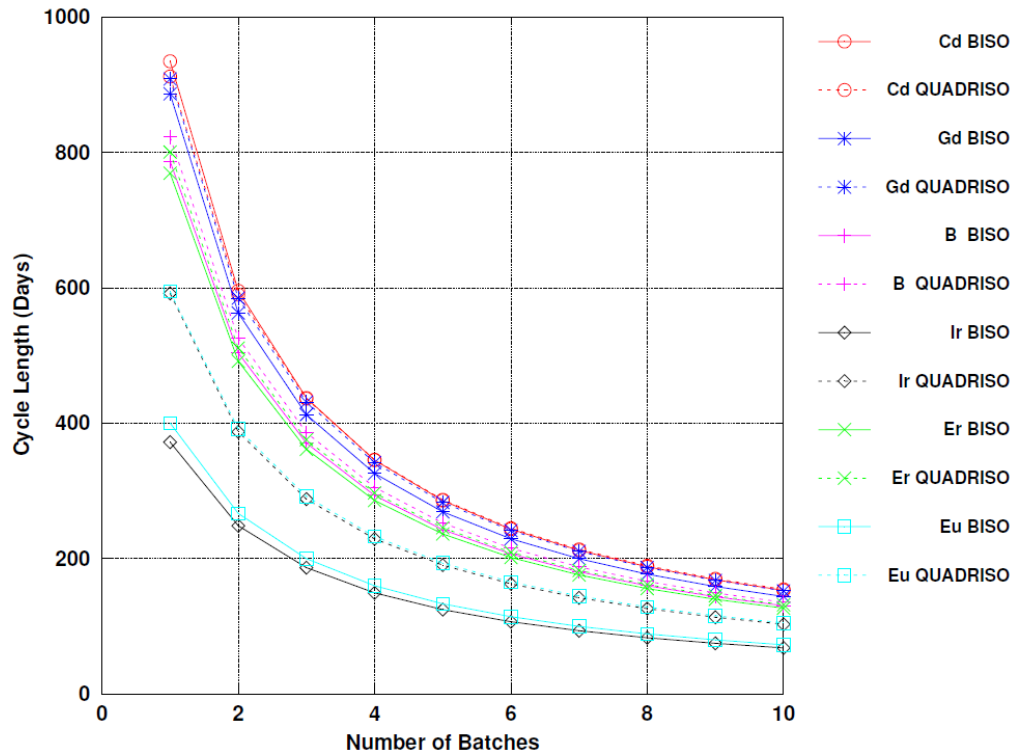


Figure 6-2. Cycle Length Effects of using Burnable Poisons

Fuel and Core Design Options of LSCR

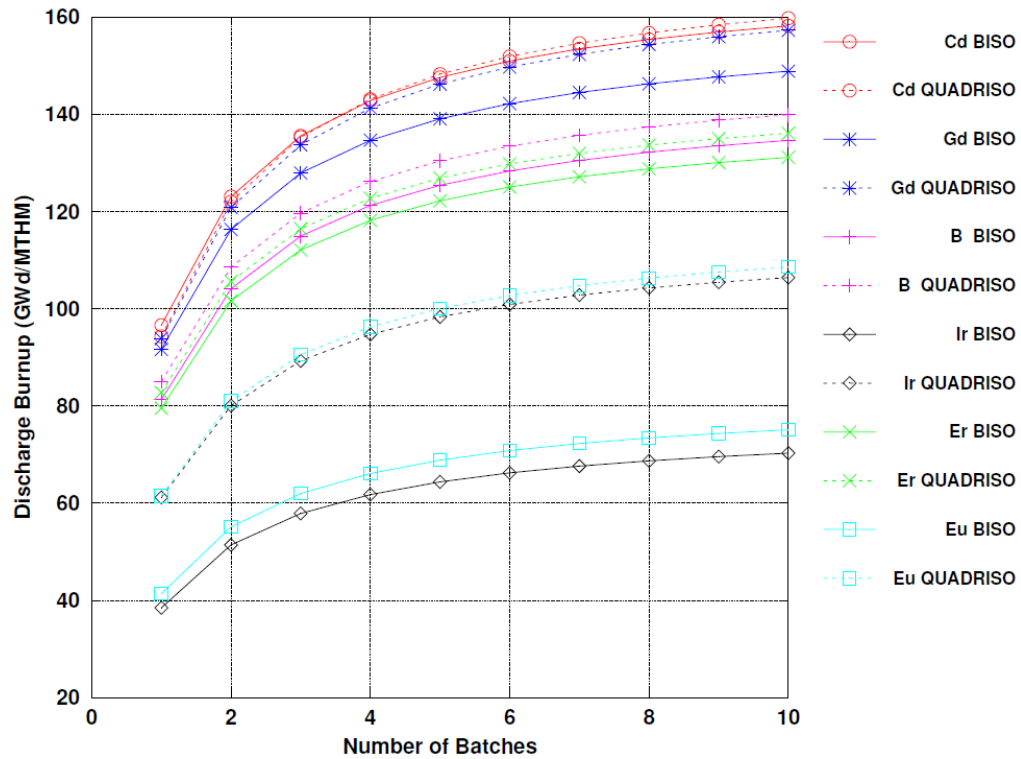


Figure 6-3. Maximum Discharge Burnup Effects of using Burnable Poisons

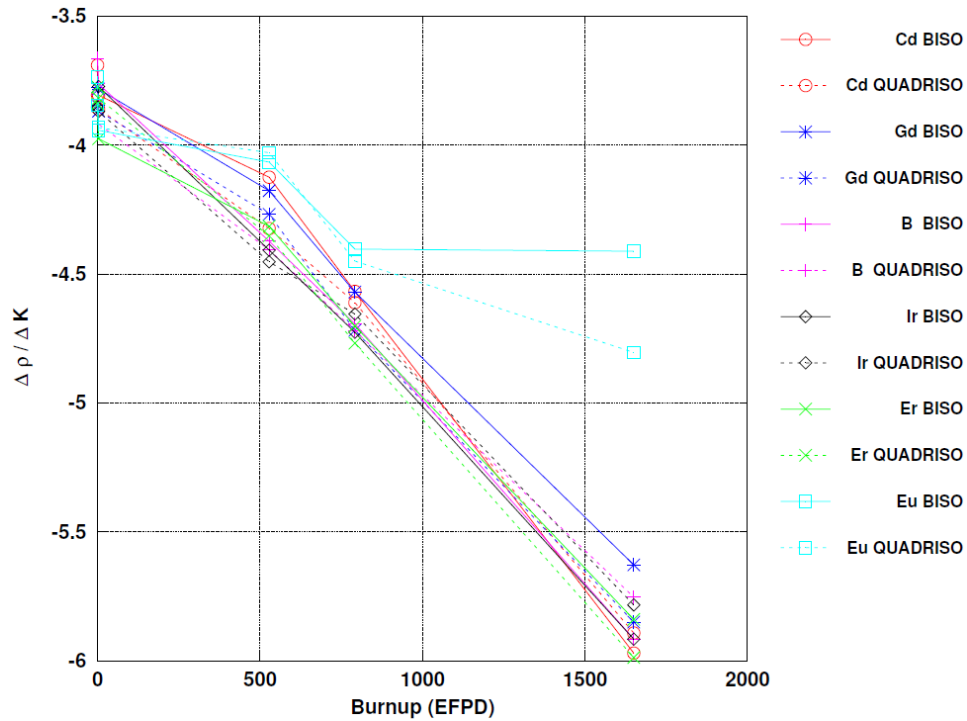


Figure 6-4. Fuel Temperature Coefficient High Temperature Effects of using Burnable Poisons

Fuel and Core Design Options of LSCR

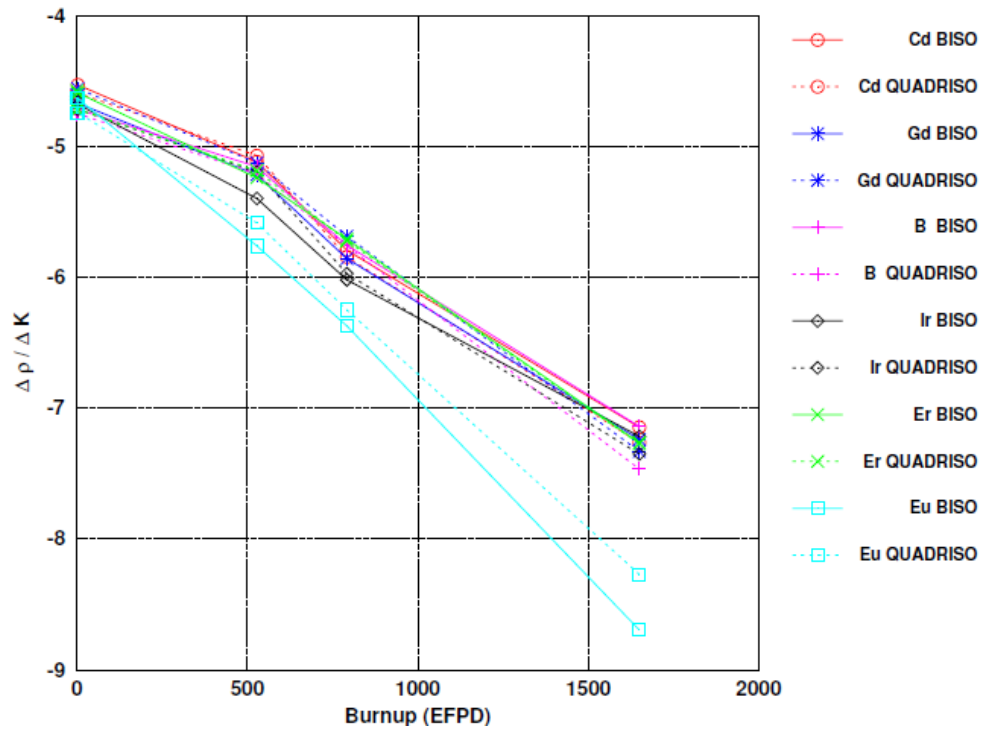


Figure 6-5. Fuel Temperature Coefficient Low Temperature Effects of using Burnable Poisons

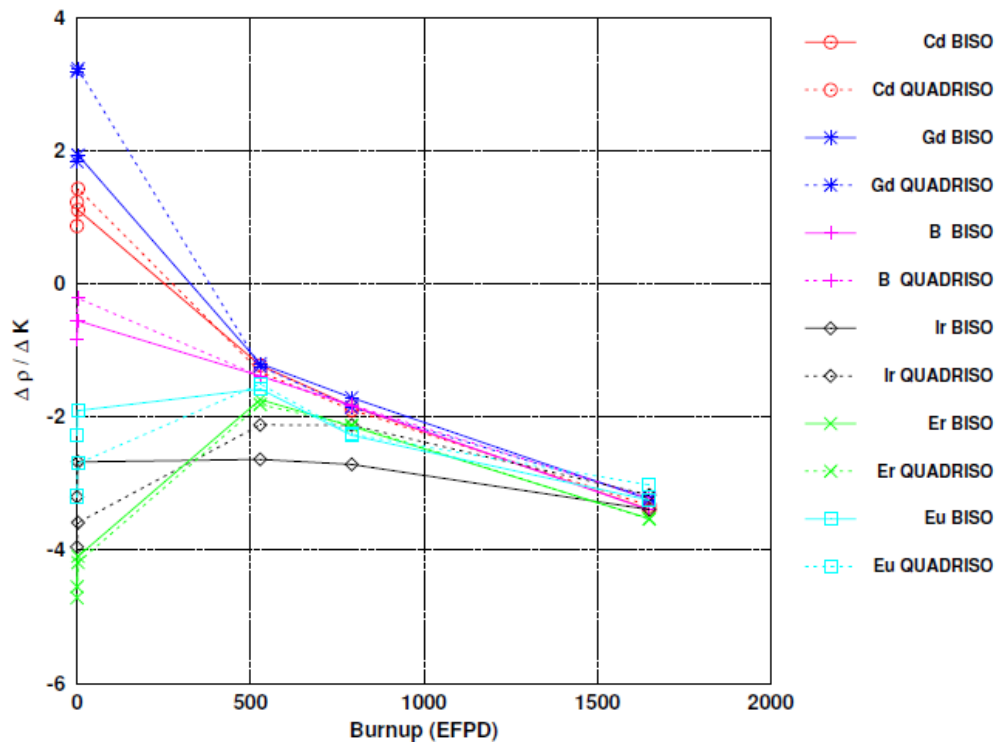


Figure 6-6. Plate Temperature Coefficient Effects of using Burnable Poisons

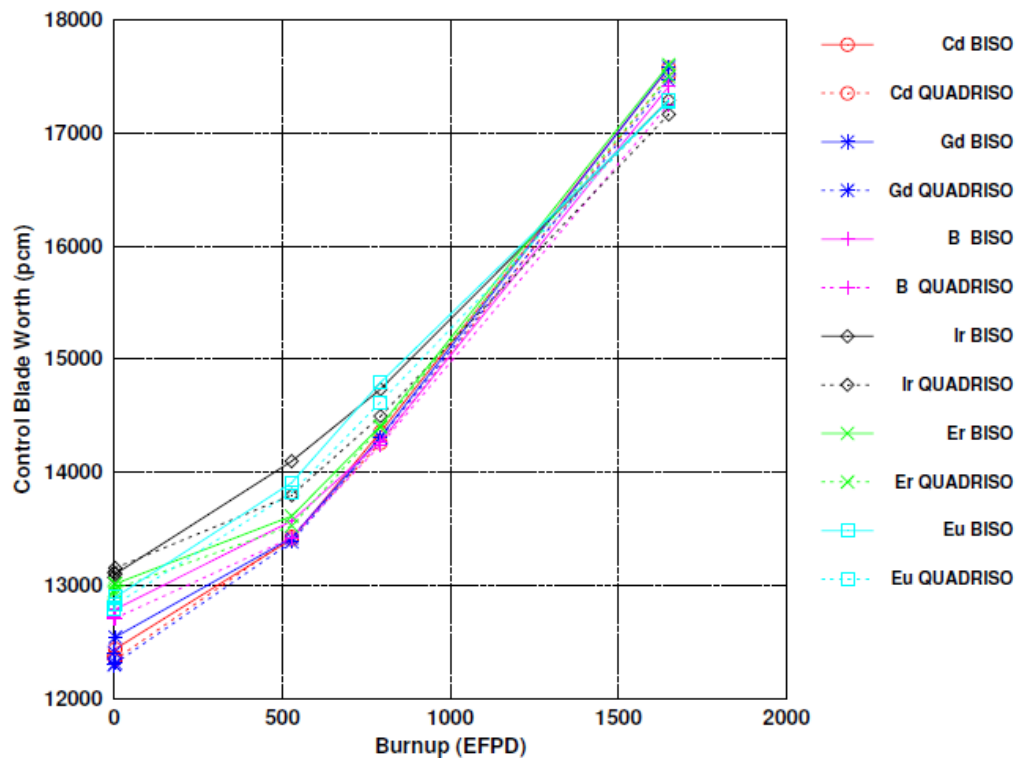


Figure 6-7. Control Blade Worth Effects of using Burnable Poisons

6.2 Control Blades

The AHTR design employs Y-shaped control blades. One notable problem with the current base design is the lack of sufficient control / shutdown capability of the control blade. This is a combined effect of both blade material and blade geometry. Therefore, altering of the blade design was investigated to identify plausible means of improving the control blade worth by means of increasing the control blade length and changing the control blade material. It should be noted that other design limitations such as assembly mechanical integrity and material melting points were temporarily ignored for academic purposes. Control blade length was chosen over thickness in that length would introduce the control material to assembly regions of greater thermal flux as the blade volume increased.

Increasing the blade length and subsequently altering the control blade slot geometry to accommodate had a negligible effect on all neutronic parameters of interests other than the control blade worth which dramatically increased with increasing control blade length. This indicates that extending the control blade length provides a likely avenue for obtaining greater control blade worth for little design change.

With regards to alternative control blade materials, AgInCd, B₄C, and tungsten were all found to generally perform better than MHC from a neutronic perspective. Reactivity coefficients were also investigated for the control blade inserted condition for the various materials. It should be noted that these were done in terms of absolute k-infinity difference rather than reactivity difference being that subcritical systems tend to exaggerate reactivity difference depending on the degree of subcriticality. MHC (molybdenum-hafnium-carbide) was found to have the most negative fuel temperature coefficient, but was generally less negative for both plate temperature and coolant density coefficients. Again, melting and mechanical aspects of these materials were ignored for this analysis and must be considered.

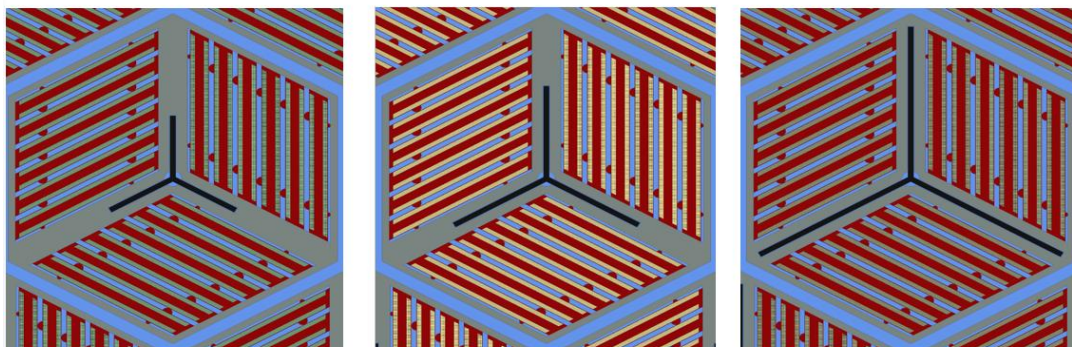


Figure 6-8. Increased Control Blade Length: Base Case (Left), 47% Longer (Middle), 141% Longer (Right)

Fuel and Core Design Options of LSCR

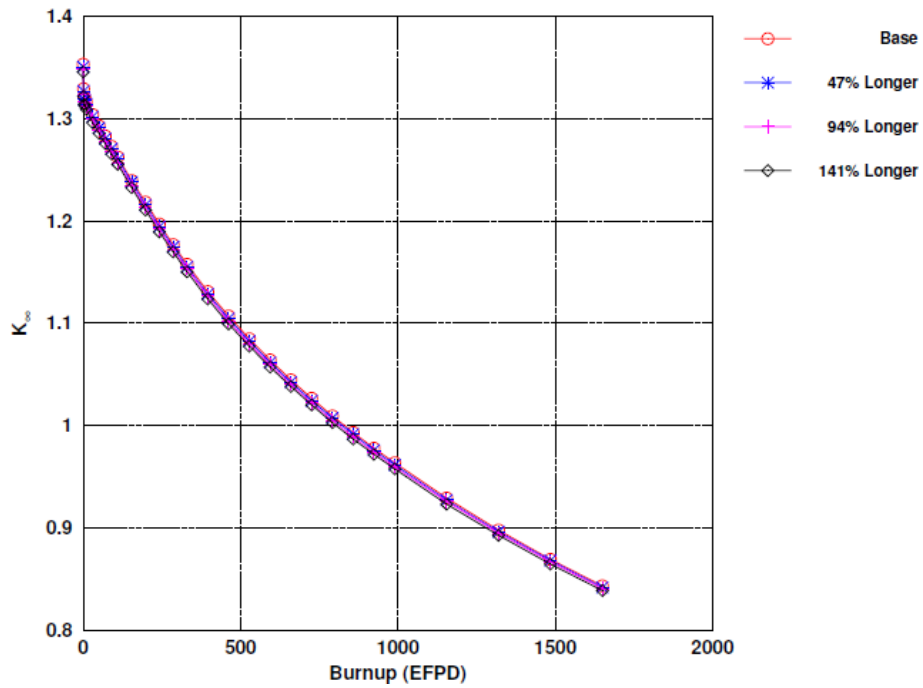


Figure 6-9. Effects of Altering Control Blade Channel Size upon k -infinity

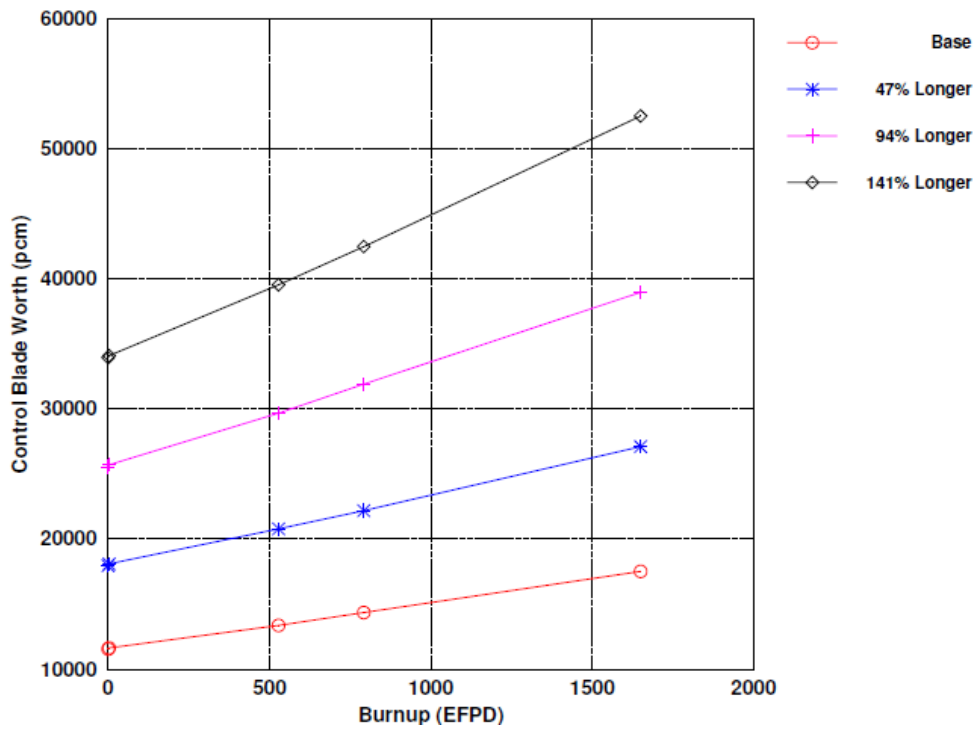


Figure 6-10. Control Blade Worth Effects of Altering Control Blade Size

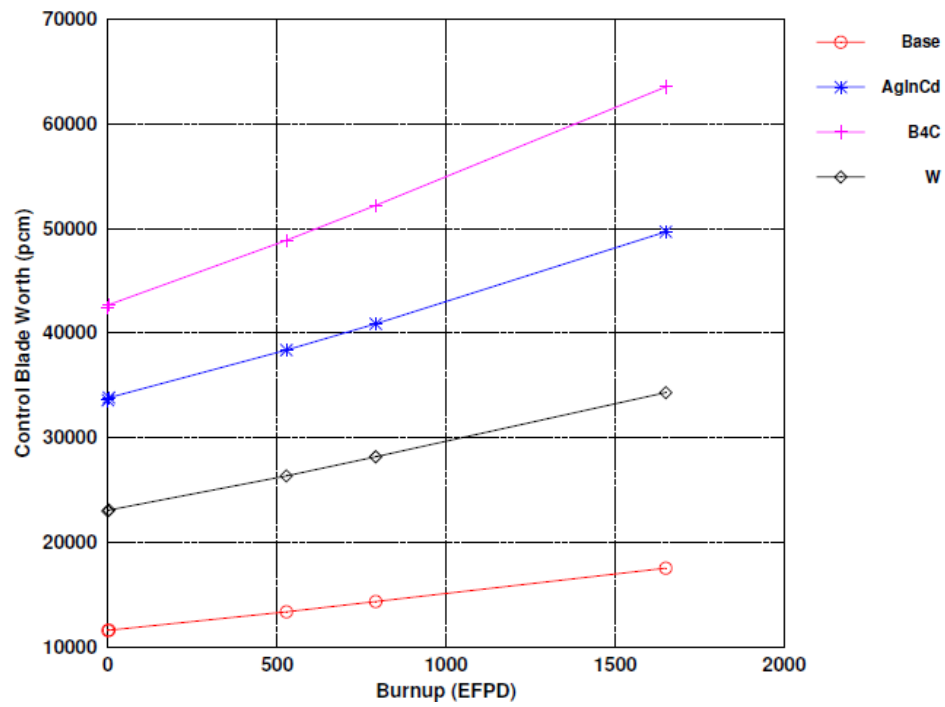


Figure 6-11. Control Blade Worth Effects of Altering Control Blade Material

7. Thermal-Hydraulics Studies and Pseudo-Continuous Refueling (Tasks 5)

7.1 Single channel

Different types of thermal-hydraulic evaluations have been performed on the AHTR coolant channel in order to perform parametric studies and to allow the modeling of the heat transfer in RELAP5-3D.

7.1.a Matlab model and evaluations

A MATLAB model to predict the temperature distribution along the channel and the fuel plate was developed, as a simple tool for preliminary and sensitivity studies. After the calculation of the main dimensional parameters, the thermal-hydraulic properties of the coolant and the thermal properties of the fuel, axial and radial mesh points were defined and the temperature distribution of the coolant and the plate was obtained from two discretized energy balances and the Fourier law. *Figure 7-1* shows an example of plate temperature distribution obtained from the MATLAB model.

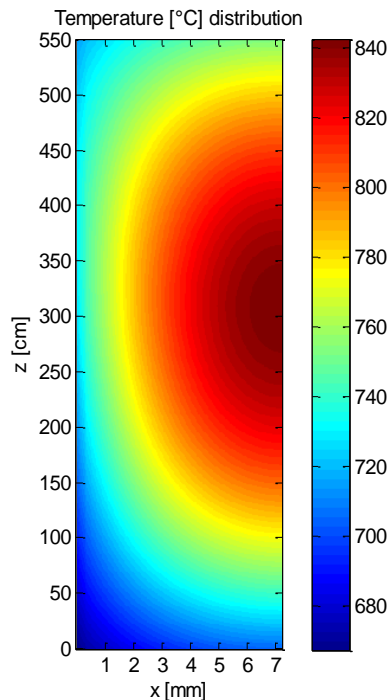


Figure 7-1. Typical temperature distribution of the average AHTR fuel plate

In relation to the power density distribution, the axial and transversal profile were evaluated. Considering the axial power distribution, a chopped cosine-shaped profile was assumed and an optimal extrapolated length of 7 m was determined, in order to obtain a 1.3 axial peaking factor, which is typical of this reactor design. The model was slightly modified to account for transversal power profile variations and different power distributions were tested, in order to see how much this affects the maximum fuel temperature. The results show that a variation of the power density in the central area of the fuel stripe, due for example to eventual flux depression, does not strongly change the maximum fuel temperature; the main factor that affects the maximum temperature is the average distance of the power density distribution from the surface of the plate. Considering very different transversal power density distributions, a relatively small variation in the maximum fuel temperature was obtained.

The MATLAB model was used to perform sensitivity studies on some of the main parameters of the AHTR fuel assembly: graphite conductivity, cladding thickness, meat thickness, TRISO particle packing fraction, coolant gap thickness.

The irradiation of graphite was found to be a strong factor in the determination of the temperature distribution: the increase in the maximum temperature from the beginning to the end of life due to thermal conductivity degradation is large, about 80°C;

The maximum temperature has a relevant dependence on the sleeve thickness, about 15°C/mm for the average fuel assembly and 25°C/mm for the hottest assembly. The reason for this strong dependence is the fact that all the power generated in the fuel must pass through the sleeve, before being removed by the coolant, producing a high temperature drop across the sleeve.

Considering the fuel stripe thickness, the maximum fuel temperature depends mainly on the average distance of the fuel from the surface, which is much more sensitive on the sleeve thickness than on the fuel stripe thickness variation. From the previous consideration we can say that the maximum fuel temperature is not strongly affected by the fuel stripe thickness, if the power level of the reactor is considered constant.

A high TRISO particle packing fraction is desirable, since high packing fraction means thinner fuel stripe and so lower power temperature.

In relation to the fuel thermal performance, another important parameter that was evaluated is the coolant gap thickness. Since this model assumes the capability of the primary pumps to force the nominal mass flow rate in any condition, a reduction of the channel dimensions has a positive effect on the temperature distribution, because the heat transfer is enhanced, but the negative effect is the increase of the flow velocity and the pressure drop across the core.

A similar evaluation was performed, implementing constant pumping power instead of constant mass flow rate: in this case thinner coolant gap leads to higher fuel temperature, since the mass flow rate through the core is reduced, due to higher pressure drop. In this condition, the limiting coolant thickness in terms of maximum fuel temperature and thermal-hydraulic performance was found to be about 6 mm.

The next figure shows the maximum temperature distribution as a function of the coolant gap and fuel stripe thickness.

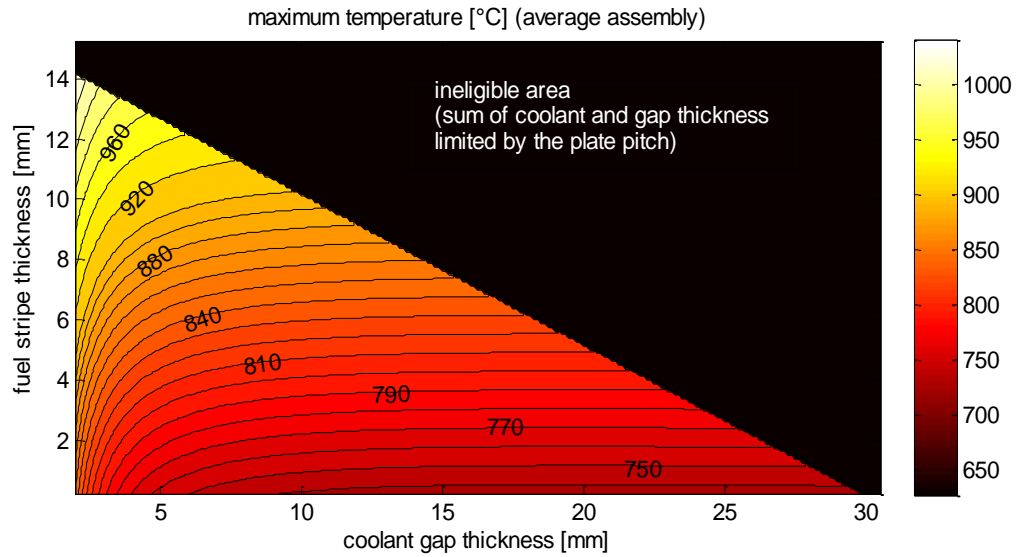


Figure 7-2. Maximum temperature distribution as a function of the coolant gap and fuel stripe thickness

Considering the results of the sensitivity studies and of the power profile simulations, the MATLAB model seems to be a simple and good tool for the evaluation of the AHTR fuel assembly features and design; these studies prove that the assembly configuration adopted for the AHTR is able to provide good cooling features and keep relatively low operating fuel temperatures.

7.1.b RELAP5 single channel evaluations

A simple RELAP model was developed to understand the thermal-hydraulic features of a single channel into the “average” AHTR hexagonal assembly.

The nodalization diagram of the model is shown in *Figure 7-3*.

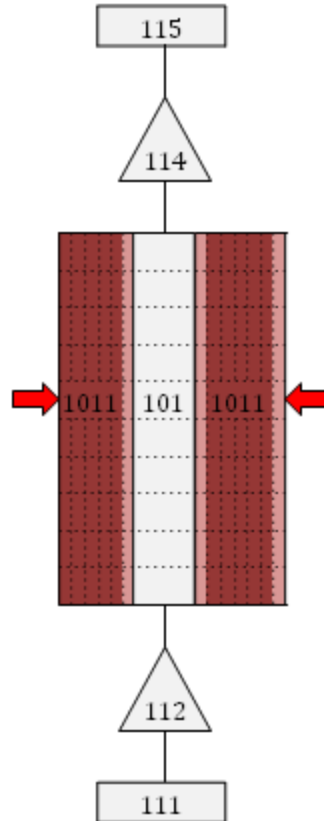


Figure 7-3. Single channel RELAP5-3D model

The hydraulic model is composed by a single coolant channel (pipe 101), in which the coolant is pumped into the channel by a time-dependent junction (tmdpjun 112) and the inlet flow temperature (650°C) is fixed by a time-dependent volume (tmdpvol 111) located before the junction.

The outlet flow, through a single junction (sngljun 114), is collected in a time-dependent volume, which is needed to keep the atmospheric pressure constant (1 atm) at the top of the pipe.

The heat structure 1011 is a single plate with both the left and right boundaries connected to the pipe through a convective boundary condition; the heat structure is composed by 13 transversal intervals: two outside small intervals to represent graphite sleeves, an inside wider interval for the graphite meat and 5 intervals (equally spaced) for each fuel stripe.

The power is distributed axially as a chopped cosine with a 7 m extrapolation length and transversely with a uniform profile, but only in the fueled region.

The RELAP5-3D model was compared to the MATLAB model previously developed and, as a first case, a constant power distribution, in both axial and radial direction, was selected.

The results from the two models are in good agreement, with reference to the following quantities: coolant temperature profile, heat flux profile, heat transfer coefficient profile, radial plate temperature profile, surface and centerline plate temperature profiles. The most relevant difference was found to be in the heat transfer coefficient (0.7%), which anyway is still a very small difference in terms of temperature distribution. The maximum temperature difference between the two models is 2°C, which is relatively small, and the comparison between the two models was considered successful.

A comparison has been made between the MATLAB and RELAP model results for a chopped cosine power profile, with a 7 m extrapolated length.

In this case the difference between the two models was more relevant since the power profiles implemented in the two codes was different: for the MATLAB model the profile was almost continuous, while for the RELAP model the step-shaped profile was more evident because of the much lower number of axial mesh points.

Since the difference in the maximum fuel temperature was small (about 5°C), the approximation introduced by the fact that the RELAP model has less mesh points was considered acceptable.

In order to assure the main part of the difference between the two models to come from the different power profile, the MATLAB model was adapted to the RELAP power profile and the results were satisfactory.

A RELAP model with 20 axial nodes, instead of 10, was implemented and the difference, in terms of maximum fuel temperature, was found to be about 3°C, 2°C smaller than the 10 nodes case; anyway in order to reduce the dimensions of the output file, the 10 nodes model was selected, even if the error is slightly higher.

The centerline temperature profile for the 20 nodes model is shown in *Figure 7-4*.

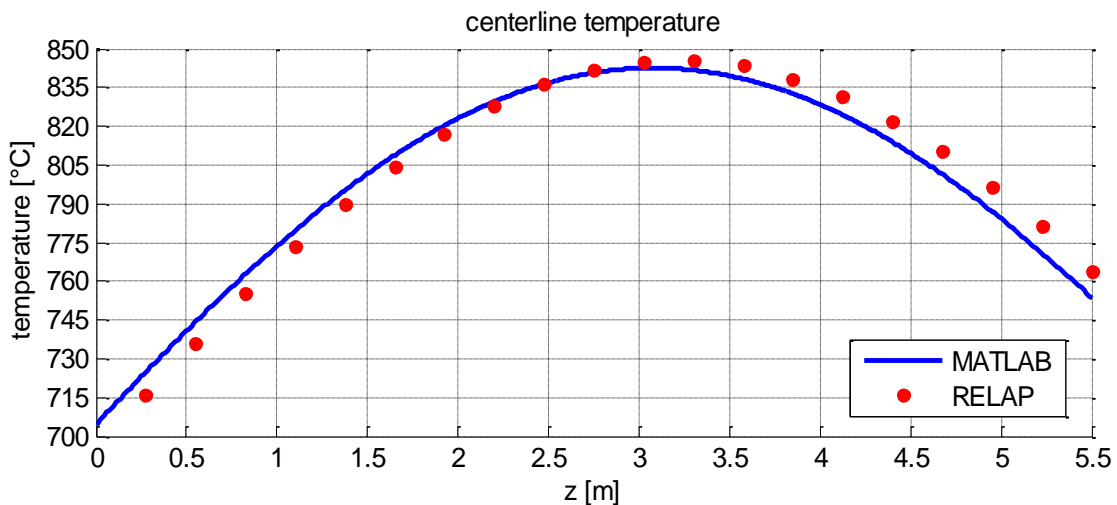


Figure 7-4. Centerline temperature profile for the 20 axial nodes model

Fuel and Core Design Options of LSCR

The RELAP single channel model was considered satisfactory and suitable for implementation in a full core model.

7.2 Assembly models

7.2.a 1/3 assembly RELAP5 model

A RELAP5-3D model of one third of the fuel assembly was developed, in order to get a more accurate temperature distribution description of the core.

The model is composed by seven intra-assembly channels, six fuel plates, three heat structures that represent the box wall, two inter-assembly channels, the upper and lower plenum, a pump and two tanks (inlet and outlet); the heat transfer by conduction between the fuel plates and the box walls is modeled through conduction enclosures, a RELAP5-3D feature that allows to model the heat conduction among the surfaces of the heat structures.

The nodalization diagram of the model is shown in *Figure 7-5*.

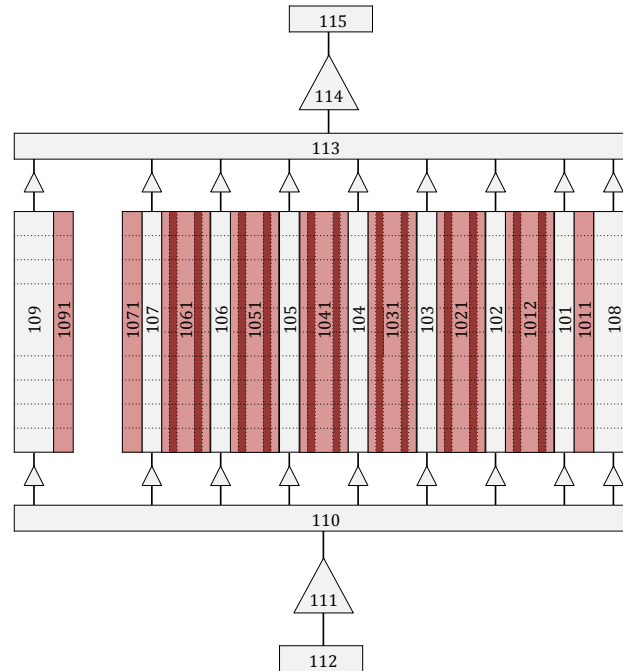


Figure 7-5. Nodalization diagram of the RELAP5-3D model of the AHTR fuel assembly

The model was evaluated for steady state conditions; the outlet temperature was found to be in good agreement with the values expected from the single channel model, but two of the intra-assembly channels had hotter outlet temperature, about 20°C higher than the average outlet temperature. This is due to the fact that even if the flow area is half the cross-section of the normal intra-assembly channels, the mass flow rate is about one third the mass flow rate of the intra-assembly channel, due to higher friction losses. The outlet temperature was found to be

about 20°C lower than the average outlet temperature, proving that the inter-assembly flow provides higher cooling on this configuration.

In order to improve the model for the heat conduction among the heat structures of the fuel plates and the box wall, the following modifications were applied:

- Homogenized fuel stripe and sleeve; this approximation allows to use higher gap conductances for the conduction enclosure model, enabling higher and more reasonable box wall temperatures;
- Higher conductance for the box wall material; this allows to obtain higher temperatures for the box wall.

The two models provide a better description in terms of temperature distributions, but were considered not satisfactory.

In order to improve the modeling of the heat conduction, a slightly different fuel plate concept was developed, for which the conduction enclosure happens between the box wall and the external surfaces of the graphite meat, instead of the plate sleeve; the connections of the enclosure model are shown in *Figure 7-6*.

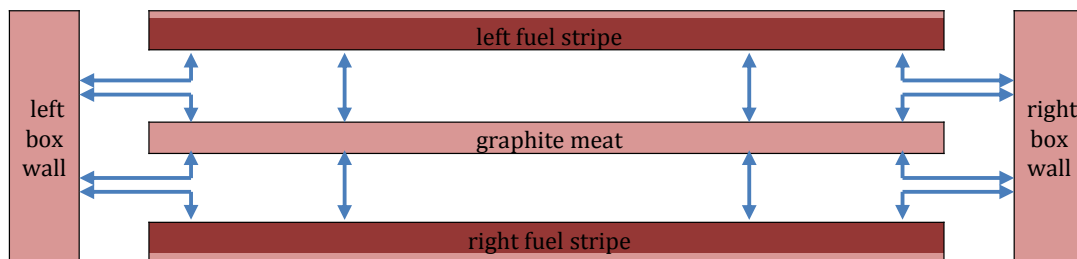


Figure 7-6. Conduction enclosure of the fuel plate (top view)

The results of the model were considered satisfactory, since the temperature distribution of the box wall was sufficiently high and the description of the other assembly elements was not modified with respect to the previous models.

Starting from this model, a final modification was introduced, considering a single outside channel: in this case the outlet temperature of the outside channel was an average of the two temperatures obtained from the previous model, but this allows to take into account the fact that the cross-flow tends to average the temperatures of the inter-assembly channels.

The overall results for the assembly model were considered satisfactory, but some simplifications are required in order to build a full core model.

Two simplifications were tested:

- Single fuel plate, single intra-assembly channel, single inter-assembly channel and single heat structure for the box wall. The results from this model were not satisfactory because of the strong approximation in the evaluation of the box wall temperature;
- Single fuel plate, single intra-assembly channel and single inter-assembly channel; this model was in good agreement with the full assembly model, so it was selected for a potential full core model.

Considering all the models developed, two general issues require further assessment:

- Modeling of the core pressure drops; the design of some details of the fuel assembly and the core is partially incomplete, so the pressure loss coefficients must be arbitrarily estimated;
- The heat conduction model is monodimensional and allows heat exchange only between external surfaces of heat structures;

Despite these issues, the models were considered accurate enough to be integrated in a core model.

7.2.b 3D thermal-hydraulic analysis of the assembly

Introduction

One approach being examined to address short fuel cycle in AHTR is on-power refueling. This requires detailed investigation of the full core thermal-hydraulic performance in that transient. This section presents the evaluation of the steady state 3D thermal-hydraulic behavior of the AHTR fuel assembly as the first step in that direction. Since the problem is relatively large from both thermal and hydraulic standpoints, some approximations will be assumed in the development of the model in order to allow a faster evaluation of the results.

Axial Heat Conduction

The fuel plate of the AHTR is a 3D conducting structure, but the heat conduction prevails in one direction. If the axial heat conduction is negligible, a much simpler treatment of the heat conduction is allowed, a lot less computationally demanding. We expect the axial conduction to be negligible, since the temperature gradient in the vertical direction is 1000 times smaller than the one in the horizontal one, but we want to obtain a numerical estimate of this effect.

The monodimensional approach has been compared to a 2D approach that accounts for axial conduction. The model represents a section of the fuel plate, with the z being the vertical direction (from the inlet to the outlet of the core) and x being the horizontal direction (from the centerline of the graphite meat to the surface in contact with the coolant).

The solution of the heat conduction is performed through a 2D finite volume approach, that in the case of the 1D approximation neglects the heat conduction in the z direction.

The problem is solved using a MATLAB code; the solution of the 1D linear system is obtained through the inversion function provided by MATLAB, while the solution for the 2D model is obtained through a Gauss-Seidel iterative procedure. This is due to the fact that the exact solution for the 2D model is hard to find, while an iterative procedure is a lot less computationally demanding.

As expected, the 2D solution is lower where the temperature is higher and higher where the temperature is lower, because of slightly enhanced heat conduction. Anyways we can see that the temperature difference at the maximum 0.003°C , which is a completely negligible difference, considering for example the uncertainties on k . Plus, using the 1D solution would mean being conservative.

With respect to the coolant temperature distribution, the results behave as expected: a little more power is delivered where the coolant is colder and a little less where the coolant is hotter, but the difference is absolutely negligible, of the order of 10^{-4} .

The 1D approach for the evaluation of the axial plate temperature distribution is very close to the 2D solution and it is conservative; it substantially reduces the computational requirements, which makes it suitable for many purposes.

2D and 3D channel approximation

The CFD and neutronics modeling of the AHTR core cannot be performed without making any simplifying assumption, because the domain is too large. Focusing on the CFD modeling of the assembly, one first assumption that one could make is the 2D treatment of the flow in the coolant channel. The coolant channels are of three types:

- Thick intra-assembly channel: 7 mm
- Thin intra-assembly channel: 3.5 mm
- Inter-assembly channel: 1.8 cm

The total width of these three channels is about 20 cm; the effects of treating these channels as a flow between two infinite parallel plates has been investigated, instead of considering their full 3D geometry.

The modeling approach is based on ANSYS Fluent. The main idea is that we want to compare the solution for a 2D and a 3D model. In order to do this, we first need to have a good 2D model that allows us to find the best mesh and the optimal length to capture all the involved aspects.

Starting from the geometric description of the problem, the 2D model is represented as a rectangle with a 7 mm base and 50 cm height. The 3D model is identical but with one dimension added (the thickness is 23 cm). We must note that the cross section of the real coolant channel is not a rectangle, but a parallelepiped: the short edges are inclined of 30°; anyways this should not make a relevant difference in our case, since we are mainly interested in capturing the effect of adding a 3rd dimension, but we don't need the perfect solution for the problem.

Regarding the meshing, the first aspect is the fact that these channels are very thin, so the grid spacing must be fine enough to capture the flow distribution. Also the flow is normally turbulent so the boundary layers must be able to accurately describe the steep velocity gradient. Just to have an idea, in order to have an accurate modeling of the problem, about 40 to 60 intervals are required in the y direction; a deeper analysis of the meshing is presented afterwards.

The X-Y cross section is the same for the two models (7mm*Ly), where Ly can be changed, depending on the length required for the flow to become fully developed. Just to give an idea, the fully-developed condition is reached after 30-40 cm in the 2D case, and after about 1.5 m in the 3D case.

The CFD simulations show that a 2D approximation of the channel is good in most practical cases and a full 3D model would only be required for the characterization of flow details.

Friction factor

The friction factor for the coolant channels of the AHTR has been evaluated using CFD tools.

The friction factor correlations are required in order to get an adequate distribution of the flow and the temperature in the AHTR fuel assembly.

The modeling approach is based on ANSYS Fluent.

The main geometric features of the model are the following:

- The 2D model is represented as a rectangle with a 7 mm base and 40 cm height.
- The meshing is 40 segments in the y direction, appositely biased (see previous reports for further details on this); the meshing in the x direction is 100 segments.
- The inlet velocity can be changed and the skin friction coefficient of the fully-developed region is calculated as a function of the velocity.

The overall behavior of the skin friction coefficient can then be expressed as:

$$f = \frac{24}{Re}, Re < 2000$$
$$f = 4.2721e - 7 * Re + 0.011146, 2000 < Re < 4000$$
$$f = 2.821096 * Re^{-0.710987} + 0.00510267, Re > 4000$$

Heat transfer coefficient

The heat transfer coefficient and the Nusselt number for the coolant channels of the AHTR are derived from CFD evaluations. The Nusselt number correlations are required in order to get an adequate distribution of the flow and the temperature in the AHTR fuel assembly.

The modeling approach is based on ANSYS Fluent.

The main geometric features of the model are the following:

- The 2D model is represented as a rectangle with a 7 mm base and variable height, in order to allow the flow to become fully thermally developed in both laminar and turbulent regions.
- The meshing is 40 segments in the y direction, appositely biased (see previous reports for further details on this); the meshing in the x direction is 100 segments.
- The inlet velocity can be changed and the Nusselt number of the fully-developed region is calculated as a function of the Reynolds number.

The overall behavior of the Nusselt number as a function of Reynolds can be summarized as follows:

$$Nu = 8.2353, Re < 2000$$
$$Nu = 0.0228 * Re - 37.265, 2000 < Re < 4000$$
$$Nu = 0.0378 * Re^{-0.8752}, Re > 4000$$

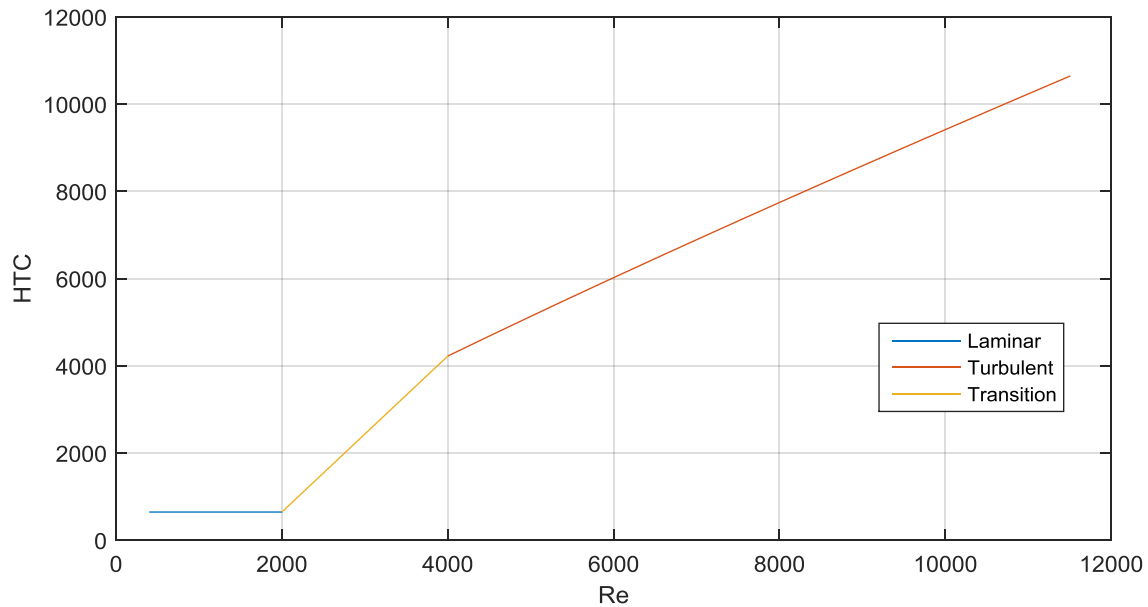


Figure 7-7. Heat transfer coefficient as a function of Reynolds

Methodology for 3D temperature distribution evaluation

The modeling is based on MATLAB and the code performs the operations explained in the following steps.

5. Definition of the mesh. A triangular mesh has been implemented, since the geometry of the assembly is exagonal. Equilateral triangles have been used (this simplifies the treatment of the equations), even if this choice requires particular attention in order to accurately represent the body.
6. Definition of matrices for the following quantities:
 - a. Direction of the triangle;
 - b. Distribution of materials;
 - c. Power density distribution;
 - d. Thermal conductivity of the materials;
7. Evaluation of the boundary connections for every triangle.
8. Evaluation of the flow velocity for the internal channels.
9. The last step consists in the iterative procedure that provides the axial distribution of temperatures:
 - a. The temperature of the coolant at the inlet of the channels is given (650°C);
 - b. The horizontal temperature distribution of the assembly is solved for that axial level;
 - c. The power delivered to each channel is obtained by integration on the boundary nodes for every channel;

- d. The temperature of the coolant at the next axial step is evaluated through an energy balance equation

The procedure from point a is repeated until the top of the assembly is reached.

Single plate temperature distribution

The single plate temperature distribution was first evaluated in order to verify the validity of the model. *Figure 7-8* shows the temperature distribution of the plate when the coolant temperature is 675°C on both sides and in the external channel. The heat transfer coefficient is set to 7500 W/(m²*K).

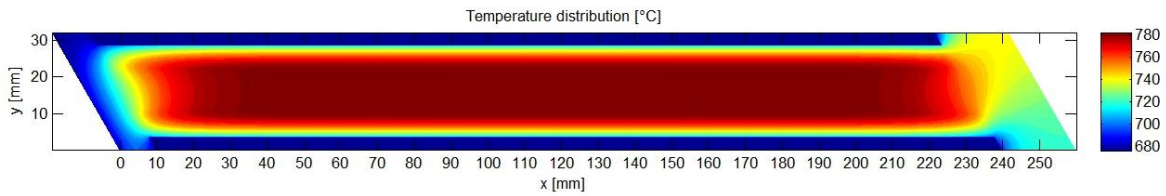


Figure 7-8. Temperature distribution of the single plate (1630x400 nodes)

The first aspect that can be noted in the figure is the fact that the temperature distribution in the central portion of the plate does not depend on the x position. For this reason, the maximum temperature of the plate can be evaluated through a very simple 1D approximation of the heat conduction:

$$T_{max} = T_c + q''' * \frac{t}{h} + \frac{q'''}{k} * \frac{t^2}{2} = 783^\circ C$$

Where t is the thickness of the fuel stripe. The numerical result is 783.5°C, in very good agreement with the analytical result.

The second aspect is the fact that the temperature distribution in the box wall and in the support shape cannot be considered representative of the full assembly, since the symmetry condition is not correctly represented in the single plate model. The area in which this error is mostly evident is the right portion of the plate, the upper part of the Y-shaped support (the temperature is in the yellow zone). Here, the heat should flow out of the right boundary, but this would be more a global feature of the assembly than of the plate. This aspect is not correctly represented here, but it will be addressed in the next section.

Full assembly temperature distribution

The temperature distribution of the fuel assembly has been evaluated. *Figure 7-9* shows the temperature distribution in different configurations. The maximum fuel temperature is about 847°C and its location is slightly above the mid-plane (z=3.25 m). As mentioned before, the lower

and upper plates are hotter (about 20°C) than the others, due to the low cooling capacity of the two thinner channels. On the XY plane, the maximum is located in the upper plate, between the graphite meat and the fuel stripe in contact with the upper channel.

With respect to the temperature distribution of the coolant channels, the external channel has a profile very similar to the one of the internal channels, so 0.5% bypass flow is an acceptable fraction. The smaller channels, the lower and the upper, are 20°C hotter than the average.

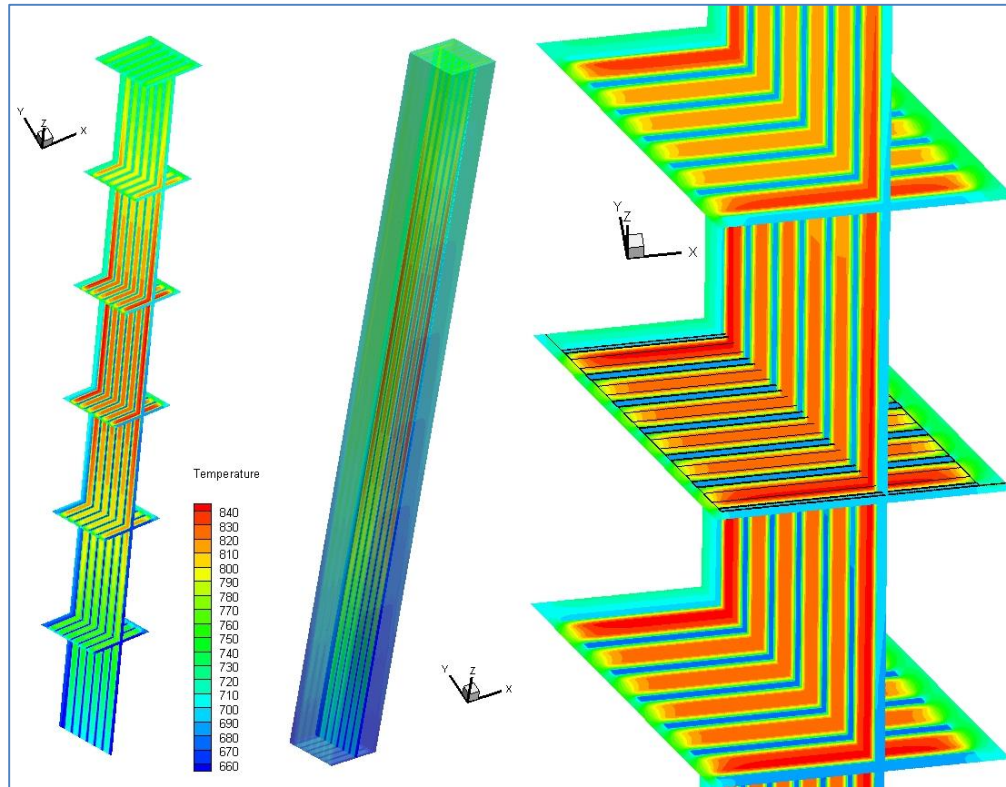


Figure 7-9. 3D Temperature distribution results

Evaluation of the effect of the thinner channels

The same analysis has been performed, increasing the size of the smaller channels by 33% (from 3.5 mm to about 4.5 mm). In these conditions the temperature distribution is more uniform and the maximum temperature is 20°C lower. The lower and upper plate have about the same temperature distribution as the others. We can also note that the new channels configuration brings lower temperature of the two thin channels; the outlet temperature is pretty uniform for the internal channels, and also the power delivered to the external channel is lower.

Considerations on assembly modeling

The main results of this simulation lead to the fact that the internal small channels are about 20°C hotter than the other channels, and this results in a higher temperature of the lower and higher fuel plates. This is a purely thermal effect which can be furtherly increased by the fact that the neutron flux distribution (and so the power density) is not uniform in the fuel plates. In order to solve this issue a different geometrical design of the internal channels might be considered.

The amount of external flow does not have a strong influence on the global behavior of the system but it is still important for determining the temperature of the box wall and the support structure. One interesting aspect that comes out of this analysis is the fact that with no external flow the temperature distribution of the structure is more uniform and this might be good from the mechanical standpoint. The option of not having any bypass flow might than be considered. The approach we have developed in this project is simple and fast, but can still provide a full 3D description of the system at a very low computational cost.

This assembly model will serve as a basis for the evaluation of the behavior of the AHTR full core thermal hydraulics.

7.3 Reactor model

A general AHTR reactor model has been created in RELAP5, allowing the simulation of the steady state conditions, as well as the LOFC accident scenario and the refueling transient.

7.3.a AHTR reactor RELAP5 model

A simplified reactor system was modeled in order to account for all the factors that affect the transient behavior; in particular, the model includes the following components:

- Reactor core, core channels, permanent and removable radial reflector and lower and upper support plates;
- Lower and upper plenum;
- Barrel;
- Downcomer channels;
- Reactor vessel;
- Intermediate loop (1/3);
- DRACS loop and air circuit (1/3);

The reactor core was modeled as a 10-rings cylinder and each cylinder was modeled as a single fuel assembly; the heat exchange area of the heat structures and the cross-section of the channels were increased by a specific multiplicative factor in order to account for the fact that each modeled assembly represents more than one real assembly.

Heat structures have been used to model the radial reflector, the barrel and the reactor vessel. The radial reflector is composed of two heat structures, the innermost representing the replaceable reflector and the outermost representing the permanent reflector.

The results from the simulations show that the outlet temperature of the core is not uniform; it spans from 685°C for the outermost channel to 735°C for the central channel. While the outlet temperature depends on the radial position, the temperature profile is not affected by the distance from the centerline of the core.

Although the outlet temperature is not uniform, it spans over a relatively small range ($\sim 50^{\circ}\text{C}$) of temperatures, which means that a redistribution of the mass flow rate might not be required. The flow velocity and the mass flow rate have an almost constant profile, which slightly increases from the outermost to the central ring, where the coolant is hotter and the buoyancy effects are stronger. In relation to the results obtained from single-assembly or single-channel model studies, the average value for the flow velocity obtained from the reactor model is lower (~ 1.8 m/s, while for the single-channel model it was ~ 1.96 m/s), because a certain fraction of the total reactor mass flow rate does not pass through the core, but forms a by-pass flow through the DRACS downcomer channels.

The maximum fuel temperature, in the radial direction goes from $\sim 770^{\circ}\text{C}$ for the outermost ring, to $\sim 940^{\circ}\text{C}$ for the central ring (the maximum fuel temperature for the average assembly was found to be $\sim 843^{\circ}\text{C}$). The location of the axial maximum fuel temperature is not strongly affected by the radial coordinate and it is slightly above the middle of the core.

7.4 Mechanical and thermal evaluations on the fuel assembly

7.4.a Evaluation of lift force on the assembly

General approach

The force exerted on the fuel element due to buoyancy and coolant flow has been evaluated. A significant issue with Liquid Salt Cooled Reactors is the fact that the density of nuclear-grade graphite is lower than the density of the coolant (FLiBe) at operating conditions, with the following consequences:

- In order to prevent fuel flotation during loading into the core (offline refueling), the fuel element must be designed so that its average mass density is fairly higher than the average density of the coolant. For the same reason, a hold-down (upper) plate is required during normal operation.
- If the online refueling option is considered, the weight of the fuel element must balance not only the static buoyant force (if it is present), but also the drag force due to the fluid flow.

A standard 1D approach is used for this evaluation.

Methods and calculations

The typical design parameters for the AHTR are used in the calculation. The total power (nominal: 3400 MW_{th}) can be changed, resulting in an equivalent coolant mass flow rate change through the core (assuming the total temperature rise is constant, 50°C). This allows the evaluation of the force for different power levels.

The geometric parameters for the core and the fuel assembly are the same used in previous works; the following approximation is used, in order to simplify the calculation: the power along the height of the core is distributed over 6 m (total core height), neglecting the presence of two 25 cm-long portions of fuel plate that do not produce power at the inlet and outlet of the core.

Initially, some general features of the flow are evaluated from the design parameters, such as the velocity of the flow into the assembly, viscosity, density, Reynold's number and friction factor as a function of the elevation within the core. The results are similar to those obtained in previous works, so they are not presented here; in particular, the mass density and the friction factor are required for the evaluation of the force.

The total force acting on the fuel assembly is given by the following contributions:

$$F = F_w - F_b - F_d$$

Where F_w , F_b , F_d are absolute values and the positive direction for F is downward, meaning that if F is negative, the fuel assembly will accelerate upward, if F is positive, the fuel assembly will move downward, or it will be stable if it is laying on the lower support plate.

Results and considerations

The first evaluation can be performed in nominal operating conditions. In this case the total resulting force is -9194 N, meaning that the fuel assembly, in absence of constraints, would move upward with an acceleration of about 6 m/s². This is why the upper plate is required during normal operating conditions.

Another evaluation that can be performed is the power level, and the equivalent mass flow rate, that is required to make the force equal to 0. In order to do this the power level was multiplied by a reduction factor and this factor was adjusted until the lift on the assembly is about 0. This results in a reactor power equal to 23.5% of the nominal value. This means that the mass flow rate in the core must be reduced by 76.5% to avoid the flotation of the assembly when the upper hold-down plate is removed. In order to avoid potential instability during online refueling, the mass flow rate probably needs to be reduced even more.

Full online refueling cannot be applied; the power requires to be lowered to avoid the flotation of the elements; the maximum power level allowed for low-power online refueling is about 20% of the nominal power. An increase of the average mass density of the assembly may help to increase this power level. The alternative option is that a hold-down mechanism is used during refueling. In this case full online refueling can be considered a viable option.

Options for improving the online refueling procedure

In order to enhance feasibility of the online refueling, several design changes may be considered.

Control rod design

In order to increase the weight of the assembly, even if not adding more absorber, it might be possible to change the dimensions of the control rod inserted into the Y-shaped support.

The control rod length is already equal to the length of the fuel assembly, so we could change the shape of the cross section, meaning the thickness of the rod or the extension of the three branches into the Y-shaped support, as shown in *Figure 7-10*.

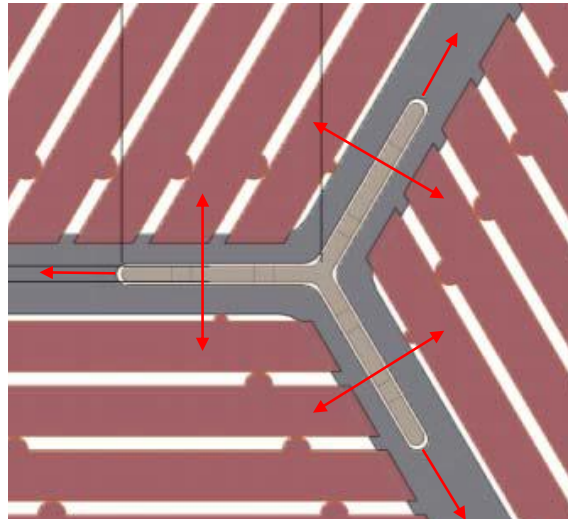


Figure 7-10. Possible control rod design changes.

This would make the assembly heavier and more controllable; the only constraint is the fact that a large control rod might compromise the structural integrity of the support shape and the element.

The weight of the control rod is about 150 kg, and the rest of the assembly is about 1400 kg. The equivalent weight that would be required to hold down the assembly in normal operating conditions for the design parameters is about 1000 kg, so a slight change in the design of the control rod would not substantially affect the stability of the assembly. It may help, if combined with other modifications.

Coolant gap thickness.

In the on-line refueling approach, HM loading is not as limiting as in batch reload, so we don't have to put as much fuel as possible; we may be able to use higher cross sectional fraction for coolant flow, reducing lift, and at the same time improving moderation and fuel utilization. The following plot in Figure 7-11 shows the downward force as a function of the plate thickness.

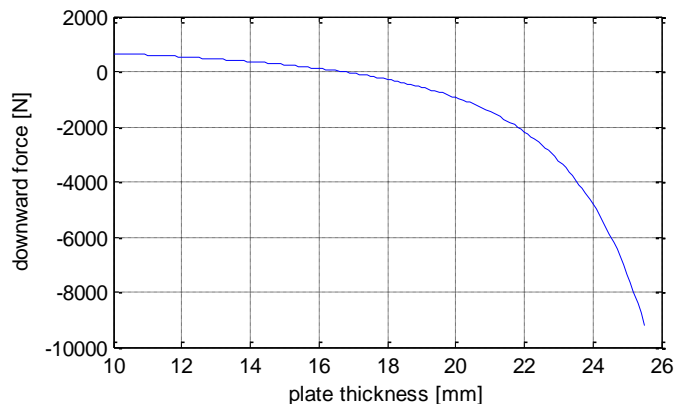


Figure 7-11. Downward force as a function of the plate thickness.

The nominal value is 25.5 mm, corresponding to about 9000 N upward (negative). These values have been obtained assuming that the plate thickness can be changed, and the coolant gap thickness adapted consequently, keeping constant overall dimension of the assembly. The dimension of the fuel stripe is not relevant in this calculation since the density has been assumed to be similar to the density of graphite. However, probably a reduction of the fuel stripe thickness would be required for a reduced plate dimension in order to keep adequate moderation capability.

The plot shows that the upward drag force drops rapidly for thicknesses close to the nominal value (67% reduction for 2.5 mm variation) and then the slope becomes smaller. The equilibrium point, where the total force on the assembly at full power conditions is reached for plate thickness equal to about 16 mm, about 10 mm less than the nominal value. The nominal value for the coolant gap is 7 mm, which would become 17 mm if the dimension of the plate is reduced to the equilibrium point.

Use of Beryllium oxide.

Beryllium oxide can be added to the fuel element structure; it would increase the weight of the assembly and it might help from the neutronics standpoint. Some questions remain to be resolved, such as how the beryllium oxide would affect the integrity of the graphite matrix, or how much would be its contribution to the total weight of the assembly.

Temperature rise in the core.

It may be interesting, regarding the online refueling design, to consider a temperature increase in the core higher than the nominal value, which is 50 K.

This limit is mainly due to materials, but the effective margin in this case must be evaluated. The original temperature levels for the high temperature reactor were higher, approaching 1000°C, but the values used for the AHTR are lower, because we want to be able to reach these temperatures without having to develop a completely new alloy.

7.4.b Heat loss to bypass flow

The full assembly model described in the previous sections has been used to find the 3D temperature distribution in the assembly and the axial temperature distribution of the coolant channels.

Figure 7-12 represents the temperature distribution of the fuel assembly at the top (outlet of the core) when the external mass flow rate is about 3% of the total. In this case the outlet temperature of the external channel is 680°C, lower than the average core outlet temperature $T_{out}=700^{\circ}\text{C}$.

We can note that the lower and upper plates are substantially hotter, about 50°C, than the other plates; this is due to the fact that the two thin internal channels are not capable of removing enough power since the flow velocity is too low. The other 4 plates have a pretty similar temperature distribution. We can also note that the box wall is cooler than the average temperature of the support shape.

The amount of external flow can be changed in order to obtain different temperature distributions. If the fraction of external flow is about 1.35% the outlet temperature of the external flow is 700°C, equal to T_{out} . If there is no external flow at all the temperature of the wall is of course much higher, but it is uniform with respect to the average temperature of the support structure, which is about 750°C.

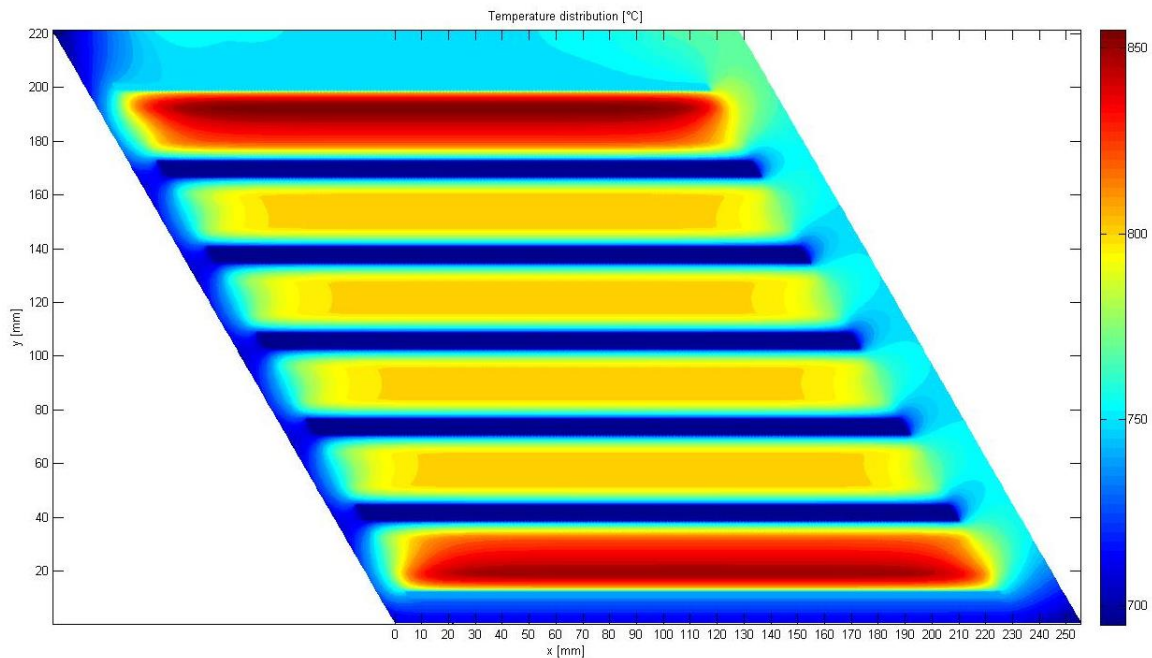


Figure 7-12. Temperature distribution at the top of the plate for 3% external flow

7.5 Computational Fluid Dynamics evaluations

7.5.a 2D CFD modeling

A general evaluation of the approaches for the CFD modeling of the upper and lower plenums of the AHTR has been performed, using a simplified 2D approach.

It was not always possible to obtain a fully converged steady state solution for any type of flow. Several reasons can cause this to happen and this report aims to address at least partially this aspect.

One reason could be the fact that the solution, particularly for the laminar case, is not steady, due to some vortex exchange at the outlet of the core, between nearby channels. One other reason could be that the models used for the solution of this particular problem are not adequate; for example one type of solver could be more suitable than others.

Another aspect that this report aims to furtherly develop is the type of model that will be used for the flow. For the turbulent case, all the models have been developed for the steady state case, but the fuel element removal is a transient, so these models might not be accurate enough. The first thing to be said is the fact that the transient would be relatively slow in time, so a quasi-static approach might be viable, and the turbulent models might be acceptable for this purpose. Also, it would be good to compare the results to experimental or previously reported data, in order to get a preliminary validation of the models. This would be helpful from the standpoint of the transient evaluation with turbulent models and the choice of the turbulent model for the steady state case. Regarding this last point, since the flow is only slightly turbulent and there are solid walls, the $k\omega$ model might be the best choice, but also the $k\epsilon$ model should provide comparable results.

The following sections present the evaluation of some of these aspects for the upper plenum first, and then for the lower plenum. The solution of the flow in the lower plenum, in general, seems to be easier than the upper plenum, since the flow from the assembly outlets to the upper plenum produces substantial vorticity, which is more complicate to resolve.

Upper plenum modeling

The modeling of the upper plenum has been analyzed by looking at the single coolant channel, at a pseudo fuel assembly and at a group of three pseudo fuel assemblies. Several methods have been considered in order to find the one that best represents the results from the literature.

A model with three assemblies has finally been evaluated.

The turbulent solution has also been evaluated. The realizable $k\epsilon$ model presents the best convergence; this solution is presented in *Figure 7-13*. It is hard to converge the others to a steady solution.

This model might underestimate the dimension of the vortices.

The $k-\epsilon-\omega$ transition model was tested successfully with a coarser mesh, showing a good convergence behavior.

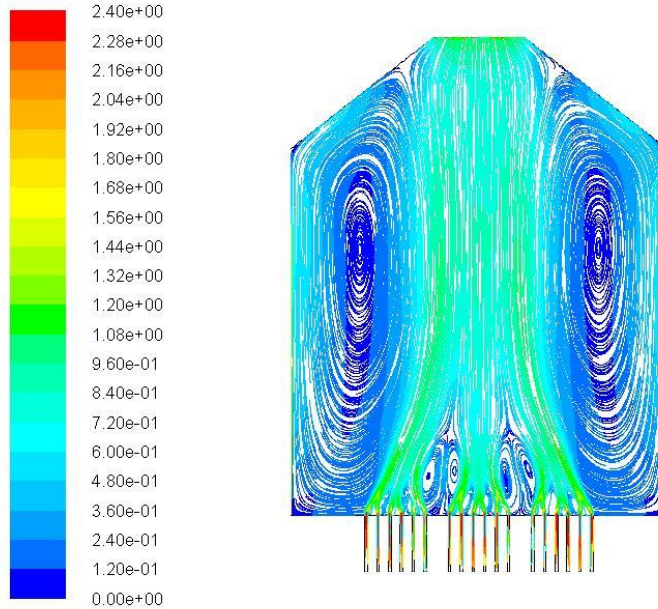


Figure 7-13. Turbulent solution, $Re=9100$ (pathlines colored by velocity magnitude)

Lower plenum modeling

The models used for the analysis of the lower plenum zone are a single coolant channel and an array of six coolant channels representing a simplification of a 2D fuel assembly.

For the turbulent case, the inlet velocity is 0.35 m/s, corresponding to 2.07 m/s average in the channel, Reynolds equal to 9419. The turbulence model is $k\omega$ SST.

The solution converges smoothly to 10^{-3} in 70 iterations with PISO method.

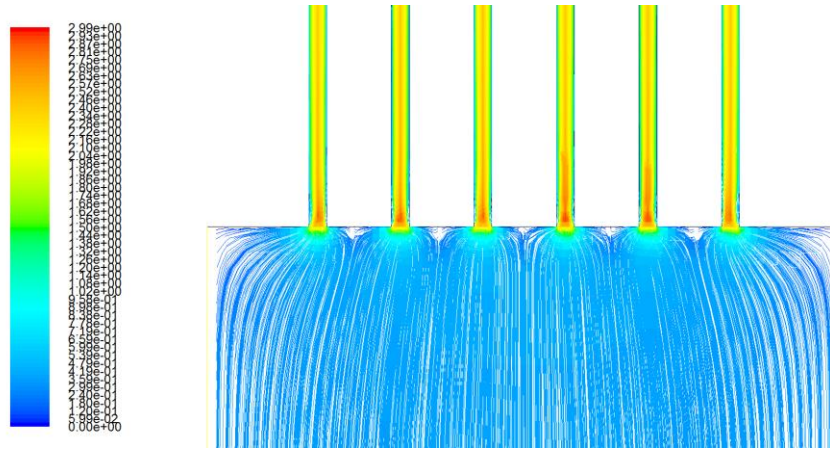


Figure 7-14. Assembly inlet, turbulent solution

Moving to the $k\omega$ model, with the PISO method, it converges in 72 iterations. It converges in 62 iterations with the coupled solver. However, if the residuals are decreased, it does not converge anymore and the residuals reach a steady value, similarly to what was happening for the single channel case. In this case, though, the difference between the $k\epsilon$ and $k\omega$ is substantially smaller.

Concluding remarks

The following considerations summarize the outcomes of this analysis:

- The small problems, such as the sudden expansion or the backward step, are simpler to analyze and converge, for both laminar and turbulent case. The $k\omega$ and $k\omega$ SST turbulence models provide the best solutions in these cases.
- The larger problems are more difficult to converge and the $k\epsilon$ models seem to converge better than $k\omega$ models. The reason might be the fact that $k\omega$ is better for bounded flow with walls, $k\epsilon$ is better for free flow, such as the one that develops in the plenum where the jets are located (outlet of the channels). Realizable $k\epsilon$ in this case seems to provide the best solution.
- The laminar versions of the problems tend to be unstable even for very low Reynolds, due to vortex exchange between jets at the outlet of the channels. Apart from this, the laminar solutions found through this analysis seem relatively accurate.
- The jets at the outlet of the channels tend to couple together in the turbulent case; different solutions are then possible, depending on the coupling sets.
- For the lower plenum modeling, the $k\omega$ SST model can be used for initial evaluations. For the upper plenum the realizable $k\epsilon$ model might be easier to converge for initial evaluations.

7.5.b 3D CFD modeling

The flow in a section of the lower plenum has been simulated. The modeling of the flow in the lower plenum is a relatively large problem so the analysis is first performed on a small portion of the lower plenum, corresponding to the volume that is located before the inlet of each specific assembly.

Geometry

The geometry of the assembly inlet had been modified in order to simplify the problem. The real assembly inlet is more complicated, it is formed by 21 thin channels, that would require a relatively large mesh to simulate, and they would require some attention in order to obtain convergence of the simulation.

Mesh

The mesh has the following features:

- Outlet vent boundary condition for the outlet;
- The minimum, maximum mesh size and growth rate are 1 cm, 5 cm and 1.15;
- Only one size function has been used, for the hexagonal edges at the lower plate; hard size function with maximum size 5 cm and growth rate 1.15;
- Tetrahedral meshing for conversion to polyhedral mesh;
- Prisms: 2 layers; aspect ratio equal to 5 for the outlet and curved wall, aspect ratio equal to 1.15 for the other two surfaces, in order to obtain specific values of y^+ and use the wall function;

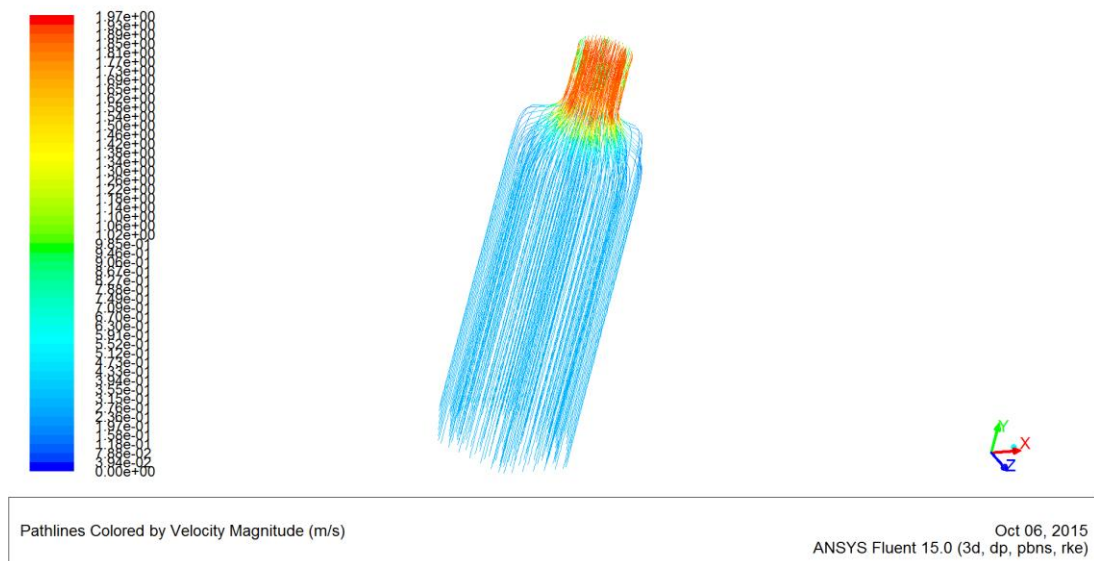


Figure 7-15. Streamlines

The 3D CFD simulation of the lower plenum portion of the reactor requires a large mesh and can be very intensive from the computational standpoint.

7.5.c General CFD flow evaluations

The flow distribution for the AHTR's core has been studied on several levels in order to characterize the steady state conditions of the flow, as well as to provide a modeling approach for more advanced studies, such as the online refueling. This work extends beyond the scope of the current project. It is still in progress and it will be completed in future work, but it has already provided sufficient information to indicated feasibility of on-line refueling from the T/H standpoint. The general modeling approach and the initial results for some specific problems are illustrated here.

The flow at the channel level has been performed in previous work and described in other quarterly reports. The scope of this analysis is on the flow distribution in the lower plenum (inlet of assemblies) and upper plenum (outlet of assemblies).

Several types of studies are being performed for each one of them. For the lower plenum:

- Flow at the inlet of a single channel;
- Flow at the inlet of the assembly;
- Flow in the lower plenum;
- Analysis of the outlet-vent boundary condition.

For the upper plenum:

- 2D analysis of the flow of 7 parallel channels;
- 3D flow analysis at the outlet of the assembly.

Assembly-level evaluations in the lower plenum

The numerical simulation of the flow in the volume of the lower plenum that constitutes the inlet of a single assembly has been performed. The flow distribution obtained from this simulation is not expected to be the same as the one that would happen in the lower plenum, because in the full lower plenum the flow coming from the downcomer is deflected by the bottom of the vessel, so the flow direction is not purely vertical. However, many modeling aspects are similar, so this problem is considered relevant with respect to the modeling of the lower plenum.

A second aspect that has to be considered is the fact that the modeling of each single inlet of the channels might require a very large mesh, so the adoption of simplifications might help in this evaluation.

The following pictures (*Figure 7-16*) show the reference geometry of the channel inlets compared to potential simplifications of the model.

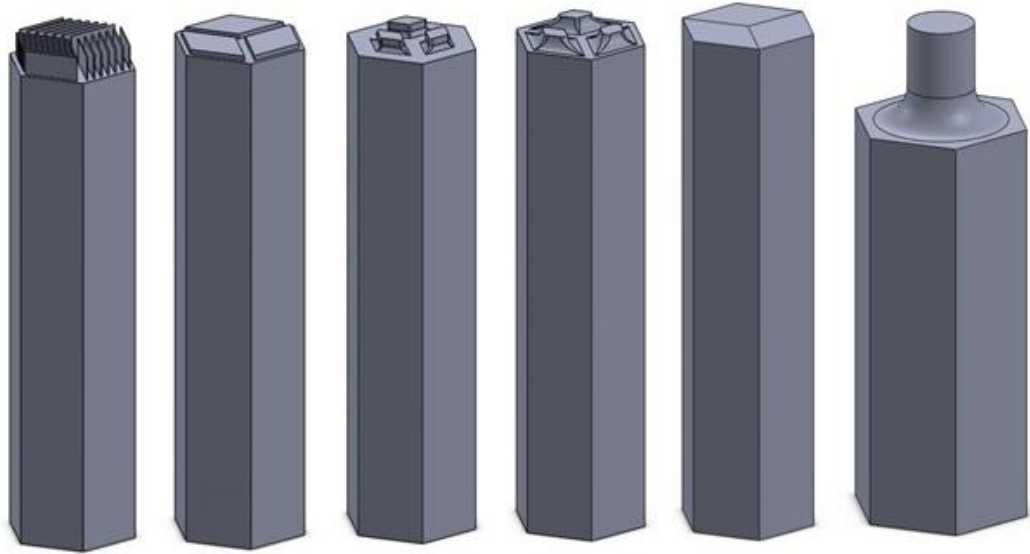


Figure 7-16. Solidworks models of the assembly inlet

The modeling of the flow in the lower plenum is a relatively large problem so the analysis is first performed on a small portion of the lower plenum, corresponding to the volume that is located before the inlet of each specific assembly.

Analysis of flow in the upper plenum

The analysis of the flow in the upper plenum has been started. Initially the flow at the assembly and channel level is being performed.

2D model of 7 channels.

This model represents the flow at the outlet of one third of assembly, in the upper volume, which collects the flow from 7 internal channels (5 thick and 2 thin, 7mm and 3.5mm).

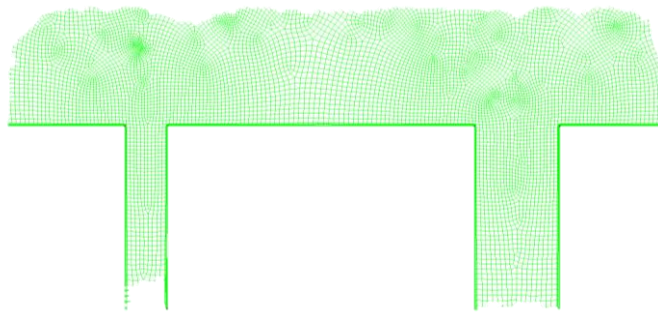


Figure 7-17. Mesh at the outlet of the channels (2D model)

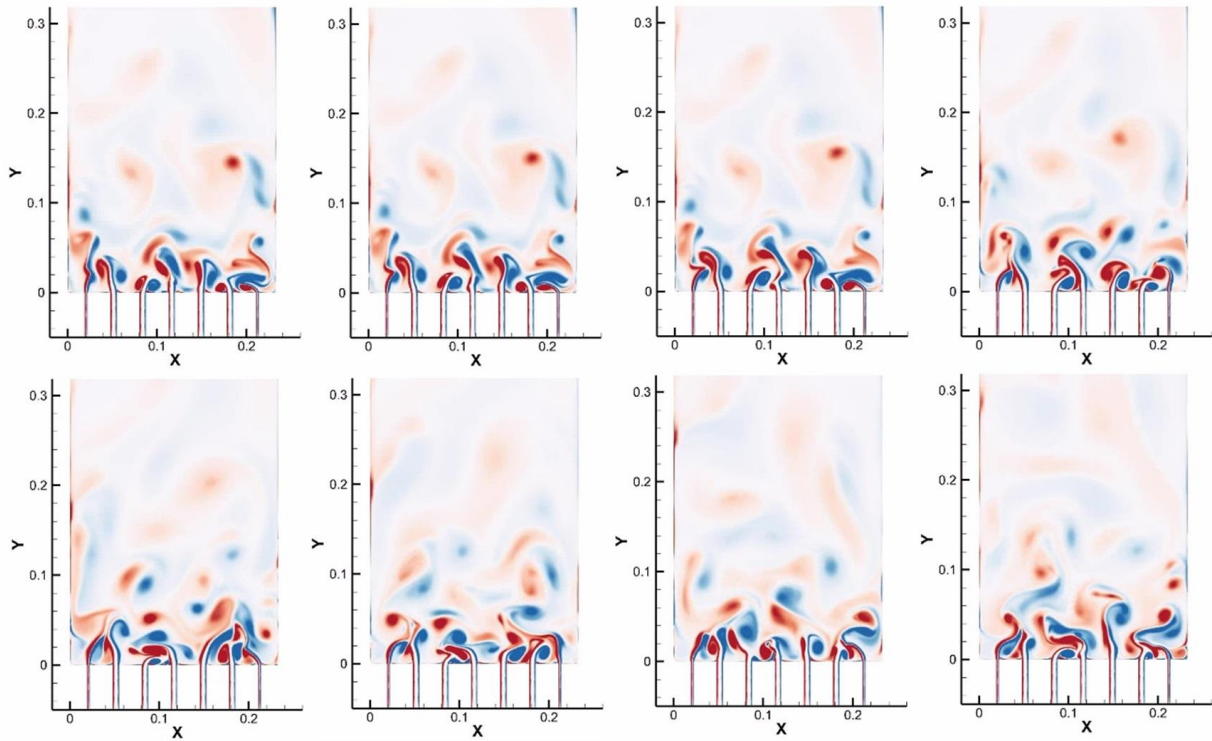


Figure 7-18. Geometry of the model and preliminary results (Scale Adaptive Simulation) for the normal vorticity at random instants of time

Preliminary results (Figure 7-18) show some level of interaction between vortices at the outlets of parallel channels.

Assembly outlet

Preliminary 3D analysis of the flow at the outlet of the assemblies has been set up. Figure 7-19 shows the geometry model used for the analysis. Since the mesh requirements for this analysis are relatively large only preliminary analysis has been performed and meaningful results are still under evaluation.

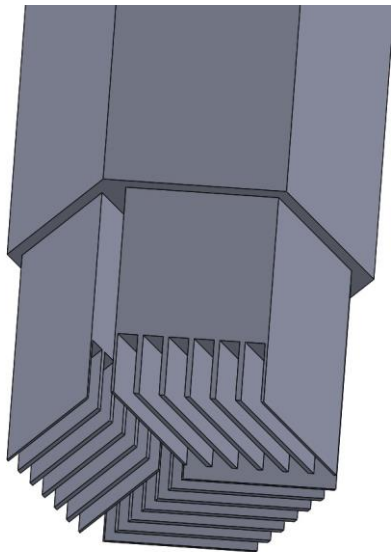


Figure 7-19. Geometric configuration for simulation of assembly outlet

While this work extends beyond the scope of the current project and is still in progress, its results so far indicate feasibility of on-line refueling from the T/H standpoint.

7.6 Neutronics in support of thermal-hydraulic modeling

7.6.a Scale core model, reactivity feedback, power profiles

A SCALE model of the fuel assembly was developed in order to calculate the power distributions and the reactivity feedback coefficients, needed as an input for the RELAP5-3D core model.

Two main fuel assembly designs have been proposed and studied by ORNL:

- The 2011 design has 19.75% enriched fuel and 32.91 MT of heavy metal loaded into the core; this results in a ~6 mm thick fuel stripe;
- The 2012 design has 9% enriched fuel and 17.48 MT of heavy metal loading into the fuel core; the fuel stripe is thinner, about 2.5 mm.

Both of the two configurations have been evaluated in this work.

Multigroup model

The evaluation of the reactivity was performed through the 3D Monte Carlo transport code implemented in SCALE (KENOIV).

The evaluation of the nuclear cross sections is required in order to calculate the reactivity of the fuel assembly and two options are available for the KENO model, the continuous energy library (ce_v7) and the multigroup library (v7-238).

Since no approximations for the cross-section evaluation are performed in the continuous energy mode, this would be the easiest solution, but the ce_v7 library gives cross-section functions only for some given temperature values (typically 600K, 900K and 1200K) and SCALE does not allow cross section interpolation in the continuous energy mode.

So the multigroup mode must be selected and the Dancoff factor for the TRISO particles must be optimized through a comparison with the continuous energy model calculation.

The following procedure was used to estimate the Dancoff factor:

- A certain temperature distribution was selected, so that the cross sections were available both for the continuous energy and multigroup model;
- The continuous energy model was run; the multigroup model was also run with different values for the Dancoff factor;
- The k resulting from the continuous energy model was interpolated into the fit of the multigroup results and the Dancoff factor was determined.

The results for the 2011 and 2012 core design are shown in the next plots; the multigroup results are interpolated through a quadratic fit.

The Dancoff factor obtained from the interpolation was used for the calculation of the reactivity feedback and the power distributions; for the 2011 case the obtained Dancoff factor is 0.90156, while for the 2012 thinner fuel stripe, the Dancoff factor is 0.88179.

Reactivity feedback

Two contributions to the reactivity feedback have been evaluated in this work: the temperature of the fuel and the temperature of the coolant; a variation of the coolant temperature results also in a variation of the coolant density, so even the coolant density variation is accounted for in this modeling.

The evaluation of the reactivity feedback is performed through the following steps:

- Selection of the range of fuel and coolant temperature variation;
- Calculation of the k for each possible set;
- Calculation of the reactivity for each point as $(k-1)/k$;

Calculation of the reactivity coefficient as the slope of the interpolating line.

It is clear that the k -infinity, and so the reactivity, depends mainly on the fuel temperature, while coolant temperature and density play a smaller role. We could expect this, since the amount of coolant, in terms of volumetric fraction, into the core, is small, of the order of 10%.

The reactivity insertion due to increasing coolant temperature is small but positive, so this could lead to safety issues, in case the reactivity insertion due to partial or total core voiding would make the system prompt critical. Anyway, since the coolant temperature coefficient is small and the fuel temperature coefficient is large, we expect this aspect not to be a problem.

We can see that for the beginning-of-life fuel configuration the coolant temperature reactivity feedback is negative with an average value of $-4 \text{ pcm}/^\circ\text{C}$ and tends to become smaller (absolute value) when the fuel temperature increases.

Considering the coolant temperature reactivity feedback, the average value is positive, about $+0.5 \text{ pcm}/^\circ\text{C}$, and the temperature dependence is not clear. The coefficient is positive but it is relatively smaller than the fuel temperature coefficient.

Power profiles for RELAP5 simulations

The SCALE model was used to evaluate the axial power density distribution and the transversal power profile; the volumes of the geometries were added to the input file in order to calculate the fission densities, which are proportional to the power density distribution.

The power profiles have been evaluated in the axial and transversal directions, resulting in 1.3 and 1.005 peaking factor respectively.

7.6.b Neutronics modeling for online refueling

A KENO model of the AHTR is used to model the neutronics of the core during the refueling transient. Several SCALE models have been developed in the past years for the modeling of the neutronics and the fuel cycle analyses on the AHTR core. These models can be easily modified and adapted for the study of the refueling transient.

Structure of the KENOVI input file

The KENO input file is based on a model previously developed by Lewis, for the evaluation of LSCR fueling options. Note that in this model a homogenization of the outer shells of the TRISO particle with the graphite matrix is performed, in order to reduce the computational time by a factor 2 without compromising the accuracy of the results. The following figure shows a cross section of the core with no material composition dependence on the radial location of the assemblies.

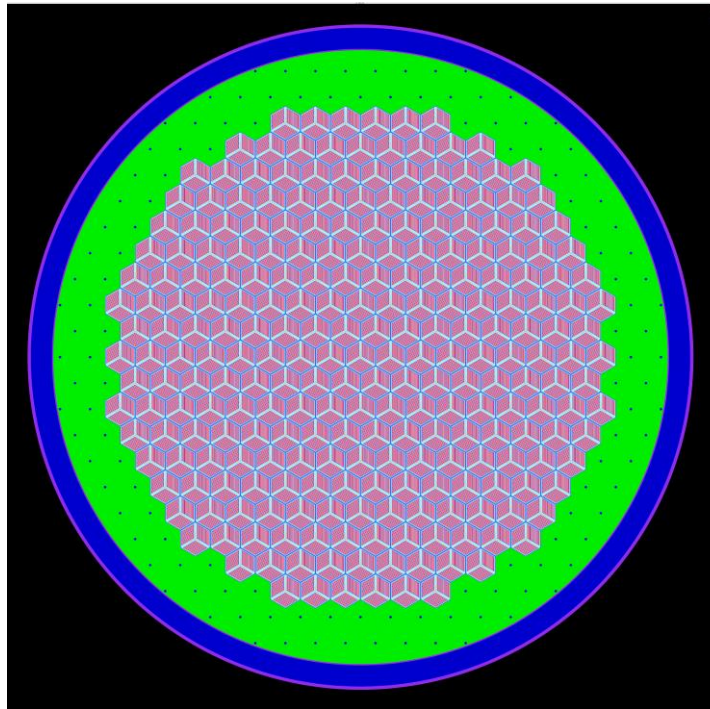


Figure 7-20. Horizontal cross section of the core

7.6.c Input File Creation

A MATLAB script has been developed that writes the input file for the KENO simulation.

The script accepts the following inputs:

- General parameters: file name, check parameter (if 1, the check option in scale is activated), arrays parameter (if 0, the TRISO array is replaced with a homogenized layer of fuel material) and mesh parameter (if 1, the mesh is written in the input file);
- Material configuration. This is a matrix that has as many lines as the number of materials that will be written to the input file. Each material represents a possible assembly material configuration. The parameters that must be defined per each material are the

temperatures of the fuel, cladding and flibe. Other parameters will be incorporated in the future, especially the enrichment of the fuel.

- Definition of groups of elements. Each possible assembly location in the core is identified by a number (3 digits, the first one is the ring, from 0 to 10, the second and third digits represent the location in the ring, clockwise). Each location is filled with a unit type, represented by a unit ID. Each unit is defined later. With this step, we can define how the units are displaced in the core.
- Definition of the unit types. This is a matrix; each line represents a unit, ordered by ID number. For each unit the following parameters are set: the elevation (in cm), the number of axial intervals and the presence of the control rod in each interval of the assembly.
- Definition of the unit properties. This is a cell array; each cell represents a unit, ordered by ID. For each cell two arrays are defined, that define the length and the material of each axial interval in that specific assembly.

With these parameters, the MATLAB script can write the scale input file in the following order: material compositions for the assemblies; material composition of the reflector, the plenums and the barrel; cell data; parameters; geometry for each assembly, for each axial level; geometry for global unit (vessel, core, plenums); array of assemblies; array of TRISOs in each assembly; plots; boundary conditions (vacuum); grid.

This procedure allows saving time in adapting the model to the specific needs.

Control rod insertion

Figure 7-21 shows the location of the assembly in which the control rod is inserted.

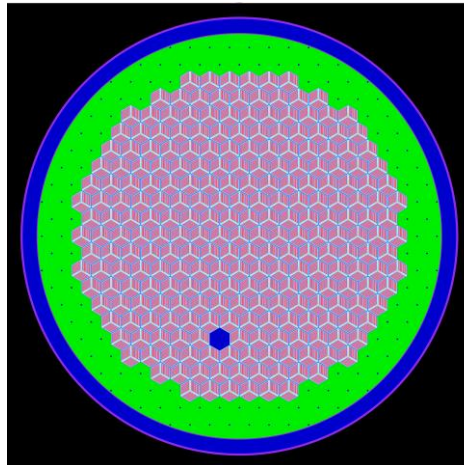


Figure 7-21. Location of the assembly in which the rod is inserted

Three simulations are run (100 generations, half skipped, 100000 particles per generation); the control rod is completely extracted, 50% inserted and completely inserted in the three cases respectively. The uncertainty is still relatively large if compared to the reactivity variation due to the insertion, so we might want to reduce it. Anyways, we can still get an impression of the dependence of the reactivity of the core when the control rod is inserted; in particular, we can say that this control rod is worth about 100 pcm.

Assembly extraction

Similarly to the control rod case, three simulations are run (same general parameters) where the assembly is completely inserted, 50% lifted and completely lifted.

Similar considerations are true here, in the sense that the uncertainty is probably too large to derive an accurate correlation, but we can say that the complete extraction of the assembly from the core provokes a decrease in reactivity of about 100 pcm.

Concluding Remarks

This preliminary work provides a good basis for the approach that will be used for the analysis of the assembly removal. The most important aspects that need to be resolved before performing a complete analysis are:

- How many particles and generations should be used. How many generations should be skipped. The answer depends on the desired results.
- How to model the core: how many rings? How many units? Also, what temperatures and enrichments should be used?
- What type of information is required from the analysis? What do we need to extract from the output files?
- How to perform the analysis, for both the insertion of the control rods and the lifting of the assembly.

The final objectives of this analysis probably require to be improved and clarified, but the approach seems to potentially be capable of providing the desired information, no particular issues have been encountered.

7.7 Online refueling

7.7.a Description of online refueling procedure

The feasibility of the fuel assembly removal during operation with nominal or reduced power would allow better utilization of the fuel and more economic electricity production. The associated fuel assembly removal transient for the AHTR represents a fundamental aspect of the reactor design. In order to study this type of transient, since the structure of the core is very particular, a full understanding of the neutronics and fluid dynamics in the core is required.

Figure 7-22 shows a simple diagram of the flow in the core and the removed assembly, during the transient, indicating increased flow in the channel with the fuel assembly being removed, and reduced flow (potentially challenging thermal performance) in the neighboring channels. Future work will develop models for the simulation of this transient.

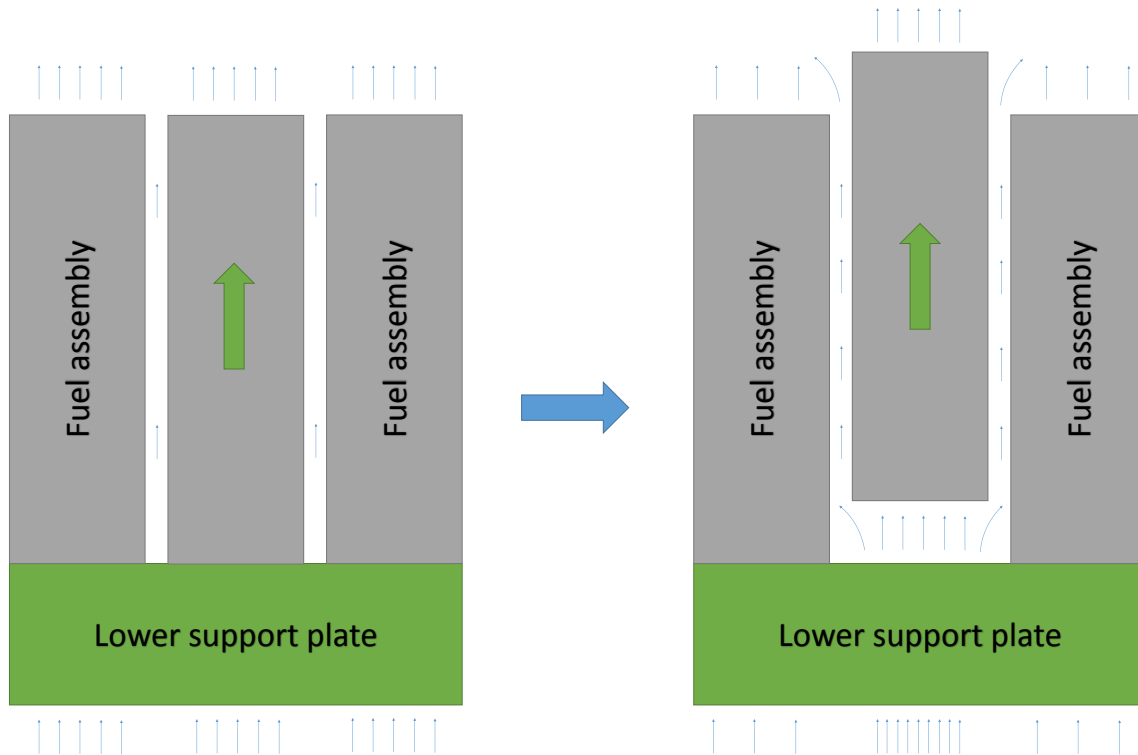


Figure 7-22. Fuel assembly removal transient

Particular aspects that have been considered in the study are:

- Modeling of the single coolant channel;
- Flow in the lower support plate (how the flow splits between the inter- and intra-assembly coolant channels);

- Effects of cross-flow for the inter-assembly channels;
- Flow distribution after the detachment of the fuel assembly from the lower support plate.

7.7.b Pseudo-continuous refueling

The LSCR core model was adapted for the modeling of the assembly removal transient. This type of transient plays an important role in the study of the LSCR reactor, enabling the possible capability for an on-line or pseudo-online refueling option.

The LSCR core presents a low heavy metal loading of the core, due to the use of TRISO fuel and graphite moderation, which reduces the amount of energy extractable from a single fuel assembly and consequently its core lifetime. If a normal refueling procedure (similarly to light water reactors) were adopted, a large amount of the reactor lifetime would be spent in off-line refueling operations, leading to a decrease in the energy delivered to the grid and to an increase of the electricity production cost.

Two reasons contribute to the previous effect: the high frequency of refueling operation pauses, due to the low fuel loading in the core, and the long duration of the refueling operation, due to the high temperature and thermal capacity of the primary coolant. The first reason is intrinsic to the reactor type features, so it cannot be changed, but the second reason can be easily addressed through the adoption of a pseudo-online or online refueling. The use of an online (no power reduction) or pseudo-online (partial or total power reduction for a short time, shorter than the Xe build-up effects) procedure substantially reduces the time lost in refueling operation and enables a multi-batch option with a number of batches much higher than a normal refueling procedure, meaning an increase in the fuel burn-up of almost a factor 2, which is the maximum theoretical limit for continuous refueling.

The previous consideration makes the online refueling an interesting and suitable option, due to the low heavy metal loading features of the LSCR. From the neutronic standpoint (multi-batch fuel cycle), some evaluations have been performed by ORNL,⁶ but the thermal hydraulic consequences still need to be evaluated.

The feasibility of this procedure is relatively challenging, since the density of the fuel and the coolant are not very different, and the system, with reference to the current design, is not yet capable to enable this option, but the thermal hydraulic analysis at the fuel assembly level can be performed by making simplifying assumptions. The following sections present the modeling and the results for this transient type.

Fuel assembly removal transient

The thermal hydraulic core model described in previous reports was used for the transient evaluation; the 6th ring of the core model was modified: the single super-assembly, representing the 36 fuel assemblies of the 6th ring, in the initial model was changed to two fuel super-assemblies, one representing 35 fuel assemblies of the 6th ring, and one representing the assembly which is to be removed from the core. The 6th ring was selected, because it represents the average condition of the fuel in the core; the properties and structure of the assemblies were not changed.

The initial conditions for the system were set to the steady-state condition and the transient was structured in four different parts:

1. The decay heat power is activated in the removed assembly; after the activation, the system evolves for 50 s;
2. Reduction of the form loss coefficient at the entrance of the inter-assembly channels connected to the removed assembly from 1500 (nominal value) to 0; duration: 20 s;
3. Rise of the removed assembly; duration 200 s (3 min and 20 s);
4. Stay of the removed assembly in the upper plenum; duration 200 s (3 min and 20 s);

In relation to the first part, the power in the core was determined by the point kinetics model, similarly to the LOFC transient, and the power of the removed assembly was given by an empirical formula for ²³⁵U decay heat.

In relation to the second part, a valve component was used to model the inlet junction of the inter-assembly channels near to the removed assembly, in order to be able to increase the mass flow rate in the interested channel from the initial value to the higher value reached immediately after the detachment of the fuel assembly from the lower support plate.

In relation to the third point, a particular approach has been adopted, since RELAP5 does not allow to model a volume whose height can change with time. A discretized transient was performed: the height of the core was divided into different levels and, for each level, starting from the conditions at the previous level, the geometric configuration was changed (the elevation of the assembly was increased by a discrete amount) and the system was let evolve for the respective amount of time. This procedure was repeated for each axial step, every 10 cm from 0 cm to 6.7 m (full ejection of the assembly from the core), for a 3 s rise time per step.

In relation to the fourth part of the transient, the assembly was left in the upper plenum for a certain amount of time, before being moved to the used fuel storage pool.

Fuel assembly removal: considerations

Both the inlet and outlet temperature decrease in time, but the temperature in the upper plenum decreases by 0.5°C, while in the lower plenum the decrease is by an amount equal to 0.2°C; since the total core mass flow rate is unchanged, this means that the total core power is reduced,

which is in reasonable agreement with the fact that a control rod was fully inserted in one of the 252 fuel assemblies.

Despite the lower overall coolant temperature rise across the core, both the maximum and average fuel temperature increase, by 2°C and 1°C, respectively; this is due to the fact that even if the total core mass flow rate is constant, its distribution is different: the pressure losses are step by step reduced in the channel of the removed assembly, so the mass flow rate that effectively cools down the core becomes lower, causing an overall increase in the fuel temperature. A lower mass flow rate in the active part of the core means that the mass flow rate in the channel of the removable assembly is increased.

The total mass flow rate in the assembly channel is, in steady state conditions, about 100 kg/s and it increases in three steps:

- From 100 kg/s to 200 kg/s during the initial detachment of the assembly from the plate;
- From 200 kg/s to 400 kg/s during the rise of the assembly in the channel, until 270 s;
- From 400 kg/s to 600 kg/s during the final jump in the upper plenum.

The two components of the flow, the inter- and intra-assembly mass flow, show a different evolution in time: the inter-assembly flow increases, because of the progressive reduction of the friction losses, while the intra-assembly flow decreases from 100 kg/s to about 0 kg/s, when the assembly is completely removed.

The reduction of the intra-assembly mass flow rate causes an increase in the fuel temperature of the removed assembly; initially, the temperature decreases, because of the insertion of the control rod, but when the assembly is completely moved in the upper plenum, the maximum fuel temperature increases to about 700°C. Anyway this value is well below the maximum fuel temperature in nominal operating conditions, so the integrity of the fuel plates is not compromised.

The overall response of the LSCR to the transient shows that the system, from a global point of view, is not strongly affected by the removal of a fuel element; from a local standpoint, the removed fuel assembly does not show a high temperature increase, but the final flow velocity in the channel, about 3.5 m/s, is higher than the nominal design value by a factor 2, resulting in possible corrosion of the structures. This is only an illustrative and incomplete preliminary analysis, with not all phenomena taken into account. It does however indicate that on-line pseudo-continuous may be viable. The model requires further work in order to have a better characterization of all the aspects of the transient.

7.7.c 2D modeling of the assembly removal

The fuel assembly removal transient consists of the lifting of the fuel assembly in the core with coolant flowing through the system. 3D modeling is required to give a full description of the transient, but a preliminary 2D modeling is tested in order to address general issues regarding this type of analysis, which will be extended to the full 3D case.

This work aims to give a general description of the problem and it addresses two main aspects for the modeling: coupling of boundary conditions for the 1D representation of the assembly channels and dynamic meshing for the lifted assembly.

The first aspect simplifies the problem, allowing to model the assemblies in a simpler way and reducing the computational demand. The second aspect is directed to the evaluation of a way to model moving objects into the core.

General aspects

The CFD simulation code Fluent is used for the thermal hydraulic analysis. The code can perform steady state and transient CFD evaluations, and it is coupled to a 1D modeling of the internal channels of the assemblies.

Generally speaking, Fluent can be coupled to a system code (such as RELAP) and several approaches have been developed in order to do this.

The general issue that emerges in doing this is the fact that it is relatively difficult to develop a coupling approach that is general enough to be applied in different contexts. This means that it is simpler to develop a particular approach for each particular case.

Another aspect that must be accounted for when trying to couple a system code and a CFD code is the stability of the coupled system from the numerical standpoint. Normally, the two coupled systems are less stable than each single system by itself, meaning that the convergence of the transient simulation at every iteration is weaker. In this case an appropriate choice of the time step is required in order to improve the convergence.

In this work, due to the simplicity of the problem, the CFD code is not directly coupled to a system code but instead an approach is used in order to model 1D channels in the fuel assembly. In other words, in this case the system code is represented by a simple 1D model of the channels. Overall, this approach is relatively simple and versatile; it can be easily applied in several conditions and it is most probably suitable for a full 3D application.

One more aspect that needs to be mentioned in the introduction is that the aim of the work is the ability of modeling a transient with a moving assembly. The tool that allows doing this is the dynamic meshing capability built in Fluent. This tool has potential applications in the evaluation of the transients in accidental conditions and it will be applied in this case for the modeling of the lift of the fuel assembly.

User Defined Functions.

In Fluent, the characteristics of the coupling with the system code, as well as the modeling of the dynamic features of the transient, are defined through the User Defined Functions (UDF).

UDFs allow the addition of new physical models to the code, as well as the customization of the boundary conditions; the reason why Fluent allows the integration with UDFs is the fact that Fluent is a general-purpose simulation code that cannot predict all possible need of the users.

UDFs are programmed in C language and are interpreted by the solver or compiled before starting the program. These functions allow the setup of several features of the simulation, such as definition of custom boundary conditions and material properties, definition of the parameters in the transport equations, and definition of the mesh motion.

Two types of UDF will be used in this work, one for the definition of the boundary conditions for the coupling with the 1D channels, the other for the motion of the center of gravity of the assembly.

The UDFs can access the data of the simulation, such as the geometry data or the field variables. Macros are available to perform certain operations such as retrieving the value of a variable on a particular face, collecting the geometric data of the cells or defining the profile of a variable at a boundary.

Dynamic mesh

The Moving/Deforming Mesh (MDM) feature of Fluent is used to model the lift of the assembly; this feature allows the motion of the boundary and cell zones of the mesh. It can be used for linear or rotational rigid motion, deflection and deformation of surfaces, free motion of objects. The MDM is compatible with all Fluent physical models and solvers and it can be parallelized.

Three types of mesh adaption are available in order to fulfill this task:

- Layering: this option is available only for layered mesh and involves the creation/elimination of the cells at the inlet/outlet. It is useful for linear motion.
- Smoothing: it is based on the spring analogy, meaning that the connectivity of the nodes remains unchanged and the distance between the nodes is modified based on a spring constant. It is limited for small mesh deformation.
- Remeshing: addition or elimination of cells according to specified dimensions; the connectivity can change.

The approaches are usually combined in order to obtain the best mesh adaption procedure; the combination of the methods requires the use of non-conformal interfaces (different mesh on the two sides) at the boundary of different meshing zones.

In this work a rigid body motion will be modeled; the path of the motion is determined by a UDF that specifies the position of the center of gravity of the moving body as a function of time. An example of this function will be presented later on.

The MDM has some limitations, among which the fact that an object cannot move from one fluid zone to another.

Another important limitation, relevant in this case, is the fact that some valve applications require a minimum number of layers at the interface between two rigid bodies in order to maintain the topology of the mesh. In other words, a valve cannot be completely closed. In our case, this happens where the assembly, at the beginning of the transient, is touching the lower support plate.

Two options are available to address this issue:

1. The transient starts from a very thin gap, so that the flow through that gap is negligible.

2. The gap is kept closed at the beginning of the transient by a wall interface; this interface is switched to interior once the lifting of the assembly starts. This is made possible by the fact that the boundary condition type can be changed at some point during the transient simulation.

The first option is easier to model, so it will be initially used; the second option is preferable because it gives a more correct representation of the problem.

Coupling of boundary conditions

The internal channels of each assembly are modeled as 1D channels. The friction pressure drop (and the heat transfer, if needed) is determined through friction correlations.

Since the fluid is incompressible and the density is considered constant with the temperature (see previous reports for further considerations on this aspect), the average velocity of the flow is constant along the channel. The 1D modeling of the channels and the coupling of the boundary conditions are based on this approximation.

The 1D modeling of the internal channels is required in order to reduce the computational requirements for the full core model. In fact, the number of channels in the core is relatively large (21 channels per assembly, 252 assemblies) and a full CFD modeling of each single channel is prohibitive.

This section presents an evaluation of a simple approach to model the channels using Fluent UDFs.

Considerations on the method

The convergence of the simulations is an important factor for the modeling of the upper plenum and, in general, the outlet volumes when performing this kind of simulations. This was an issue that had to be faced in this work but it is not the main objective of the analysis, so it can be partially neglected.

Globally, the results for the 1D modeling of the single channel are good. The advantage of the 1D modeling is that many flow conditions can be modeled at the same time, through the use of appropriate friction drop correlations. This is not possible in a full CFD simulation, where a physical model has to be selected for the entire simulation (turbulent vs. laminar). This aspect is a noticeable advantage of the 1D modeling over the CFD and it is probably the main reason why 1D system codes are still the most popular modeling approach for thermal hydraulics in nuclear engineering.

With respect to this specific problem, the correlations seem to correctly represent the flow in the 6 m long channels; the entrance length effect and the outlet velocity profile can be correctly represented by the introduction of partial modeling of the inlet and the outlet of the channel, but they do not represent a major issue for the model.

2D simplified modeling

A 2D example of the assembly removal transient has been modeled. The purpose of this simulation is mainly to illustrate the approach and not to obtain the physical results of the simulations or evaluate the correctness of the models for the flow solution.

Setup and Results

A viscous model (k- ϵ -omega) has been used for the Fluent simulation. Again, this is probably not the best modeling of the flow in that region, but it is the one that most easily converges in these conditions. Further analysis will be performed in the future in order to improve this aspect.

The assembly is lifted at 3 cm/s and the transients lasts about 1 minute.

The following sets of figures show the velocity magnitude contours as a function of time for the system and its details at the inlet and outlet of the assembly (Figure 7-23, Figure 7-24).

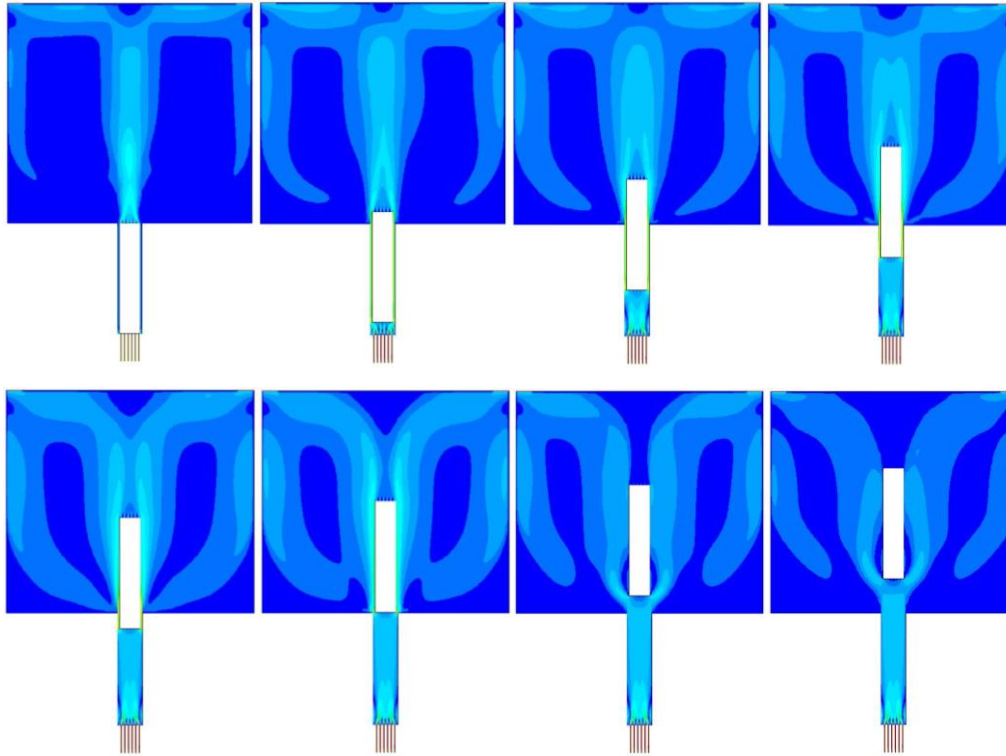


Figure 7-23. Velocity magnitude contours as a function of time

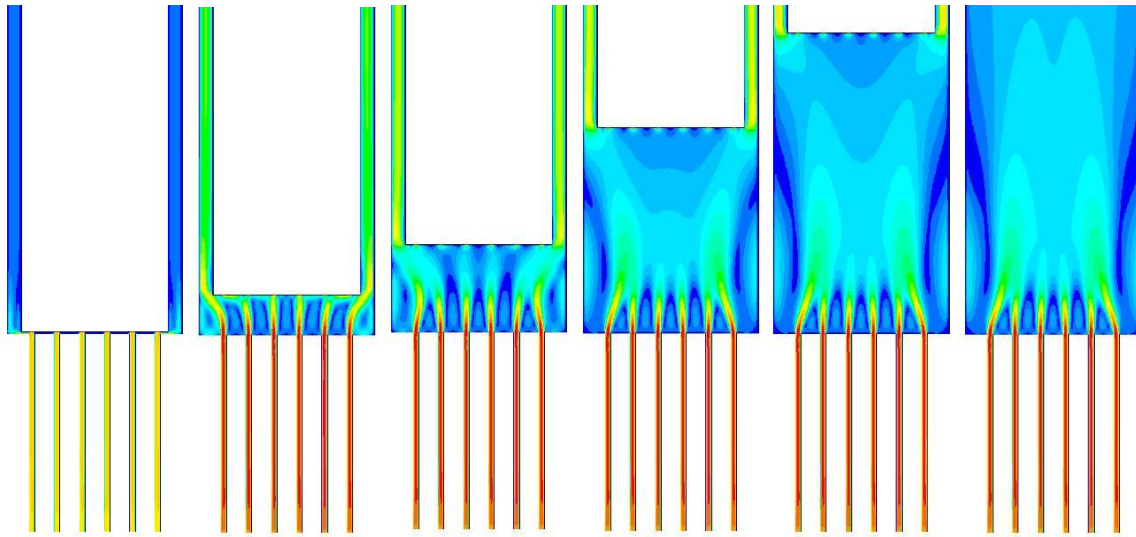


Figure 7-24. Velocity magnitude contours at the assembly inlet

Conclusions

The approach is capable of analyzing this transient and it can provide useful information. The convergence of the numerical models is an important aspect of this analysis, since the full problem involves several types of flow. Further analysis is needed to improve the results. This issue is particularly important in the plenums, where the velocity and vorticity of the flow is variable with the location. Particular attention should be used for the modeling of the turbulent jets at the outlet of the assemblies (top of the core).

The 1D approach for the modeling of the internal channels provides means to achieve good results by reducing the computational requirements of the simulations. Again, the most realistic approach involves at least a partial modeling of the inlet and outlet of the channel in order to obtain a correct flow distribution, but acceptable results can still be obtained if this aspect is not considered relevant.

Three main aspects need to be addressed in order to move to a full 3D representation of the transient.

- Applicability of the physical models. The modeling of the flow in the upper plenum with CFD has to be meaningful from a physical standpoint. The correct models and convergence criteria are fundamental in order to reach a good level of approximation.
- Extrapolation of the meshing aspects and the dynamic meshing to a 3D geometry. The type of cells and the meshing techniques are more involved for the 3D case than the example that was presented here.
- Evaluation of the computational requirements. The full core problem is a very large problem; the 1D approximation of the channels reduces the computational demand, but the problem remains large. The calculations could be performed in parallel; for this

reason, it would be useful to get a better impression of what is the dimensionality of the problem in computational terms.
Overall, it seems that the full core 3D transient model can be simulated through a procedure similar to the one presented in this work.

8. Full Core Depletion Analyses

8.1 3-D Coupled Neutronic and Thermal Hydraulic Depletion Demonstration

All previous calculations performed with NESTLE within the previous benchmarking sections were forced to run without thermal hydraulic feedbacks so to be able to compare to the SERPENT models. Though no formal benchmarking of the neutronics and thermal-hydraulic coupled model could be conducted --because there is simply nothing to compare to-- an illustrative NESTLE simulation is herein presented for demonstration purposes of the final product generated by this research project.

A reactivity curve can be observed in Figure 8-1 along with other metrics of interest shown in Figure 8-2 and Figure 8-3. Looking at Figure 8-2 it can be seen that all metrics tend to follow expected behaviors for the uniform core loading model that was used. Power and fuel temperature begin centrally peaked at beginning of cycle but gradually flatten as the fuel is burned out. Coolant density decreases as it flows from the bottom of the core to the top and fuel burnup proceeds from the inside out. As mentioned before, no formal testing of the coupled model was conducted due to time constraints and the lack of a practical means of provide a reference solution, but this demonstration does help to illustration the strength of the two-step method and provides a proof of principle and stepping stone for future research

The 3-D coupled calculation herein illustrated employed 24 depletion state points to model the AHTR fuel cycle. These results were generated on a single Intel Core i7 4770 Haswell processor in 21 minutes of wall-time (e.g. less than a minute per state point). In contrast, a single state point neutronic simulation of an equivalent model using SERPENT 2 and without thermal hydraulic feedbacks required 1.24 hours of wall clock time when using 1200 nodes with 16 core AMD Opteron processors each, or 19,200 processors of the ORNL TITAN supercomputer, equivalent to 23,808 CPU-hours (2.7 CPU-years). Considering that multiple T/H iterations will be required to converge on a coupled solution for each state point, it can be said that obtaining a similar solution would take days or even weeks on a state-of-the-art high performance platform. Therefore, implementation within a typical modern cluster with a few hundred processors can be readily deemed as intractable.

In short, this easily demonstrates the utility of the two-step procedure in that it provides a coupled solution with substantially less runtime and resource requirements. It should be noted that when considering the cost savings of the two-step procedure, one should also consider the upfront computational costs of generating the lattice physics cross-section libraries. For this particular demonstration, models were simulated for 7 branch conditions with both control blades inserted and withdrawn over 24 burnup points, totaling 336 state-point calculations.

These simulations were conducted over 15 nodes comprised of Intel Core i7 4770 Haswell processors, using all 4 cores on each processor, and were completed in 7.8 hours of wall clock time. It should be noted that these run times will increase as larger numbers of neutron histories and improved accuracies are pursued. Though the cross-section library generation computational cost is significant, it is dramatically dwarfed by the computational costs associated with obtaining a coupled solution with the aforementioned SERPENT 2 based approach. Additionally, this cross-section library can be utilized for simulating more than just the uniform fresh core depletion calculation provided in this demonstration, such as multi-batch heterogeneous burnup distribution simulations. It can easily be seen then that with a few somewhat computationally expensive cross-section library generating simulations, one can perform a plethora of 3-D full core simulations at various conditions and core loadings at essentially negligible computational costs.

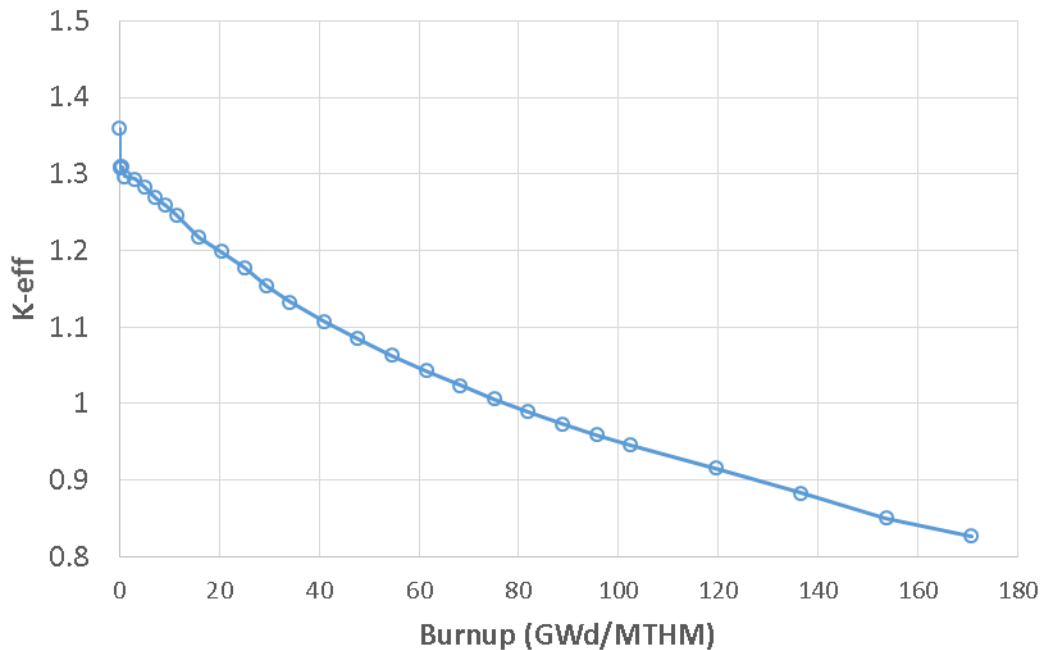


Figure 8-1. K- effective Profile for Illustrative Coupled Neutronic and Thermal Hydraulics AHTR Depletion Calculation in 3-D with NESTLE

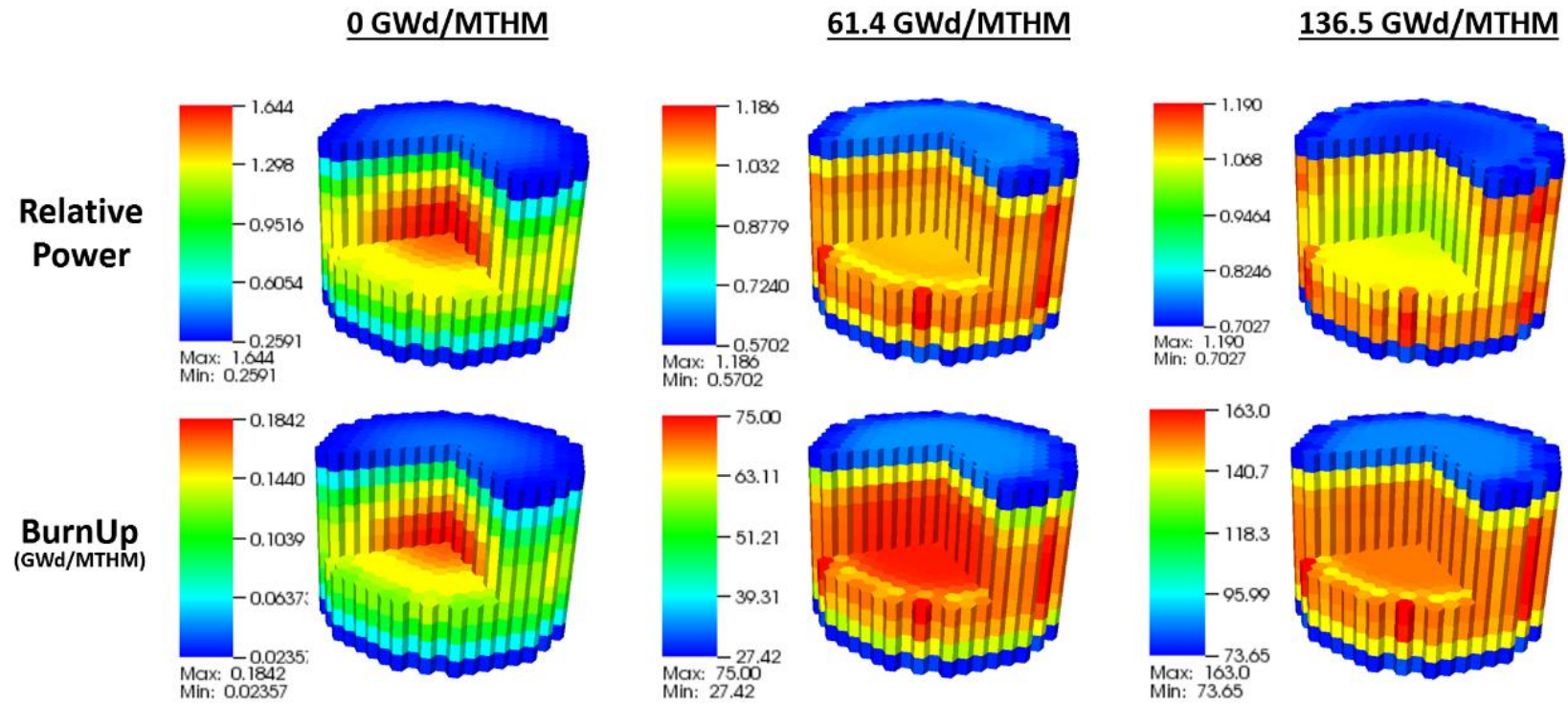


Figure 8-2. 3-D Relative Power and Burnup Distributions for Coupled Neutronics and Thermal Hydraulic AHTR Depletion Calculations with the Two-Step Procedure

Fuel and Core Design Options of LSCR

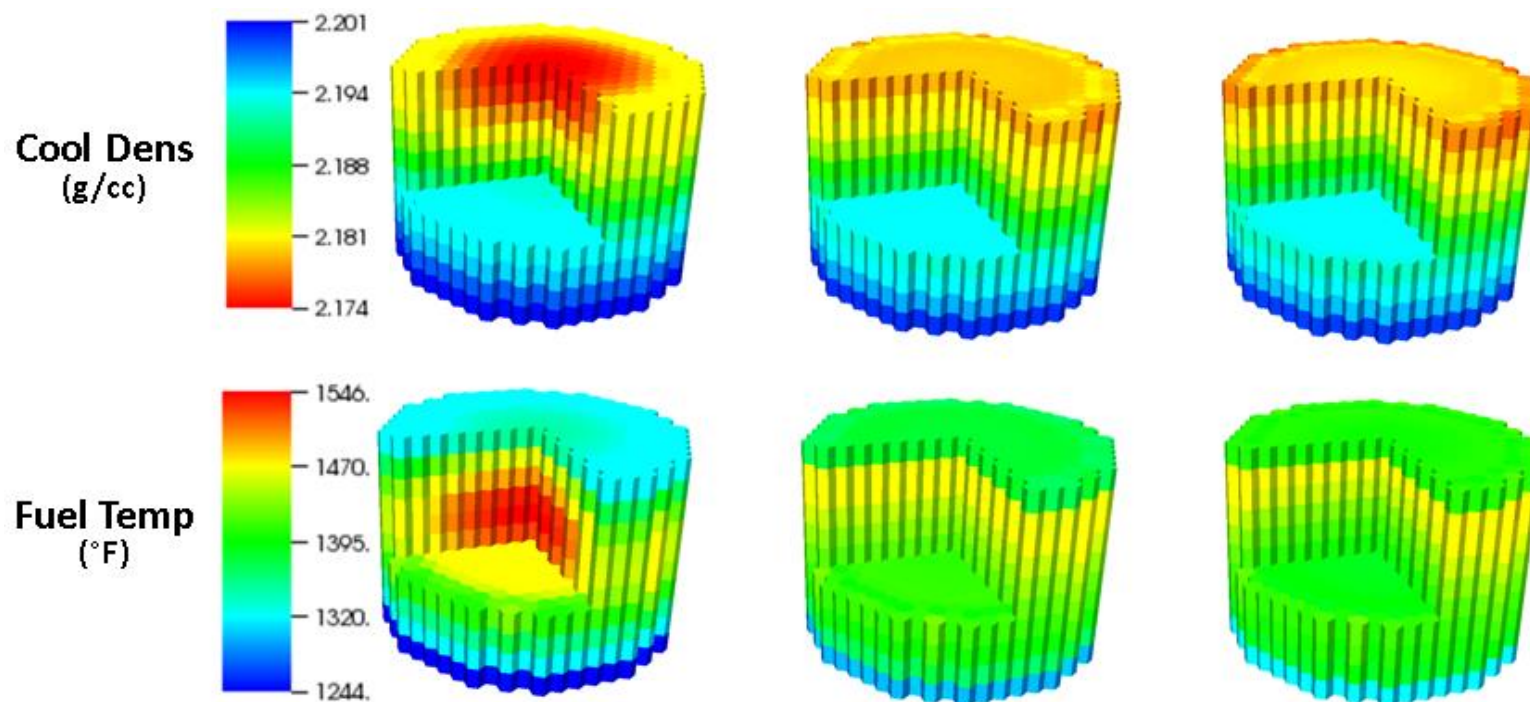


Figure 8-3. 3-D Coolant Density and Fuel Temperature Distributions for Coupled Neutronics and Thermal Hydraulic AHTR Depletion Calculations with the Two-Step Procedure

8.2 FHR Multi-batch Loading Study

Previous studies employed a homogeneous bundle type across the core. Therefore, by employing an optimization tool developed at UTK called LWROpt [1,2] (Light Water Reactor Optimizer) a Loading Pattern (LP) optimization was performed on a simplified FHR model. LWROpt is a multi-cycle fuel cycle optimization code that uses Parallel Simulated Annealing (PSA) by mixing of states [3] to perform LP and new fuel inventory optimizations and also has a heuristic control rod pattern search. The objective of the optimization performed for the FHR was to reduce power peaking from the initial guess while achieving an EOC k -effective greater than or equal to 1.0. NESTLE was used for all of the model evaluations including those performed by LWROpt. The following sections contain descriptions of: the model used and the initial guess, LWROpt input parameters and optimization setup, and the results of the optimization.

8.2.a FHR Model used for the Optimization

The simplified model used for the optimization was a 2D model with a radial reflector and one sixth core with cyclic (rotational) symmetry. This model was selected because it is the simplest geometry available in NESTLE for hexagonal models that somewhat resembles an actual reactor. Only one fuel type was used in the model, but three regions were used in order to make the model more realistic than the previous homogenous models. The fuel type used was the base 19.75% enriched homogeneous assembly design and the regions consisted of: fresh fuel, 49150 MWD/MTU burned, and 98300 MWD/MTU burned. All of the assemblies in each region were given exactly the same burnup so this model could be considered a simplified reload model or an approximation of a first cycle with three different fuel types. The cycle burnup of 49150 MWD/MTU was determined by iterating the region 2 and 3 burnups in the initial guess design to find values that would correspond to 1 and 2 cycles worth of burnup and produce a slightly subcritical core at EOC. Slightly subcritical was desired because the optimizer should be able to extend the cycle length.

A plot of the Loading Pattern (LP) for the initial guess is shown in Figure 1. This LP was generated by hand with some attempt at optimization, but the real goal was just to get something reasonable to compare the optimized LP with (the initial guess has little effect on the results of the optimization). The EOC k -effective for this LP was 0.99947. A plot of the BOC Relative Power Fraction (RPF) for this LP is shown in Figure 2. The maximum RPF at BOC was 1.6522 with a reasonable power distribution except for the outer edge is too low, which necessitates larger power peaking in the interior of the core. Note that because the fuel assemblies do not contain any Burnable Poisons (BPs) and no control rods were used the maximum RPF decreases or remains constant throughout the cycle.

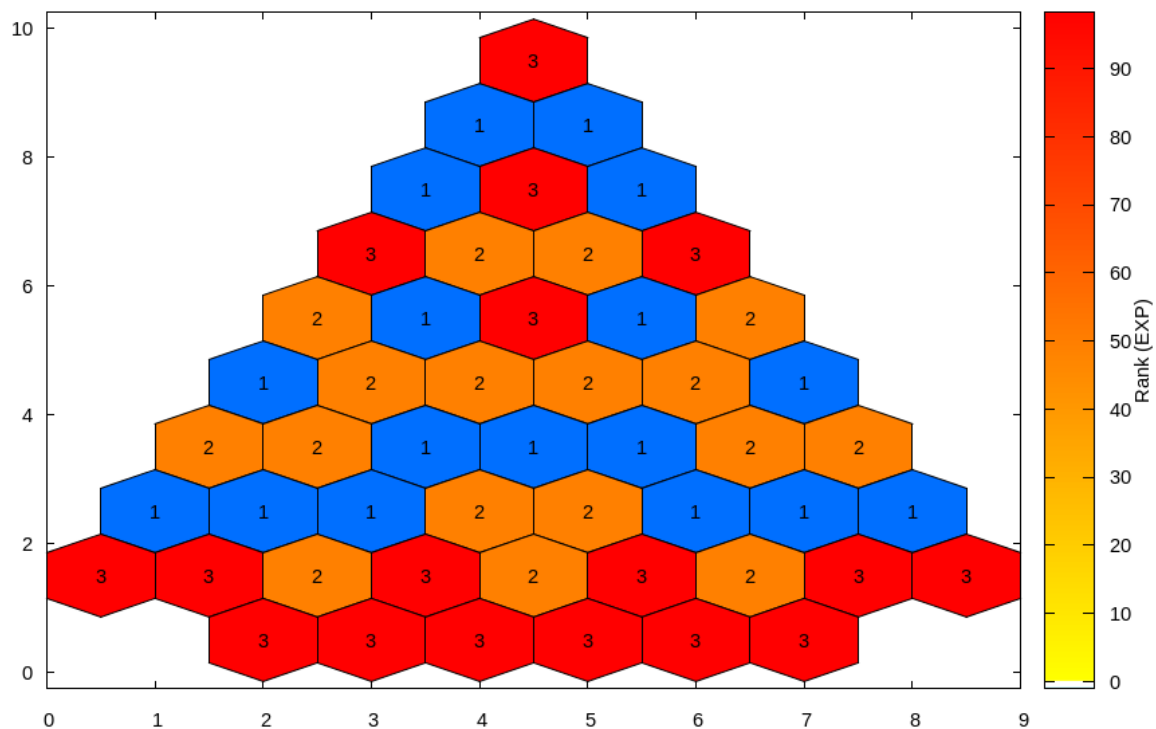


Figure 1. Loading pattern for the hand generated initial guess with region numbers

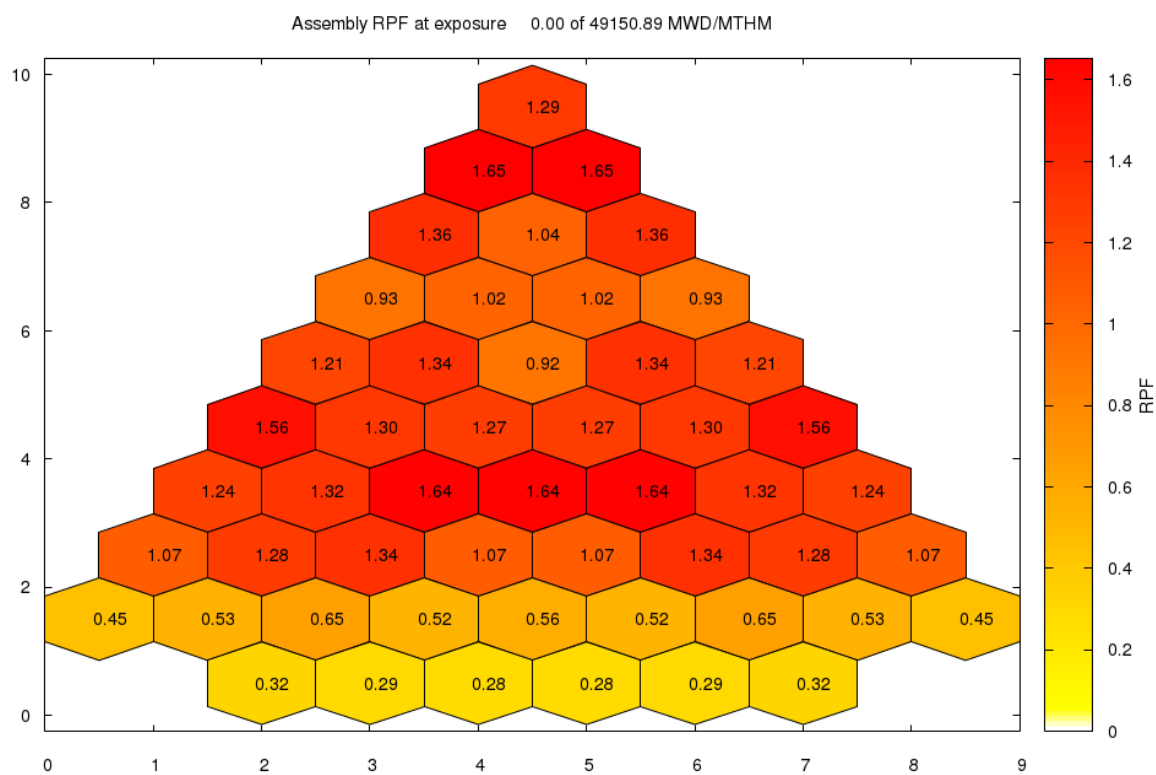


Figure 2. BOC assembly RPF for the initial guess.

8.2.b Optimization Setup

The optimization was setup to be very thorough since the model being optimized was very simple. The major PSA input parameters were set as follows: the annealing temperature initialization parameter, alpha, was set to 2.0, which is pretty typical, but the annealing temperature adjustment parameter, lambda, was set to .05, which is much less than the typical value of 1.0, this results in a slower rate of decrease of the annealing temperature and, therefore, a more thorough optimization. The optimization was performed using 128 processes on 16 Intel Core i7 (Haswell) 3.4 GHz processors. Since the model only contains one new fuel type and the region size was not being optimized only two LP change types were used: exchanging two used assemblies and exchanging a used assembly and a fresh assembly. The one exception to the region size being constant is that the center assembly's region was not fixed (this is currently not possible in LWROpt), which allowed for minor changes to the region sizes.

One unique feature of LWROpt that was used in this optimization that hadn't been used much previously was sampling the mixing of states LPs from the archive at regular intervals instead of always sampling from the current solutions on each process. For this optimization this sampling was done every 20 cooling steps (a cooling step is a set of inner iterations after which the annealing temperature is updated) starting with cooling step 100.

The weights and constraints used in the calculation are given in Table 8-1. The minimum k-effective limit was set to 1.0 (critical) with a weight of 1000.0. The limit for maximum RPF was set to an unachievable 1.0 because there was no actual target value just the goal of minimizing it as much as possible. To make this work the RPF weight was set to 1.0, much less than the k-effective weight, to ensure that LWROpt would focus on RPF only after the k-effective limit had been satisfied.

Table 8-1. Constraint weights and limits used for the optimization

Parameter	Weight	Limit
Min k-effective	1000.0	1.0
Max RPF	1.0	1.0

The only major issue encountered while testing LWROpt on the FHR model was that LWROpt currently assumes that all reload fuel assemblies are unique. This is generally a very good assumption, but because of the way this optimization was set up (with regions in which all of the assemblies have the same burnup) it was a very bad assumption for this model. This, however, did not prevent the optimization from working it just meant that nearly half of the reload fuel exchanges (roughly a quarter of all changes) had no effect on the LP. Because a significant number of LP changes didn't actually change the LP the standard deviation of the objective function (function that includes all constraints and is what is actually minimized by the optimization) was under predicted causing the annealing temperature to be lower than it should have been which leads to a less thorough optimization. The final issue caused by the lack of reload fuel differentiation is that it allows the

archive (list of the best LPs found) to fill up with a bunch of copies of the same solution, which is would have just been an annoyance in this case except that it reduces the effectiveness of the alternative solution sampling.

Results

LWROpt was able to optimize the LP for the simplified FHR model and in fact found a substantially better LP than the initial guess (Figure 8-4). This is shown by Table 8-2, which includes the constraint values for both the initial guess and the optimized LP. A plot of the RPF for the optimized LP is included in Figure 8-5. This plot shows that the optimized LP has more power along the outer edge of the core than the initial guess, which allows for lower internal power peaking as well as a higher EOC k-effective. The run-time of the optimization was about half a day (using 128 processors) and because of the issue with reload fuel differentiation mentioned previous was manually terminated because it never would have converged. Note that the best solution was found in about a third of the time the optimization was allowed to run and so if the afore mentioned issue was fixed the runtime might have been significantly less.

Table 8-2. Comparison of the constraint values for the initial guess and optimized LPs

Model	k-effective	RPF
Initial Guess	0.99947	1.6522
Optimized	1.0000	1.3790

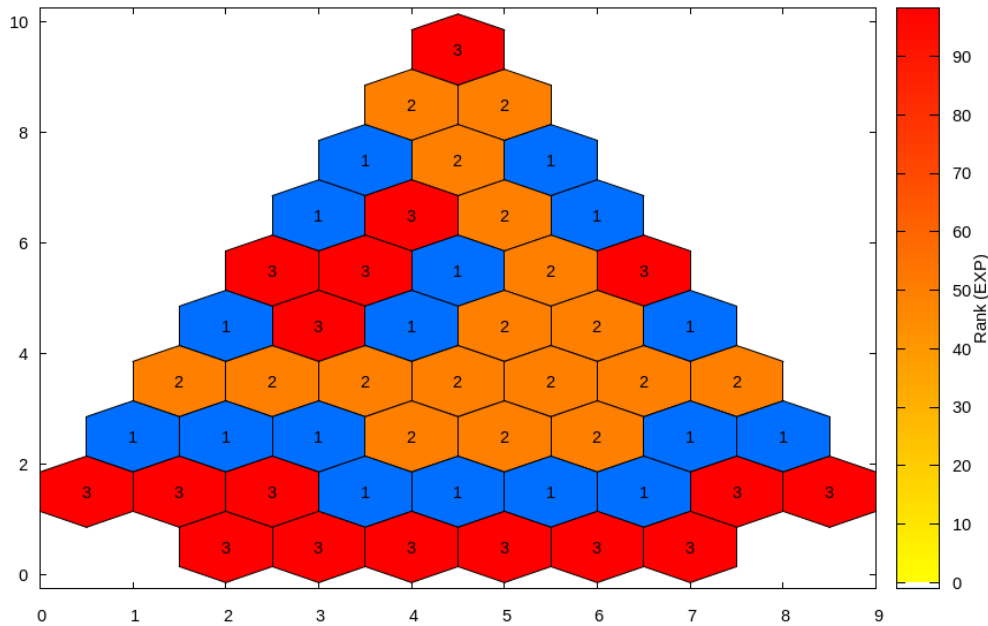


Figure 8-4. Best LP found in LWROpt optimization

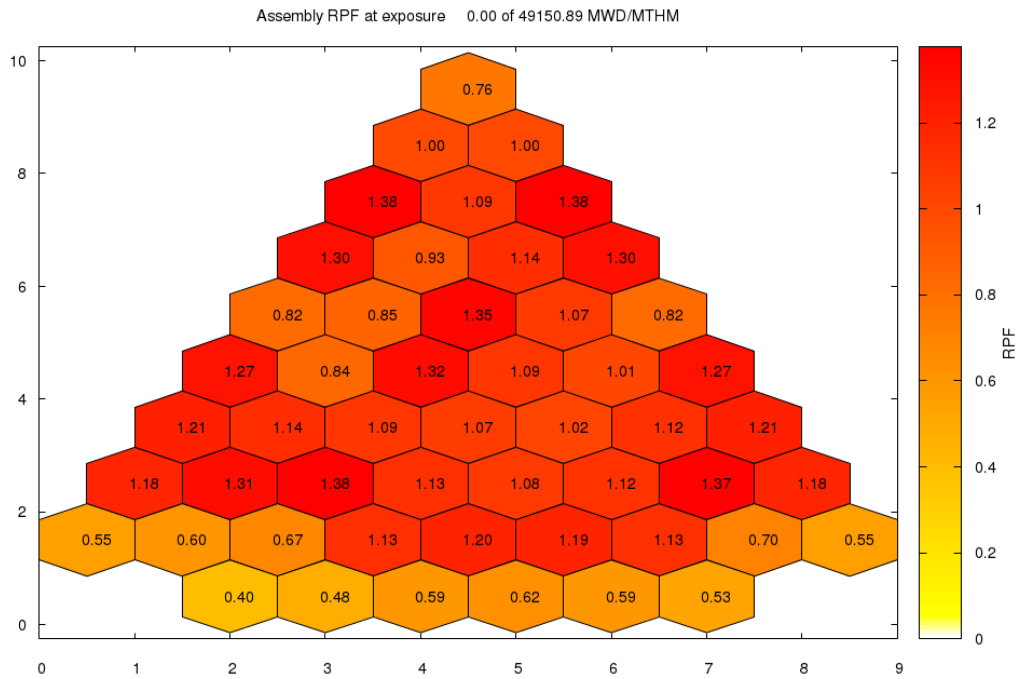


Figure 8-5. BOC RPF for the best LP found by LWROpt

8.3 References for this Section

1. Keith E. Ottinger and G. Ivan Maldonado. "BWROPT: A multi-cycle BWR fuel cycle optimization code". Nuclear Engineering and Design 291 (2015), pp. 236–243.
2. Keith E. Ottinger et al. "SMR Fuel Cycle Optimization and Control Rod Depletion Using NESTLE and LWROPT". Proc. ANFM 2015. Hilton Head Island, SC: American Nuclear Society, Mar. 2015.
3. King-Wai Chu, Yuefan Deng, and John Reinitz. "Parallel Simulated Annealing by Mixing of States". Journal of Computational Physics 148 (1999), pp. 646–662.

9. Fuel Cycle Cost Evaluation and Optimization (Tasks 1-3)

9.1 Re-stating the problem

While FHRs offer high thermal efficiency and inherent safety features, there are challenges related to some features of plank fuel. Specifically, this fuel type is characterized by low heavy metal loading, which may lead to reduced cycle length. To illustrate this point, consider a typical PWR, where 25-30% of the total core volume is occupied by fuel, uranium oxide. In contrast, in an FHR with plank fuel, depending on the exact fuel and fuel stripe geometry and packing factor of TRISO particles, the volumetric portion of fuel, uranium oxycarbide, is some 15-100 times lower (for the considered TRISO particle geometry and packing factor in the 10-40% range). This significantly reduced heavy metal (HM) loading may be partially compensated by increased enrichment, but the fissile loading (per core volume) will still be significantly lower than in a PWR, challenging cycle length and increasing refueling frequency as well as outage cost.

Higher TRISO packing fraction will indeed increase fissile loading, but it will also reduce moderation and thus lead to worsened fuel utilization and lower discharge burnup, requiring more fuel to produce same energy, thus increasing fuel cycle cost. The issue is amplified with the expected relatively high TRISO fuel fabrication cost and consequently fuel cost, so that a poor fuel utilization may have a significant impact on FCC, much stronger than in a LWR where fuel cost is a relatively limited fraction of the overall cost of electricity (COE).

Thus, we are faced with two opposing objectives, longer refueling interval and reduced outages (requiring increased HM loading) and better fuel utilization (achieved by better moderation, requiring reduced HM loading), necessitating careful optimization of fuel design. At the same time, impact on the COE is not trivial, and uncertainties in the assumptions are relatively large, making this a challenging optimization problem.

One additional specific challenge is the following. For PWRs, fuel cost includes fuel fabrication cost. This cost is assumed to be related primarily (only) to amount of HM and not to specific fuel design, is therefore expressed in \$/kgHM, and typically amounts to \$200-300/kgHM, in any case only marginally impacting the total COE. Moreover, the assumption of the design independence of fuel fabrication cost is reasonably accurate, since all PWR fuel designs are fairly similar.

For FHRs, a much broader range of design variations is considered. For example, reducing the enrichment by a factor of two (20% to 10%), and reducing the packing fraction by a factor of two, would require fabricating twice as many TRISO particles and four times as many fuel elements to keep the same fissile loading, which would significantly change the fabrication cost per kg HM. Therefore, we have developed a model and methodology allowing to account for these effects.

9.2 Methodology for calculating fuel cost and fuel cycle cost

9.2.a Previous and preliminary analyses

This methodology ultimately developed in this project builds upon the previous work by many authors. A selection of several references to directly relevant previous work follows.

The AHTR design was developed by ORNL and is documented in several technical reports and papers including [1-3]. ORNL initial FCC analysis is summarized in [4].

The initial AHTR analysis framework at Georgia Tech for neutronics and FCC was established by S. Lewis in [5]. The FCC analysis and optimization was performed together with sensitivity analysis to address uncertainties in assumptions. While a broad range of fuel fabrication costs was evaluated, no design-specific adjustment was applied, i.e., in each case it was assumed the same in \$/kgHM for all designs. Thermal-hydraulic constraints used in this FCC evaluation were obtained by analysis described in [6]. Due to the double heterogeneity of FHR plank fuel, its core physics analysis presents significant challenges. Previous work by ORNL (e.g., [7,8]) was expanded, in particular to incorporate in a practical manner Dancoff correction to improve accuracy of results [9,10].

These improvements in core physics simulations, together with the updated costs of uranium and enrichment, were integrated to obtain updated FCC results and sensitivity analysis, considering low, mid and high cost scenario). However, fuel fabrication cost was still defined as being design-independent in terms of \$/kgHM. The results are summarized in Master Thesis by S. Lewis [5].

9.2.b Improved fuel fabrication cost model and FCC model

Recent research under this project [11] introduced a fuel design dependent model for AHTR fuel fabrication cost; the results are summarized here. While the values of many parameters are not well known, or only known with a very large uncertainty, this model in principle allows correctly evaluating FCC, i.e. accounting for the impact of fuel design on FCC.

The overall approach for calculating FCC is given in [12]. In addition to the cost of uranium ore, conversion and enrichment, the approach accounts for the cost of fuel fabrication, expressed in \$/kgHM. However, it is usually tacitly assumed that this cost is given, fixed, and design independent. As already exemplified, while it is a reasonable assumption when analyzing PWR FCC, where a more accurate treatment would have only a very minor impact, this is not true for AHTR plank fuel.

To address this issue, a fabrication and cost model was developed [11] that explicitly accounts for design specifics of AHTR fuel. Main characteristics of that model are that it accounts for:

- Traditional cost of making enriched uranium (which is still expressed in \$/kgHM)
- Separate cost of fabricating TRISO kernels (which, for a fixed TRISO design, may be translated into \$/kgHM)
- Cost of materials and fabrication efforts needed to make AHTR fuel elements (which is significantly fuel design dependent)

- QA efforts
- Fuel fabrication plant cost (construction and maintenance), which combined with the annual assumed throughput translates into design-dependent fabrication cost per kgHM

Further details are available in [11].

The model requires specific inputs for all relevant variables. Since actual AHTR fuel has never been fabricated, some of these values are not known, i.e., may only be estimated with a fairly large uncertainty. This has been addressed through a sensitivity analysis performed using the low, high, and best estimate values. This produces correct, fuel-design-based estimates, based on our current state of knowledge; as that knowledge improves, updated estimates can be obtained.

Without going into unnecessary details, we will discuss two important fuel cost components, cost of fabricating TRISO particles and cost of fuel element structural materials and fuel element fabrication.

Cost of fabricating relatively small batches of TRISO particles is currently fairly expensive. However, it is assumed that once a large-scale production is established, this cost will go significantly down. The fact that there is no industrial-scale facility leads to a very large uncertainty, several orders of magnitude.

The TRISO particle design assumed in this study is fixed, with the kernel diameter of 0.427 mm, consistent with a representative TRISO design. For a fixed TRISO particle kernel dimension, there is a direct correlation between the fabrication cost per particle, and per kgHM. The initial bench scale production of TRISO particles in 1960s' was associated with a very high cost of ~\$0.20/particle, or about \$500,000/kgU. This is expected to significantly drop with a large scale production, but it is difficult to predict an exact number. Based on references [13] and [14], the range for the fabrication cost used in this study has been assumed as \$2,500-\$25,000/kgU, illustrating this large uncertainty. The low value is about 10 times higher than that for LWRs. After accounting for the higher fissile content (e.g., 20% vs. 5%), it remains 2-3 times higher (in terms of \$ per fissile HM). It is a significant fraction of FCC, but it is still less than the cost of uranium or enrichment. However, the upper value is more than the cost of uranium and enrichment combined, and thus could become the main driver for fuel design decisions.

Cost of structural materials, primarily graphite, is not as high but it is sufficiently high to matter, and it illustrates design-dependent portion of FCC. For illustration, for the range of designs considered (packing fraction in the 10% to 50% range with 7 fuel layers), uranium loading varies between 3.2 kgU and 9.3 kgU, per fuel plate, while the graphite mass per plate changes much less, from 54 kg to 46 kg. In other words, the mass ratio of graphite-per-uranium changes from ~17 to ~5, depending on the design, and consequently that non-fuel portion of FCC changes by a factor over 3 when expressed per kgHM, illustrating how the total FCC becomes fuel design dependent.

9.3 Analyses and brute-force scoping coverage of the fuel design phase space

An integrated analysis was performed combining all relevant aspects. Brute force approach was applied, i.e., FCC was evaluated for all combinations of all values of all design parameters. Optimization-based analysis was later performed, described in Section 9.7

9.3.a Depletion Analysis, Cycle Length and Discharge Burnup

AHTR plank fuel designs was considered. Variation of design variables included enrichment in the 5% to 20% range and packing fraction of TRISO variables in the 10% to 50% range. Depletion analysis was performed using SCALE to determine straight burn (single batch) achievable discharge burnup, which for single batch also represents the cycle length. Given the expected relatively high cost of FHR fuel, straight burn fueling which results in poor fuel utilization is not expected to be an economically viable option. Linear reactivity model (LRM), Ref. [12], was used to estimate corresponding values (cycle length and discharge burnup) for a multi-batch reloading approach. Increasing the number of batches will increase discharge burnup and thus improve fuel utilization, while at the same time it will decrease cycle length and thus make outages more frequent and more costly relative to the energy produced.

Table 9-1. Discharge BU (GWd/MTU) and cycle length (EFPD) for 1 through 3 batches.

Batch		1		2		3	
Enrichment	Packing Factor	Cycle Length (d)	Dis. BU (GWd/MTU)	Cycle Length (d)	Dis. BU (GWd/MTU)	Cycle Length (d)	Dis. BU (GWd/MTU)
5%	10%	86.01	21.22	57.34	28.29	43.01	31.82
	20%	125.16	19.55	83.44	26.07	62.58	29.32
	30%	124.77	14.84	83.18	19.78	62.39	22.25
	40%	101.34	9.95	67.56	13.27	50.67	14.93
	50%	59.67	5.05	39.78	6.73	29.83	7.57
10%	10%	278.48	68.69	185.65	91.58	139.24	103.03
	20%	356.53	55.69	237.69	74.25	178.27	83.53
	30%	342.99	40.78	228.66	54.38	171.50	61.17
	40%	336.08	33.01	224.05	44.01	168.04	49.51
	50%	276.04	23.35	184.02	31.13	138.02	35.02
15%	10%	433.12	106.83	288.75	142.44	216.56	160.25
	20%	566.98	88.56	377.99	118.07	283.49	132.83
	30%	595.86	70.85	397.24	94.46	297.93	106.27
	40%	578.75	56.84	385.84	75.78	289.38	85.26
	50%	525.17	44.42	350.11	59.22	262.58	66.63
19.75%	10%	597.21	147.30	398.14	196.41	298.61	220.96
	20%	756.92	118.22	504.61	157.63	378.46	177.33
	30%	886.40	105.39	590.93	140.52	443.20	158.09
	40%	822.77	80.80	548.52	107.74	411.39	121.20
	50%	786.03	66.48	524.02	88.64	393.02	99.72

Results of this analysis are shown in Table 9-1 for combinations of fuel enrichment and TRISO particles packing factors. For every combination, cycle length and discharge burnup is shown, for a single batch as well as for the 2-batch and 3-batch reloading. Results were also generated for 4 through 6 batches, but for the space limitations are not included here.

We note that some cases result in a very short cycle. While, in principle, the lowest overall FCC should be the selected solution (and the outage cost is accounted for in the model), utilities require certain minimum cycle length. Annual refueling would certainly be acceptable. Six-months refueling may be acceptable if there is a significant economic incentive. Assuming 20 days refueling and operation at 96% average capacity, this translates into 331 and 156 EFPD, respectively.

The lowest considered 5% enrichment does not provide the required cycle length. 10% enrichment may provide annual refueling, but only in single-batch straight-burn case, which leads to poor fuel utilization. It may provide semi-annual refueling with 2-batch and 3-batch refueling. This may be an option if external limitations require limiting enrichment to 10%. 15% enrichment may provide annual cycle with 2-batch refueling. 20% enrichment enables achieving annual cycle with 3-batch or 4-batch (not shown here) refueling, as well as 18-month 2-batch cycle.

While there results already suggest where we may expect to obtain the lowest FCC, the analysis will be performed for the full range of options to gain insight in qualitative behavior of FCC vs fuel design.

9.3.b Enriched Uranium Cost

Uranium ore, conversion and enrichment costs was assumed based on the UXC public data on May 5, 2015, as \$35 per lb U3O8, \$7.50 per kgU, and \$70 per SWU, respectively. Using standard models [12], and assuming tails 0.20%, one can calculate cost of enriched uranium, depending on the enrichment, shown in Table 9-2.

Table 9-2. Cost of enriched uranium (\$/kg)..

Enrichment	Cost (\$/kgU)
5%	1545
10%	3349
15%	5178
19.75%	6927

9.3.c Fuel Fabrication and Fuel Cycle Cost

Fuel fabrication cost included TRISO fabrication cost (\$0.001-\$0.1 per TRISO particle, or \$2,500-\$25,000/kgU), cost of non-fuel materials in fuel element (graphite being the main contributor to the cost, which based on the fuel design translates into \$605-\$1960 per kgU, for details see Ref. [11]), and fuel element fabrication cost itself (without TRISO fabrication). The latter is based on considering

a fuel fabrication plant, its cost and output. The plant capital cost is assumed in the \$0.5-1.5B range, return on investment 4%-12%, annual plant O&M cost \$120M, annual output 27,000-81,000 fuel planks, which translates into anywhere between \$250/kgU and \$5,600/kgU, based on the combination of the assumptions. The total fabrication cost amounted to \$4,900-37,500/kgU, depending on the fuel enrichment, design, and assumed costs. QA cost amounting to 10% of the materials and fabrication cost is accounted for as well.

It is not practical to evaluate all combinations of all assumed cost variables. Instead, three representative cases have been defined, denoted “Lo”, “Mid” and “Hi”, that each combine, respectively, low, middle and high estimates of all relevant variables. Clearly, the resulting total cost estimate will have a very large spread between the Lo case (all low costs) and Hi case (all high costs), but it reflects the state of present knowledge with large uncertainties. A more balanced estimate may be obtained with Monte Carlo sampling for assumed cost distributions; this may be the subject of future study. Total fuel cost for the Lo-Mid-Hi cases, including enriched uranium, is shown in Table 9-3.

Table 9-3. Total fabrication cost (\$/kgU) summary for various fuel designs and cost scenarios.

Packing Fraction	10%	20%	30%	40%	50%
Lo	6996	5813	5336	5068	4892
Mid	13713	12115	11471	11109	10872
Hi	37494	34346	33076	32362	31895

9.3.d Refueling outage

Outage cost is represented by a bulk amount, irrespective of the fuel design, which is a reasonable assumption, at \$20M (low) and \$50M (high) per outage.

9.3.e Integrated FCC

Integrating all the previous analyses and results, the total FCC, including outage cost, may be obtained in \$/kgU. When this cost is divided by the discharge burnup, the FCC-related cost of electricity in \$/MWh may be obtained as a function of the following variables:

- Fuel design (enrichment and packing factor)
- Fuel and fuel fabrication cost (Lo-Mid-Hi)
- Outage cost (Lo-Hi)
- Reloading strategy (number of batches).

Results of FCC analysis are summarized in Tables IV-VI, for Lo, Mid and Hi fuel fabrication costs, respectively. Each table presents results for 4 variables: enrichment (from 5% to 19.75%), packing factor (from 10% to 50%), outage cost (\$20M and \$50M), and number of batches (1 to 6). The

\$/MWh values are color-coded, separately in each table, with low cost values highlighted green, and high cost values highlighted red.

Table 9-4. Fuel cycle cost (FCC) (\$/MWh), including the outage cost, for the 'Lo' fuel fabrication cost scenario.

Lo Fabrication Costs												
	Outage Cost - \$20 Million						Outage Cost - \$50 Million					
	Number of Batches						Number of Batches					
	1	2	3	4	5	6	1	2	3	4	5	6
5%	Packing Factor 10%						Packing Factor 10%					
	\$43.3	\$37.3	\$37.5	\$39.2	\$41.5	\$44.1	\$53.0	\$51.9	\$56.9	\$63.4	\$70.6	\$78.0
	\$15.9	\$13.4	\$13.2	\$13.7	\$14.3	\$15.1	\$18.9	\$17.9	\$19.2	\$21.1	\$23.3	\$25.6
	\$11.8	\$9.8	\$9.6	\$9.8	\$10.2	\$10.6	\$13.7	\$12.7	\$13.4	\$14.6	\$15.9	\$17.4
	\$9.7	\$8.0	\$7.7	\$7.8	\$8.0	\$8.4	\$11.1	\$10.1	\$10.5	\$11.3	\$12.2	\$13.3
10%	Packing Factor 20%						Packing Factor 20%					
	\$39.2	\$32.7	\$32.1	\$32.8	\$34.2	\$35.8	\$45.9	\$42.7	\$45.4	\$49.5	\$54.2	\$59.1
	\$16.8	\$13.8	\$13.3	\$13.4	\$13.8	\$14.4	\$19.2	\$17.3	\$18.0	\$19.3	\$20.8	\$22.5
	\$12.5	\$10.1	\$9.7	\$9.7	\$9.9	\$10.2	\$14.0	\$12.3	\$12.6	\$13.3	\$14.3	\$15.3
	\$10.8	\$8.6	\$8.2	\$8.1	\$8.2	\$8.4	\$11.9	\$10.3	\$10.4	\$10.9	\$11.5	\$12.3
15%	Packing Factor 30%						Packing Factor 30%					
	\$47.5	\$38.9	\$37.6	\$38.0	\$39.2	\$40.7	\$54.1	\$49.0	\$50.9	\$54.7	\$59.2	\$64.1
	\$21.4	\$17.3	\$16.5	\$16.4	\$16.8	\$17.2	\$23.9	\$20.9	\$21.3	\$22.5	\$24.0	\$25.7
	\$14.8	\$11.8	\$11.1	\$11.0	\$11.1	\$11.3	\$16.2	\$13.9	\$13.9	\$14.5	\$15.3	\$16.2
	\$11.5	\$9.1	\$8.5	\$8.4	\$8.4	\$8.5	\$12.4	\$10.5	\$10.4	\$10.7	\$11.2	\$11.8
19.75%	Packing Factor 40%						Packing Factor 40%					
	\$67.3	\$54.6	\$52.2	\$52.3	\$53.5	\$55.2	\$75.5	\$66.9	\$68.6	\$72.9	\$78.2	\$84.0
	\$25.4	\$20.3	\$19.2	\$19.0	\$19.2	\$19.7	\$27.9	\$24.0	\$24.1	\$25.2	\$26.7	\$28.4
	\$17.8	\$14.1	\$13.2	\$12.9	\$13.0	\$13.2	\$19.3	\$16.2	\$16.0	\$16.5	\$17.3	\$18.2
	\$14.6	\$11.4	\$10.6	\$10.4	\$10.4	\$10.5	\$15.6	\$13.0	\$12.6	\$12.9	\$13.4	\$14.0
19.75%	Packing Factor 50%						Packing Factor 50%					
	\$128.1	\$103.1	\$97.8	\$97.6	\$99.2	\$101.9	\$142.1	\$124.1	\$125.8	\$132.5	\$141.2	\$150.8
	\$35.0	\$27.8	\$26.0	\$25.7	\$25.8	\$26.3	\$38.0	\$32.3	\$32.1	\$33.2	\$34.9	\$36.9
	\$22.3	\$17.5	\$16.3	\$15.9	\$15.9	\$16.1	\$23.9	\$19.9	\$19.4	\$19.9	\$20.7	\$21.6
	\$17.4	\$13.6	\$12.5	\$12.2	\$12.1	\$12.2	\$18.4	\$15.2	\$14.6	\$14.8	\$15.3	\$15.9

Table 9-5. Fuel cycle cost (FCC) (\$/MWhe), including the outage cost, for the 'Mid' fuel fabrication cost scenario.

Mid Fabrication Costs												
	Outage Cost - \$20 Million						Outage Cost - \$50 Million					
	Number of Batches						Number of Batches					
	1	2	3	4	5	6	1	2	3	4	5	6
Packing Factor 10%							Packing Factor 10%					
5%	\$71.8	\$58.7	\$56.5	\$57.0	\$58.6	\$60.7	\$81.5	\$73.2	\$75.9	\$81.2	\$87.7	\$94.6
10%	\$24.7	\$20.0	\$19.1	\$19.1	\$19.6	\$20.2	\$27.6	\$24.5	\$25.1	\$26.6	\$28.6	\$30.7
15%	\$17.5	\$14.1	\$13.4	\$13.3	\$13.6	\$13.9	\$19.4	\$17.0	\$17.2	\$18.1	\$19.3	\$20.7
19.75%	\$13.8	\$11.0	\$10.4	\$10.4	\$10.5	\$10.8	\$15.2	\$13.1	\$13.2	\$13.9	\$14.7	\$15.6
Packing Factor 20%							Packing Factor 20%					
5%	\$68.7	\$54.8	\$51.7	\$51.2	\$51.9	\$53.0	\$75.3	\$64.8	\$65.0	\$67.9	\$71.8	\$76.3
10%	\$27.2	\$21.5	\$20.2	\$19.9	\$20.0	\$20.4	\$29.5	\$25.1	\$24.9	\$25.7	\$27.1	\$28.6
15%	\$19.0	\$15.0	\$14.0	\$13.7	\$13.8	\$14.0	\$20.5	\$17.2	\$16.9	\$17.4	\$18.2	\$19.1
19.75%	\$15.7	\$12.3	\$11.4	\$11.2	\$11.2	\$11.3	\$16.8	\$13.9	\$13.6	\$13.9	\$14.5	\$15.1
Packing Factor 30%							Packing Factor 30%					
5%	\$85.5	\$67.5	\$63.0	\$61.8	\$62.0	\$62.9	\$92.2	\$77.5	\$76.3	\$78.5	\$82.1	\$86.3
10%	\$35.3	\$27.7	\$25.7	\$25.1	\$25.1	\$25.3	\$37.7	\$31.3	\$30.6	\$31.2	\$32.4	\$33.8
15%	\$22.8	\$17.8	\$16.4	\$16.0	\$15.9	\$16.0	\$24.2	\$19.9	\$19.2	\$19.5	\$20.1	\$20.9
19.75%	\$16.9	\$13.1	\$12.1	\$11.7	\$11.6	\$11.7	\$17.8	\$14.5	\$14.0	\$14.1	\$14.4	\$15.0
Packing Factor 40%							Packing Factor 40%					
5%	\$123.4	\$96.6	\$89.6	\$87.4	\$87.2	\$88.0	\$131.6	\$109.0	\$106.0	\$108.0	\$111.9	\$116.8
10%	\$42.4	\$33.0	\$30.5	\$29.6	\$29.4	\$29.5	\$44.9	\$36.7	\$35.4	\$35.8	\$36.8	\$38.2
15%	\$27.6	\$21.5	\$19.7	\$19.1	\$18.9	\$18.9	\$29.1	\$23.6	\$22.6	\$22.7	\$23.2	\$24.0
19.75%	\$21.5	\$16.6	\$15.2	\$14.7	\$14.5	\$14.5	\$22.5	\$18.1	\$17.3	\$17.2	\$17.6	\$18.1
Packing Factor 50%							Packing Factor 50%					
5%	\$238.0	\$185.5	\$171.1	\$166.2	\$165.2	\$166.0	\$252.0	\$206.4	\$199.0	\$201.1	\$207.1	\$214.9
10%	\$58.8	\$45.6	\$41.9	\$40.5	\$40.1	\$40.1	\$61.8	\$50.1	\$47.9	\$48.0	\$49.1	\$50.7
15%	\$34.8	\$26.9	\$24.6	\$23.7	\$23.4	\$23.4	\$36.4	\$29.3	\$27.8	\$27.7	\$28.2	\$28.9
19.75%	\$25.7	\$19.8	\$18.1	\$17.4	\$17.1	\$17.1	\$26.8	\$21.4	\$20.2	\$20.0	\$20.3	\$20.8

Table 9-6. Fuel cycle cost (FCC) (\$/MWhe), including the outage cost, for the 'Hi' fuel fabrication cost scenario.

Hi Fabrication Costs												
	Outage Cost - \$20 Million						Outage Cost - \$50 Million					
	Number of Batches						Number of Batches					
	1	2	3	4	5	6	1	2	3	4	5	6
5%	Packing Factor 10%						Packing Factor 10%					
	\$172.	\$134.	\$123.	\$119.	\$118.	\$119.	\$181.	\$148.	\$142.	\$144.	\$147.	\$153.
	2	0	4	8	8	3	9	6	8	0	9	2
	\$55.7	\$43.3	\$39.8	\$38.5	\$38.2	\$38.3	\$58.7	\$47.7	\$45.8	\$46.0	\$47.2	\$48.8
	\$37.4	\$29.0	\$26.7	\$25.8	\$25.5	\$25.6	\$39.3	\$31.9	\$30.5	\$30.6	\$31.3	\$32.3
19.75%	\$28.3	\$21.9	\$20.1	\$19.4	\$19.2	\$19.2	\$29.7	\$24.0	\$22.9	\$22.9	\$23.4	\$24.1
5%	Packing Factor 20%						Packing Factor 20%					
	\$172.	\$132.	\$120.	\$116.	\$114.	\$113.	\$179.	\$142.	\$134.	\$132.	\$134.	\$136.
	4	6	8	1	1	5	0	6	2	7	1	8
	\$63.6	\$48.9	\$44.5	\$42.7	\$41.9	\$41.6	\$65.9	\$52.4	\$49.1	\$48.5	\$48.9	\$49.8
	\$41.9	\$32.2	\$29.3	\$28.0	\$27.5	\$27.3	\$43.4	\$34.4	\$32.2	\$31.7	\$31.9	\$32.5
19.75%	\$32.8	\$25.2	\$22.8	\$21.9	\$21.4	\$21.3	\$33.9	\$26.8	\$25.1	\$24.6	\$24.7	\$25.1
5%	Packing Factor 30%						Packing Factor 30%					
	\$219.	\$167.	\$152.	\$145.	\$142.	\$141.	\$226.	\$177.	\$165.	\$162.	\$162.	\$164.
	4	9	2	5	3	0	1	9	6	2	4	3
	\$84.0	\$64.2	\$58.2	\$55.5	\$54.3	\$53.7	\$86.4	\$67.9	\$63.0	\$61.6	\$61.6	\$62.2
	\$50.8	\$38.8	\$35.1	\$33.5	\$32.7	\$32.3	\$52.2	\$40.9	\$37.9	\$37.0	\$36.9	\$37.2
19.75%	\$35.7	\$27.2	\$24.6	\$23.5	\$22.9	\$22.7	\$36.6	\$28.7	\$26.5	\$25.8	\$25.7	\$25.9
5%	Packing Factor 40%						Packing Factor 40%					
	\$320.	\$244.	\$221.	\$210.	\$205.	\$203.	\$328.	\$256.	\$237.	\$231.	\$230.	\$231.
	5	5	0	6	5	0	8	8	4	2	2	8
	\$101.						\$104.					
	8	\$77.6	\$70.1	\$66.7	\$65.1	\$64.2	3	\$81.3	\$75.0	\$72.9	\$72.5	\$72.9
19.75%	\$62.2	\$47.3	\$42.7	\$40.7	\$39.6	\$39.1	\$63.6	\$49.5	\$45.6	\$44.3	\$43.9	\$44.1
19.75%	\$45.8	\$34.8	\$31.4	\$29.9	\$29.1	\$28.7	\$46.8	\$36.4	\$33.4	\$32.4	\$32.1	\$32.2
5%	Packing Factor 50%						Packing Factor 50%					
	\$623.	\$474.	\$428.	\$407.	\$396.	\$391.	\$637.	\$495.	\$456.	\$442.	\$438.	\$439.
	8	8	3	3	6	0	7	8	2	2	5	9
	\$142.	\$108.					\$145.	\$112.	\$103.	\$100.		
	1	1	\$97.4	\$92.6	\$90.1	\$88.8	2	6	5	2	\$99.2	\$99.4
19.75%	\$78.6	\$59.7	\$53.8	\$51.1	\$49.7	\$48.9	\$80.2	\$62.1	\$57.0	\$55.1	\$54.5	\$54.5
19.75%	\$55.0	\$41.8	\$37.6	\$35.7	\$34.7	\$34.1	\$56.1	\$43.4	\$39.7	\$38.4	\$37.9	\$37.9

The following observations can be made:

1. Each 4-by-6 “sub-table” shows the cost for variable enrichment and variable number of batches, for certain packing factor, and for either low outage cost (left) or high outage cost (right).
2. In each sub-table, for all cases, the lowest cost is achieved with highest enrichments. This is to be expected, since the high fuel fabrication cost is then spread over more fissile material.
3. Optimum number of batches is in all cases greater than one, confirming that for the expensive fuel, straight burn with poor fuel utilization is not an option.
4. In general, high fabrication cost will make the issue of fuel utilization more significant. Additionally, low outage cost may allow using more batches, since the penalty due to frequent refueling is not as large, and fuel utilization and discharge burnup are improved. Thus, Hi fabrication cost combined with low outage favors going to 4 or more batches from the purely cost analysis, even though the cycle length may become unacceptably short for the utility. This may be moot in any case, since the Hi fuel cost case may not be economically viable.
5. On the other end, Lo fabrication cost and high outage cost would put more emphasis on balancing the opposing costs of outage and fuel, resulting in fewer batches being optimum. For the cases of interest (20% enrichment, and 20-30% packing factor, 2 or 3 batches provide optimum.
6. Considering 5 vertical sub-tables in each case (for 5 different packing factors), and focusing on the preferred 20% enrichment (and perhaps 15%), one can observe that lower costs are found for the packing factor in the 10%-30% range. Higher packing factors provide more fissile material, but also lead to significantly undermoderated cores with poor fuel utilization. On the low end, 10% packing fraction, one would need to fabricate notably more fuel assemblies, increasing the cost and partly offsetting improved utilization. Also, cycle length requirement (see Table I) may preclude some of the combinations.
7. Utility may be willing to accept slightly higher cost, perhaps a few percent, for somewhat longer cycle. In some of the previously discussed cases, this may push decision to fewer batches (e.g., 2 rather than 3 for Lo-fab and Hi-outage cost, and 3 or 4 rather than 4-6 for Hi-fab Lo-outage cost), and to higher packing fraction (20% or 30% rather than 10% or 20%).

In summary, for the assumptions used in this study and resulting FCC-related COE, combined with utility preference for longer cycle, the optimum fuel designs and refueling strategies would employ 20% enrichment, 20%-30% packing fraction, and 2-4 batches, with fine-tuning as previously discussed.

9.4 Importance of fuel-design-dependent FCC analysis

Let us use the results to illustrate the need for the fairly complex fuel-design-dependent FCC model introduced in this work. We argued that, in contrast to LWR, due to higher AHTR fuel fabrication cost, and potentially significant impact of fuel design on FCC, it needs to be taken into account in adequate detail. Figure 9-1 confirms and illustrates this claim using representative results for 10% enriched fuel, 2-batch refueling, and Hi outage cost.

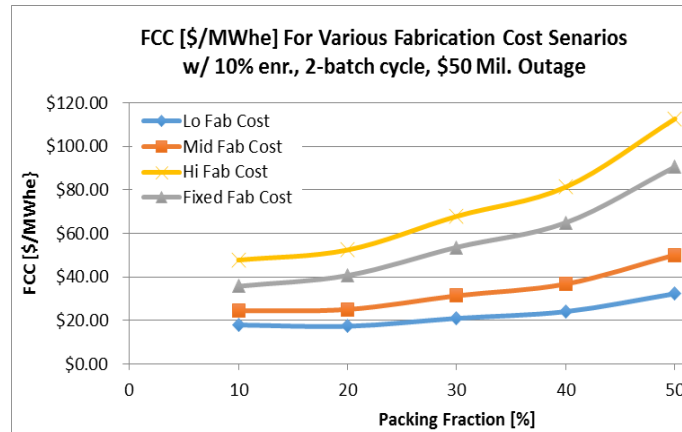


Figure 9-1. Fuel plate FCC vs. packing fractions for different fabrication cost scenarios (all cases assume 10% enriched fuel, 2-batch refueling).

Figure 9-1 depicts FCC vs, packing fraction; moreover, it compares the three fuel-design-dependent FCC cost scenarios (Lo-Mid-Hi) introduced in this paper against the gray curve which assumes fuel-design-independent fabrication cost, i.e., constant in terms of \$/kgU. Behavior of the Hi fab case is similar to that of the fixed fab cost case. The reason is that the Hi fab cost case is to large extent driven by the high cost of fabricating TRISO particles, and that cost component (for the assumed fixed TRISO particle design) is indeed fixed in terms of \$/kgU. Therefore, both the fixed and fuel dependent curve exhibit similar behavior, pointing to the low packing fraction as the optimum choice.

However, in the Low fab case, impact of the fuel-design-dependent cost component is non-trivial, Low packing fraction fuel is now visibly penalized by the higher cost of fabricating more fuel elements, and as the result the fuel-design-dependent cost and fixed cost curves lead to different optimum solutions. The former is now notably flatter, and as the result packing fraction range 10%-40% seems competitive. In other words, the fixed fuel fabrication cost model produces biased results that potentially may point to a non-optimum fuel design.

9.5 Findings of the parametric scoping FCC study

Due to its inherently low heavy metal loading and high fuel fabrication cost, plank fuel used in AHTR provides specific challenges to cycle length and FCC. Moreover, simplified assumptions on fuel fabrication cost, such as those traditionally used in LWR FCC analysis, do not provide accurate results. Therefore, an FCC model is introduced that does account for a specific plank fuel design (enrichment, packing fraction, geometry, etc.) and allows identifying fuel design region(s) with near-optimum FCC. Lowest FCC is generally achieved in fuel designs employing highest allowed LEU enrichment (19.75%) with enhanced moderation (packing fraction in the 10%-30% range), and with multibatch refueling (2 batches for high outage cost; 3-4 batches for low outage cost). Additionally, sensitivity analysis was performed to address large uncertainties in the assumptions. While the specific results may need to be revisited as more accurate information on all FCC components cost becomes available, the important contribution of this paper is in introducing an integrated framework with models and methodology enabling evaluation of fuel-design-dependent FCC, and, with the

information currently available, generating preliminary but comprehensive results to guide future AHTR design improvements. Moreover, the sensitivity analysis provides insight into the impact and importance of various parameters.

9.6 References for sections 9.1 to 9.5

1. S. Greene, J. Gehin, D. Holcomb, J. Carbajo, D. Ilas, A. Cisneros, et al., "Pre-Conceptual Design of a Fluoride-Salt-Cooled Small Modular Advanced High-Temperature Reactor (SmAHTR)," *ORNL/TM-2010/199*, Oak Ridge National Laboratory, Oak Ridge, TN (2010).
2. D. Holcomb, D. Ilas, A. L. Qualls, F. Peretz, V. Varma, E. Bradley, et al., "Current Status of the Advanced High Temperature Reactor," *Proc. ICAPP '12*, Chicago, IL, June 24-28, 2012, on CD-ROM, American Nuclear Society, LaGrange Park, IL (2012).
3. D. Ilas, D. Holcomb, V. K. Varma, "Advanced High-Temperature Reactor Neutronic Core Design," *Proc. PHYSOR 2012 - Advances in Reactor Physics - Linking Research, Industry, and Education*, Knoxville, TN, April 15-20, 2012, on CD-ROM, American Nuclear Society, LaGrange Park, IL (2012).
4. D. Holcomb, F. Peretz, A. L. Qualls, "Advanced High Temperature Reactor Systems and Economic Analysis," *ORNL/TM-2011/364*, Oak Ridge National Laboratory, Oak Ridge, TN (2011).
5. S. M. Lewis, *Simplified Core Physics and Fuel Cycle Cost Model for Preliminary Evaluation of LSCR Fueling Options*. Master's Thesis, Georgia Institute of Technology, Nuclear and Radiological Engineering, Atlanta, GA (2014).
6. P. Avigni, B. Petrovic, "Fuel Element and Full Core Thermal-Hydraulic Analysis of the AHTR for the Evaluation of the LOFC Transient," *Annals of Nuclear Energy*, **64**, 499-510 (2014).
7. A. T. Cisneros, D. Ilas, "Neutronics and Depletion Methods for Parametric Studies of Fluoride-Salt-Cooled High-Temperature Reactors with Slab Fuel Geometry and Multi-Batch Fuel Management Schemes," *Proc. PHYSOR 2012 - Advances in Reactor Physics - Linking Research, Industry, and Education*, Knoxville, TN, April 15-20, 2012, on CD-ROM, American Nuclear Society, LaGrange Park, IL (2012).
8. R. Kelly, D. Ilas, "Verification of a Depletion Method in SCALE for the Advanced High Temperature Reactor," *Proc. PHYSOR 2012 - Advances in Reactor Physics - Linking Research, Industry, and Education*, Knoxville, TN, April 15-20, 2012, on CD-ROM, American Nuclear Society, LaGrange Park, IL (2012).
9. M. Huang, B. Petrovic, "Use of MCDancoff Correction Factor for Multi-Group Fuel Depletion Analysis of Liquid Salt Cooled Reactors", *Proc. PHYSOR 2014*, Kyoto, Japan, September 28 – October 3, 2014, on CD-ROM (2014).
10. M. Huang, *MC Dancoff correction to the LSCR SCALE model*, Private communications (July 6, 2014).
11. C. Kingsbury, B. Petrovic, "Updated Fuel Cycle Cost Model of the Fluoride-salt-cooled High-temperature Reactor (FHR) Based on Neutronic Calculations Using MC Dancoff Factors", *Proc. Advances in Nuclear Fuel Management V (ANFM 2015)*, Hilton Head Island, SC, March 29 – April 1, 2015, on CD-ROM, American Nuclear Society, LaGrange Park, IL (2015).

12. R. Cochran, N. Tsoulfanidis, *The Nuclear Fuel Cycle: Analysis and Management* (2nd ed.), American Nuclear Society, LaGrange Park, IL (1990).
13. D. Shropshire, K. Williams, J. Smith, B. Dixon, M. Dunzik-Gougar, R. Adams, et al., "Advanced Fuel Cycle Cost Basis," *INL/EXT-07-12-107 Rev. 2*, Idaho National Laboratory, Idaho Falls, ID (2009)
14. E. Grubert, et al., "Pebble Bed Modular Reactors Versus Other Generation Technologies: Costs and Challenges for South Africa", *Proc. GLOBAL 2011*, Makuhari, Japan, Dec. 11-16, 2011, on CD-ROM (2011).

9.7 FCC optimization model

Previous sections described the initial brute-force parametric scoping study. This section describes optimization based on an optimization algorithm.

The fuel plank design optimization methodology for the LSCR is developed to search for the optimal configuration that minimizes fuel cycle cost. This methodology addresses the neutronics modeling challenges of double heterogenous fuel. It also includes the use of the non-linear reactivity model since the linear-reactivity model is not sufficiently accurate for modeling 19.75% enriched fuel with a slightly harder neutron spectrum. The methodology starts with preparing data that is necessary for accurate depletion calculations including average temperatures in the fuel, coolant, and moderator. Also, the multi-group transport calculations are corrected with the MCDancoff Factor to account for the double heterogenous geometry. The depletion calculations then provide reactivity over the cycle length used to calculate multi-batch cycle lengths with the non-linear reactivity model. A full core leakage correction factor, depending on the carbon-to-heavy metal ratio, is applied to correct the cycle length since the transport model used for optimization is a fuel assembly model. Artificial neural network regression models are created to approximate the MCDancoff Factors over the design space and then used again to approximate the whole physics model which is combined with the cost model to create the objective function used for optimization. Figure 9-2 shows a flow chart of the design optimization methodology.

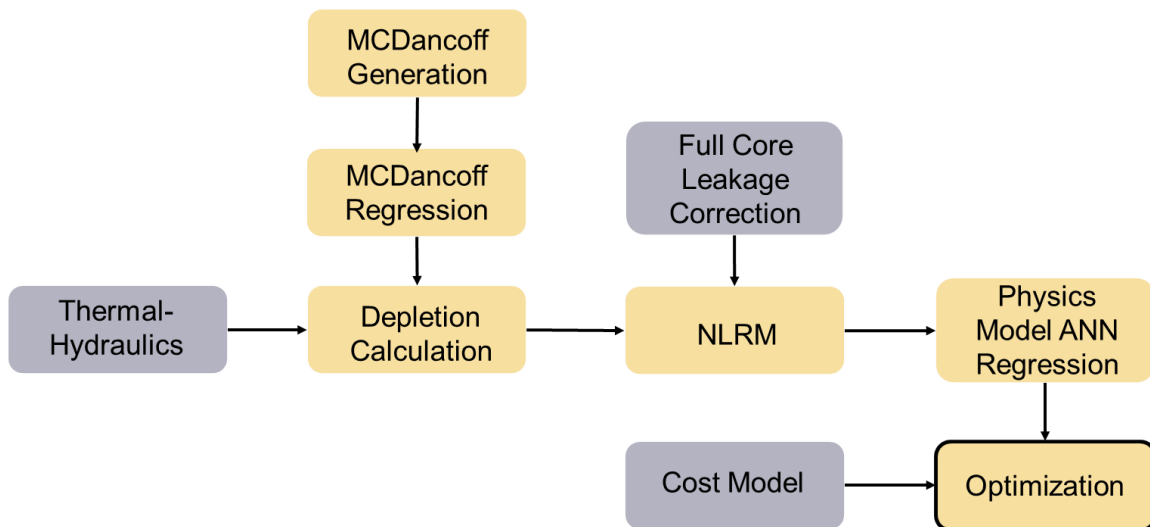


Figure 9-2. Flowchart of the overall fuel design optimization methodology.

9.7.a Artificial Neural Network Models

Artificial Neural Network (ANN) regression models are used to create a MCDancoff Factor surrogate model and a multi-batch cycle length NLRM surrogate model over the design space. The type of ANN used to perform regression in this research is the Multi-layered Perceptron (MLP). The networks architecture is characterized by input nodes each connected through weighted edges to the hidden

layers of nodes. The MLP used for regression in this study uses multiple layers of hidden nodes and is considered a deep neural net. One hidden layer of nodes is sufficient for a theoretically perfect fit, but additional layers provides a quicker convergence. Figure 9-3 shows the architecture for the MLP used to provide a regression model for the MCDancoff Factor.

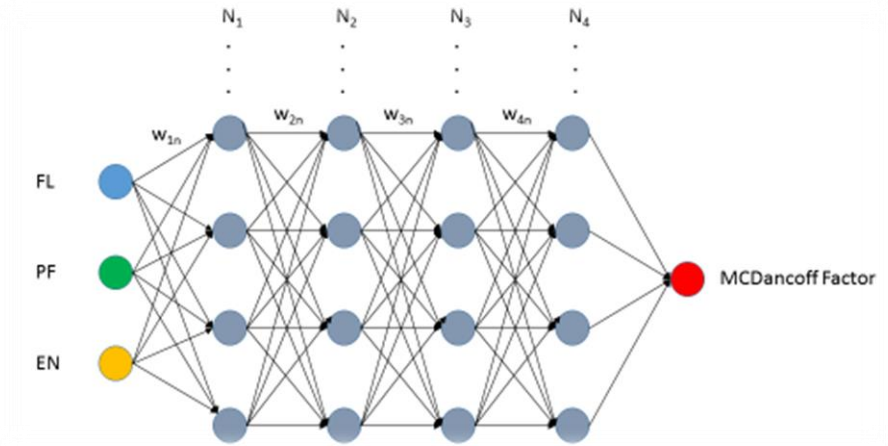


Figure 9-3. Architecture of the MLP with 3 inputs and one output. The hidden layers are shown to have arbitrary size.

$$output = \sum_{i=1}^I w_i f^i \left(\sum_{j=1}^J w_j f^j \left(\sum_{k=1}^K w_k f^k \left(\sum_{l=1}^L (w_l x_l - \theta_l) - \theta_k \right) - \theta_j \right) - \theta_i \right)$$

The above equation shows the sum of weights, w , multiplied by the activation function, f , which is a function of sum the previous layers output minus a bias, usually set to 1. The input layer multiplies the input value, x , by the respective weight. Each layer feeds its output forward until it reaches the output layer. The ANN model must be trained in order to give a good fit. The model is trained using data sampled with Periodic Latin Hypercube Sampling. The method used to train the data is Backward Propagation with Stochastic Gradient Decent. In order to provide a faster and deeper convergence the algorithm was modified to use a pulsed exponentially decaying learning rate, which corresponds to the step length when descending the gradient. ANN models are known to be unstable models. In order to reduce the instability of the results bootstrap aggregation is used in the NLRM regression model in order to produce consistent optimization results.

ANN regression provides a significantly better fit than multiple polynomial regression. Figure 9-4 shows a comparison between the two regression models. The ANN regression curves shows better interdependence between the variables and how they affect the approximated MCDancoff Factor. Table 9-7 shows the resulting error in the fit for the multiple polynomial and ANN regression models. The ANN model has a standard error 57% lower than the multiple polynomial regression model. The standard error is very close to the standard deviation of K-infinity of the CE transport model, meaning that the ANN fit is as good as it can be.

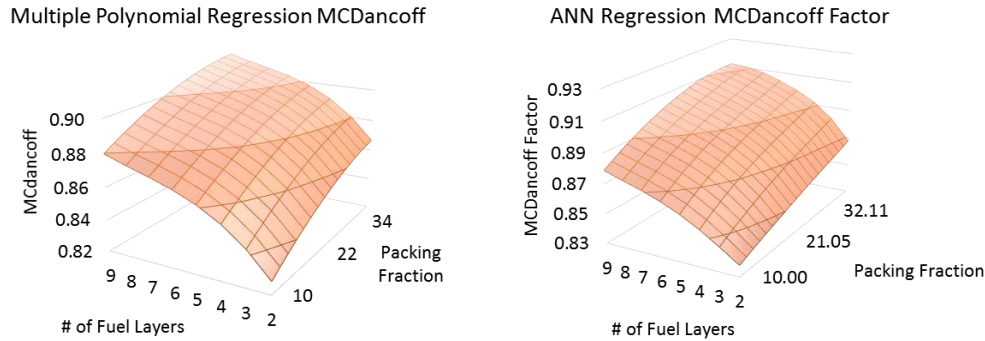


Figure 9-4. ANN MCDancoff Factor regression model compared with Multiple Polynomial regression MCDancoff Factor model.

Table 9-7. Results comparing the fit of the regression models.

Regression Method	Std Error (pcm)	Max Residual (pcm)	R ²
Multiple Polynomial	56	140	0.99880
ANN	32	98	0.99961

9.7.b Cost Model Integration

The fuel cost model developed by Chris Kingsbury was integrated with the NLRM regression model and expanded to include number of fuel layers as an additional parameter. The fuel cost model is automated in python in order to evaluate designs sampled within the optimization algorithm. The final fuel cycle cost calculation, which is the objective function to minimize over is within the optimization algorithm script which imports the fuel cost model. Table 9-8 shows the cost model over the design space with enrichment held constant at 19.75%.

Table 9-8. Fuel manufacturing cost model in \$/kgU.

FL/PF	10.00	12.14	14.29	16.43	18.57	20.71	22.86	25.00	27.14	29.29	31.43	33.57	35.71	37.86	40.00
2	65521	61938	59275	57205	55542	54170	53017	52030	51176	50426	49763	49172	48640	48159	47721
3	55684	53295	51520	50140	49031	48116	47347	46690	46120	45621	45179	44784	44429	44109	43817
4	50765	48973	47642	46607	45775	45090	44513	44020	43592	43218	42886	42590	42324	42084	41865
5	47814	46380	45315	44487	43822	43273	42812	42417	42075	41776	41511	41274	41061	40869	40693
6	45846	44652	43764	43074	42520	42063	41678	41349	41064	40815	40594	40396	40219	40059	39913
7	44441	43417	42656	42065	41590	41198	40868	40586	40342	40128	39939	39770	39618	39480	39355
8	43387	42491	41825	41308	40892	40549	40261	40014	39800	39613	39447	39299	39166	39046	38937
9	42567	41771	41179	40719	40349	40045	39788	39569	39379	39213	39065	38934	38816	38709	38611

The cost model shows the cost of manufacturing fuel per kg U increases with decreasing heavy metal loading. However, increased fuel loading leads to poorer fuel utilization, and doesn't necessarily improve cycle length for regions of the design space that are heavily undermoderated. The objective

function, which determines fuel cycle cost shows the contributions of fuel utilization and cycle length to the fuel cycle cost. The objective function is shown below:

$$FCC = \frac{Cost_{fuel\ manufacturing} [\$/kgU]}{BU [GWd/tHM] * 24 [h/d] * \eta} + \frac{(Cost_{outage} [\$])}{(CL [FPD] * 3400 [MWth] * 24 [h/d] * \eta)} (\$/MWh)$$

9.7.c Optimization

The Differential Evolution Algorithm (DE) is a global heuristic optimization algorithm under the category of evolutionary algorithms. It is somewhat similar to Genetic Algorithms (GAs) since it has a population of designs with variables that are exchanged amongst the designs. However, GA's exchange variables through mating while DE mutates its population by linear transformations randomly between each member of the population. In general DE outperforms GA both in reliability of solutions and in runtime. Figure 9-5 is the flowchart of how DE progresses.

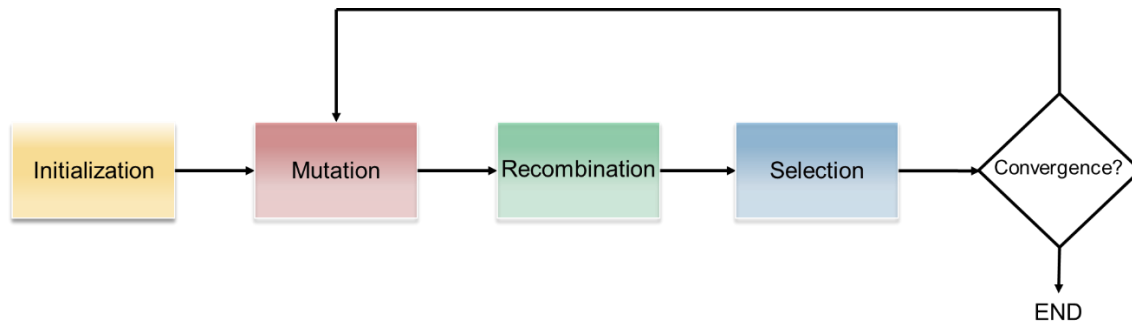


Figure 9-5. Flowchart of DE global heuristic optimization algorithm.

First the parameters are initialized. Then the population is generated randomly over the design space. Next, the loop of the algorithm starts with mutation over the population. Each member of the population goes through mutation in series. The parameter vector of the member of the population is called the target vector. Three other member parameter vectors are chosen at random to generate the donor vector through a linear transformation. Then in recombination the trial vector is generated when the parameters from the donor vector donates each parameter value to the target vector with a probability of acceptance given by the crossover ratio, an input parameter between [0,1]. Finally, in the last step of the generation, selection, the trial vector and the target vector are evaluated based on the objective function. The trial vector and the target vector are compared on merit and the better of the two determines the parameters of the member in the next generation. If the target vector is the better design, then it remains in the population until it is mutated resulting in a better design. This process of mutation, recombination, and selection repeats until convergence. Figure 9-6 shows a visualization of the mutation step. Figure 9-7 shows a visualization of recombination.

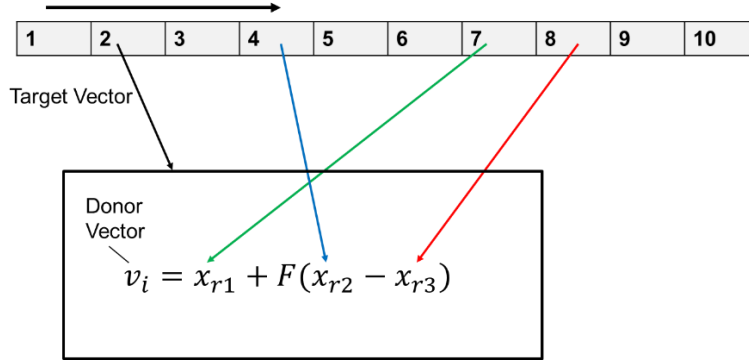


Figure 9-6. Visualization of mutation. The red, green, and blue arrow show 3 random members contributing their parameter vectors to the mutation linear transformation.

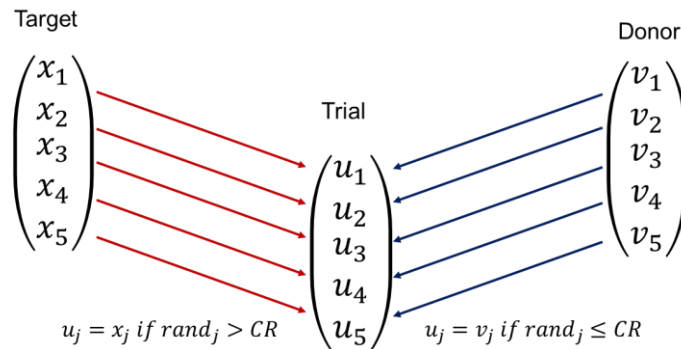


Figure 9-7. Visualization of recombination. Each value of u_j comes from either x_j or v_j depending on a random number and if it is larger than CR .

The optimization calculations are performed with a population of 100 and a convergence criterion of 300 generations without improvement. Eight ANN trained with bootstrap training sets with averaged outputs provide the physics model for the DE algorithm. The resulting optimal design has 3.77 fuel layers, 40% packing fraction, 19.75% enrichment, and a 3.4 batch fuel cycle giving a fuel cycle cost of 24.028 \$/MWh. The optimum design has a CHM ratio of 389. This is much higher than the base 2011 Oak Ridge National Laboratory design, but is very similar to the updated design described in more recent papers.

By using surrogate models and algorithmically searching for the optimum the solution is significantly improved. Previous optimization work which did not include number of fuel layers as a parameter and did not use an algorithmic search gave a fuel cycle cost of 26.0 \$/MWh. Global heuristic optimization algorithms enable efficient optimum search over many parameters in a non-linear design space. It would be impractical to simply sample many cases over many dimensions to try and find a best solution. Figure 9-8 shows how the best solution in the population changes and moves over the design space to the optimum. Table 9-9 is a table of sampled designs showing the optimum calculated by DE is better than sampling many cases. Figure 9-9 shows the evolution of the best solution in the population through the multi-dimensional design space. Figure 9-10 shows the convergence of the solution as the algorithm progresses through the generations. It can be seen that the DE algorithm converges quickly and efficiently. The runtime is roughly 8 minutes.

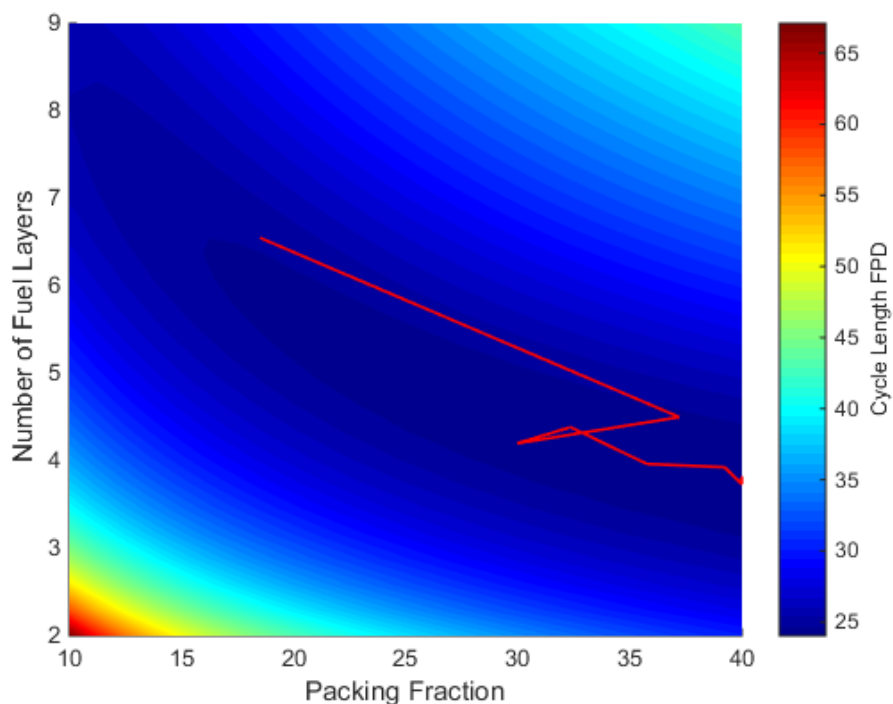


Figure 9-8. Evolution of the best solution over the design space with enrichment held constant at 19.75% and number of batches held at 3.33.

Table 9-9. Results from optimization showing the algorithmic solution is better than tabulated results.

FL/PF	31.25	32.5	33.75	35	36.25	37.5	38.75	40
2	34.316	33.599	32.928	32.303	31.72	31.178	30.674	30.207
2.291667	31.427	30.822	30.264	29.749	29.276	28.84	28.44	28.071
2.583333	29.194	28.694	28.238	27.824	27.446	27.103	26.79	26.505
2.875	27.484	27.081	26.718	26.391	26.098	25.834	25.597	25.384
3.166667	26.201	25.885	25.604	25.356	25.138	24.945	24.775	24.627
3.458333	25.273	25.035	24.83	24.654	24.504	24.377	24.271	24.185
3.75	24.643	24.481	24.347	24.241	24.158	24.096	24.054	24.029
4.041667	24.277	24.188	24.127	24.091	24.077	24.083	24.107	24.146
4.333333	24.152	24.141	24.156	24.194	24.253	24.329	24.421	24.525
4.625	24.259	24.329	24.424	24.54	24.673	24.821	24.98	25.147
4.916667	24.587	24.742	24.918	25.112	25.318	25.533	25.756	25.982
5.208333	25.121	25.359	25.613	25.878	26.151	26.429	26.708	26.987

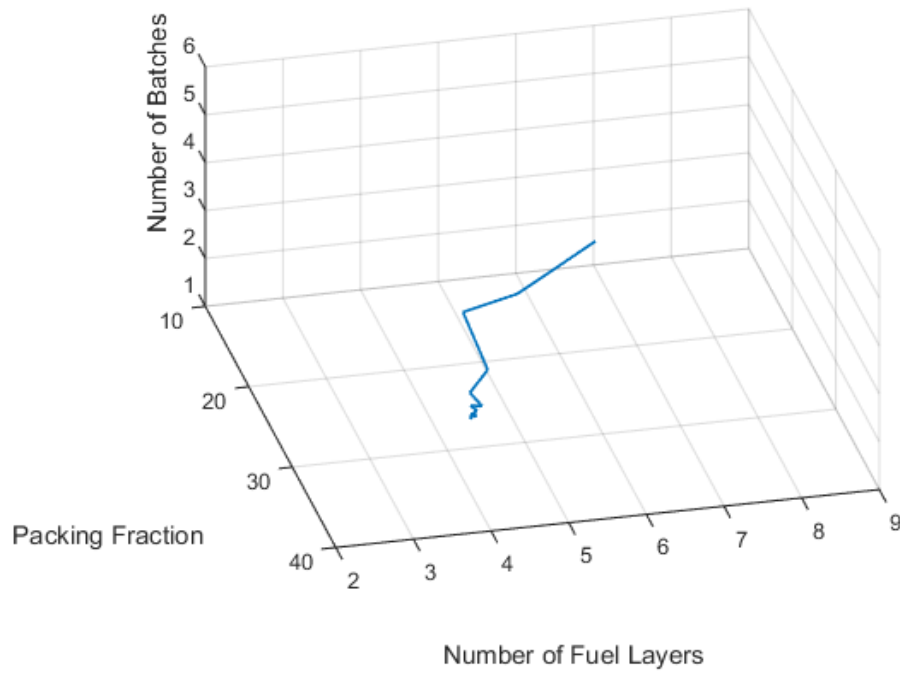


Figure 9-9. Evolution of the best solution in the multi-dimensional design space.

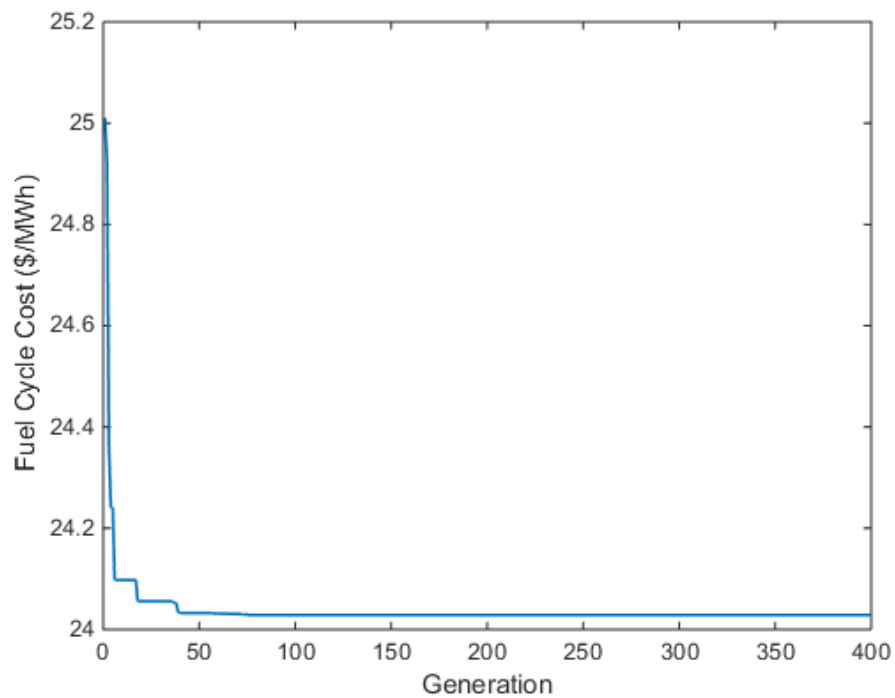


Figure 9-10. Fuel cycle cost (\$/MWh) quickly converging as algorithm progresses through generations.

10. Thorium Fuel and In-Situ Breeding (Tasks 4)

10.1 QUADRISO Arrangement

Based on the studies carried out by Talamo [1] indicating the increased reactivity of the QUADRISO arrangement, it was believed that this might make the once through open cycle a more viable option and so some simple tests cases were run in which a ThO_2 layer of various thicknesses was placed around the fuel kernel and inside the porous carbon layer, while all other QUADRISO layer thicknesses were kept the same and particle packing fraction adjusted to preserve the fuel kernel mass between models. It should be noted that because the Heavy Metal mass of the fuel was increased with the addition of thorium, the specific power of the models was adjusted to reflect this increase. Additionally, because the thorium was added with no adjustment to particle layer thicknesses or kernel radius it should be kept in mind that moderating carbon in the matrix was displaced.

The results can be observed in Figure 10-1, Figure 10-2, Figure 10-3, Figure 10-4, Figure 10-5, and Figure 10-6 (NOTE: masses that are provided correspond to a 2D model for a single assembly so no specific units are provided being that it would be $\frac{g}{cm \cdot assembly}$). It can be deduced from looking at the plots that the thorium layer shields the kernel initially providing a shielding effect, but as the thorium burns out, and other fissile isotopes burn in (i.e. ^{233}U and ^{239}Pu) the reactivity begins to recover and eventually achieves non-thorium reactivity levels around 1700 EFPD. Talamo's study [1] determined that it might be possible to employ kernel homogenization to achieve a greater initial lowering of K_{eff} if desired. Unfortunately, it can be seen that the thorium fuel does not achieve as high a burnup as the non-thorium fuel and overall has a higher end of life fissile inventory from the decreased burning of ^{235}U and ^{239}Pu , and production of ^{233}U . Similar fuel inventory results are expected for a kernel homogenization based on the study by Talamo [1].

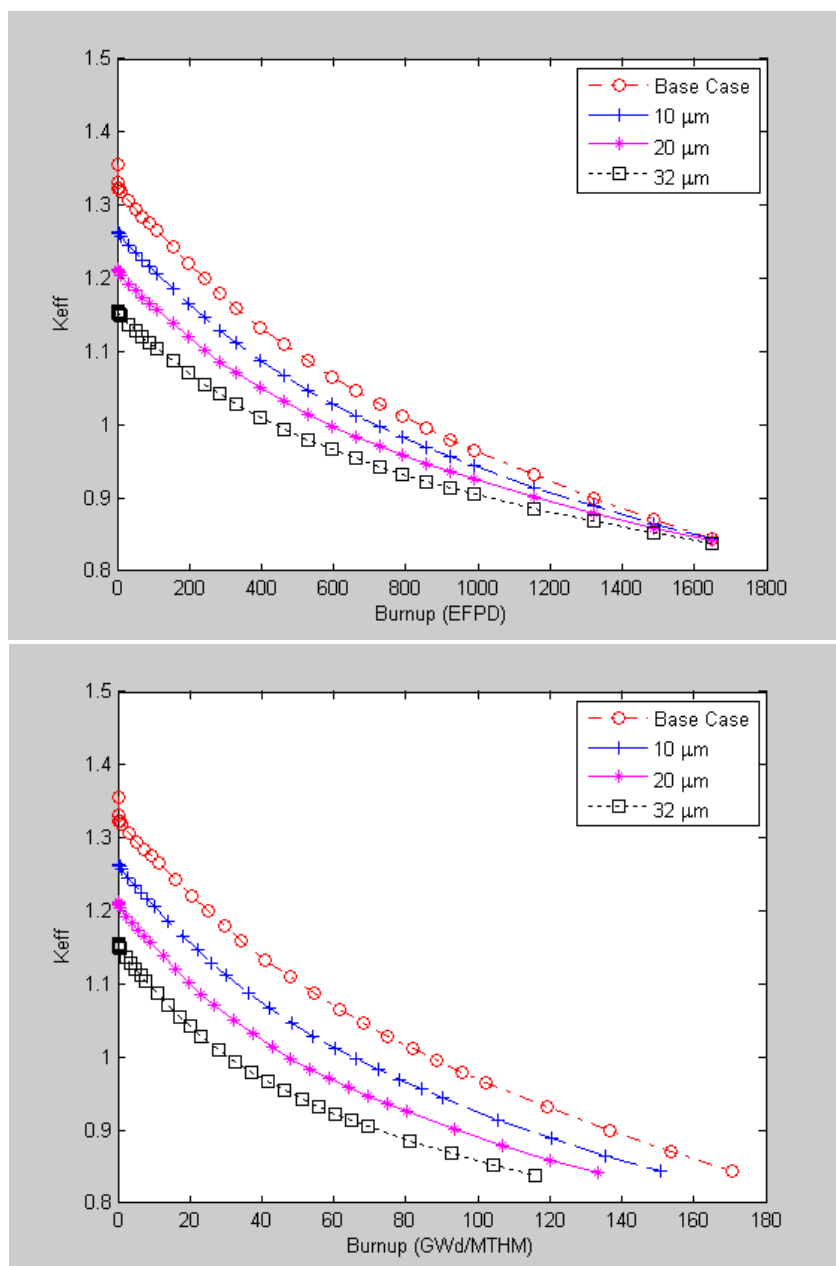


Figure 10-1. K -infinity vs. EFPD and vs Burnup

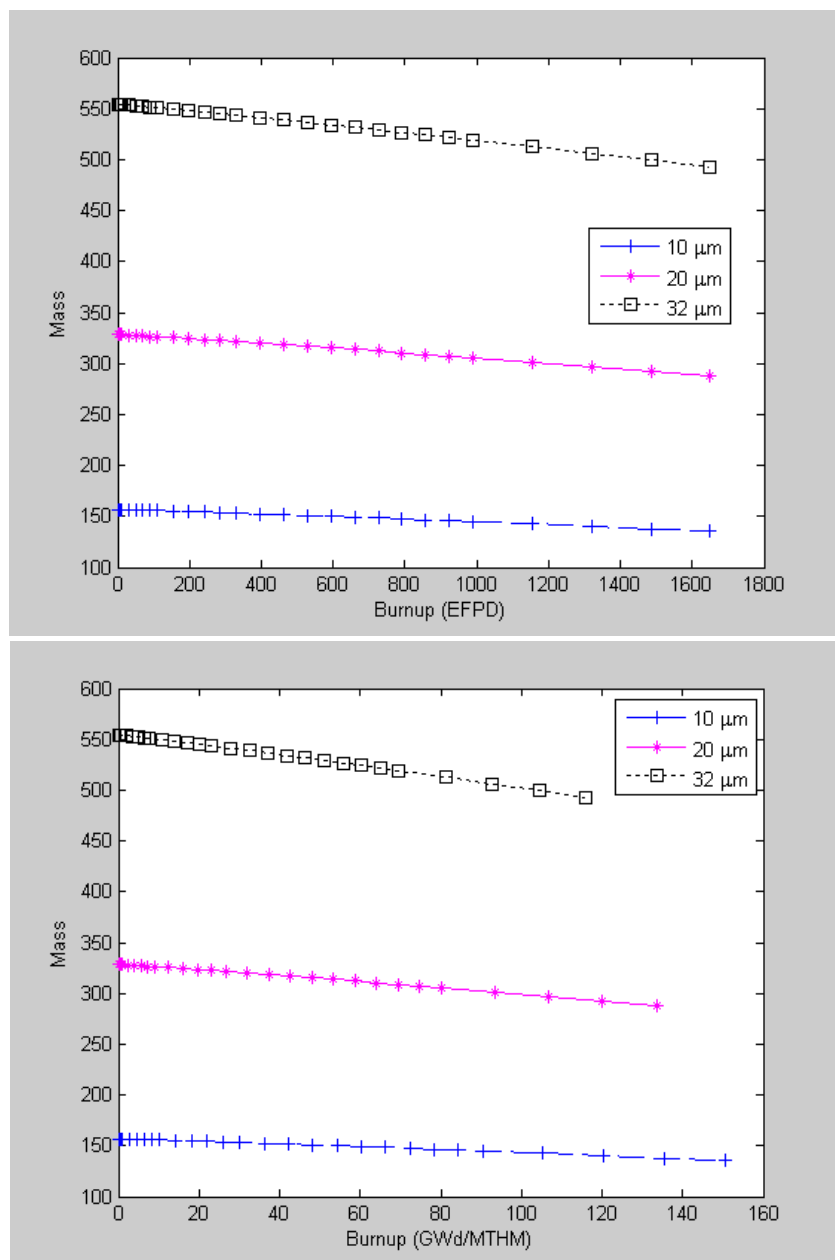


Figure 10-2. ^{232}Th Mass vs. Burnup (top) and vs EFPD (bottom)

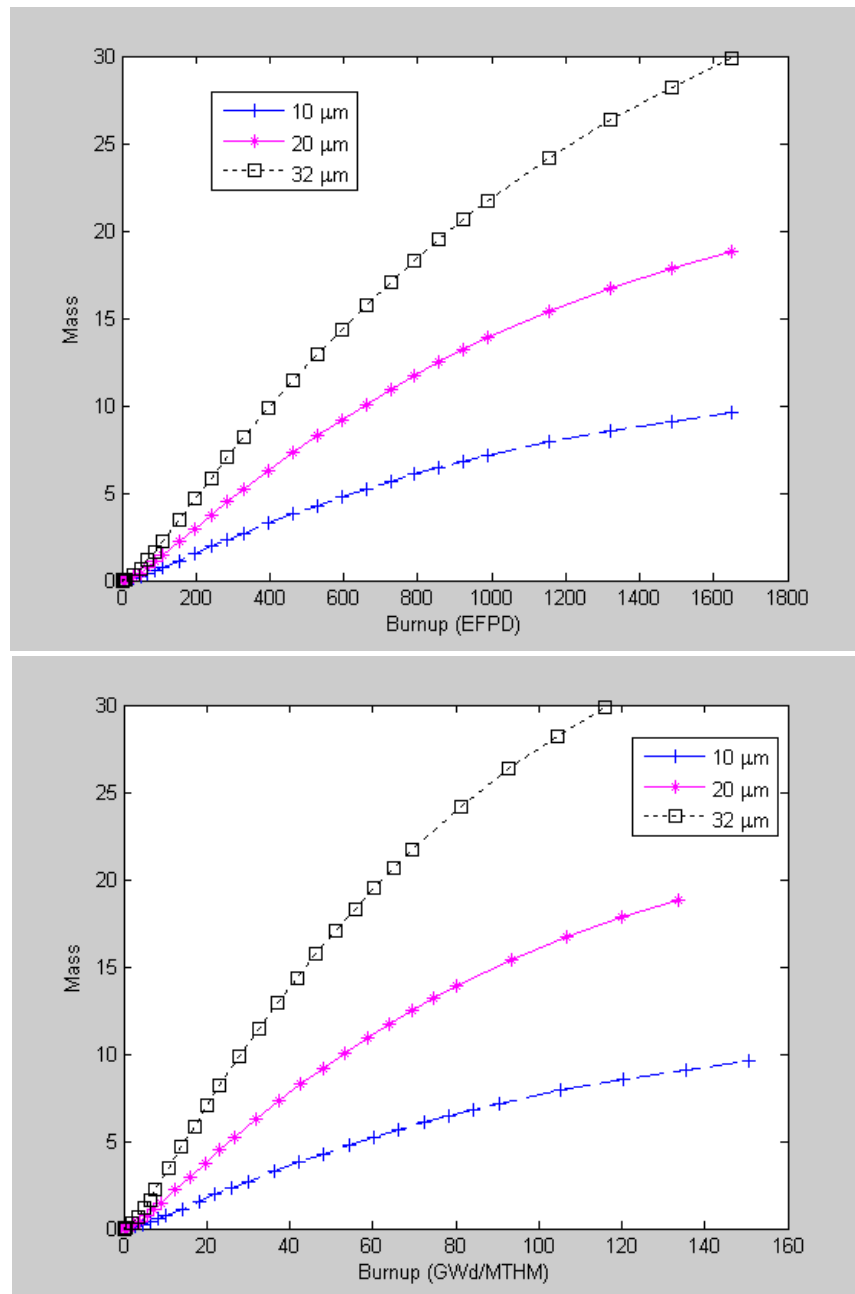


Figure 10-3. ^{233}U Mass vs. Burnup (top) vs EFPD (bottom)

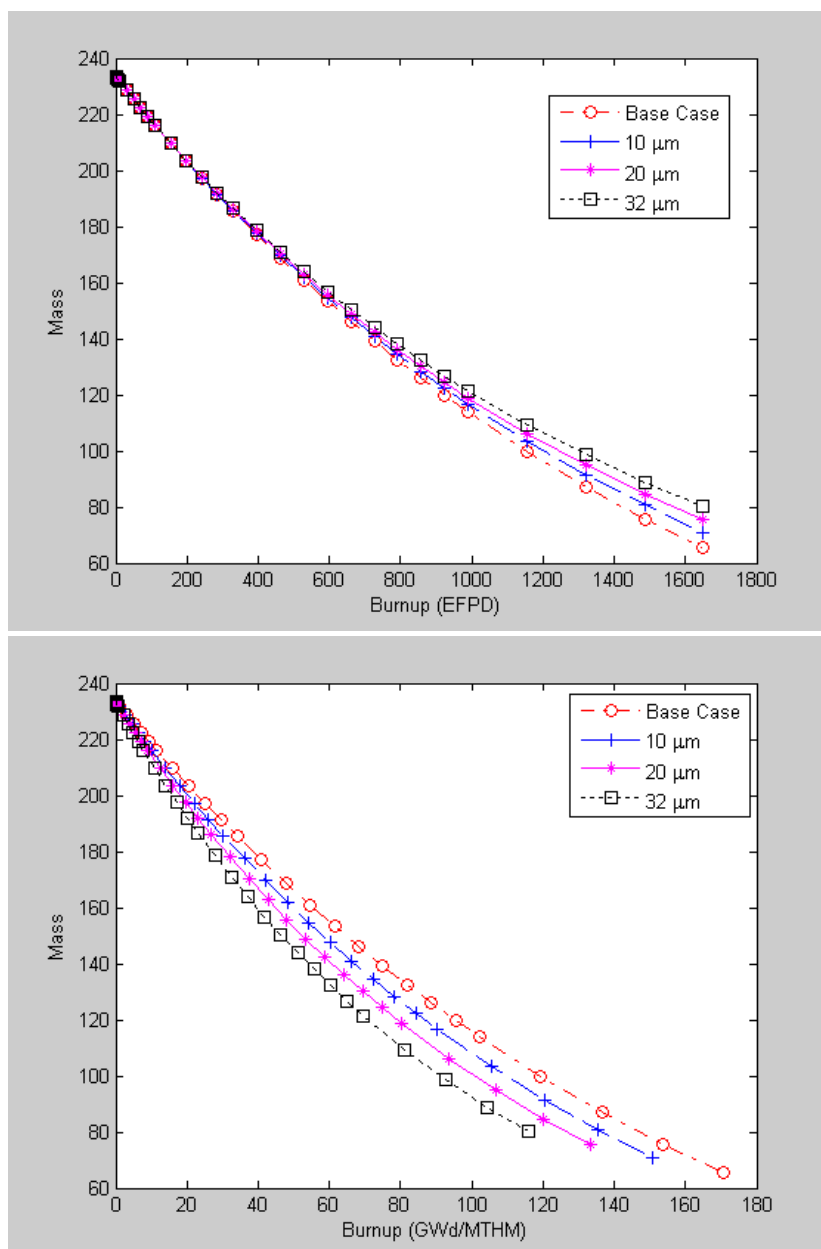


Figure 10-4. ^{235}U Mass vs. Burnup (top) vs EFPD (bottom)

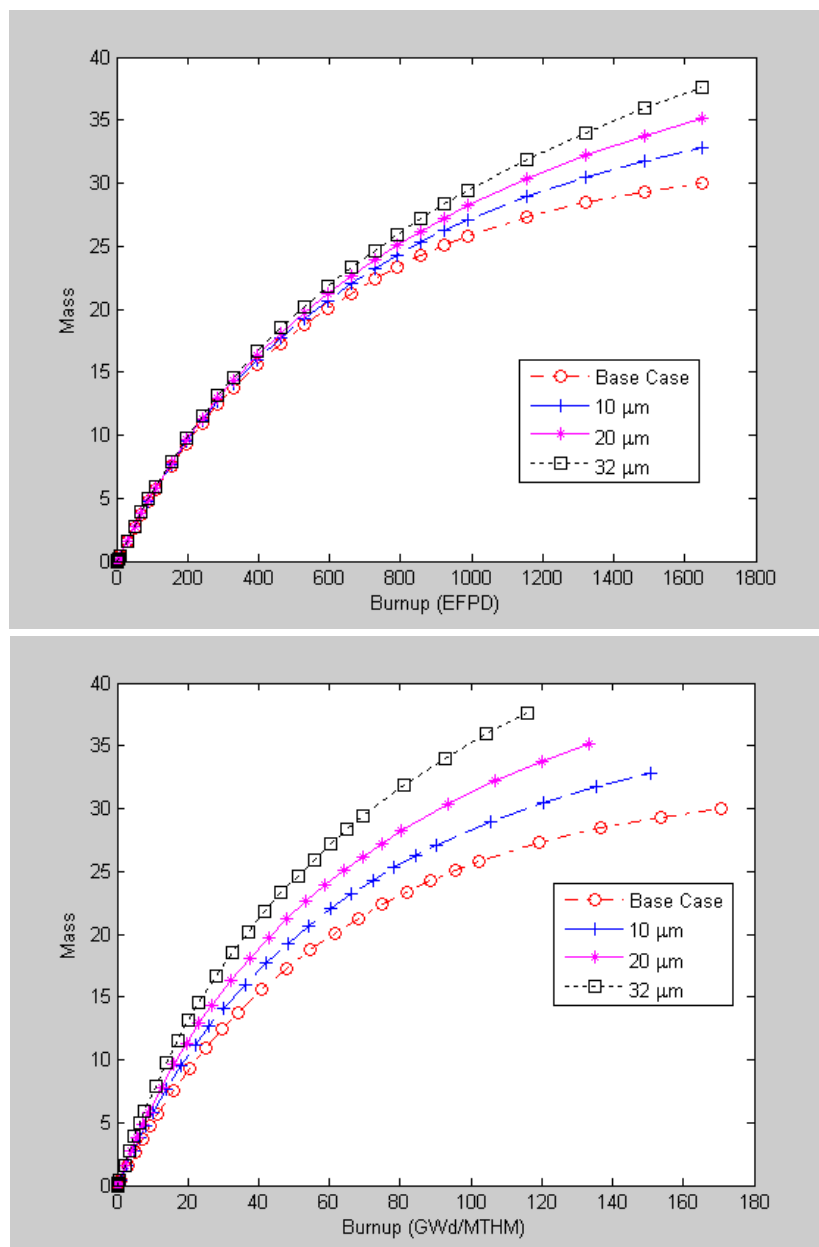


Figure 10-5. ^{239}Pu Mass vs. Burnup (top) vs EFPD (bottom)

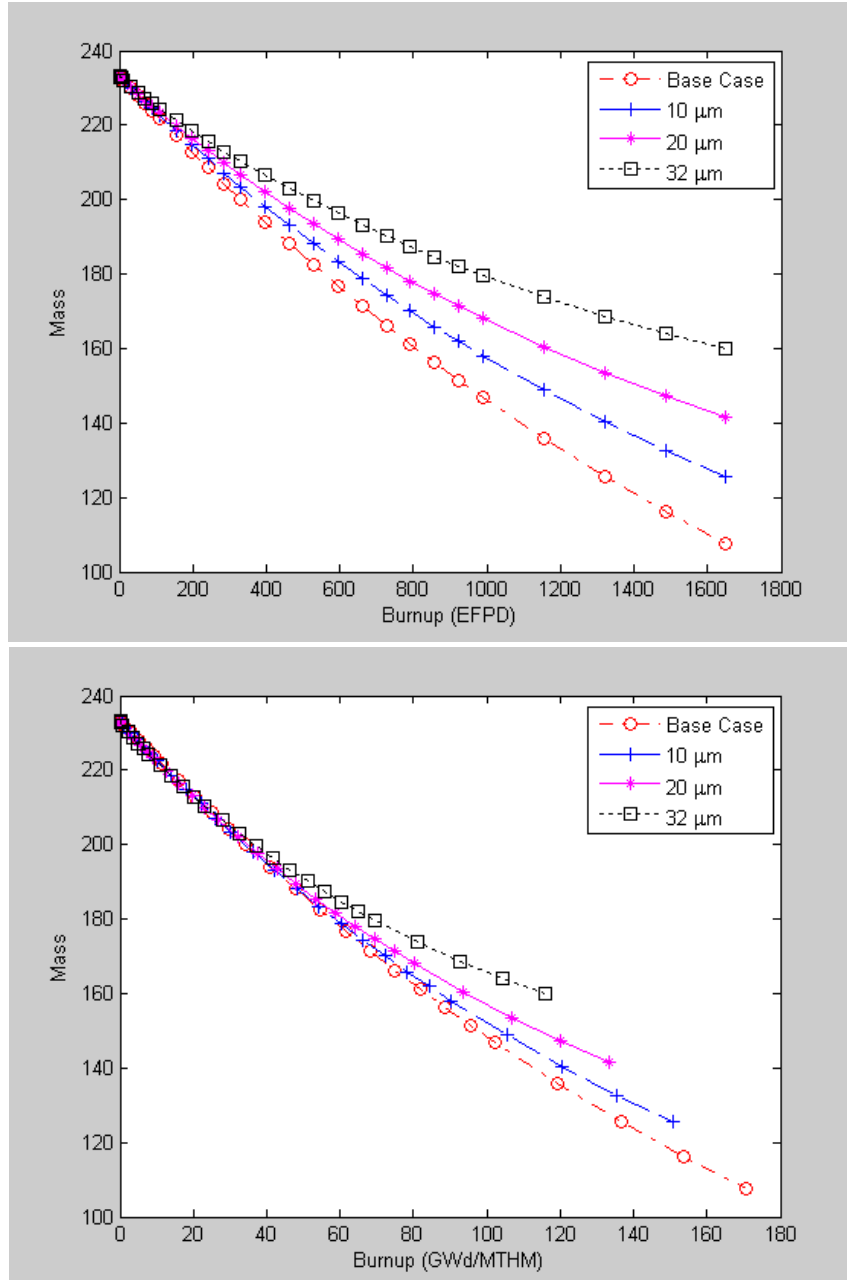


Figure 10-6. Combined ^{233}U , ^{235}U , ^{239}Pu , and ^{241}Pu Mass vs. Burnup

Though the QUADRISO approach may be a viable means of applying Thorium in an AHTR, alternative approaches must also be investigated. One of the first of these alternatives is a Thorium / Uranium fuel kernel mixture. Both $(\text{Th,U})\text{O}_2$ and $(\text{Th,U})\text{C}_2$ mixed kernels have been considered in previous studies / experiments and as such are considered more proven or tested than the QUADRISO case [2,3]. Additionally, such a design would be considered better from a proliferation standpoint being that the U^{233} produced from the Thorium transmutation will be mixed with the lower enriched uranium of the kernel, and so cannot be easily extracted. Unfortunately, unlike previous mixed kernel experiments and studies which allowed for increased uranium enrichment to ensure adequate fissile

inventory, AHTR is expected to keep enrichment below 20%. As such, it is expected that effective fuel life time will be negatively impacted. Models were created for both oxide and carbide cases and ranged from 5 mole % thorium oxide / carbide to 90 mole % thorium oxide / carbide. A collection of results are presented in Figure 10-7 through Figure 10-12. As can be seen in the figures, reactivity decreases significantly with increasing thorium concentration, Protactinium production increases, and overall fissile inventory is lower. Results were fairly comparable between oxide and carbide models, though some small difference do exist.

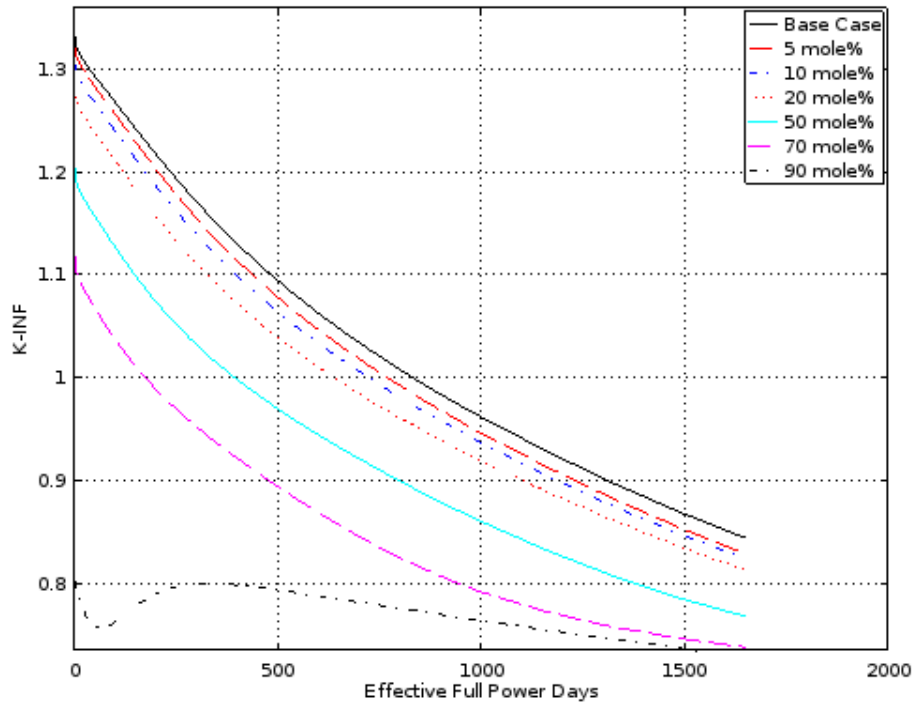


Figure 10-7. Reactivity Plot (Th,U)O₂ Mixed Kernel

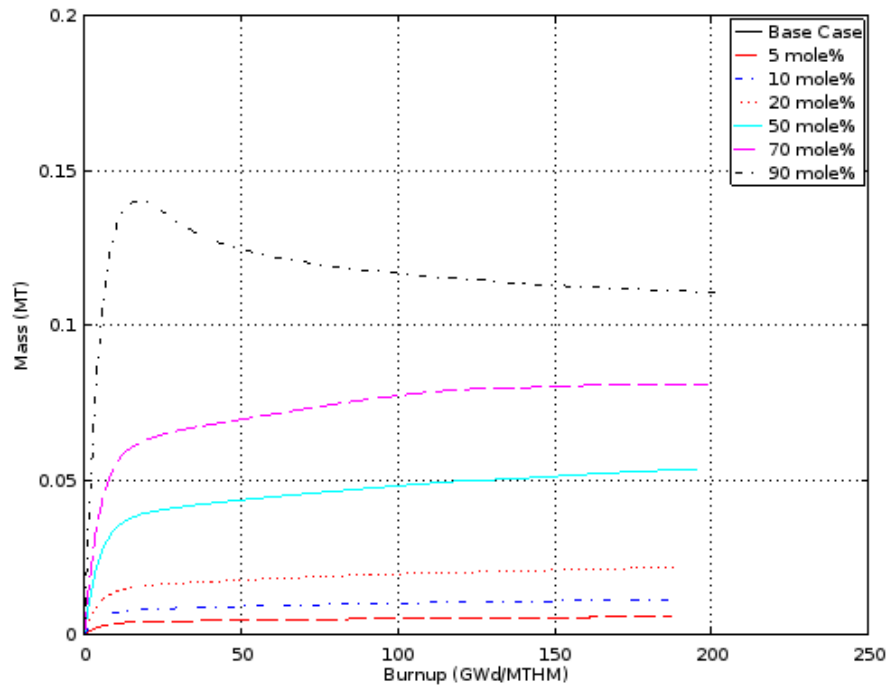


Figure 10-8. Pa^{233} Mass Plot $(\text{Th,U})\text{O}_2$ Mixed Kernel

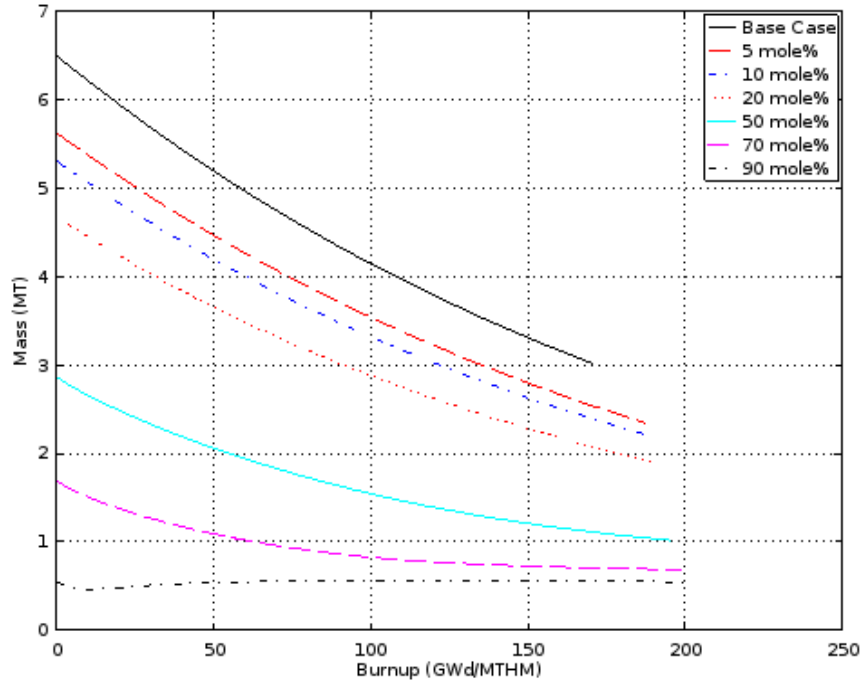


Figure 10-9. Total Fissile Mass Plot $(\text{Th,U})\text{O}_2$ Mixed Kernel

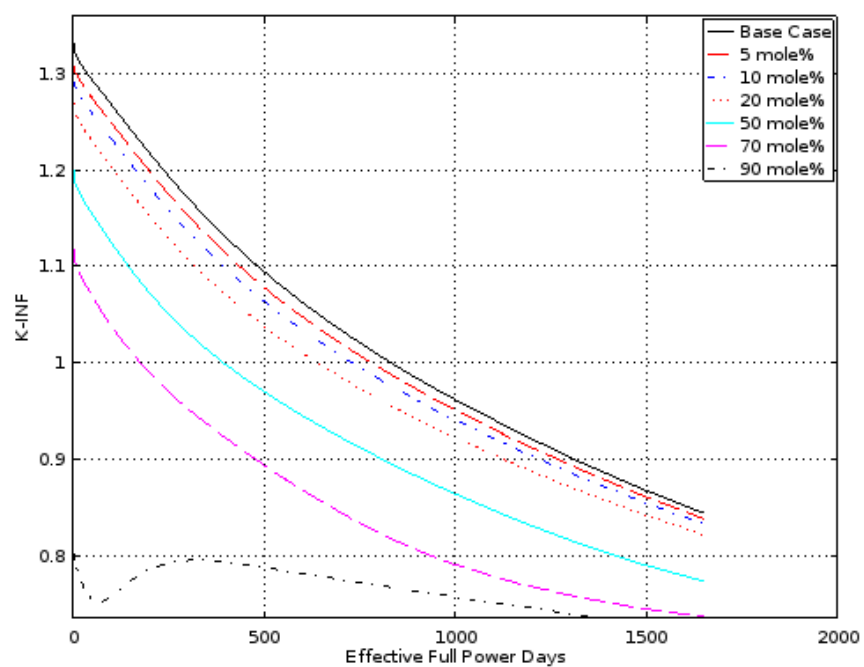


Figure 10-10. K -infinityPlot $(Th,U)C_2$ Mixed Kernel

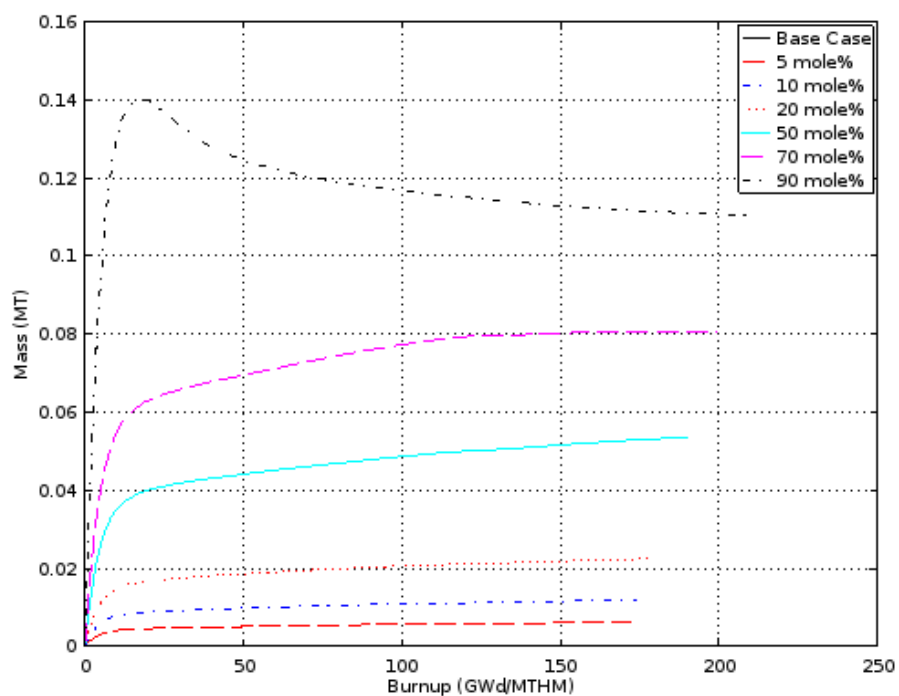


Figure 10-11. Pa^{233} Mass Plot $(Th,U)C_2$ Mixed Kernel

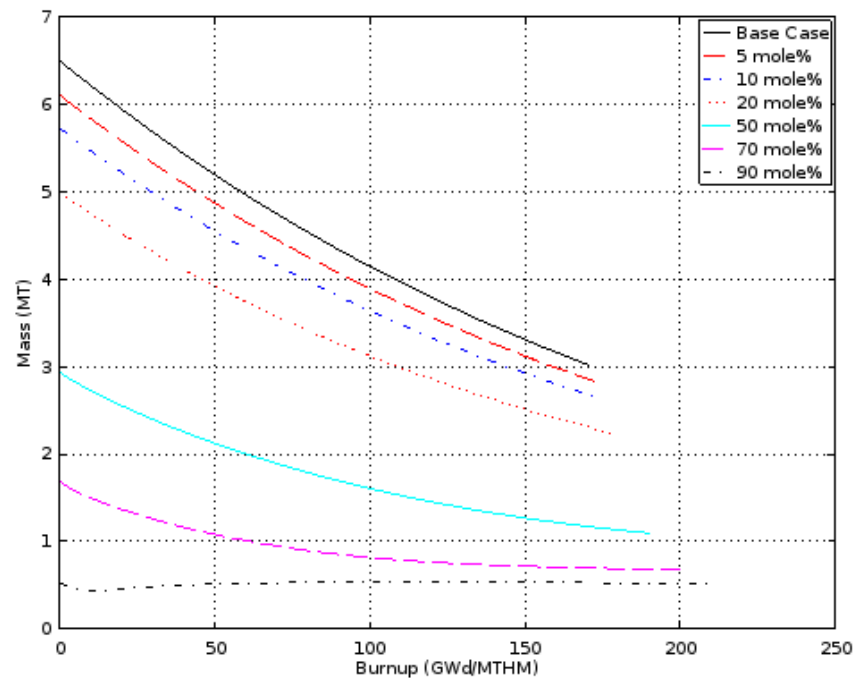


Figure 10-12. Total Fissile Mass Plot (Th,U)C₂ Mixed Kernel

10.2 Thorium Bearing Plate Arrangement

An alternative to the mixed kernel design is to designate select plates in a fuel assembly as Thorium only bearing fuel plates. The premise of such a design is that such Thorium only bearing plates might be extracted from an assembly once Protactinium near equilibrium is achieved and new “fresh” Thorium plates put in their place. In this manner, more U^{233} production might be achieved over simply doing a mixed kernel design. To begin an analysis of such a design, we first consider the effects of locating a Thorium plate in different plates positions as illustrated in Figure 10-13. It is known that different plate positions will experience different flux and power level (see Figure 10-14), and as such we can expect differing levels of Protactinium production and impact on reactivity if we change the position of the Thorium plates. To study this, models were created in which a single Thorium in different plate positions. The results of these models are summarized in Figure 10-15 and Figure 10-16 (NOTE: an error in the Plate 2 model prevented completion of the run and so the results for Plate 2 are absent). It can be seen that greater reactivity and Protactinium production are achieved by placing the Thorium plates in positions 1 or 6 rather than in positions 2,3,4 or 5.

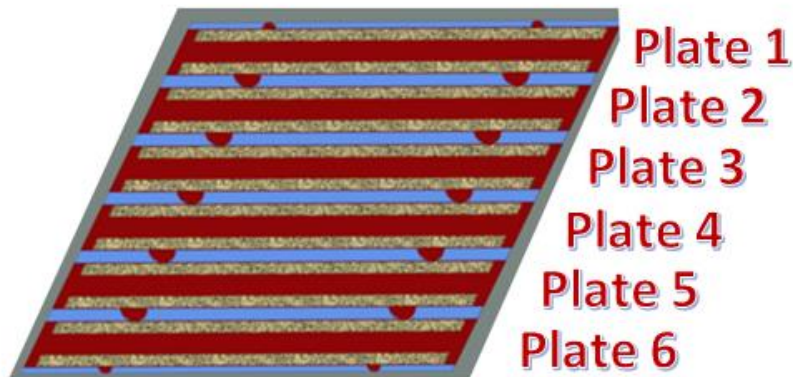


Figure 10-13. Illustration of Plate Positioning

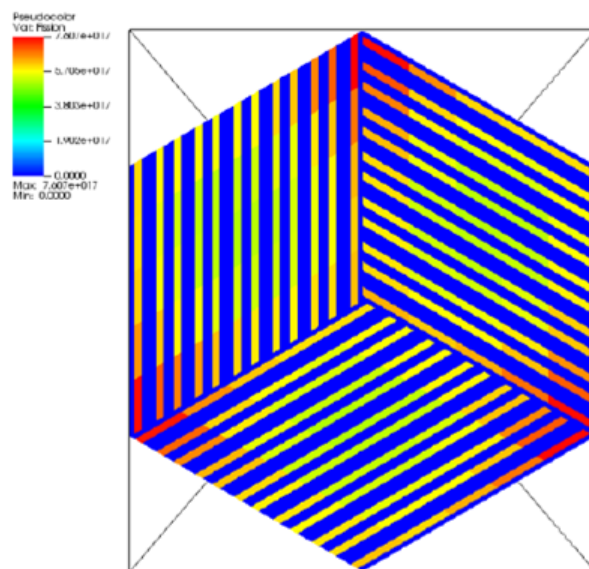


Figure 10-14. Illustration of Plate Power Distribution

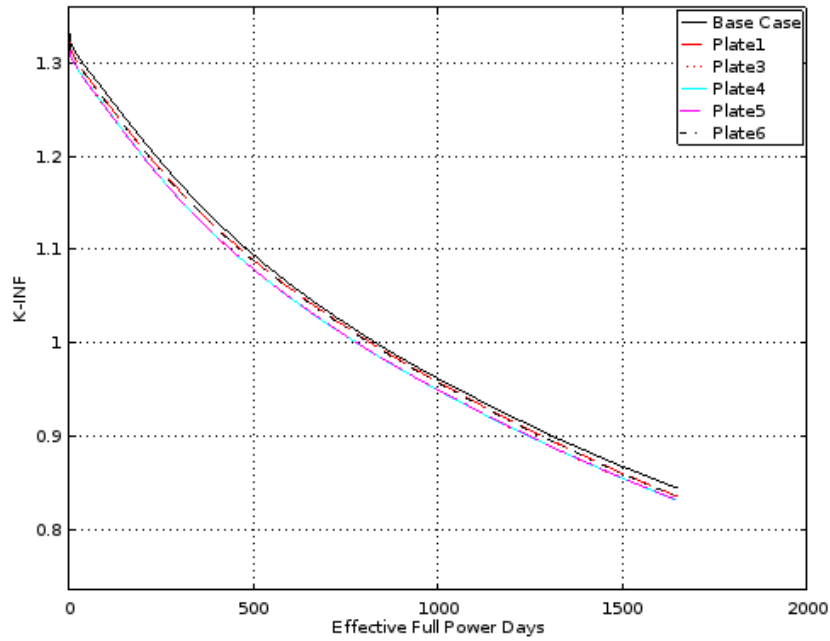


Figure 10-15. K-infinity Plot vs Plate Positioning

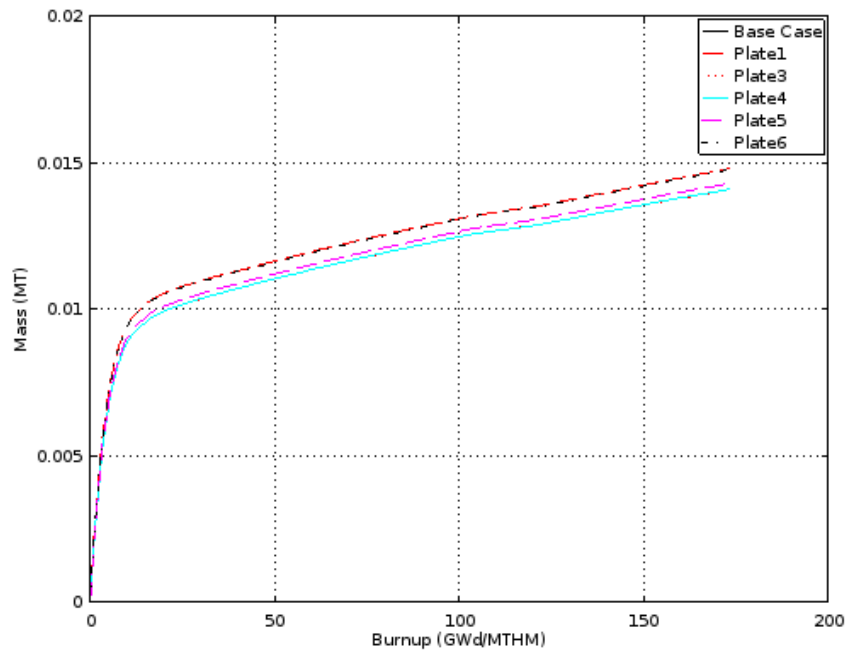


Figure 10-16. Pa^{233} Mass Plot Plate Positioning

After considering the position, next was considered the number of Thorium plates used. In the 1 Plate case, the Thorium plate was located in position 1, for 2 Plates positions 1 and 6, and for 4 Plates position 1,2,5, and 6. The results of these cases are provided in Figure 10-17, Figure 10-18, and

Figure 10-19. It can be seen that the 1 and 2 Plate cases did lower reactivity some, but not as dramatically as when 4 Plates were added, where the reactivity dropped significantly. The 2 Plate model appears to provide the best balance between amount of Protactinium produced vs. amount reactivity is decreased.

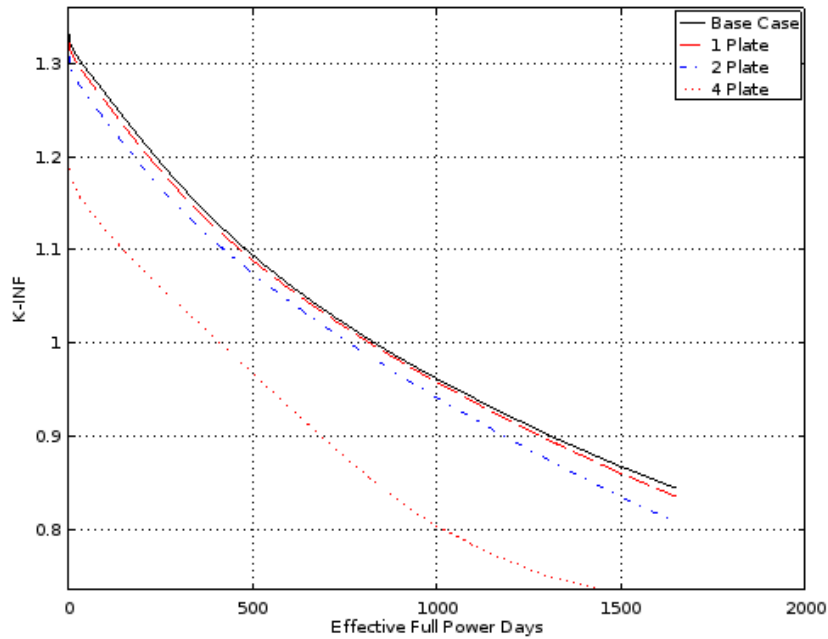


Figure 10-17. K-infinity Plot Number of Plates

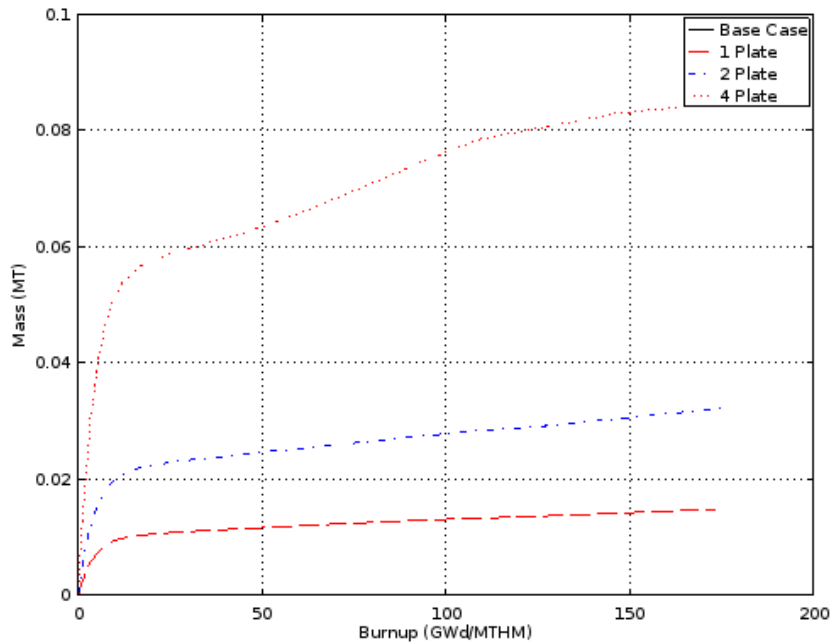


Figure 10-18. Pa^{233} Mass Plot Number of Plates

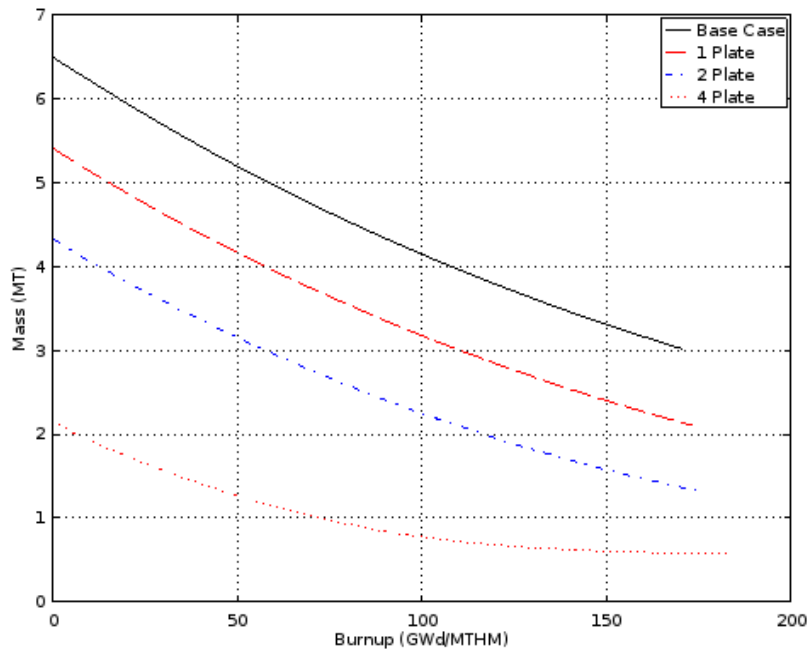


Figure 10-19. Total Fissile Mass Plot Number of Plates

10.3 References for this Section

1. A. Talamo, M.A. Pouchon, F. Venneri, "Alternative Configurations for the QUADRISO Fuel Design Concept", Journal of Nuclear Materials, 383, pg 264-266, 2014
2. "Thermophysical Properties Database of Materials for Light Water Reactors and Heavy Water Reactors", International Atomic Energy Agency, IAEA-TECDOC-1496, 2006
3. L.L. Taylor, "Fort Saint Vrain HTGR (Th/U carbide) Fuel Characteristics for Disposal Criticality Analysis" U.S. Department of Energy, DOE/SNF/REP-060, 2001

11. Summary of Finding and Recommended Future Work

The research performed in this project addressed the issue of low heavy metal loading and the resulting reduced cycle length with increased refueling frequency, inherent to all FHR designs with solid, non-movable fuel based on TRISO particles. Studies performed here focused on AHTR type of reactor design with plate (“plank”) fuel.

The work included both development of models and methodologies needed to adequately analyze this type of reactor, fuel, and its fuel cycle, as well as extensive analyses and optimization of the fuel and core design.

Modeling challenges reflected the fact that no commercial code system has full capability to efficiently model this type of fuel assembly design with double heterogeneity, nor a system existed for coupled neutronics/thermal-hydraulics full core analyses. Therefore substantial efforts were needed to successfully resolve these challenges.

The development of models and methodology included:

- In-depth analyses were performed to understanding subtleties of AHTR reactor physics, and reasons for inaccuracies in current models.
- Two codes (SCALE and SERPENT) were selected for analyses to provide additional confidence in results through cross-verification.
- Specific modeling and analysis methodology approaches were developed and implemented to extend applicability of these codes to AHTR fuel. Examples include addressing random packing of TRISO particles, improving accuracy of multigroup method via the so called systematic MCDancoff factor approach, and implementing non-linear reactivity model.
- Sensitivity studies were performed to establish practical simulation methodology, providing results of adequate accuracy at acceptable computational resources.

Moreover a two-step hybrid methodology (stochastic generation of functionalized nuclear data combined with deterministic multigroup calculations) was developed to enable practical (rapid) evaluation of AHTR performance, full core 3-D model, with thermal-hydraulic feedback and depletion capability. . Simulations. Similar capabilities exist for LWRs, but not for AHTRs, and this new methodology and computational tools (expanded version of NESTLE) significantly improve our FHR/AHTR analysis and evaluation capability.

A novel comprehensive fuel cost model was developed. In the past, a standard model for pelletized oxide fuel cost was typically extrapolated and applied to TRISO based FHR fuel. However, due to the substantially different fuel design in AHTR, this could lead to (and or analysis demonstrated that, indeed, it does lead to) biased results. The new model accounts for specific and inherent features of plank fuel, e.g. potentially high fabrication cost of TRISO particles, and substantially different amount of structural materials and fuel elements needed to accommodate the same amount of HM for

different fuel assembly designs. This model presents another significant new capability for analysis of AHTR.

Finally, a method for optimizing fuel assembly design was developed to allow effective search for optimum solution(s).

These improvements in modeling and analysis methodology enabled successfully completing project tasks, and obtaining the following findings that will guide future AHTR development and optimization.

Parametric studies were performed to scope the design space, primarily with respect to fuel enrichment (5% to 19.75%) and TRISO packing fraction (10% to 50%), but also examining impact of other design parameters (such as fuel plate thickness, number of plates, etc. As expected, the main driver for neutronic performance is the carbon-to-heavy metal (CHM) ratio, but fine tuning the design (i.e., achieving the same CHM with less or more lumped fuel) may provide further incremental improvements. Increasing the HM loading (e.g. via PF increase) increases somewhat the cycle length, but less than the amount of added fuel would suggest, due to reduced amount of moderator and worse fuel utilization, On the other hand, increasing the amount of moderator improves fuel utilization and discharge burnup, but reduces the amount of fuel and cycle length. This trade-off must be carefully optimized, by considering fuel cycle cost (FCC), as subsequently discussed.

One possibility to address this issue could be using thorium-bearing fuel with in-situ breeding. However, analyses that were performed have shown that over the range of scenarios thorium-based fuel failed to achieve a break-even performance, even less gains. Therefore, focus and efforts were shifted back to other options.

Two primary means for reactivity control were evaluated, use of burnable absorbers and use of control rods. Their purpose is somewhat different and both are envisioned to be used. Burnable absorbers were examined using several absorber materials, in BISO and QUADRISO configuration. Given their similar performance, BISO may be preferred due to simpler fabrication. With respect to absorber depletion rate, no ideal candidate was identified. Some materials depleted faster than desired, some slower than desired. Additionally, feedback coefficient was positive in some cases. A follow-up study looking at more complex designs should aim to develop improved solutions. Control rod (CR) worth was evaluated as well. The baseline design did not provide satisfactory shut down margin. Therefore, CR design modification was evaluated consisting of extending the CR wing length. This provides adequate hold-down, assuming that this solution is acceptable from the fuel element structural viewpoint.

Systematic thermal-hydraulic studies were performed, from simple in-house 1-D models and analyses, to 2-D and simplified 2-D analyses, to using the REALP code, and eventually using CFD in fairly complex simulations to assess flow distribution in on-line refueling transients. The results of these thermal-hydraulic studies were used:

- To inform neutronics analyses

- To provide single-channel parameters to be used in two-step full core coupled neutronics/thermal-hydraulics simulations
- To inform FCC optimization on thermal performance limits (regressed to simplified models)
- To evaluate thermal performance in pseudo-continuous refueling transients

The pseudo-continuous refueling aims to resolve the low HM loading issue by replacing/refueling fuel elements, one at a time, in regular and frequent intervals, while the reactor is operating at full power, or a fraction of power (on-line on-power refueling). Conceptually, this is similar to continuous refueling, or to the pebble bed refueling approach, and thus has potential to reduce FCC, provide flexibility, and reduce excess reactivity, but would also potentially introduce new significant other challenges. Analyses were performed considering primarily the flow redistribution and thermal performance. Additional issues of buoyancy, lift force, timing sequence and similar were considered as well. Performed analyses suggest that this approach is feasible from the neutronics and thermal-hydraulics standpoint, but the mechanical aspect, refueling topology, and alternative reactivity control need to be further studied.

The two-step procedure was used to evaluate full core parameters and perform preliminary fuel shuffle optimization studies. It was effective in reducing the radial assembly peaking factor by 27% from the baseline uniform loading.

The new comprehensive fuel cost model was combined with uncertainties in fuel cost and outage cost assumptions, and with extensive parametric studies (considering fuel enrichment, packing fraction, and number of batches), to identify preferable region(s) of fuel design space. This region generally tends to favor higher enrichment, in particular for higher fuel fabrication cost since more fissile material is processed per kgU. Low outage cost deemphasizes importance of longer cycle allowing use of more batches with improved fuel utilization, while the high outage cost necessitates using fewer batches to achieve longer cycles. While higher packing fraction increases HM loading, negative effect of reduced moderation and worsened fuel utilization typically overrides increased cycle length. Overall, preferable fuel designs tend to have enrichment in the 15% to 19.75% (with higher values preferred), and the packing fraction not higher than 30% (and sometimes in the 10% to 20% range). These analyses were performed with a fixed number of TRISO particle layers.

On the other hand, optimization performed with the developed optimization algorithm and tool, does not require performing calculations for all possible combinations, while at the same time considers variable number of layers and optimum points between the initial discrete values. Using this tool to optimize FCC led to consistent results as the previous brute force search approach, but provided additional insights. This tool offers an effective way to perform future optimization studies if additional changes in fuel design are to be considered. It is important that in both cases fuel design options were identified that have potential to be competitive in the broader context of AHTR attractive features.

Enabled by the new tools and capabilities developed in this project, the extensive analyses performed have identified promising fuel design parameters, under the assumptions considered, and elucidated

intricate inter-relations between different parameters. Future more detailed analyses will benefit from the new tools available, from the good starting point, and from the improved understanding of the critical trade-offs. In particular, recommended future work includes:

- Further optimize reactivity control – both burnable absorbers, and control rods, as well as a separate approach for pseudo-continuous refueling
- Utilize two-step procedure/tools to perform:
 - Realistic full core design and multicycle evaluation
 - Realistic reactivity control over the cycle
 - Evaluate full core thermal performance
 - Optimize feed enrichment
 - Evaluate feedback for safety/transients considerations
- Refine FCC optimization:
 - For the fuel design phase space of practical interest
 - Using updated assumptions, in particular reduced uncertainty in TRISO cost
 - Consider fuel lumping arrangements to reduce FCC

On a broader level:

- Consider alternatives to TRISO fuel, and
- Use developed tools to plan future experiments related to AHTR

Overall, the project has completed the planned tasks and achieved its target objectives. Its results advance the status of AHTR research and provide guidance to addressing the issue of low HM loading.

Appendix A– Baseline AHTR Design Specifications

AHTR Reference Design for Codes Verification and Validation (ver. 0)

Prepared by: Pietro Avigni, Michael Huang
Reviewed by: Bojan Petrovic

Nuclear and Radiological Engineering
Georgia Institute of Technology

September 27, 2015

1. Introduction

The objective of this report is the definition of a reference AHTR primary system and core design for benchmarking purposes. This is not an optimized design but a reference/starting point for codes cross-validation and further evaluations and optimization.

The report will define geometric properties and materials, based on the work developed at ORNL and related projects over the past decade years. The report provides a description of the features of the plant from a large-scale point of view to the small scale.

The general design of the AHTR is described in two ORNL reports ([1], [2]); the two reports use slightly different numbers for specific design parameters, because the more recent design has been partly optimized. We decided to consider the most recent design as a reference design for the general parameters, but some features that are not fully defined in the most recent report are taken from the initial, non-optimized design.

2. General overview of the plant design

The AHTR has a power of 3400 MWth and the efficiency is expected to be about 45%, corresponding to 1530 MWe. The primary coolant is Flibe ($2\text{LiF}-\text{BeF}_2$), the intermediate salt is KF-ZrF₄. The power cycle is based on supercritical water, similarly to coal plants.

Passive safety systems are implemented, such as DRACS, in order to minimize the requirements for external support during accident scenarios.

Figure 2-1 shows the layout of the plant; the rest of the paragraph will further define some global design parameters.

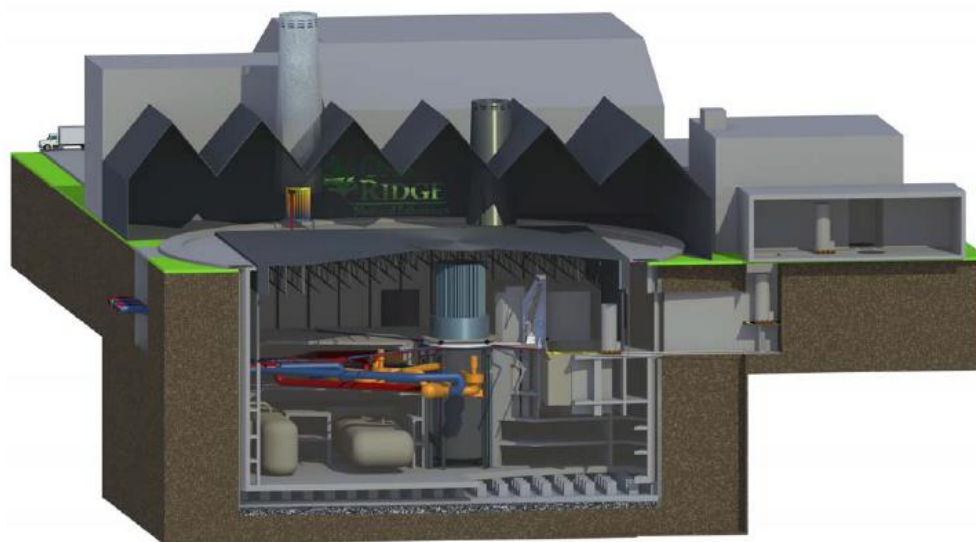


Figure 2-1. Overview of the plant [2]

The fuel type is based on TRISO particles and it is in the form of uranium oxy-carbide (UCO). The enrichment is 9%wt in the most recent design (19.75% in the original preconceptual design). More details on the fuel structure will be given later on.

The core is formed by 252 active fuel assemblies, with hexagonal cross section and 18 fuel plates each. The moderator and reflector material is graphite. The active core height is 5.5 m.

The primary salt is Flibe and it has a temperature increase of 50K on average, across the core, including the bypass flow; the inlet temperature is 650°C and the outlet is 700°C. The mass flow rate can be calculated from these design parameters: assuming that the average specific heat of the coolant is 2415 J/(kg*K), the mass flow rate is the core thermal power divided by the temperature increase and the specific heat, which is approximately 28150 kg/s.

The core vessel is not pressurized.

Table 2-1. General plant parameters

Parameter	Value	Units
Core thermal power	3400	MW
Overall thermal efficiency	45%	-
Fuel type	TRISO	-
Uranium composition	UCO	-
Number of fuel assemblies	252	-
Moderator and reflector material	Graphite	-
Active core height	5.5	m
Primary coolant salt	Flibe	-
Core inlet temperature	650	°C
Core outlet temperature	700	°C

General information about the intermediate salt circuit, the power cycle and the decay heat removal system can be found in the mentioned reports. It is not of fundamental importance for the benchmark design description of the in-vessel primary system.

3. Vessel and out-of-core structure

This section provides a brief description of the vessel and the structure outside of the reactor core. Figure 3-1 provides an overview of the AHTR vessel and core.

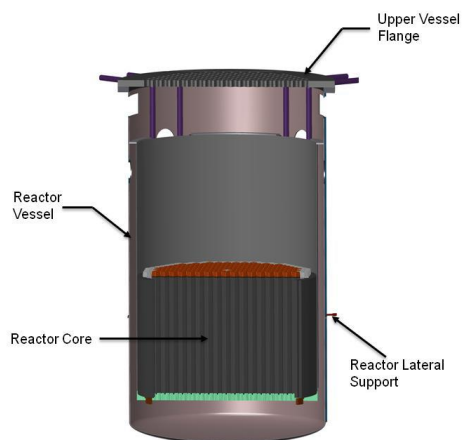


Figure 3-1. Vessel and core configuration [2]

3.1 Upper plenum

The upper plenum is delimited by the upper support plate and the vessel flange.

The upper portion of the plenum is filled with Argon cover gas (not pressurized). The temperature of the argon cover gas is 250°C. The height of the cover gas volume is 3.19 m, as shown in section 5. The lower part of the upper plenum is filled with Flibe coming from the core. The average temperature of the Flibe is about 700°C. The depth of the salt with respect to the upper plate is 7.15 m.

The guide tubes for leader rods occupy the upper plenum during normal operation. These rods are retractable, in order to provide access for refueling.

Figure 3-2 shows the configuration of the upper vessel internals.

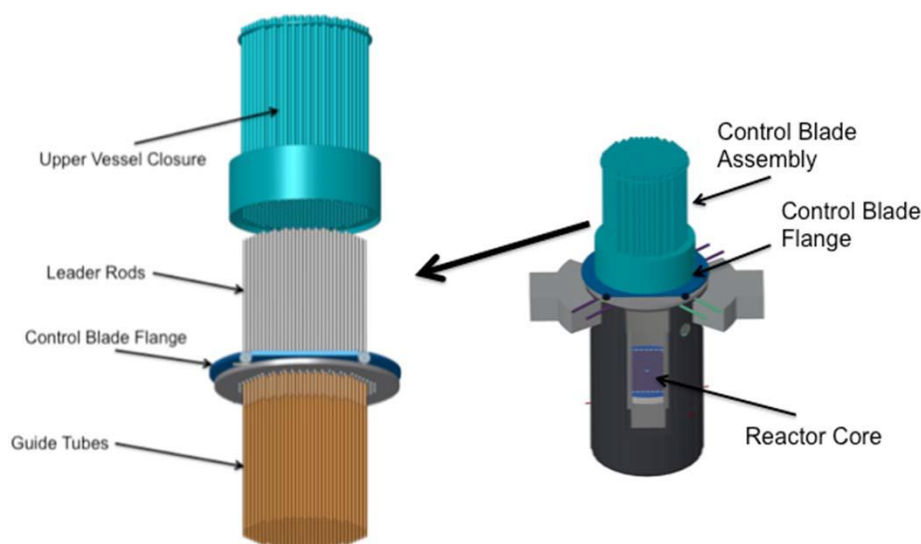


Figure 3-2. Overlook of the upper plenum, the guide tubes and the upper vessel closure [2]

3.2 Reactor vessel

It is roughly a cylinder, with refueling lobe extension in the upper half.

It is hung from its upper flange.

Table 3-1 provides the main design parameters of the reactor vessel.

Table 3-1. Global parameters of the reactor vessel

Parameter	Value	Units
Exterior vessel diameter	10.5	m
Vessel height	19.1	m
Primary salt depth above upper support plate	7.15	m
Primary piping interior diameter	1.24	m
Number of DRACS	3	
Core barrel material	C-C Composite	
Vessel and primary piping material	800H with alloy N lining	

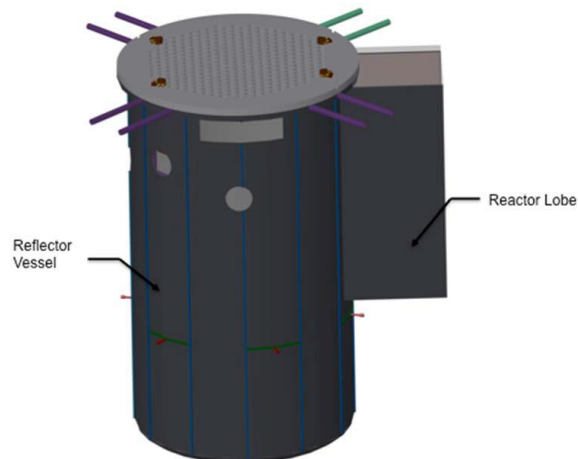


Figure 3-3. Outer configuration of the reactor vessel [2]

The vessel is made of alloy 800H, which has an allowable yield strength of 20 MPa at 700°C.

The vessel thickness is not defined in the reference reports. It is assumed to be 5 cm, even though from a mechanical standpoint a larger thickness might be required.

The Alloy N lining prevents corrosion and it is 1 cm thick.

3.3 Top Flange

The top flange has a 11.6 m diameter and it is 35 cm thick.

It is a truss structure with 1.5 cm top and bottom plates, in order to reduce the weight.

The volume fraction of the solid material is 13.45% (the reference volume is a cylinder that wraps the flange).

It is kept at 250°C by the Argon gas that separates it from the coolant in the upper plenum.

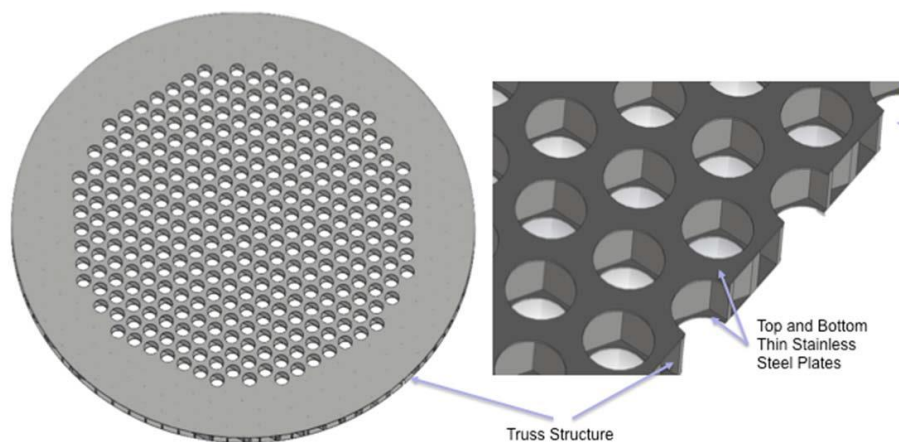


Figure 3-4. Top flange configuration [2]

3.4 Core barrel and downcomer

The core barrel separates the core from the downcomer/DRACS HX region. It is 2 cm thick and it is made of C-C composite. The interior face (towards the core) of the barrel has a thin plating of boron carbide (thickness 1 cm) that attenuates neutron radiation to reactor vessel.

The internal diameter is 9.56 m and the outside diameter is 9.62 m.

The operating temperature is 650°C (same as inlet core temperature). The flow direction is downward in the downcomer region.

The downcomer region is divided azimuthally into 8 angular zones. 3 downcomer sections, 3 DRACS sections, 1 maintenance cooling system, 1 refueling lobe.

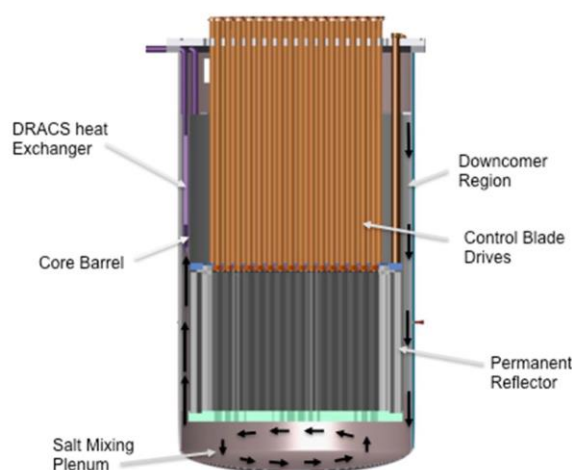


Figure 3-5. Vertical cross section of the vessel and the core [2]

4. Reactor core

The reactor core contains 252 fuel assemblies, positioned according to a hexagonal pattern. The central assembly is not fueled, but serves as a moderator block (it has the same composition and structure as the outer removable reflector blocks). The gap between two nearby assemblies is 1.8 cm. The equivalent diameter of the reactor core is 7.81 m for the fueled part.

One ring of replaceable reflector assemblies surrounds the last ring of fueled assemblies, and then a permanent reflector completes the core. The equivalent diameter of the core including the replaceable reflector is 8.69 m. The outer radius of the permanent reflector is 9.56 m.

The core height is 6 m, of which 5.5 m is the active core; top and bottom nozzle/reflector regions are 25 cm each, the support plates are 35 cm thick, so the overall core plus plates height is 6.7 m.

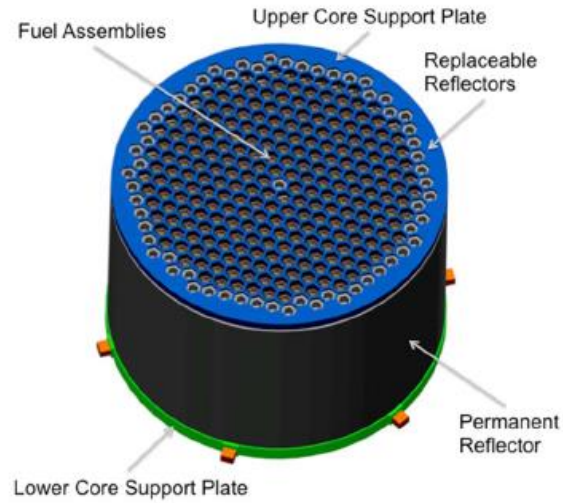


Figure 4-1. View of the core reflector, upper and lower support plates [2]

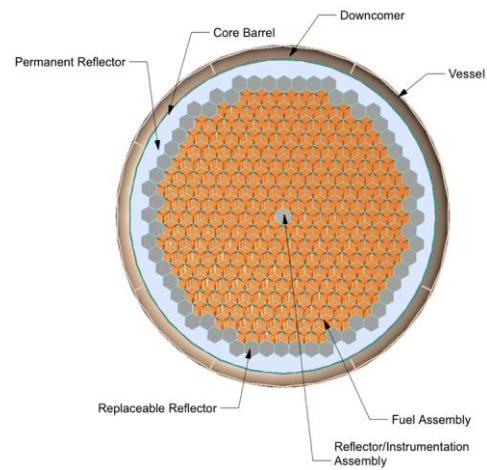


Figure 4-2. Horizontal cross section of the core [2]

Fuel assemblies in the preliminary core are grouped into 10 radial regions, as shown in Figure 4-2.



Figure 4-3. SCALE model, horizontal cross section [2]

4.1 Replaceable reflector

It is located around the last fueled ring; it is a single ring of removable reflector blocks. (Fuel assemblies marked dark gray in Figure 4-2).

The reflector blocks are made of graphite and have the same size and shape as the fueled assemblies. In the reference design they are not provided with a control rod, but in principle a control rod could be added to each reflector block to facilitate the control of the reactor power.

No coolant channels are present in the reflector block, but they could be added if cooling is required.

4.2 Permanent reflector

Surrounds the removable reflector ring. It is made of solid graphite sections.

It conforms to the replaceable reflector fuel assemblies ring on the inner side, and has a cylindrical outer shape.

4.3 Lower support plate

The lower support plate provides support to the core and the reflector. It is a honeycomb structure attached to the reactor vessel through lateral junctions.

The material is SiC-SiC composite; the thickness is 35 cm.

Channels cuts are made into the lower plate to direct the flow into the fuel assemblies (Figure 4-4).

Also, indexing hole and guides serve to align the fuel assemblies during refueling.

A simplified model for the lower support plate for neutronic analysis has the following composition, with respect to the wrapping cylinder:

- 14.96% volume fraction is Flibe at 650°C;
- 85.04% volume fraction is graphite at 650°C;

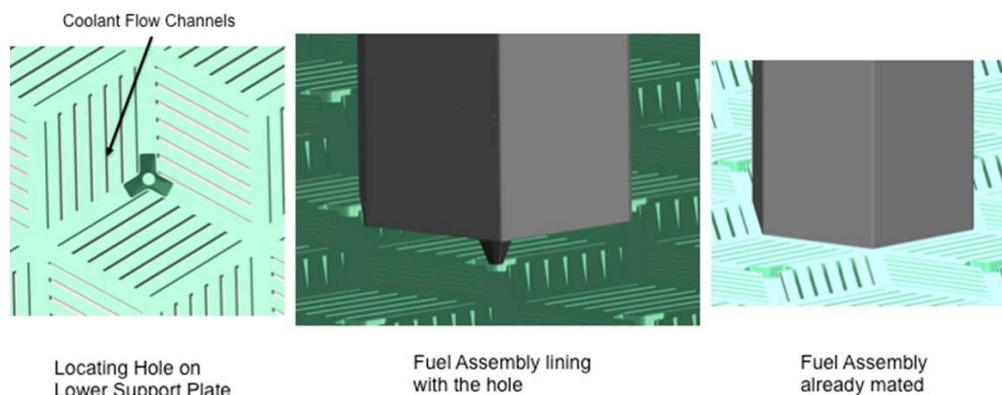


Figure 4-4. Detail of the lower support plate [2]

4.4 Upper support plate

The upper support plate holds components in place, against the upward salt flow. It is 35 cm thick and made of SiC-SiC composite (same as upper support plate). Four drive rods are used to lower and raise the plate during refueling outages.

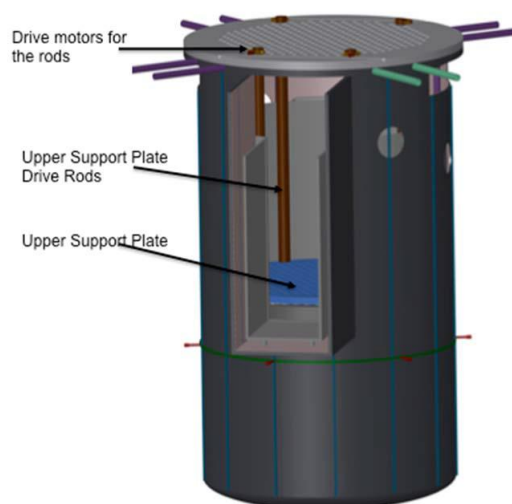


Figure 4-5. view of the upper plenum and the drive rods [2]

The plate makes tangential contact with hemispherical contacts on grappling collar of assembly (Figure 4-6). The webbing on the upper core support plate fills the inter-assembly gap (reduction of flow vibrations).

A simplified model for the lower support plate for neutronic analysis has the following composition, with respect to the wrapping cylinder:

- 78.9% volume fraction is Flibe;
- 21.1% volume fraction is graphite;

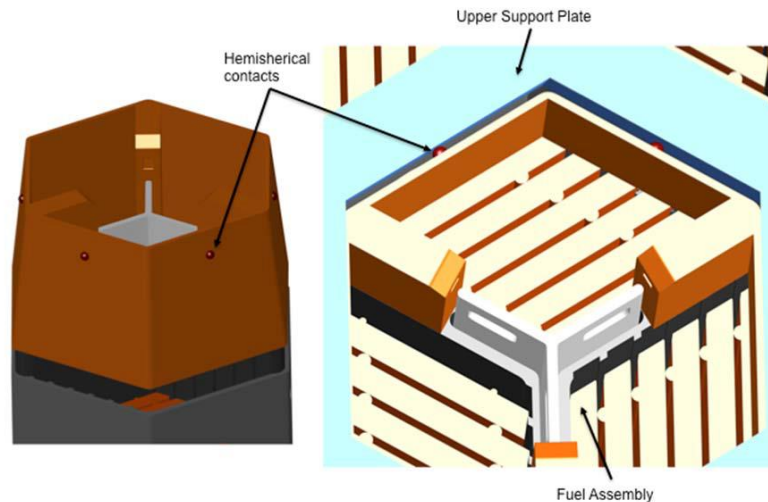


Figure 4-6. Contact between assembly grappling collar and upper support plate [2]

5. Simplified geometry for neutronic analysis

This section presents the overall dimensions of the AHTR vessel and core.

Some parameters have been assumed, since they are not fully specified in the original design description.

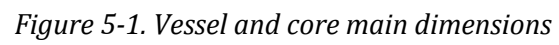
The following assumptions have been made:

- The height of the lower plenum is assumed to be 2 m; this results in a nitrogen volume height in the upper plenum of 3.19 m. Increasing the lower plenum height results in a decrease of the nitrogen volume height.
- The vessel thickness is 5 cm (plus 1 cm liner).
- The height of the downcomer (with respect to the lower face of the lower support plate, corresponding to the top of the lower plenum) is assumed to be 13 m.

Table 5-1 presents the dimensions of the vessel and core in the radial direction. Figure 5-1, Figure 5-2 and Figure 5-3 present the main dimensions of the system.

Table 5-1. Diameters in the vessel regions

Parameter	Value	Units
Core OD	7.81	m
Replaceable reflector equivalent OD	8.69	m
Permanent reflector equivalent OD	9.56	m
Boron layer OD	9.58	m
Barrel OD	9.62	m
Downcomer OD	10.38	m
N liner OD	10.40	m
Vessel OD	10.50	m



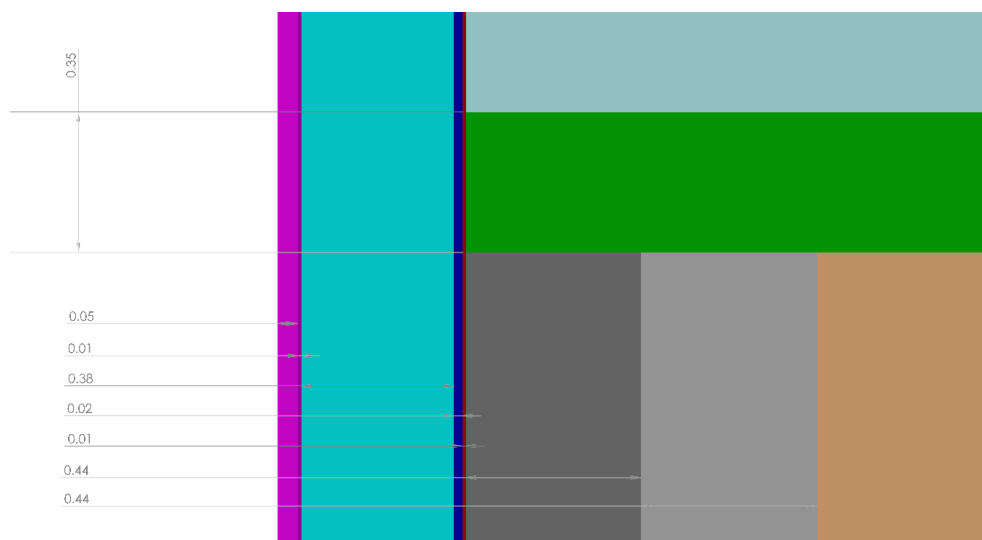


Figure 5-3. Dimensions. Top of core – detail

6. Fuel assembly

The fuel assembly is made of 18 fuel plates, grouped in 3 clusters of 6 plates each. Each plate is 2.55 cm thick. The entire fuel assembly fabricated with high temperature materials.

The plates in the assembly are 6 m long, the active (fueled) part is 5.5 m (of the total 6 m), and the remaining part (25 cm on top and bottom) are made of reflector material. The plates are enclosed in a hexagonal carbon-carbon fuel channel box (density 1.95 g/cm³), which is 1 cm thick.

The outer apothem of the box is 22.5 cm, corresponding to 45 cm distance between two parallel outer faces of the box wall.

The three symmetric regions (groups of plates) are separated by a Y shaped support structure that is 4 cm thick and made of C-C composite (density 1.95 g/cm³).

The coolant channels are 0.7 cm thick, except for the first and last channel of every region, that are half of the full thickness (0.35 cm).

Figure 6-1 shows the reference dimensions of the horizontal cross section of the assembly, while Figure 6-2 shows some dimensions that can be derived from the reference dimensions.

A three dimensional view of the fuel assembly structure is given in Figure 6-3.

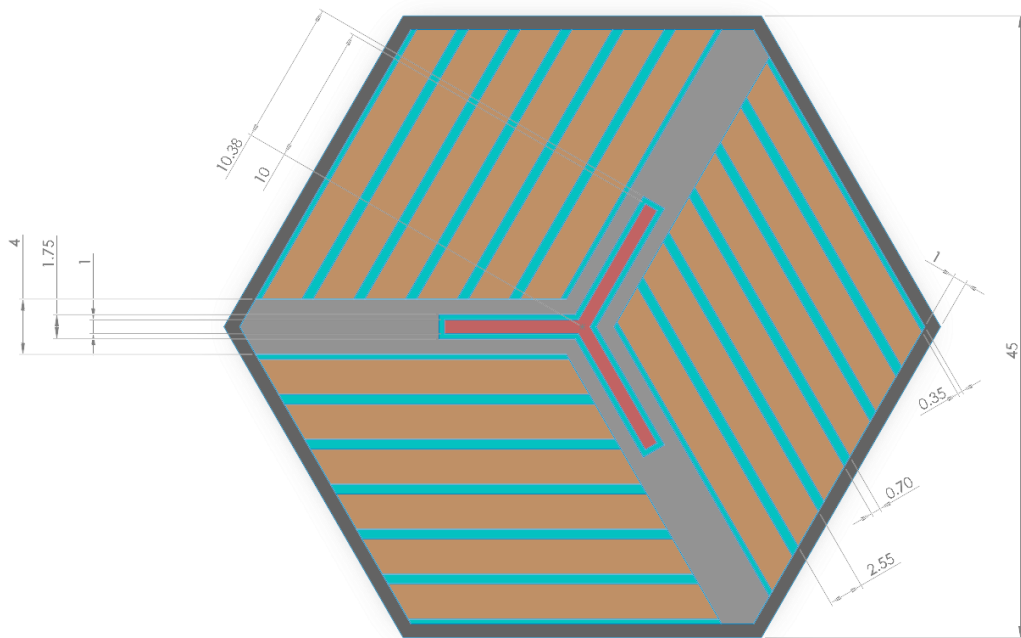


Figure 6-1. Assembly reference dimensions

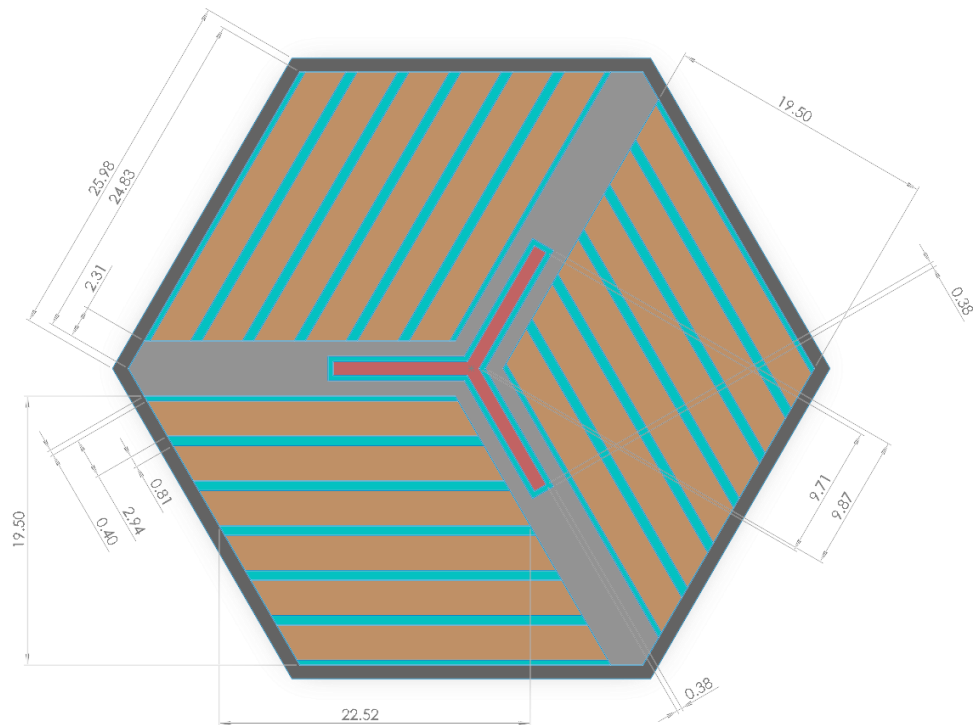


Figure 6-2. Assembly derived dimensions

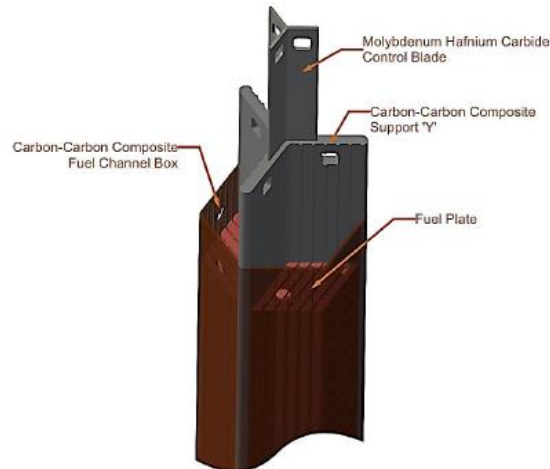


Figure 6-3. Fuel assembly structure [2]

The gap between nearby assemblies is 1.8 cm, in order to accommodate for any mechanical distortion. The triangular fuel assembly pitch is then 46.8 cm. Figure 6-4 shows the horizontal cross section of 7 nearby assemblies.

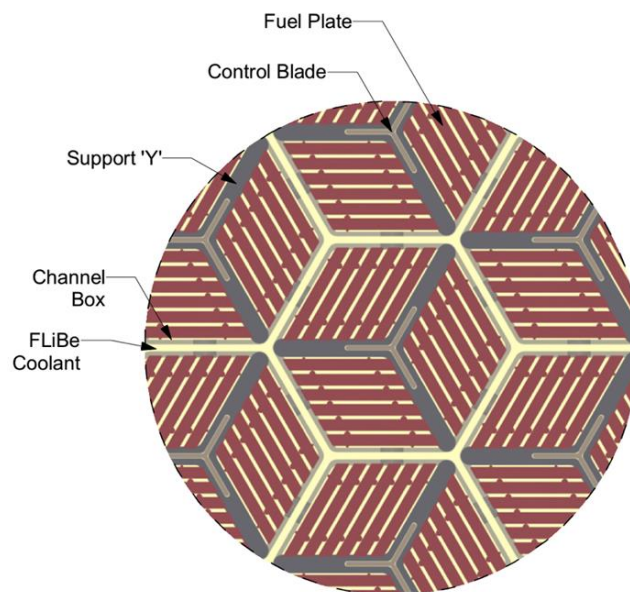


Figure 6-4. Horizontal positioning of the assemblies in the core [2]

6.1 Control blade

Each assembly has its own control rod; each control rod has low reactivity worth.

The control rod is Y-shaped and it is inserted into the central Y-shaped support. The control rod is made of molybdenum hafnium carbide (MHC) alloy, that functions as absorber and structural. MHC is a commercial, particle-strengthened molybdenum-based alloy with 1.2%w hafnium and 0.1%wt carbon. The density is 10.28 g/cm³.

The leader rod attaches at the top of the control rod, using grapping holes. The leader rod serves to move the control rod up and down.

The dimensions of the rod and the slot are:

- CR slot: each wing is 10.38 cm long (with respect to center of assembly) and 1.75 cm thick.
- CR: each wing is 10 cm long (with respect to center of assembly) and 1 cm thick.

Figure 6-5 shows the control rod geometric configuration.

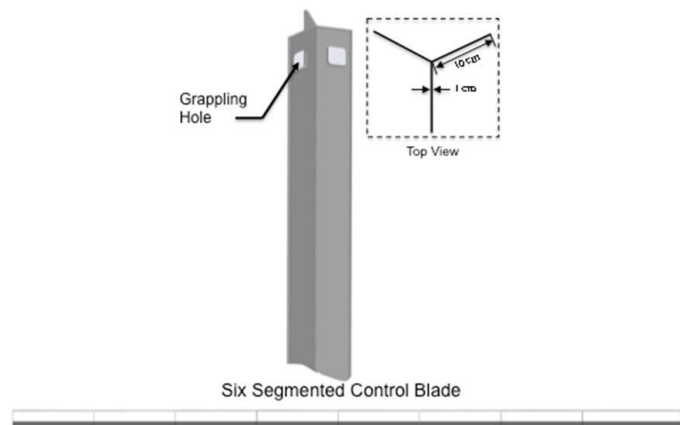


Figure 6-5. control blade geometry [2]

6.2 Grappling collar and drive mechanism

The grappling collar (Figure 6-6) interfaces with upper plate and provides grappling interface for fuel handling.

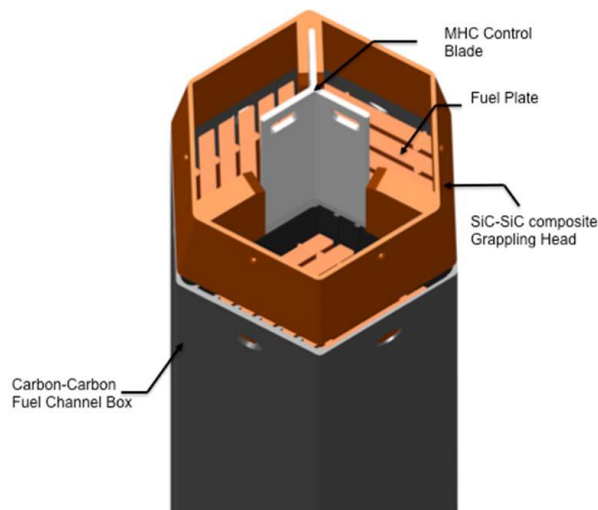


Figure 6-6. Grappling collar detail [2]

Each control blade has a leader rod that extends from the top of the control rod to the vessel flange. Each leader rod is encased in a control blade guide tube (Figure 6-7). Leader rod and guide tube are made of SiC-SiC composite.

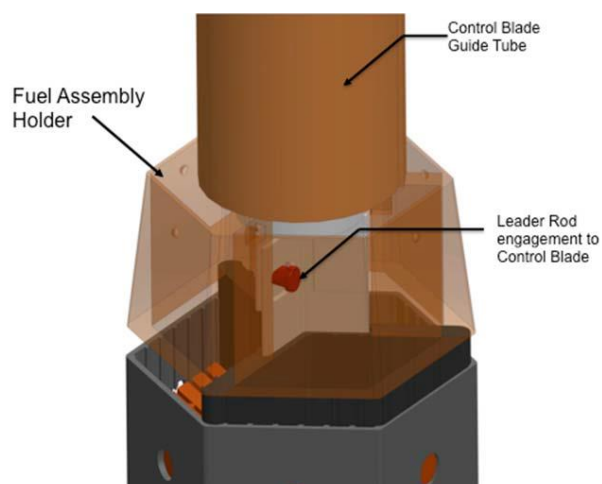


Figure 6-7. guide tube and grapple collar detail [2]

7. Fuel plate

The LSCR fuel plank is shaped as a parallelepiped with two fuel stripes sandwiching a central carbon slab. There is a thin 1mm pyrocarbon sleeve around the fuel stripes to prevent erosion of TRISO particles. The TRISO fuel particles are randomly dispersed within the fuel strip with a 40% packing fraction in the 2011 model. This can be modeled with a TRISO spherical square lattice with a pitch of 0.09265 cm. The newer 2012 reference design has a carbon to heavy metal ratio that is twice as high at 400 compared to the 2011 design. It also has 9% enrichment down from 19.75% enrichment. The enrichment was lowered to reduce the fuel cycle cost and the initial capital investment. It is not clear how the CHM ratio was modified. The fuel stripe could be made smaller or the packing fraction can be reduced to produce a higher CHM ratio. It is recommended that the fuel stripe thickness be set to contain six fuel layers and a 20% packing fraction. This gives a square pitch of 0.116736 cm. High density graphite matrix is inside the fuel stripe in between the TRISO particles. The density of the carbon matrix is 1.75 g/cm³. Burnable poison particles included near the center of the plate. There are two semi-cylindrical spacers on each of the fuel planks. Figure 7-2 gives a general idea of the configuration of the plate; Figure 7-2 and Figure 7-3 present the dimensions of the plate.

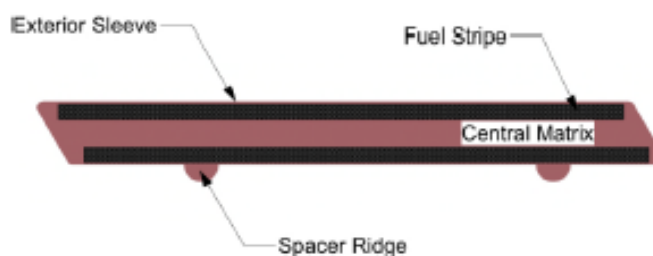


Figure 7-1. Geometrical configuration of the fuel plate [2]

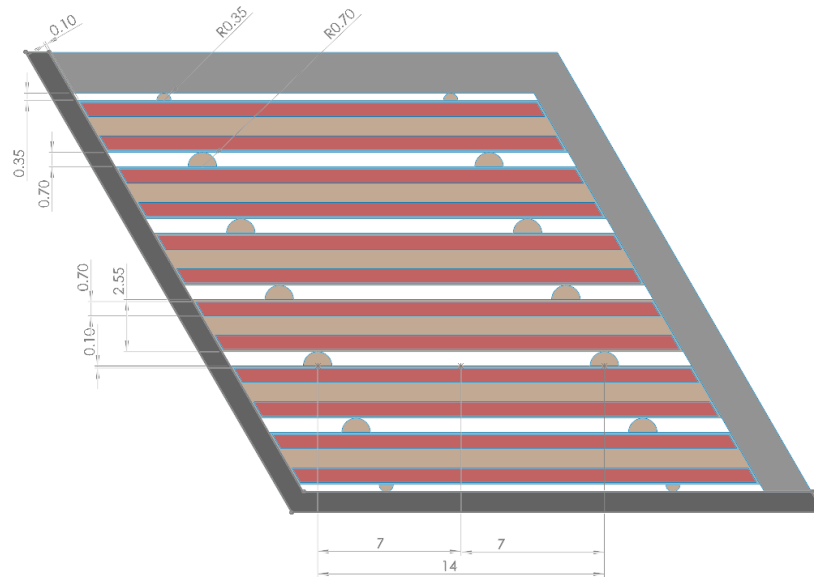


Figure 7-2. Dimensions of the fuel plate

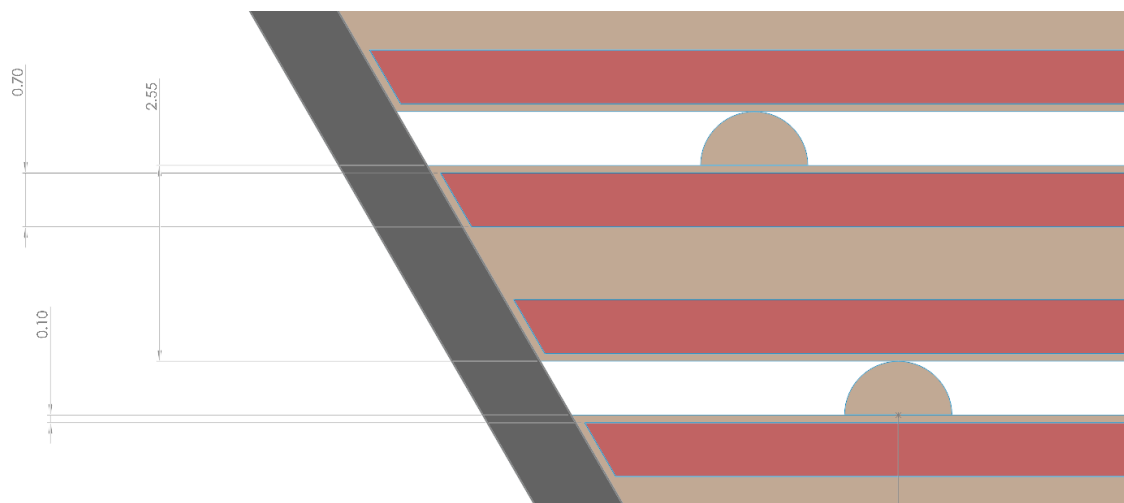


Figure 7-3. Dimensions of the fuel plate - detail

8. Fuel - TRISO particle

The TRISO fuel particle consists of four layers: an outer pyrocarbon layer, a silicon carbide layer, an inner pyrocarbon layer, and a less dense carbon buffer layer. Inside of these layers is a uranium oxycarbide fuel kernel. **Error! Reference source not found.** shows the geometry with the outer layers cut out of the TRISO fuel particle. This fuel is the same as the AGR fuel developed under DOE-NE sponsorship. The reference irradiation experiment for the fuel type used for the AHTR is AGR-5/6.

Fuel enrichment 9%. **Error! Reference source not found.** shows the respective dimensions of the TRISO fuel particle.

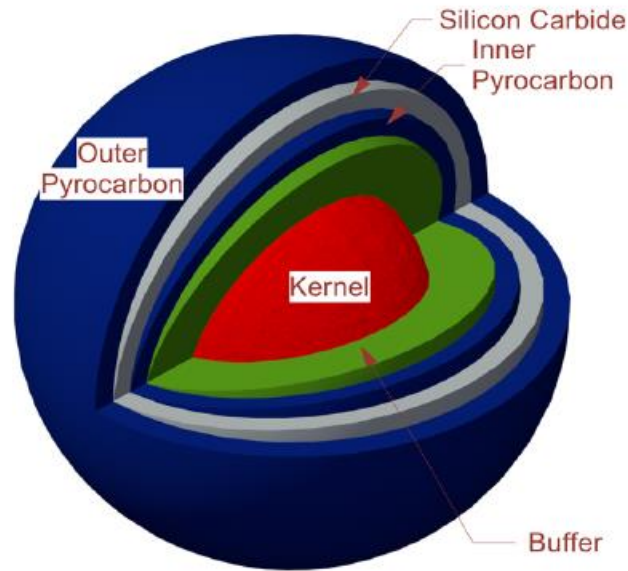


Figure 8-1. Triso particle geometry configuration [2]

Table 8-1. Triso particle parameters

Region	Parameter	value μm	Material	ρ (g/cm ³)
Kernel	diameter	427	UCO	10.9
Buffer	thickness	100	Porous graphite	1
IPyC	thickness	35	Pyrolytic graphite	1.9
SiC	thickness	35	SiC	3.2
OPyC	thickness	40	Pyrolytic graphite	1.87
Fuel Particle	diameter	847	----	----

8.1 Burnable Poison

The burnable poison is located in Pyrocarbon overcoated sintered grains of Eu_2O_3 powder; these grains are placed at the center of the plate (Figure 8-2).

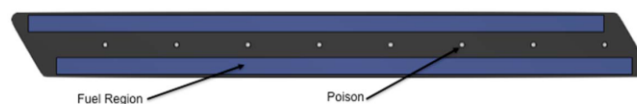


Figure 8-2. Burnable poison grains in the plate [2]

Eu_2O_3 has high thermal stability. The melting point is at 2350°C . The density of Eu_2O_3 is 5g/m^3 . The size and number of Eu_2O_3 grains can be optimized (studies available are not very accurate). The final reference design would be 5 grains with radius of 350 micron, In order to provide the required 6 months cycle [2]. For this configuration, the excess reactivity of the core is maintained below 5% for the entire equilibrium cycle.

9. Coolant

FLiBe ($2\text{LiF}\cdot\text{BeF}_2$) is used as coolant for the primary system. The Beryllium provides some moderation.

Lithium is ideally isotopically pure Li7 to minimize tritium production. 99.995%wt Li7 enrichment is generally considered the reference enrichment that can be practically achieved.

The salt is transparent.

The density is 1950 kg/m^3 at 700°C (it is temperature dependent). The melting point is 459°C .

10. References

1. Holcomb, D. E., Ilas, D., Varma, V. K., Cisneros, A. T., Kelly, R. P., & Gehin, J. C., "Core and Refueling Design Studies for the Advanced High Temperature Reactor," ORNL/TM-2011/365, Oak Ridge National Laboratory, Oak Ridge, Tenn. (September 2011).
2. V. K. Varma, D. E. Holcomb, F. J. Peretz, E. C. Bradley, D. Ilas, A. L. Qualls, N. M. Zaharia, "AHTR Mechanical, Structural, and Neutronic Preconceptual Design," ORNL/TM-2012/230, Oak Ridge National Laboratory, Oak Ridge, Tennessee (September 2012).